Imperial College of Science, Technology and Medicine
Department of Electrical and Electronic Engineering

Novel Bio-Chips for real-time detection of acidification in the tumour microenvironment

Melina Beykou

October 2024

Submitted in part fulfillment of the requirement for the degree of
Doctor of Philosophy of Imperial College London

Declaration of Originality

I hereby declare that this thesis, the research work reported and described here are entirely my own work during this PhD degree. Any research information and contributions by others are acknowledged and cited accordingly throughout.

Copyright Declaration

The copyright of this thesis rests with the author. Unless otherwise indicated, its contents are licensed under a Creative Commons Attribution-NonCommercial 4.0 International Licence (CC BY-NC).

Under this licence, you may copy and redistribute the material in any medium or format. You may also create and distribute modified versions of the work. This is on the condition that: you credit the author and do not use it, or any derivative works, for a commercial purpose.

When reusing or sharing this work, ensure you make the licence terms clear to others by naming the licence and linking to the licence text. Where a work has been adapted, you should indicate that the work has been changed and describe those changes.

Please seek permission from the copyright holder for uses of this work that are not included in this licence or permitted under UK Copyright Law.

Dedicated to my Dad.

Abstract

Cancer incidence remains a global public health concern. Timely diagnosis leads to a diverse set of treatment and disease management avenues to increase quality of life. Tumour acidification, primarily due to a metabolic phenomenon, the Warburg effect, has yet to be harnessed for early diagnostic technologies. Concurrently, ion imaging has emerged as a sensitive and rapid technology to detect ion fluctuations. The Ion-Sensitive Field-Effect Transistor (ISFET) harbours an innate pH sensitivity and has been implemented in Complementary Metal-Oxide Semiconductor (CMOS) technology, rendering it a Lab-on-Chip technology amenable to scalable diagnostics. In this thesis we present the amalgamation of ISFETs and cell culture for cancer detection, where the morphodynamics and physiological responses of cells at the sensor interface play a central role in evaluating this technology for cancer diagnosis applications. We investigate the pH changes associated with cell cultures under standard laboratory conditions and show that tumorigenic cells acidify their extracellular environment, despite excess buffering capacity of commercial media formulations. Investigation into the biocompatibility of the ISFET array implemented in unmodified CMOS, yields evidence supporting the use of ISFETs in physiologically relevant applications. Cancer cell volume, viability and adhesion remain comparable to plastic culture vessels. Surface treatment with collagen, fibronectin, or poly-l-ornithine and laminin (PLOL) recovered mechano-responsiveness, Sensor sensitivity was not inhibited. We implement a dual assay on the Titan array to 1) detect net pH change in cancer cell cultures in a short time-course and 2) rapid pH changes known to coordinate the stages of mitosis. Cell mitosis is corroborated using timelapse microscopy to determine the coordination of the population undergoing nuclear envelope breakdown. Finally, morphological, proteomic and extracellular pH changes associated with a senescent-like profile derived in breast cancer cells treated with CDK4/6 inhibitor, Palbociclib reveals the potential of pH as a biomarker for drug-resistant cell states and subtypes.

Acknowledgements

I would like to express my heartfelt appreciation to my supervisory team as well as the past and present members of their labs who have made these past four years an invaluable and memorable experience.

First of all, I would like to thank Prof. Pantelis Georgiou for his unwavering support in my research vision. Your critical insights and passion for innovation has allowed me to mature as a researcher whilst also expanding my creativity for novel diagnostic solutions. It has been an honor and a privilege to contribute to your research lab. You foster a collaborative and supportive environment amongst PhD students and postdocs in the lab that inspires us all.

I would also like to thank, Prof. Chris Bakal, co-supervisor at the Institute of Cancer Research, London. His passion for his work, thoughtful advice and expertise in the field have helped guide the direction of this thesis. He has given me amazing opportunities to expand my skillset and form multiple collaborations in diverse projects. In particular, through outreach work in the Terry Fox foundation I have had the privilege to meet individuals who are passionate about cancer diagnosis and have contributed significantly to providing perspective to the work we dedicated these four years to.

Most significantly, I would like to thank Dr. Nicolas Moser with whom I have had the honor of being one of his first PhD students from start to finish. Throughout these four years, he has supported, mentored, challenged, broadened my understanding of electrical engineering and provided me with every possible tool to excel in my PhD. He has supported and carefully listened to all the little things and big things that have taken place during these four years with patience and thoughtfulness. There are no words to reflect the difference he has made in my daily life throughout my years in the lab and I cannot wait to see the bright future he has in store.

I would also like to extend a warm thank you to my thesis viva examiners who made the experience fun and enjoyable, Prof. Sandro Carrara from EPFL and Dr. Amanda Foust from Imperial College London. I would also like to thank the examiners I have had the opportunity to have fruitful discussions with during my PhD, Dr. Amanda Foust and Prof. George Poulogiannis. They have given me valuable insights and suggestions to guide this thesis during my PhD milestones. I am also grateful for the Imperial and ICR staff who have ensured that

I felt supported and helped me obtain opportunities to extend the outreach of my research contributions and cultivate my communications skills. At the Convergence Science Centre, Dr. Dipa Gurung and Lauren Hancock, and at ICR the Communications team, who have exposed my research to the public and even led me to present my work to members of Parliament in the House of Commons.

The collaborations that I have had the opportunity to contribute to have broadened my experience during this PhD. In particular, I am grateful to Prof. Clare Isacke and George Skiadas for our ongoing collaboration on proteomics datasets. Moreover, it has been a joy to work with Yilin Sun and her supervisory team, who is an exceptional PhD colleague. For the proteomics research, which is too vast to be included in its entirety in this thesis, my thanks goes to Dr. Theodoros Roumeliotis who has helped guide my proteomics research and has been a been a wonderful mentor in the field.

The research groups both at Imperial College London and the ICR have made my PhD experience all that more enjoyable. In particular, I would like to make an honourable mention to Dr. Vicky Bousgouni, who is not only an amazing scientist and lab manager with an expertise in cell culture and microscopy that has helped hone my skills over the years, but who has also become a close friend. Most of all, I am grateful for her unwavering support and friendship over the years. Our coffee afternoons would also not be complete without Dr. Alexandra Kanellou and Dr. Evi Karali with whom we have had many laughs. I would also like to thank Matthew De Vries with whom we started this PhD journey and although we have not had particular common scientific interests, a passion for science and innovation has yielded many interesting discussions and a wonderful lab environment over the years. Also many thanks to Reed Naidoo who has been a great new addition to the lab and has helped support me in times when I could not be present in the lab during this past year.

At Imperial, I would like to particularly thank Costanza Gulli for our interesting and creative discussions on sensor detection. Her invaluable help and contribution to my understanding of ISFET detection has made this thesis come to life. I would like to thank her not only for the scientific contributions to cell detection on chip but also for her wonderful friendship. I am also very thankful to Rolando Charles, who as a UROP student has been a joy to be around and an important contributor to our work with Costanza. I would also like to extend my thanks to Dr. Lewis Keeble who has helped me realise all sorts of exciting ideas and provided training

on several specialised technologies. Katerina Mantikas and Francis Lali, thank you to both for helping with chip preparation and for being the most organised people in the lab, without whom I could not have completed this PhD in time. I would like to extend my thanks to Lei Kuang for his help with the Lacewing UI and his advice debugging experiments as well as Dr. Junming Zeng for his support to keep on going when chip experiments did not go as planned in the electronics lab. In lieu of naming the entire lab and ProtonDx members, I want to thank Tasha Walker, Elliott Quigley, Prateek Tripathi, Ryan Armiger, Dr. Matthew Cavuto and Dr. Ruth Reid for creating a fun and sociable environment in the office and making me feel a part of the group despite the challenges of sharing my time in two institutions.

To my closest friends and partner, thank you for all the words of encouragement and patience you have shown over the years after I carried on about my research ideas for the thousandth time. In my mind, you have achieved an honorary PhD just by having to go through these four years along with me.

Last but never least, I would like to thank my parents, Foteini and Romilos, without whom completing these four years would not have been possible. There is nothing harder than having to spend these years away from them but their positive attitude and unconditional love helped me power through. To my mum, you are the strongest person and without your constant encouragement to keep on going I may not have had the courage to complete this piece of work in time.

This thesis is dedicated to my Dad, who promised he would read the entire thesis and finally figure out what I was talking about for the last four years, but who never got the chance to see it through to the end. He was not only a wonderful parent but my confidante, advisor and my greatest supporter. We finally did it Dad!

Contents

Abstract **iii**

Acknowledgements **v**

1 Introduction **5**

1.1 Motivation 5

1.2 Research Objectives 7

1.3 Thesis Organization 8

1.3.1 Tumour acidification: leveraging pH for cancer diagnosis 9

1.3.2 Biosensors for ion imaging 9

1.3.3 Translation of mammalian cell culture protocols on ISFETs 9

1.3.4 Biocompatibility of ISFET arrays in unmodified CMOS technology . . . 9

1.3.5 Dynamic pH fluctuations in cancer cells on modified CMOS technology . 10

1.3.6 Proteomic characterisation and pH study of drug resistance 10

1.4 List of publications 10

2 Tumour acidification: leveraging pH for cancer diagnosis 15

2.1 The pathway to cancer diagnosis 16

2.2 Cancer biomarkers 18

2.3 Tumour acidification 19

2.3.1 Energy metabolism in cancer: The Warburg effect 21

2.3.2 Extracellular acidification mechanisms 23

2.4 pH detection *in vivo* 24

2.5 Summary 26

3 Sensors for ion imaging 33

3.1 Characteristics and classification of biosensors 34

3.2 Mammalian cell-based biosensors 35

3.3 Electrochemical detection 38

3.3.1 Complementary Metal-Oxide Semiconductor (CMOS) technology 39

3.4 Ion-Sensitive Field-Effect Transistors (ISFETs) in CMOS 43

3.5 Related works: Extracellular pH on CMOS-based ISFETs 45

3.5.1 Reported work in the literature 45

3.5.2 Lacewing: CMOS-based ISFET arrays integrated on a Lab-on-Chip platform 48

3.6 Summary 52

4 Translation of mammalian cell culture protocols on ISFETs 59

4.1 Introduction 60

4.1.1 pH regulation in cell culture media formulations 60

4.2 Molecular Methods 61

4.2.1 Cell lines 61

4.2.2 pH measurements 62

4.3 Experimental Setup 62

4.4 Characterisation of pH changes in cell culture media from cancerous and non-cancerous cell lines 63

4.5 pH detection on the Titanicks ISFET array 67

4.6 Summary and Future direction 70

5 Biocompatibility of ISFET arrays in unmodified CMOS technology 75

5.1 Introduction 76

5.2 The cell-ISFET interface 76

5.3 Materials & Methods 77

5.3.1 ISFET array configurations 77

5.3.2 Extracellular matrix deposition 78

5.3.3 Focused Ion-Beam Scanning Electron Microscopy (FIB-SEM) 78

5.3.4 Maintenance & Passaging on plastic and ISFET arrays 79

5.3.5 Focal adhesions 79

5.3.6 Immunofluorescence staining and confocal microscopy 80

5.3.7 Image processing and segmentation 80

5.3.8 Statistical analysis 81

5.4 Results & Discussion 81

5.4.1 ISFET arrays versus tissue culture plastic for cell culture 82

5.4.2 Extracellular matrix component (ECM) deposition on ISFET arrays . . . 86

5.4.3 Focal adhesion formation on a Si_3N_4 interface 90

5.4.4 Sensor sensitivity with collagen and fibronectin-coated ISFET arrays . . 92

5.4.5 Cell morphogenesis, proliferation and mechanotransduction of non-tumorigenic cell culture on a Si_3N_4 surface of ISFET arrays 92

5.4.6 Cell morphogenesis, proliferation and mechanotransduction of non-tumorigenic cell culture on ECM-treated ISFET arrays 94

5.5 Summary and future direction 97

6 Mitotic Peak Detection by pH in Cancer Cells 104

6.1 Introduction 105

6.1.1 Mitosis: an event coordinated by pH 105

6.2 Molecular Methods 108

6.3 Experimental setup and user interface 108

6.4 Microscopy 110

6.5 Data Analysis 111

6.6 Results & Discussion 113

6.6.1 Real-time detection of cancer cell acidification on CMOS ISFET array . . 113

6.6.2 Delineation of a mitotic peak detected on Titan ISFET arrays 116

6.6.3 Towards sustainability in LoC: characterisation of the effect of standard cell trypsinization protocols on ISFET passivation surface 124

6.7 Summary 125

7 Proteomic characterisation and pH study of drug resistance 131

7.1 Proteomic characterisation of triple negative breast cancer cells following CDK4/6 inhibition 132

7.2 Methodology 134

7.2.1 Cell culture 134

7.2.2 High-pH Reversed-Phase peptide fractionation and phosphopeptide enrichment 136

7.2.3 LC-MS analysis 137

7.2.4 Database search and quantification 137

7.2.5 Immunofluorescence staining & Microscopy 138

7.2.6 Data analysis 138

7.2.7 Data Records 139

7.2.8 Code availability and data processing 139

7.3 Technical Validation 139

7.3.1 Reproducibility of Replicates 139

7.3.2 Mass spectrometry 141

7.4 Results & Discussion 141

7.4.1 The Warburg effect in a senescent-like cell population 145

7.5 Summary and future direction 151

8 Conclusion **160**

8.1 Future work recommendations 161

A Palbociclib proteomics supplementary tables **163**

A.1 Regulated KEGG pathways 163

A.2 Antibodies and dyes for proteomics validation. 163

B Breast cancer cell line subtypes total proteome panel **166**

B.1 Normalisation 167

B.2 KEGG pathway enrichment of breast cancer cell subtypes 168

List of Tables

2.1 Imaging modalities for mapping pH in the clinic. 25

3.1 CMOS-based capacitance and impedance sensors for cancer cell applications. . . 42

3.2 CMOS ISFET sensors for mammalian cell detection. 51

5.1 MCF10A complete cell culture media 79

5.2 Primary and secondary antibodies for immunofluorescence staining 80

7.1 Proteomic samples overview. 135

A.1 KEGG pathways regulated in response to Palbociclib 164

A.2 Immunofluorescence antibodies and dyes 165

B.1 KEGG pathway 1D enrichment in breast cancer subtypes 168

List of Figures

2.1 Energy metabolism in normal versus cancer cells. 22

3.1 Biosensor modular schematic summary. 35

3.2 Ion-Sensitive Field-Effect Transistor (ISFET) in Complementary Metal-Oxide Semiconductor (CMOS) technology. 43

3.3 Site-binding model and ISFET passivation layers. 44

3.4 Related works of mammalian cell-based ISFET detection in CMOS 47

3.5 ISFET macromodels designed by Dr. Nicolas Moser for the Lacewing platform. . 49

3.6 Titanicks α and γ hardware. 50

3.7 Titan ISFET array hardware. 50

4.1 Conditioned media pH changes monitored in a triple negative breast cancer cell line, MDA-MB-231, and an epithelial mammary cell line, MCF10A. 65

4.2 Growth curve of breast cancer and control cell lines. 66

4.3 Voltage trace of α-Titanicks ISFET array treated with acidified cell culture media and conditioned media from breast cancer cell lines. 67

4.4 γ-Titanicks pH sensitivity detection with pH buffers 6, 7 and 8. 69

4.5 Detection of complete DMEM media on γ-Titanicks. 71

5.1 An in depth magnification into the attachment of a single breast cancer cell at the intersection of ISFET pixels. 82

5.2 FIB-SEM of breast cancer cells, MDA-MB-231, seeded on ISFET arrays. 83

5.3 Experimental workflow and cell morphology of triple-negative breast cancer cell line, MDA-MB-231, on tissue culture plastic versus the Si_3N_4 ISFET gate surface. 85

5.4 Characterisation of changes in proliferation and YAP/TAZ expression of Triple negative breast cancer cells, MDA-MB-231, on plastic cell culture plates versus the Si_3N_4 ISFET gate surface. 87

5.5 Cell adhesion, cell shape, proliferation and YAP/TAZ expression of cancer cells on Si_3N_4 interface treated with extracellular matrix components. 89

5.6 Focal adhesions of cancerous cells on standard tissue culture conditions (WT) and ISFET chip coated with fibronectin. 91

5.7 Sensor sensitivity of Titan ISFET array coated in collagen or fibronectin as evaluated with buffers. 93

5.8 Non-tumorigenic mammary epithelial cells, MCF10A, morphology and behavioural response to culture on ISFET chips with Si_3N_4 interface. 95

6.1 Model summary of cell mitosis phases. 106

6.2 Summary of key ion channel types in pH sensing in mitosis. 107

6.3 Experimental timeline and setup 109

6.4 Lacewing v5 for Titan user interface model. 110

6.5 Representative chemical readout measurements for osteosarcoma cells on Titan arrays. 114

6.6 Mean Total drift and mean standard deviation between media control and cancer cell wells on Titan. 115

6.7 Representative confocal microscopy images of nuclei labelled with H2B-mCherry in a 4-well manifold of a Titan ISFET array. 116

6.8 Mean normalised drift and standard deviation between cancer cells and media cultured on Titan CMOS ISFET arrays. 117

6.9 Growth and mitotic stage of U2OS CDK1 AS cells on 2D plastic treated with ATP analog inhibitor NM-PP1 versus untreated controls. 118

6.10 Case study for the detection of an acidification peak at mitotic entry. 120

6.11 Spatiotemporal layout of the time of peak in each Titan well. 121

6.12 Timelapse microscopy of NM-PP1-treated U2OS CDK1 AS H2B mCherry on a Titan ISFET array. 122

6.13 Summary of pHe, pHi and pHn changes upon nuclear envelope breakdown from early prophase to late prophase/early metaphase stage of mitosis. 124

6.14 Characterisation of hafnium and silicon elements at the Titan passivation surface after trypsinization. 126

7.1 CDK4/6 inhibitor, Palbociclib, arrests cells in the G1 phase of mitosis. 132

7.2 Overview of drug treatment regime with CDK4/6 inhibitor Palbociclib. 136

7.3 Reproducibility of proteomic samples. 140

7.4 Technical validation of mass spectrometry analysis. 141

7.5 Validation of senescence-like morphology and immunofluorescence staining of key senescence biomarkers. 143

7.6 Validation of key senescence markers in total proteome and phosphoproteome. . 144

7.7 Validation of key senescence markers in total proteome and phosphoproteome. . 145

7.8 Significantly upregulated and downregulated proteins upon 7 days Palbociclib treatment of MDA-MB-231. 146

7.9 KEGG pathway enrichment of significantly upregulated proteins in 7 days treated Palbociclib MDA-MB-231 samples (FBS and starved samples) versus their respective DMSO control samples. 148

7.10 Physical network analysis of significantly upregulated and downregulated total protein upon Palbociclib treatment of MDA-MB-231 cells. 149

7.11 Enrichment of proteins found in KEGG pathways for oxidative phosphorylation. 150

7.12 Graphical summary of the Warburg effect in a senescent-like population arising from CDK4/6 inhibition in triple negative breast cancer cells. 151

7.13 pH changes in cell culture of Palbociclib-treated MDA-MB-231 cells. 152

7.14 Long-term culture of MDA-MB-231 in Palbociclib supplemented media and washout rescue. 153

B.1 Normalised counts for total proteome of each cell lines sample replicate in the dataset. 167

Abbreviations

LoC	Lab-on-Chip
PoC	Point-of-Care
ISFET	Ion-Sensitive Field-Effect Transistor
CMOS	Complementary Metal-Oxide Semiconductor
IARC	International Agency for Research on Cancer
ATP	Adenosine Triphosphate
MRS	Magnetic Resonance Spectroscopy
MRI CEST	Magnetic Resonance Imaginge Chemical Exchange Saturation Transfer
PET	Positron Emission Tomography
CT	Computed Tomography
NHS	National Health Services
HDI	Human Development Index
SNP	Single Nucleotide Polymorphism
CEA	Carcinoembryonic Antigen
PSA	Prostate-Specific Antigen
TME	Tumour microenvironment
EMT	Epithelial-to-Mesenchymal Transition
pHe	Extracellular pH
pHi	Intracellular pH
TCA cycle	Tricarboxylic acid cycle
CO_2	Carbon dioxide
HCO_3^-	Bicarbonate ion
H^+	Hydrogen ion
CA	Carbonic Anhydrase
MCT4	Monocarboxylate transporter 4
Na^+	Sodium ion
NHE1	Na^+/H^+ exchanger 1
NBC	Sodium bicarbonate co-transporter

AE	Anion Exchanger
HIF-1a	Hypoxia-inducible factor 1a
EPR	Electron Paramagnetic Resonance
SPR	Surface Plasmon Resonance
LSPR	Low Surface Plasmon Resonance
FRET	Förster Resonance Energy Transfer
PCF	Photonic Crystal Fiber
QCM	Quartz Crystal Microbalance
IC	Integrated Circuit
ECIS	Electric-Cell Substrate Impedance Sensing
EIS	Electrical-Impedance Spectroscopy
FED	Field-Effect Device
K^+	Potassium ion
Ca^{2+}	Calcium ion
ISE	Ion Sensitive Electrode
LAPS	Light-Addressable Potentiometric Sensing
MOSFET	Metal-Oxide Semiconductor Field-Effect Transistor
-OH	Hydroxyl group
SiO_2	Silicon dioxide
Si_3N_4	Silicon nitride
Al_2O_3	Aluminium oxide
Ta_2O_5	Tantalum pentoxide
UV	Ultraviolet
FET	Field-Effect Transistor
LAMP	Loop-Mediated Isothermal Amplification
SNV	Single Nucleotide Variant
FET	Field-Effect Transistor
CMS™	Cell Monitoring System
FBS	Foetal Bovine Serum
DMEM	Dulbecco's Modified Eagle's Medium
TNBC	Triple Negative Breast Cancer
P/S	Penicillin/Streptomycin
HPLM	Human Plasma-like Medium
ISO	International Organization for Standardization
PLOL	Poly-l-ornithine and Laminin
FIB-SEM	Focused Ion-Beam Scanning Electron Microscopy
HMDS	Hexamethyldisilizane

TIRF	Total Internal Reflection Fluorescence
BSA	Bovine Serum Albumin
PCB	Printed Circuit Board
TC	Tissue Culture
KDE	Kernel Density Estimation
KS	Kolmogorov-Smirnov
CDF	Cumulative Distribution Function
ECM	Extracellular Matrix
FN	Fibronectin
FA	Focal Adhesion
WT	Wild-type
CDK	Cyclin-Dependent Kinase
$\mathbf{V_m}$	Membrane potential
ASIC	Acid-Sensing ion channel
$\mathbf{V_{ref}}$	Reference Voltage
PFA	Paraformaldehyde
EDX	Energy dispersive X-ray
Rb	Retinoblastoma protein
$\mathbf{HR^+}$	Hormone Receptor positive
FET	Field-Effect Transistor
TEAB	Triethylammonium Bicarbonate
TCEP	Tris-2-Carboxyethyl Phosphine
IAA	Iodoacetamide
TCA	trichloroacetic acid (TCA)
$\mathbf{NaN_3}$	Sodium azide
PCA	Principal Component Analysis
Log2FC	Log2 Fold Change
IFN	Interferon
IAA	Iodoacetamide
2-DG	2-deoxyglucose

Chapter 1

Introduction

1.1 Motivation

Cancer incidence has emerged as "the silent pandemic" of the 21st century. With almost 20 million cases of 36 different cancer types recorded globally in 2022, cancer is the fastest growing public health concern [1, 2]. The burden of cancer incidence and mortality rates is also reflected in the strain on public health infrastructures as well as economic and social health on a global scale. Epidemiological trends of cancer incidence reported by the WHO International Agency for Research on Cancer (IARC) extrapolate that global cancer cases will reach 35 million by 2050 [1]. Although the incidence problem seems to be getting worse, the mortality rate and quality of life of patients diagnosed early has improved drastically [3, 4]. Early diagnosis of cancer gives patients a wider range of treatment options and access to effective cancer management [5]. In recent years, governing bodies and the research community have shifted their focus to promote initiatives centred on cancer prevention and early detection of cancer progression. However, current diagnosis patterns in the clinic are limited by reactive testing based on symptom onset [4, 5].

The spectrum of early diagnosis can vary from the pre-symptomatic stages of disease to the identification of tumour recurrence. In the UK, the introduction of three screening programmes against breast, cervical and bowel cancer in at-risk age groups, have shown promising results to culminate the cases of the respective cancer types diagnosed prior to any symptom onset [6–9]. The effectiveness of national screening programmes has been reflected in the decline of late-stage diagnoses of these cancer types [1, 9]. The main challenges facing screening programmes is not only voluntary participation and disproportionate engagement of individuals with access to healthcare schemes, but also the heterogeneity of cancer types [4, 10]. Cancer-type dependent biomarkers have shown variable reliability due to the heterogeneity of this disease making it that much more challenging to identify. For example, PSA levels have been good predictors of prostate cancer onset but also show variable levels in different demographics and genetic

backgrounds leading to over-diagnoses [10]. Limitations surrounding biomarkers for specific cancer types and encompassing disease heterogeneity can be challenging [11].

Cancer biomarkers come in many different flavours: genetic (DNA), transcriptional (RNA), epigenetic, proteomic and cellular properties [12]. Despite the search for cancer biomarkers and their predictive powers being a key focus of the research community and facing much success, few biomarker assays and technologies have been approved for wider clinical validation and testing [11]. This highlights a major challenge of early diagnosis - the development of sensitive, affordable and specific technologies for cancer detection.

Today, a hundred years since its inception, metabolic re-programming known as the "The Warburg Effect" has re-gained traction as a biomarker for cancer progression, drug resistance and tumour recurrence [13–15]. The importance of cellular homeostasis in energy metabolism can be highlighted by its role in all aspects of cell proliferation and growth, including transcription, translation and anabolic pathways which provide the building blocks for life [13]. Mammalian cells require energy in the form of adenosine triphosphate (ATP) in order to survive. There are two main pathways via which ATP production from glucose can take place – oxidative phosphorylation and glycolysis. In 1924, Otto Warburg demonstrated that cancer cells preferentially undergo a switch to aerobic glycolysis for their predominant energy metabolism whilst also maintaining levels of oxidative phosphorylation [16–18]. Similar to muscle cells during vigorous exercise, excess lactate production leads to its breakdown and H^+ extrusion from cells in order to maintain acid-base homeostasis, leading to an acidic tumour microenvironment and an alkaline intracellular pH [19]. The creation of an inversed pH gradient has been shown to be independent of cancer type and origin and has implications for key cancer hallmarks such as proliferation, immune evasion, metastatic clones, apoptotic resilience and transcription dysregulation [13, 14, 19]. The widespread phenomenon of the Warburg effect both bio-energetically and as a biophysical property of tumour microenvironment acidification makes it a potential biomarker for cancer early diagnosis.

Whilst pH mapping of tumours *in vivo* is not currently standard practice, the prognostic value of extracellular acidification has led to the development of various imaging modalities. More specifically, Magnetic Resonance Spectroscopy (MRS), MRI Chemical Exchange Saturation Imaging (MRI CEST), Positron Emission Tomography (PET), fluorescent probes for optical imaging (e.g. SNARF1) as well as photoacoustic imaging, are some of the many techniques which have been validated both *in vitro* and *in vivo* to provide a mapping of the pH landscape in the tumour microenvironment [20, 21]. Despite the discovery of several pH-sensitive probes and substrates to satisfy the complexities of the tumour microenvironment, the aforementioned techniques are limited by low throughput, low quantitative accuracy, low affordability and intrusiveness.

Current patterns highlight a key gap in early diagnosis strategies: a shortage of rapid, sensi-

tive and non-invasive diagnostic technologies which leverage universal, biophysical properties of cancer cells and perform direct functional readouts of early disease onset. New tools and technologies to bridge the gap between innovative research and patient benefit could provide a new avenue for cancer diagnosis in the clinic. Following Moore's law for the miniaturization of transistors in integrated circuits, Complementary Metal-Oxide Semiconductor (CMOS) technology has given rise to an era of silicon-based biomedical sensors with electrochemical capabilities which centre on scalability and affordability [22]. This has led to a whole host of bio-inspired technology for Point-of-Care (PoC) diagnostic devices, including optical and electrochemical Lab-on-Chip (LoC) techniques where the latter has the opportunity of being a label-free technology. LoC integrated Ion-Sensitive Field-Effect Transistor (ISFET) arrays for biochemical detection are a particularly great solution for integration in CMOS. [23]. The inherent pH sensitivity which arises in ISFET arrays manufactured in unmodified CMOS has been leveraged for a number of applications including DNA and RNA detection for infectious diseases, and epigenetic modifications [24–27]. Although investigation of cell detection by ISFETs utilizing the unique properties of pH as a biomarker for cancer progression has been researched by a few groups in the last 20 years, translation to potential PoC technologies has not been achieved despite the promising data arising from pH mapping of tumours [28–30]. While PoC diagnostics hold promise for low-cost, accessible and rapid diagnostic solutions, they are not yet a widespread reality in the commercial market. Although promising, barriers including regulatory approval, standardisation of results as well as repeatability and sensitivity remain a hindrance to market adoption. This technology and knowledge gap has motivated the research presented here to provide an understanding of the morphodynamics at play in LoC technologies and develop a rapid and sensitive cell detection on-chip assay to be leveraged towards an early cancer diagnostic technology.

1.2 Research Objectives

This research aims to bridge the current disconnect in CMOS-based ISFET research and cell-based detection for biological studies of cancer tissue with regards to early cancer diagnosis. The importance of physiologically relevant morphology, mechanistic response, growth and attachment is evaluated on 0.35 μm CMOS ISFET arrays and extracellular matrix components are proposed as surface treatments to improve biocompatibility without compromising sensor sensitivity. Extracellular pH is investigated as a potential biomarker for detection of cancer cells in *in vitro* cell cultures, cell division and cell states arising with drug treatment by CDK4/6 inhibitor, Palbociclib. This study utilises 0.35 μm CMOS ISFET arrays, as opposed to the more advanced 28nm CMOS process, due to the typical scale of mammalian cells where the order of magnitude is 10-100 μm. The 0.35 μm CMOS process offers sufficient resolution to interface with the larger biological features while keeping power consumption, cost and com-

plexity manageable. Additionally, this study utilises three ISFET array designs by Dr. Nicolas Moser. The α-Titanicks 78 x 56 ISFET array features a Si_3N_4 passivation layer whilst the γ-Titanicks is an array of the same size featuring a 20nm HfO_2 passivation layer. The Titan design is a larger array of 290 x 204 pixels with a 20nm HfO_2 layer.

The following research objectives have guided this research and will be addressed in this thesis:

1. What is the scale of pH changes which can be attributed to malignant breast cancer cell lines and healthy mammary epithelial cells under standard culture conditions?
2. How does the complex formulation of DMEM culture media affect sensor sensitivity in α and γ Titanicks?
3. Is the ISFET passivation layer biocompatible and does it affect cell attachment, morphology, viability or mechano-response? What is the biocompatibility comparison with commercial culture vessels?
4. Does surface treatment with extracellular matrix components change the biocompatibility and/or sensitivity of the sensor surface?
5. What are the net pH changes (start versus end), drift profile and noise arising from cell culture of cancer cells on the Titan ISFET array?
6. Can we design an assay to detect a cellular event, such as mitosis, where pH change is abrupt and detect it on the ISFET array in real time?
7. In a cancer cell population where partial drug resistance is observed by a cell cycle inhibitor, what are the proteomic characteristics of this senescent-like cell population and how do they compare to the untreated cancer cells? What is the metabolic profile of this cell state?
8. Can we identify a change in cell culture pH arising in this senescent-like cell state? How do any pH changes compare to those observed in untreated cancer cells and healthy cells?

1.3 Thesis Organization

This thesis is structured into 8 chapters including an introduction to the objectives addressed with this research. The organisation of chapters follows a sequence of 1) Biological context, 2) Sensor technologies , 3) cell-sensor interface evaluation and 4) cell-based applications on ISFET arrays, and a final chapter on future directions for the ISFET sensor in cancer cell detection.

1.3.1 Tumour acidification: leveraging pH for cancer diagnosis

Chapter 2 introduces the diagnostic avenues followed to obtain a cancer diagnosis and the ongoing burden of cancer incidence on a global level. We discuss the benefits and challenges of early diagnosis with a focus on the discovery of novel biomarkers. Tumour acidification is presented as a potential biomarker candidate for early diagnosis of multiple cancer types. Context of the origins of tumour acidification is given, with a centre role for the Warburg effect and we discuss the complexities of acid-base homeostasis *in vivo*. Finally, the current technologies for pH imaging and detection in the clinic are summarised.

1.3.2 Biosensors for ion imaging

Chapter 3 presents the components and transducer classification of biosensors (mechanical, optical and electrochemical). Furthermore, we discuss the challenges associated with mammalian cell-based applications of biosensors. Additionally, we review available literature in optical, mechanical and electrochemical biosensors for cancer cell detection. In the field of electrochemical sensors we focus on the implementation of Complementary Metal-Oxide Semiconductor technology and introduce the Ion Sensitive Field Effect Transistor (ISFET). We discuss related works of cell-based ISFET technologies for cancer detection and lastly, introduce the ISFET arrays (α, γ- Titanicks and Titan) utilised in this thesis.

1.3.3 Translation of mammalian cell culture protocols on ISFETs

Chapter 4 discusses the cell culture media formulation and buffering system employed in standard cell culture protocols. We evaluate the effect of cell culture media on α and γ - Titanicks sensor sensitivity with buffers in the physiological range. Moreover, the pH changes associated with cell culture of tumorigenic and non-tumorigenic cells is evaluated with growth confirmation. The conditioned media from triple negative breast cancer cell lines is investigated on γ-Titanicks chips to determine pH change and the effect of cell culture media on the sensor.

1.3.4 Biocompatibility of ISFET arrays in unmodified CMOS technology

Chapter 5 investigates the biocompatibility of ISFET arrays implemented in unmodified CMOS technology. We assess cell attachment and examine markers of cell viability, growth and mechano-responsiveness through microscopy and image segmentation techniques and compare

to commercially available cell culture vessels. We use a linear classifier to evaluate the morphology of tumorigenic and non-tumorigenic cells of the same tissue origin. Furthermore, we determine changes in focal adhesion formation on the ISFET interface. Lastly, an assessment of surface matrix treatments for enhancement of biocompatibility properties on ISFET arrays is evaluated.

1.3.5 Dynamic pH fluctuations in cancer cells on modified CMOS technology

In chapter 6 we introduce the intracellular and extracellular pH changes associated with coordinating the stages of mitosis. We develop an on-chip assay to detect long-term pH changes and abrupt pH changes attributed to mitosis in real-time. We show morphological changes and cell growth associated with an "acidification peak" of mitosis. Finally, we characterise the surface at the experiment end-point using a trypsinization protocol and show sustainable practices are an option in complex, cell culture on chip.

1.3.6 Proteomic characterisation and pH study of drug resistance

Chapter 7 explores the spectrum of cell states which arise in response to drug resistance. It introduces the cell cycle mechanisms integral to mammalian cell division and the drug targets which are available. CDK4/6 inhibitors and the resulting cell state which is observed in resistant cell lines is taken under consideration. We characterise the metabolic profile of this cell state and explore biomarkers for use in diagnosis of a senescence-like state which arises in response to Palbociclib. Proteomic, phosphoproteomic and secretome analysis inform potential targets for on chip detection.

1.4 List of publications

Included in this thesis

1. Beykou, M., Arias-Garcia, M., Roumeliotis, T.I., Choudhary, J.S., Moser, N., Georgiou, P., & Bakal, C. "Proteomic characterisation of triple negative breast cancer cells following CDK4/6 inhibition". In: *Scientific Data* 395.9 (Jul. 2022).

2. Beykou, M., Bousgouni, V., Moser, N., Georgiou, P., & Bakal, C. "Biocompatibility characterisation of CMOS-based Lab-on-Chip electrochemical sensors for in vitro cancer cell culture applications". In: *Biosensors and Bioelectronics* 262,(Nov. 2024).

3. Beykou, M., Gulli, C., Bousgouni, V., Moser, N., Bakal, C., & Georgiou, P. "Dynamic pH fluctuations in cancer cells on CMOS-based Lab-on-Chip ISFET arrays". *Accepted in IEEE BioCAS 2024* (October 2024).

Collaborations and related publications

1. Quicke, P., Sun, Y., Arias-Garcia, M., Beykou, M., Acker, C.D., Djamgoz, M.B.A., Bakal, C. & Foust, A.J., "Voltage imaging reveals the dynamic electrical signatures of human breast cancer cells". In:*Communications Biology* 5.1 (Nov. 2022), pp. 1–14.

2. Leslie, T.K., Tripp, A., James, A.D., Fraser, S. P., Nelson, M., Sajjaboontawee, N., Capatina, A. L.,Toss, M., Fadhil, W.,Salvage, S. C., Garcia, M.A., Beykou, M., Rakha, E., Speirs, V., Bakal, C., Poulogiannis, G., Djamgoz, M.B.A., Jackson, A. P., Matthews, H.R., Huang, C.L.H., Holding, A. N., Chawla, S. & Brackenbury, W.J., "A novel Nav1.5-dependent feedback mechanism driving glycolytic acidification in breast cancer metastasis". In: *Oncogene* 43 (Jun. 2024), pp. 2578-2594.

3. Jones, I., Garcia, M.A., Pascual-Vargas, P., Beykou, M., Dent, L., Palchaudhuri, T., Roumeliotis, T., Choudhary, J., Sero, J. & Bakal, C., "YAP activation is robust to dilution". In: *Molecular Omics* (Aug. 2024).

Conferences and outreach

1. Winner of UK Circuits Systems Group (UKCAS) 3-minute PhD Pitch Competition 2020.

2. Flash Talk at the Beatson International Cancer Conference 2021.

3. High commendation for image submitted to Organ-on-Chip Technologies Network 2022 (in collaboration with Lewis Keeble, PhD student, Georgiou group, Imperial College London).

4. Ambassador for the Institute of Cancer Research at the CRICK London Cell Motility Club 2022.

5. Poster presentation at the Annual Biomedical Engineering Society meeting 2022, San Antonio, Texas.

6. Outreach with Humans of Health Research, AHSC, Imperial College London.

7. IEEE Biomedical Circuits&Systems conference 2024.

References

[1] F. Bray et al. "Global cancer statistics 2022: GLOBOCAN estimates of incidence and mortality worldwide for 36 cancers in 185 countries". In: *CA: A Cancer Journal for Clinicians* 74.3 (May 2024), pp. 229–263.

[2] World Health Organization (WHO). *Cancer prevention and control in the context of an integrated approach*. Tech. rep. December. 2017, pp. 1–9.

[3] N. Bannister and J. Broggio. *Cancer survival by stage at diagnosis for England (experimental statistics) - Office for National Statistics*. 2016.

[4] D. Crosby et al. "Early detection of cancer". In: *Science* 375.6586 (Mar. 2022).

[5] R. C. Fitzgerald et al. "The future of early cancer detection". In: *Nature Medicine* 28.4 (Apr. 2022), pp. 666–677.

[6] NHS. *Cancer - NHS*. 2019.

[7] IARC. *CanScreen5*.

[8] L. Zhang et al. "An international consensus on the essential and desirable criteria for an 'organized' cancer screening programme". In: *BMC Medicine* 20.1 (Dec. 2022), pp. 1–10.

[9] CRUK. *Screening for cancer — Cancer Research UK*. 2016.

[10] D. R. Blake et al. "Improving Participation in Chlamydia Screening Programs". In: *Archives of Pediatrics & Adolescent Medicine*. Vol. 157. 6. National Academies Press (US), 2003. Chap. 6, p. 523.

[11] S. K. Chatterjee and B. R. Zetter. "Cancer biomarkers: Knowing the present and predicting the future". In: *Future Oncology* 1.1 (2005), pp. 37–50.

[12] A. Passaro et al. "Cancer biomarkers: Emerging trends and clinical implications for personalized treatment". In: *Cell* 187.7 (Mar. 2024), pp. 1617–1635.

[13] D. Hanahan and R. A. Weinberg. "Hallmarks of cancer: The next generation". In: *Cell* 144.5 (Mar. 2011), pp. 646–674.

[14] B. A. Webb et al. "Dysregulated pH: A perfect storm for cancer progression". In: *Nature Reviews Cancer* 11.9 (Sept. 2011), pp. 671–677.

[15] E. Boedtkjer and S. F. Pedersen. “The Acidic Tumor Microenvironment as a Driver of Cancer”. In: *Annual Review of Physiology* 82 (2020), pp. 103–126.

[16] O. Warburg and S. Minami. “Versuche an Überlebendem Carcinom-gewebe”. In: *Klinische Wochenschrift* 2.17 (Apr. 1923), pp. 776–777.

[17] O. Warburg, F. Wind, and E. Negelein. “The metabolism of tumors in the body”. In: *Journal of General Physiology* 8.6 (Mar. 1927), pp. 519–530.

[18] O. Warburg. “On the origin of cancer cells”. In: *Science* 123.3191 (1956), pp. 309–314.

[19] P. Swietach, E. Boedtkjer, and S. F. Pedersen. “How protons pave the way to aggressive cancers”. In: *Nature Reviews Cancer* 23.12 (Oct. 2023), pp. 825–841.

[20] A. Anemone et al. “Imaging tumor acidosis: a survey of the available techniques for mapping in vivo tumor pH”. In: *Cancer and Metastasis Reviews* 38.1-2 (June 2019), pp. 25–49.

[21] X. Zhang, Y. Lin, and R. J. Gillies. “Tumor pH and its measurement”. In: *Journal of Nuclear Medicine* 51.8 (Aug. 2010), pp. 1167–1170.

[22] S. E. Thompson and S. Parthasarathy. “Moore’s law: the future of Si microelectronics”. In: *Materials Today* 9.6 (June 2006), pp. 20–25.

[23] N. Moser et al. “ISFETs in CMOS and Emergent Trends in Instrumentation: A Review”. In: *IEEE Sensors Journal* 16.17 (Sept. 2016), pp. 6496–6514.

[24] J. Rodriguez-Manzano et al. “Handheld point-of-care system for rapid detection of SARS-CoV-2 extracted RNA in under 20 min”. In: *ACS Central Science* 7.2 (Feb. 2021), pp. 307–317.

[25] N. Moser et al. “A scalable ISFET sensing and memory array with sensor auto-calibration for on-chip real-time DNA detection”. In: *IEEE Transactions on Biomedical Circuits and Systems* 12.2 (Apr. 2018), pp. 390–401.

[26] J. Broomfield et al. “Handheld ISFET Lab-on-Chip Detection of TMPRSS2-ERG and AR mRNA for Prostate Cancer Prognostics”. In: *IEEE Sensors Letters* 7.8 (Aug. 2023), pp. 1–4.

[27] M. Kalofonou and C. Toumazou. “An ISFET based analogue ratiometric method for DNA methylation detection”. In: *Proceedings - IEEE International Symposium on Circuits and Systems* (2014), pp. 1832–1835.

[28] M. Lehmann et al. “Simultaneous measurement of cellular respiration and acidification with a single CMOS ISFET”. In: *Biosensors and Bioelectronics* 16.3 (May 2001), pp. 195–203.

[29] M. J. Milgrew, M. O. Riehle, and D. R. Cumming. “A large transistor-based sensor array chip for direct extracellular imaging”. In: *Sensors and Actuators, B: Chemical* 111-112.SUPPL. (Nov. 2005), pp. 347–353.

[30] T. Sakata, H. Sugimoto, and A. Saito. “Live Monitoring of Microenvironmental pH Based on Extracellular Acidosis around Cancer Cells with Cell-Coupled Gate Ion-Sensitive Field-Effect Transistor”. In: *Analytical Chemistry* 90.21 (Nov. 2018), pp. 12731–12736.

Chapter 2

Tumour acidification: leveraging pH for cancer diagnosis

Cancer is a multi-faceted disease and heterogeneous by nature which has made early diagnosis of both primary and recurrent tumours an ongoing challenge in the global healthcare sector. Despite advances in treatments and disease management, early diagnosis remains the ideal goal to be able to combat rising incidence rates of all cancer types. Concurrently, timely diagnosis in low income settings faces barriers with costly and inaccessible technologies being a driver of cancer mortality and morbidity rates in these regions. A challenge to address in early diagnostics is the identification of a biomarker which will be: (a) non-invasive, (b) provide optimum detection of most cancer types and (c) easily identifiable with affordable diagnostics.

This chapter will present the cancer diagnosis pathway in the clinic and explore the use of tumour acidification as a biomarker for cancer diagnostics. Firstly, an introduction to common cancer diagnosis procedures found in the clinic is summarised and some of the challenges in the cancer diagnosis pipeline are presented. A brief overview of approved biomarkers for different cancer types that are routinely tested for is presented. Furthermore, the mechanisms of tumour acidification and the role of pH in cancer progression will be discussed. The final section will explore the use of pH as a biomarker both *in vivo* and *in vitro* and the advantages associated with routine pH testing of cancer cells.

2.1 The pathway to cancer diagnosis

The ongoing challenge of early cancer diagnosis is a global concern as cancer incidence rates continue to rise. Despite some national screening programmes, particularly in developed countries, there remains a large proportion of individuals who will present in primary care settings with symptoms and enter a diagnosis pathway [1, 2]. As part of a diagnosis timeline [3–5], there are 3 general phases once a physical examination and medical history has been obtained:

(a) **Laboratory tests:** routine blood tests (red blood cell count, white blood cell count), urine tests (protein, sugars etc.) and cytology (dependant on cancer type suspected).

(b) **Imaging tests:** This may include ultrasound of the suspected area, X-ray examinations, Positron Emission Tomography (PET) scan, Computed Tomography (CT) or Magnetic Resonance Imaging. These modalities are used in an exploratory manner to collect information depending on the organ, suspected cancer type and site accessibility. Both quantitative and qualitative information can be collected including metabolic state of tissue.

(c) **Biopsy and endoscopy:** Fine needle or surgical biopsy may be necessary to obtain a sample of tissue from the suspected cancerous area and perform cytology, histopathology and biomarker testing for subsequent treatment. An endoscopy procedure (e.g. colonoscopy, bronchoscopy) may be available under certain conditions.

Every stage requires both experienced healthcare professionals, including nurses, doctors, radiologists and pathologists, but are also dependant on the appropriate infrastructures, such as access to MRI machinery [2, 4]. These procedures can be inaccessible, costly, and invasive for the patient [2]. Additionally, upon referral to specialist services, waiting times for diagnosis can persist which can instill periods of anxiety and stress for prospective patients who are unsure of their diagnosis. In the UK, a 62-day target has been established by National Health Services (NHS) England, however, for many patients this target is still not met, likely due to the burden on public health services [6]. Furthermore, in light of the COVID-19 pandemic, the strain on global health services has become evident, with many patients requiring testing and treatment, who are struggling to obtain timely access due to a backlog of referrals [7, 8]. Notably, for a subset of patients the journey doesn't end with treatment as drug resistance and tumour recurrence – the re-growth of the same type of tumour, are well-known occurrences. Despite advances in chemotherapies and immunotherapies, drug resistance and tumour recurrence incidence remain high for several cancer types [9–11]. In a clinical setting, patients must undergo post-treatment testing to check for tumour growth, however imaging methods are often not included in the testing. As such, recurrence is often diagnosed upon symptom onset which

allows limited time to administer treatment [1, 10–12]. In fact, some cancer types are known to recur more frequently than others, although the stage of the primary tumour in an initial diagnosis also plays a role in recurrence incidence. For example, ovarian cancer is estimated to recur in 85% of patients and breast cancer recurrence occurs in approximately 30% of patients diagnosed with the disease [13, 14]. The inaccessibility, invasiveness and costly process of diagnosis means that patients often face long waiting times and several weeks of stress before being able to receive a diagnosis.

Challenges to early diagnosis

A review by Crosby et al. (2022) [12], set out the driving challenges to be addressed for early cancer diagnosis in order to create a comprehensive roadmap for the research community:

1. Understanding the biology behind cancer progression
2. Risk-stratification of populations
3. Biomarker discovery and validation
4. Technology development for diagnostics
5. Wide-scale evaluation of diagnostic approach

Following these guidelines, researchers have made considerable efforts to address the need for novel biomarker discovery as well as specific and sensitive LoC diagnostics which has paved the way for technological advancements in Point-of-Care (PoC) devices for cancer early diagnosis. However, a challenge still remains in considering the variable settings in which early cancer diagnostics need to be deployed.

A significant percentage of the global population faces considerable challenges when seeking an early cancer diagnosis, whether that is through a pre-symptomatic screening programme or symptomatic testing in primary care. The World Health Organisation has coined the term human development index (HDI) in order to encompass the key contributors to human health in a country and drive public health reformation globally. The metric includes life expectancy, completion of education and economic status per capita [15]. Whilst the highest rates of cancer incidence are seen in high HDI parts of the world, both low and middle HDI countries face the highest projected increase by the year 2050 [15]. In high HDI settings, the availability of cancer screening programs to individuals in at-risk groups based on hereditary factors, age or gender has increased the diagnosis rates of a number of cancer types, such as breast and cervical cancer [12]. By comparison, low HDI countries have limited availability of screening

programmes, however, initiatives by the WHO and local governments have resulted in key trials against well-known and treatable cancer types such as the ongoing cervical screening trial in Nigeria [16]. The lack of national screening in many low/middle HDI countries, highlights one of the key disparities in these regions, where early diagnosis through asymptomatic testing may not be feasible due to inaccessible healthcare in remote areas, education and national economic constraints [17]. Mortality rates for cancer types with a range of treatment options, such as breast cancer, are recorded to be the highest in African and Asian countries which is likely to be attributed to late stage disease [15]. On the other hand, countries on the European continent, have the highest incidence and mortality rates overall which may not only be attributed to more testing in certain regions but also to lifestyle and societal disparities, where individuals may benefit disproportionately from cancer diagnosis and treatment frameworks [15]. These complexities of addressing the call for early cancer diagnosis in variable HDI settings, highlights the need for both affordable, ease-of-use and rapid diagnostic tests and an integration in portable, PoC diagnostic devices in order to make early cancer diagnostics accessible to both high and low HDI regions.

2.2 Cancer biomarkers

Cancer is considered a collection of diseases characterized by malignant, cellular transformation and pathogenesis. With a better understanding of the complicated biology of cancer development and progression, so changes our definition of "cancer" and the way we perceive the challenges associated with diagnosis, prognosis and treatment of the disease. The characteristics of modern definitions centre on the aberrant proliferation of transformed cells such that natural selection will favour tumour cells which can adapt to changing conditions and lead to metastasis to other body sites [18]. This has given rise to a set of key "hallmarks" of cancer which seek to identify the driving forces and distinctive features to help develop novel diagnostic technologies. Hanahan & Weinberg proposed eight drivers of oncogenesis that drive cancer progression in all cancers amongst which immune evasion, deregulated metabolism, angiogenesis, metastasis, aberrant growth and resistance to apoptosis guide the potential markers for cancer detection [19].

A biomarker is defined as a "biological molecule found in blood, other body fluids or tissues, that is a sign of a normal or abnormal process, or of a condition or disease" [20]. Cancer biomarkers are characteristics of cancer that can be diagnostic (differentiate between healthy and malignant lesions), prognostic (determine the aggressiveness of the cancer cells) or predictive (inform treatment stratification and recurrence) [21, 22]. They typically arise from genetic mutations or alterations which are drivers of cancer progression in a particular cancer type. In the past, cancer biomarker discovery was dependant on immunological or biochemical assays

to determine the presence of a substance in blood or on a tissue sample, however, advances in "omics" technologies and bioinformatics tools have led to more rigorous investigations [22]. High-throughput technology has revolutionized biomarker discovery by allowing access to genomic, epigenomic, transcriptional, proteomic and metabolomic data for different cancer types [23]. As such, biomarkers fall into one of the following detectable categories: nucleic acids (DNA/RNA, including single nucleotide polymorphisms (SNPs) and microRNAs), epigenetic (e.g. hypermethylation), proteins (antigens/receptors/immune markers), metabolites (e.g. glucose) or cellular processes [23].

Despite many biomarkers being identified in research, few have been interrogated on a population level in both an *in vitro* and *in vivo* context. Accuracy, repeatability, specificity and patient benefit are only a few of the challenges associated with the validation of biomarkers. For example, carcinoembryonic antigen (CEA) was discovered in 1965 and is still in use today as a diagnostic and prognostic marker for colorectal cancer. A review of clinical trials has shown that CEA sensitivity is low in serum where renal clearance and blood dilution may play a role, but can also be associated with most other cancer types and other conditions, including liver disease, Crohn's disease, hypothyroidism and pancreatitis [23, 24]. Most notably, CEA can be detected in non-malignant breast conditions as well as breast cancer patients, making it a non-specific disease marker [24]. In a similar way, the use of CA-125 for ovarian cancer diagnosis can lead to over-diagnoses due to low sensitivity and accuracy in endometriosis patients [25]. Neither of these markers clinical use waned over the years but instead are now used in combination with other diagnostic tests and serum markers [26]. Finally, one of the most commonly used biomarkers is Prostate-Specific Antigen (PSA) which is screened for in the at-risk male population. In recent years a debate has arisen on whether the costs may outweigh the benefits of this biomarker test with over-diagnoses and false positives starting to increase drastically as it reaches new demographics where PSA benchmarks may remain unappreciated [12, 27]. In particular, with some of these biomarkers the translation of early diagnosis to decrease in mortality rates has not been recorded. A balance must be achieved between sensitive and specific identification of cancer cells and patient benefit deriving from an early diagnosis. The challenge still remains the search for a biomarker whose diagnostic and prognostic value will create a rapid, sensitive and specific test to benefit patient quality of life.

2.3 Tumour acidification

Decoding the dynamic components of the tumour microenvironment (TME) and its contribution to tumour growth, metastasis and resistance to therapy has been identified as a key avenue to improving cancer diagnosis. Cancer cells are the centre force of the TME, however, both intracellular and intercellular communication plays a role in cancer progression. The TME is

composed of a range of cell types including tumour cells, immune cells (T and B lymphocytes, macrophages, neutrophils, dendritic cells), the tumour stroma (endothelial cells, fibroblasts, adipocytes) and extracellular matrix (ECM) components produced from surrounding cells (e.g. collagen, proteoglycans, laminins) [28–32]. The TME provides support to tumour cells through adaptation to changing conditions and promotion of protective behaviours, including a barrier promoting drug resistance and inhibition of stress response factors to promote proliferation, anti-apoptotic signals and epithelial-to-mesenchymal (EMT) transition to lead to metastasis. Interplay of TME components, both cellular and non-cellular, act in concert for the evolutionary benefit of the tumour cells and lead to re-programming of their own functions e.g. immune-suppressive macrophages, and tumour cell functions e.g. metabolism dysregulation [30, 33].

Aberrant mitosis is directly related to at least three "hallmark" features of oncogenesis: sustained growth signals, evasion of suppressive growth signals and loss of finite replication [19]. In turn, an increased rate of proliferation in cancer cells is heavily dependant on the availability of the building blocks required for biomass growth and energy for mitosis which can be rate-limiting in normal cell growth [19, 34]. A characteristic of cancer cells which has recently gained renewed interest is the deregulation of cellular metabolism to favour aerobic glycolysis under normoxic conditions. This phenomenon results in an increased rate of energy production and is accompanied by a reversed pH gradient between cancer cells and the TME due to excess bi-product production from the glycolysis pathway. This is known as ***the Warburg effect***. As a result, the extracellular pH (pHe) of cancer cells becomes more acidic whilst intracellular pH (pHi) is alkaline in order to maintain a favourable acid-base homeostasis [33, 35].

$$\mathrm{p}He < pHi \tag{2.1}$$

Measurements of tumour pHe and pHi *in vivo* have shown that the degree of acidosis depends on tumour tissue type, perfusion rates and areas of hypoxic conditions, however on average pHe varies in the pH range 6.4-7.1, in comparison to pH values of pH 7.4 reached in most healthy tissues [36–40]. Measurements using glass electrodes have shown that the primary type of cancer but also the metastatic site can affect the resultant pHe in patients. Melanoma cases with micrometastases to the right leg showed a lower pHe (6.63) than the corresponding normal tissue (pHe 7.45), however, the difference was less striking when measuring pHe micrometastases to the breast tissue (tumour tissue pHe 6.88 versus normal pHe 7.54) [41]. Similar variability has been recorded in lung, breast, uterine tumours and sarcoma [37]. Correspondingly, pHi tends to be more alkaline in malignant cells versus their non-malignant counterparts, with pH values in tumour cells $\geq$ 7.2 [38]. The changes in pHi are overall less significant due to mechanisms employed to stabilise pHi to a viable range where replication, transcription and translation can adapt to a chronically lower pHe [30]. The interplay between these two key

characteristics of pHe and pHi create the opportunity to use pH as a biomarker for primary tumour growth and recurrence but also as an indicative factor in drug resistance [9, 32, 42].

2.3.1 Energy metabolism in cancer: The Warburg effect

All multicellular organisms require the production of energy and precursor molecules in order to increase in size and divide in the process of mitosis as well as contribute to anabolic pathways of building blocks e.g. protein synthesis, fatty acid synthesis. The key molecule feeding into energy metabolism pathways is glucose. Mammalian cells require energy in the form of adenosine triphosphate (ATP) in order to survive. There are two main pathways via which ATP production from glucose can take place – oxidative phosphorylation in mitochondria (coupled with the tricarboxylic acid (TCA) cycle) and glycolysis in the cytosol [43–45] (Figure 2.1). Under physiological conditions, non-malignant cells process glucose to pyruvate, via glycolysis, that then contributes to the oxidative phosphorylation pathway which utilizes oxygen to produce CO_2 and ATP. Notably, oxidative phosphorylation is the most efficient way to produce maximal ATP molecules with a rate of 36 ATP per glucose molecule [44]. On the other hand, under hypoxic conditions, cells revert to fermentation, which is also known as glycolysis. Glycolysis produces less ATP (2 ATP per glucose molecule) but it does so at a faster rate which makes energy more readily available to the cell [34, 45, 46]. This can happen in skeletal muscle cells where energy in the form of ATP is required at a faster rate during exercise [47].

In the 1920s, German biochemist Otto Warburg discovered, what is now considered a key feature of malignancy, a deregulated bioenergetics profile where glycolysis is preferentially employed by cancer cells to produce ATP and lactate, ultimately leading to extracellular acidification. Experimental methods using ascite tumour cells revealed an increased rate of glucose uptake and lactate production leading him to hypothesize that cancer cells were using glycolysis even under aerobic conditions [48–50]. In later years, this phenomenon was coined the Warburg effect. Historically, it is interspersed with misinterpretations, likely due to its complex regulation and inconsistent hypothesis of origin [38]. Warburg adamantly believed that the driver of this phenomenon stemmed from mutations in mitochondria leading to dysfunction and an inherent survival need for cancer cells to switch to a predominant glycolytic metabolism [48, 50]. However, this was later disproved and only a few types of cancer have been shown to have mutations in oxidative phosphorylation steps. Current understanding shows that cancer cells employ both oxidative phosphorylation and increased glycolysis rates, irrespective of oxygen partial pressures in the surrounding tissue [47, 50] (Figure 2.1). Notably, in solid tumours the Warburg effect can also be coupled with hypoxia due to poor perfusion in areas far from blood vessels where cancer cells will find themselves in oxygen-depleted regions [38, 51]. The compounding effects result in an acidic pHe and alkaline pHi which is not normally found in healthy cells.

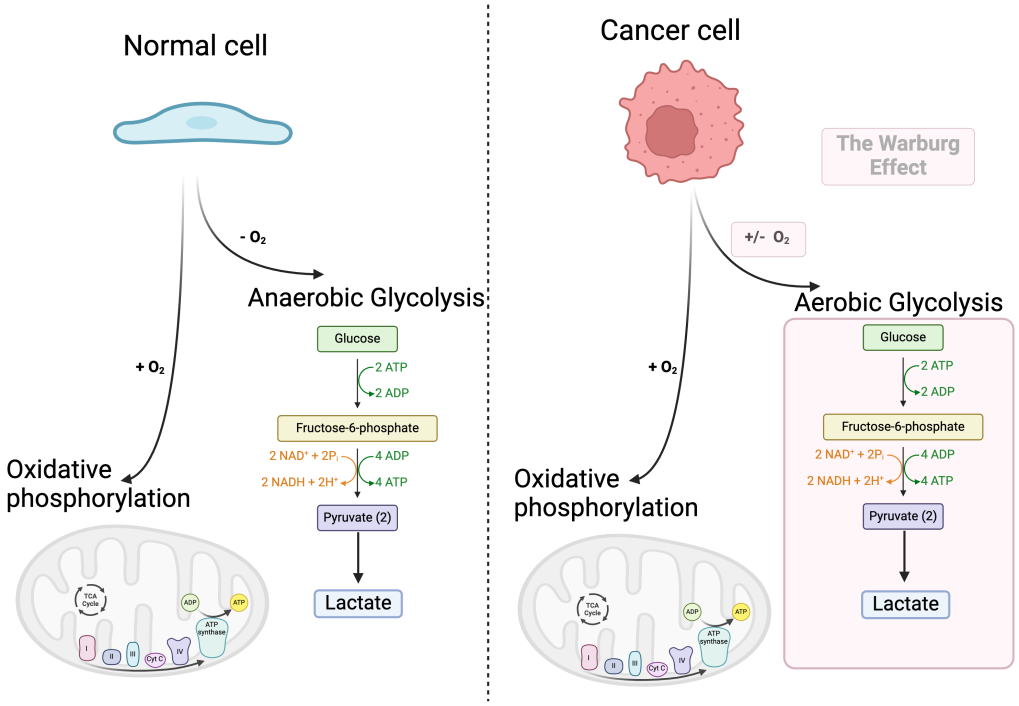


Figure 2.1: **Energy metabolism in normal versus cancer cells.** (*(Left)* Under aerobic conditions energy metabolism in normal cells utilises oxidative phosphorylation, also known as the TCA cycle, to produce ATP. Under anaerobic conditions, e.g. in muscle cells, the glycolytic pathway is followed. *(Right)* Cancer cells predominantly employ the glycolytic pathway to rapidly meet their energy requirements regardless of oxygen availability - this is known as the Warburg effect. Under aerobic conditions, the oxidative phosphorylation pathway also persists in cancer cells. (Created in BioRender. Beykou, M. (2024) BioRender.com/f68d171).

2.3.2 Extracellular acidification mechanisms

In malignant cells, aerobic glycolysis takes place in ten enzymatic steps from the uptake of glucose through central carbon metabolism breakdown to pyruvate and lactic fermentation to produce end-products: lactate and CO_2 [51, 52]. The rate of glycolysis in cancer cells results in an excess production of end-products. This is coupled with both CO_2 produced by oxidative phosphorylation and hypoxia-induced glycolysis. Single cells must cope with these end-products on the individual level in order to avoid intracellular cytotoxicity due to acid-base imbalances which results in extracellular acidification of solid tumours [30].

Carbon dioxide production and hydration: Cell membrane permeability allows the removal of the majority of excess CO_2 produced both by glycolysis and oxidative phosphorylation by diffusion. Vascular perfusion plays a considerable role in the removal of CO_2 by this method. Cells located in close proximity to blood vessels will be able to remove a proportion of the excess CO_2 available [30, 53]. Alternatively, CO_2 can be hydrated to bicarbonate ions (HCO_3^-) and H^+ ions to facilitate its removal from the intracellular space. The bicarbonate buffering system in mammalian cells is the most ubiquitous system to regulate pHi via H^+ regulation. However, the equilibrium of this reaction can be slow and cancer cells heavily depend on carbonic anhydrases (CAs) to cause a rapid efflux of HCO_3^- and H^+ ions [30, 54, 55]. More specifically, adaptive responses to extracellular acidification result in CA9 and CA12 upregulation to promote efflux in cancer cells resulting in a net H^+ extrusion [30, 54, 56].

$$CO_2 + H_2O \leftrightarrow HCO_3^- + H^+ \tag{2.2}$$

Lactate export: The role of lactate in cancer bioenergetics is well-coordinated in order to replenish the necessary components to continue a cycle of glycolysis by regenerating NAD^+ supply which is used as an electron acceptor, directly feed into the TCA cycle prior to oxidative phosphorylation as an intermediate but also to build extracellular acidification which in itself perpetuates selective advantages for the tumour [30, 44, 47, 57]. Lactate anions and H^+ are transported into the extracellular space by Monocarboxylate transporter 4 (MCT4) in order to maintain a the pH balance intracellularly but also to replenish the lactate store extracellularly for neighbouring cells which will uptake lactate anions to fuel the glycolysis cycle [30, 55].

$$CH_3CH(OH)COOH \leftrightarrow CH_3CH(OH)COO^- + H^+ \tag{2.3}$$

H^+ or bicarbonate efflux coupled to other ions: In order to achieve a stable pHi which is necessary for cell survival, additional mechanisms exist to facilitate H^+ exit from the intracellular space. Well-characterised examples include ATPases on the cell membrane which

perform ATP hydrolysis to ADP and Na^+/H^+ exchanger 1 (NHE1) [30]. Moreover, removal of HCO_3^- such as Na^+/HCO_3^+ co-transporters (NBCs) and acid-loading anion exchangers, e.g. AE2 for chloride ions, is another methodology employed to maintain homeostatic balance in the bicarbonate buffering system [55, 58, 59].

Concurrently, areas of poor perfusion due to distance from vasculature within tumours will result in cells exposed to a hypoxic environment (i.e. insufficient oxygen availability). Hypoxia in itself promotes the use of anaerobic glycolysis for energy production and activates the transcription factor Hypoxia-inducible factor 1a (HIF-1a). HIF-1a is widely accepted as an important factor in cancer progression and activates a cascade of downstream gene changes for the upregulation of glucose and lactate ion influx, lactate production and necessary enzymes for glycolysis [30, 44, 57, 60]. As such, de-coupling the Warburg effect from hypoxia-induced acidification can be challenging.

A constant feedback loop from pH-sensitive receptors and signaling molecules couples pHi and pHe to achieve a steady state of permissive pHi in order to maintain cell survival, growth and proliferation. For example, low pHi will activate ion transporters such as NHE1 to promote H^+ efflux, whilst a low pHe will have an opposing effect [30]. Cancer cells adapt to a more acidic extracellular environment by employing mechanisms to maintain their pHi at an acceptable stable state where net acid extrusion is greater than production. The cumulative effects of an increased glycolytic rate, oxidative phosphorylation, hypoxia and a feedback loop to sustain glycolysis without it becoming rate-limiting, result in net acid efflux from cells to create an acidic pHe and alkaline pHi in tumours.

2.4 pH detection *in vivo*

The significance of an acidic TME has become well-recognised amongst clinicians and researchers. The value of acidosis to detect healthy and cancerous tissue can be delineated from some of the most common diagnostic tools utilizing pHe, pHi and glucose consumption as part of qualitative imaging methods [61]. The need for quantitative evaluation of pHe and pHi to guide both diagnosis and prognosis has led to considerable advances in imaging technologies for detection of acidification of *in vivo* tissue. One of the first tools to be used by researchers to identify and evaluate pHe in tumours and healthy tissue is the glass electrode. Historically, discoveries using the glass electrode for detection of tumour pH have guided our early understanding of acidosis and the glycolytic and respiratory capacity of tumours given their glucose consumption [36, 39–41, 62]. Caveats, including variation due to trauma, application variability and limited application to pHi, led to the use of more sophisticated technologies despite microelectrodes remaining the comparative standard at the time [36]. Magnetic Resonance Spectrocospy (MRS), MRI Chemical Exchange Saturation Imaging (MRI CEST), Electron

paramagentic resonance (EPR), optical imaging with fluorescent probes (e.g. SNARF1), as well as photoacoustic imaging represent the many modalities available for pH mapping in tumours for differentiating between malignant and healthy tissue [36, 61, 63, 64](Summarised in Table 2.4).

Diagnostic technology	**Limitations**
Magnetic Resonance Imaging (MRI) (e.g. CEST MRI)	- strong radiation required - weighted estimates of intracellular and extracellular pH - limited sensitivity of exogenous probes - affected by motion
Magnetic Resonance Spectroscopy (MRS)	- poor spatial resolution - long acquisition times - neurotoxicity and instability of some probes - often more suitable for intracellular pH quantification
Positron Emission Tomography (PET)	- reliant on expression of glucose transporters (GLUT1 and GLUT2) - not a direct measurement of extracellular pH - quantitative
Electron Paramagnetic Resonance (EPR)	- technical knowledge required - toxic irradiation - signal decomposition poses a problem
Optical imaging	- Fluorescent probes with variable sensitivity and specificity - Requires surface accessibility
Photoacoustic imaging	- toxicity - complexities requiring technical knowledge

Table 2.1: Imaging modalities for mapping pH in the clinic. Information obtained from [36, 61, 63–72].

To date, the majority of comparable data between tumour and corresponding healthy tissue sites arise from ^{31}P MRS [36, 37, 61, 70]. This imaging technique exploits inorganic phosphate present in mammalian cells and its chemical shift upon exposure to a pH change, however it requires comparison to a reference source, such as phosphocreatine, which remains stable despite pH variation [61]. A significant limitation to this technology is that a greater percentage of inorganic phosphate is found intracellulary making measurements of pHe challenging to interpret. Advances in MRS technology have been able to map both pHe and pHi by using both exogenous and endogenous phosphate species. Despite this, long acquisition times, low spatial resolution and potential of toxicity from some of the species used have limited the use of MRS in modern diagnosis [36, 66, 70].

More recently, MRI CEST has emerged as a promising technology in the field of pH mapping in tumours. MRI CEST is based on the principle of proton exchange between specific substrates and bulk water in a tissue whereby with radio-frequency pulses applied, protons are saturated and transfer between substrates [61, 66]. The detection of a decrease in the proton signal from bulk water can be measured by MRI machinery to determine pH at a given site. Many variations of CEST agents exist with both advantages and limitations surrounding specificity and toxicity. An over-arching caveat is the sensitivity of this technology to agent concentrations and ambient experimental conditions as well as that pHi and pHe are calculated as weighted estimates making them non-direct measurements [36, 61, 63, 64, 66, 72]. Data arising from breast and liver tumours studied using MRI CEST show that it may be a viable possibility for

imaging pH in the clinic as it improves upon the resolution of MRI scans, however it is limited by its sensitivity [61, 63, 64, 73]. Despite mapping pH of tumours being appreciated as a key component contributing to tumour biology, it is not a commonplace procedure in the clinic in order to quantitatively determine tumour pHe. Furthermore, available imaging techniques face a number of caveats, including the requirement for bulky and expensive equipment, low throughput, high cost and low quantitative accuracy [61].

2.5 Summary

In this chapter, a summary of cancer diagnosis patterns and common biomarkers are presented. The potential of pH due to tumour acidification as a biomarker is introduced. Furthermore, the contributors to tumour acidification, the importance of pH homeostasis and the mechanisms utilised to maintain an extracellular/intracellular pH balance are discussed. Finally, imaging technologies currently available for pH mapping in tumours are summarised along with their caveats. The lack of portable, rapid and sensitive pH mapping diagnostic technologies for cancer detection will be expanded on in the next chapter.

References

[1] Y. Zhou et al. “Diagnosis of cancer as an emergency: A critical review of current evidence”. In: *Nature Reviews Clinical Oncology* 14.1 (Oct. 2017), pp. 45–56.

[2] W. Hamilton. “Cancer diagnosis in primary care”. In: *British Journal of General Practice* 60.571 (Feb. 2010), pp. 121–127.

[3] NIH. *Tests and Procedures Used to Diagnose Cancer - NCI*. 2023.

[4] A. Pulumati et al. “Technological advancements in cancer diagnostics: Improvements and limitations”. In: *Cancer Reports* 6.2 (Feb. 2023).

[5] E. P. Balogh, B. T. Miller, and J. R. Ball. “Improving diagnosis in health care”. In: *Improving Diagnosis in Health Care*. National Academies Press (US), Dec. 2016. Chap. Chapter 2: pp. 1–472.

[6] E. Aveyard et al. “Waiting Times for Suspected and Diagnosed Cancer Patients 2012-13 Annual Report”. In: (2013), pp. 3–5.

[7] L. Lohfeld et al. “Impact of the COVID-19 pandemic on breast cancer patient pathways and outcomes in the United Kingdom and the Republic of Ireland – a scoping review”. In: *British Journal of Cancer* 131.4 (May 2024), pp. 619–626.

[8] L. Neamţiu et al. “Impact of the first wave of the COVID-19 pandemic on cancer registration and cancer care: a European survey”. In: *European Journal of Public Health* 32.2 (Apr. 2022), pp. 311–315.

[9] J. W. Wojtkowiak et al. “Drug resistance and cellular adaptation to tumor acidic pH microenvironment”. In: *Molecular Pharmaceutics* 8.6 (Dec. 2011), pp. 2032–2038.

[10] U. Bick and T. H. Helbich. “Follow-Up of Patients with Breast Cancer: Imaging of Local Recurrence and Distant Metastases”. In: Springer, Feb. 2019. Chap. Follow-Up, pp. 167–178.

[11] K. Nishio et al. “Preoperative predictors for early recurrence of resectable pancreatic cancer”. In: *World Journal of Surgical Oncology* 15.1 (Jan. 2017).

[12] D. Crosby et al. “Early detection of cancer”. In: *Science* 375.6586 (Mar. 2022).

[13] A. I. Riggio, K. E. Varley, and A. L. Welm. "The lingering mysteries of metastatic recurrence in breast cancer". In: *British Journal of Cancer* 124.1 (Nov. 2021), pp. 13–26.

[14] G. Corrado et al. "Optimizing treatment in recurrent epithelial ovarian cancer". In: *Expert Review of Anticancer Therapy* 17.12 (Dec. 2017), pp. 1147–1158.

[15] F. Bray et al. "Global cancer statistics 2022: GLOBOCAN estimates of incidence and mortality worldwide for 36 cancers in 185 countries". In: *CA: A Cancer Journal for Clinicians* 74.3 (May 2024), pp. 229–263.

[16] World Health Organization (WHO). *Niger state government begins cervical cancer services in line with WHO's recommendation — WHO — Regional Office for Africa*. 2022.

[17] L. Zhang et al. "An international consensus on the essential and desirable criteria for an 'organized' cancer screening programme". In: *BMC Medicine* 20.1 (Dec. 2022), pp. 1–10.

[18] J. S. Brown et al. "Updating the Definition of Cancer". In: *Molecular Cancer Research* 21.11 (Nov. 2023), pp. 1142–1147.

[19] D. Hanahan and R. A. Weinberg. "Hallmarks of cancer: The next generation". In: *Cell* 144.5 (Mar. 2011), pp. 646–674.

[20] National Institutes of Health. *Definition of biomarker - NCI Dictionary of Cancer Terms - National Cancer Institute*. 2019.

[21] N. L. Henry and D. F. Hayes. "Cancer biomarkers". In: *Molecular Oncology* 6.2 (Apr. 2012), pp. 140–146.

[22] A. Passaro et al. "Cancer biomarkers: Emerging trends and clinical implications for personalized treatment". In: *Cell* 187.7 (Mar. 2024), pp. 1617–1635.

[23] S. Das et al. "Biomarkers in Cancer Detection, Diagnosis, and Prognosis". In: *Sensors* 24.1 (Jan. 2024).

[24] C. Hall et al. "A review of the role of carcinoembryonic antigen in clinical practice". In: *Annals of Coloproctology* 35.6 (2019), pp. 294–305.

[25] V. Dochez et al. "Biomarkers and algorithms for diagnosis of ovarian cancer: CA125, HE4, RMI and ROMA, a review". In: *Journal of Ovarian Research* 12.1 (Mar. 2019).

[26] Y. H. Wen et al. "Cancer screening through a multi-analyte serum biomarker panel during health check-up examinations: Results from a 12-year experience". In: *Clinica Chimica Acta* 450 (Oct. 2015), pp. 273–276.

[27] D. Ilic et al. "Screening for prostate cancer". In: *Cochrane Database of Systematic Reviews* 2013.1 (Jan. 2013).

[28] R. Baghban et al. "Tumor microenvironment complexity and therapeutic implications at a glance". In: *Cell Communication and Signaling* 18.1 (Apr. 2020), pp. 1–19.

[29] A. Bożyk et al. “Tumor Microenvironment—A Short Review of Cellular and Interaction Diversity”. In: *Biology* 11.6 (June 2022).

[30] P. Swietach, E. Boedtkjer, and S. F. Pedersen. “How protons pave the way to aggressive cancers”. In: *Nature Reviews Cancer* 23.12 (Oct. 2023), pp. 825–841.

[31] N. V. Popova and M. Jücker. “The Functional Role of Extracellular Matrix Proteins in Cancer”. In: *Cancers* 14.1 (Jan. 2022).

[32] N. Rohani et al. “Acidification of tumor at stromal boundaries drives transcriptome alterations associated with aggressive phenotypes”. In: *Cancer Research* 79.8 (Apr. 2019), pp. 1952–1966.

[33] V. Huber et al. “Cancer acidity: An ultimate frontier of tumor immune escape and a novel target of immunomodulation”. In: *Seminars in Cancer Biology* 43 (Apr. 2017), pp. 74–89.

[34] T. Epstein, R. A. Gatenby, and J. S. Brown. “The Warburg effect as an adaptation of cancer cells to rapid fluctuations in energy demand”. In: *PLoS ONE* 12.9 (Sept. 2017), e0185085.

[35] B. A. Webb et al. “Dysregulated pH: A perfect storm for cancer progression”. In: *Nature Reviews Cancer* 11.9 (Sept. 2011), pp. 671–677.

[36] G. Hao, Z. P. Xu, and L. Li. “Manipulating extracellular tumour pH: An effective target for cancer therapy”. In: *RSC Advances* 8.39 (June 2018), pp. 22182–22192.

[37] L. E. Gerweck and K. Seetharaman. “Cellular pH gradient in tumor versus normal tissue: Potential exploitation for the treatment of cancer”. In: *Cancer Research* 56.6 (1996), pp. 1194–1198.

[38] E. Boedtkjer and S. F. Pedersen. “The Acidic Tumor Microenvironment as a Driver of Cancer”. In: *Annual Review of Physiology* 82 (2020), pp. 103–126.

[39] J. L. Wike-Hooley et al. “Human tumour pH and its variation”. In: *European Journal of Cancer and Clinical Oncology* 21.7 (1985).

[40] A. P. Van Den Berg et al. “Tumour pH in human mammary carcinoma”. In: *European Journal of Cancer and Clinical Oncology* 18.5 (May 1982), pp. 457–462.

[41] B. S. Ashby. “pH studies in human malignant tumours.” In: *Lancet* 2.7458 (Aug. 1966), pp. 312–315.

[42] G. M. Nava and L. A. Madrigal Perez. “Metabolic profile of the Warburg effect as a tool for molecular prognosis and diagnosis of cancer”. In: *Expert Review of Molecular Diagnostics* 22.4 (2022), pp. 439–447.

[43] C. Schiliro and B. L. Firestein. “Mechanisms of metabolic reprogramming in cancer cells supporting enhanced growth and proliferation”. In: *Cells* 10.5 (May 2021).

[44] S. Y. Lunt and M. G. Vander Heiden. "Aerobic glycolysis: Meeting the metabolic requirements of cell proliferation". In: *Annual Review of Cell and Developmental Biology* 27 (Oct. 2011), pp. 441–464.

[45] S. Romero-Garcia et al. "Tumor cell metabolism: An integral view". In: *Cancer Biology and Therapy* 12.11 (Dec. 2011), pp. 939–948.

[46] M. G. Heiden, L. C. Cantley, and C. B. Thompson. "Understanding the warburg effect: The metabolic requirements of cell proliferation". In: *Science* 324.5930 (May 2009), pp. 1029–1033.

[47] S. K. Parks, W. Mueller-Klieser, and J. Pouysségur. "Lactate and Acidity in the Cancer Microenvironment". In: *Annual Review of Cancer Biology* 4 (2020), pp. 141–158.

[48] O. Warburg and S. Minami. "Versuche an Überlebendem Carcinom-gewebe". In: *Klinische Wochenschrift* 2.17 (Apr. 1923), pp. 776–777.

[49] O. Warburg, F. Wind, and E. Negelein. "The metabolism of tumors in the body". In: *Journal of General Physiology* 8.6 (Mar. 1927), pp. 519–530.

[50] O. Warburg. "On the origin of cancer cells". In: *Science* 123.3191 (1956), pp. 309–314.

[51] R. J. De Berardinis and N. S. Chandel. "Fundamentals of cancer metabolism". In: *Science Advances* 2.5 (May 2016).

[52] P. Vaupel et al. "Revisiting the Warburg effect: historical dogma versus current understanding". In: *The Journal of Physiology* 599.6 (Mar. 2021), pp. 1745–1757.

[53] P. Swietach et al. "The chemistry, physiology and pathology of pH in cancer". In: *Philosophical Transactions of the Royal Society B: Biological Sciences* 369.1638 (Mar. 2014).

[54] A. Hulikova et al. "Regulation of intracellular pH in cancer cell lines under normoxia and hypoxia". In: *Journal of Cellular Physiology* 228.4 (Apr. 2013), pp. 743–752.

[55] C. Corbet and O. Feron. "Tumour acidosis: From the passenger to the driver's seat". In: *Nature Reviews Cancer* 17.10 (Sept. 2017), pp. 577–593.

[56] P. Swietach et al. "The role of carbonic anhydrase 9 in regulating extracellular and intracellular pH in three-dimensional tumor cell growths". In: *Journal of Biological Chemistry* 284.30 (July 2009), pp. 20299–20310.

[57] O. Feron. "Pyruvate into lactate and back: From the Warburg effect to symbiotic energy fuel exchange in cancer cells". In: *Radiotherapy and Oncology* 92.3 (Sept. 2009), pp. 329–333.

[58] E. Boedtkjer et al. "Contribution of Na+,HCO3–cotransport to cellular pH control in human breast cancer: A role for the breast cancer susceptibility locus NBCn1 (SLC4A7)". In: *International Journal of Cancer* 132.6 (Mar. 2013), pp. 1288–1299.

[59] J. Michl et al. “Acid-adapted cancer cells alkalinize their cytoplasm by degrading the acid-loading membrane transporter anion exchanger 2, SLC4A2”. In: *Cell Reports* 42.6 (June 2023), p. 112601.

[60] S. K. Parks, J. Chiche, and J. Pouysségur. “Disrupting proton dynamics and energy metabolism for cancer therapy”. In: *Nature Reviews Cancer* 13.9 (Aug. 2013), pp. 611–623.

[61] A. Anemone et al. “Imaging tumor acidosis: a survey of the available techniques for mapping in vivo tumor pH”. In: *Cancer and Metastasis Reviews* 38.1-2 (June 2019), pp. 25–49.

[62] J. Naeslund and K.-E. .-. Swenson. “Investigations on the pH of Malignant Tumours in Mice and Humans after the Administration of Glucose”. In: *Acta Obstetricia et Gynecologica Scandinavica* 32.3 (1953), pp. 359–367.

[63] M. Chen et al. “Extracellular pH is a biomarker enabling detection of breast cancer and liver cancer using CEST MRI”. In: *Oncotarget* 8.28 (July 2017), pp. 45759–45767.

[64] Y. Tang et al. “Noninvasive Detection of Extracellular pH in Human Benign and Malignant Liver Tumors Using CEST MRI”. In: *Frontiers in Oncology* 10 (Nov. 2020), p. 2349.

[65] M. A. Voinov et al. “Measuring local pH at interfaces from molecular tumbling: A concept for designing EPR-active pH-sensitive labels and probes”. In: *Organic and Biomolecular Chemistry* 22.18 (May 2024), pp. 3652–3667.

[66] A. I. Hashim et al. “Imaging pH and metastasis”. In: *NMR in Biomedicine* 24.6 (July 2011), pp. 582–591.

[67] M. Hassan et al. “Fluorescence lifetime imaging system for in vivo studies”. In: *Molecular Imaging* 6.4 (July 2007), pp. 229–236.

[68] R. A. Gatenby et al. “Acid-mediated tumor invasion: A multidisciplinary study”. In: *Cancer Research* 66.10 (May 2006), pp. 5216–5223.

[69] D. A. Rottenberg et al. “In vivo measurement of regional brain tissue pH using positron emission tomography”. In: *Annals of Neurology* 15.S1 (Jan. 1984), pp. 98–102.

[70] S. Alzola-Aldamizetxebarria et al. “A Comprehensive Introduction to Magnetic Resonance Imaging Relaxometry and Contrast Agents”. In: *ACS Omega* 7.42 (Oct. 2022), pp. 36905–36917.

[71] R. J. Gillies, Z. Liu, and Z. Bhujwalla. “31P-MRS measurements of extracellular pH of tumors using 3- aminopropylphosphonate”. In: *American Journal of Physiology - Cell Physiology* 267.1 36-1 (1994).

[72] R. J. Gillies et al. “MRI of the tumor microenvironment”. In: *Journal of Magnetic Resonance Imaging* 16.4 (Oct. 2002), pp. 430–450.

[73] E. Krikken et al. “Contradiction between amide-CEST signal and pH in breast cancer explained with metabolic MRI”. In: *NMR in Biomedicine* 32.8 (Aug. 2019).

Chapter 3

Sensors for ion imaging

Since the 1950s and the invention of the first biosensor, known as the Clark electrode, there has been an exponential rise in the development and use of biosensors for biomedical applications. More specifically, biosensors play a key role in the translation of point-of-care technologies to the clinic, where specific and rapid detection of relevant biomarkers is essential for early diagnosis. Applications of biosensors to mammalian cell detection has been focused on electrogenic cell types (e.g. cardiomyocytes, neurons) and specialised cells (e.g. chondrocytes).

This chapter will review sensors and biosensors for cell-based applications with a focus on electrochemical sensing and cancer cell diagnostics. Firstly, an introduction to the components of a biosensor and the challenges associated with cell-based biosensor design for mammalian cells is presented. Furthermore, a brief summary of transducer classes in biosensors which have been implemented for mammalian cell detection with a particular focus on cancer cell applications. The following section will review electrochemical transducers. The integration of sensors in silicon manufacturing by CMOS technology and an introduction to potentiometric sensors, including ISFETs in CMOS, will be presented. Finally, review of related works of ISFET arrays in CMOS for detection of extracellular pH from mammalian cell cultures is presented and the ISFET designs which will be utilised throughout this research are introduced.

3.1 Characteristics and classification of biosensors

The term "biosensor" pertains to the amalgamation of a biological entity and a sensing module. Biosensors are integrated, analytical devices designed to selectively detect a biological analyte via a recognition event with a bio-receptor which is quantitatively or qualitatively reported as a signal by a sensing element, known as a transducer (Fig. 3.1) [1–3]. The modules of a biosensor are summarised below:

(a) **Analyte**: This is the biological or chemical component of an input sample which is of interest to be quantified. Analytes can be in the form of nucleic acids (DNA/RNA), proteins (e.g. secreted cytokines, metabolites, antigens), glycoproteins, cells (microbial or mammalian), exosomes or ions (e.g. H^+ or K^+).

(b) **Bio-receptor**: The recognition molecule that recognises the analyte in order to produce a bio-recognition event. These will correspond to the analyte and can take the form of antibodies, enzymes, nucleic acids (DNA/RNA), aptamers (single-stranded DNA/RNA) receptors or whole cells.

(c) **Transducer**: The transducer lies in proximity to the bio-receptor and registers a successful bio-recognition event which it converts to a signal. Typically transducers can be classed on the basis of the recognition event which can take the form of a: thermal, optical, mechanical or electrochemical change (e.g. pH change).

(d) **Output display**: The electronics component of a biosensor which is required to quantify and display the signal in digital format.

Biosensors have become important devices in biological and chemical testing of analytes in various fields, including food safety, water pollution, and biomedical diagnostics. However, the classification of biosensors is not uniform and often based on their field of application. Broadly, biosensors can be classified based on their recognition mechanism (affinity-based versus catalytic, label vs label-free), bio-receptor (Genosensors, Immuno-sensors, Cell-based sensors) or the principle of transduction (Optical, Mechanical or Electrochemical) [1, 3, 4]. The first analytical device to be characterised as a "biosensor" was discovered in 1956. Clark pioneered the development of an oxygen electrode to measure oxygen concentration in the blood. This was swiftly followed by an adaptation to create what is now known as the Clark Electrode by incorporating an enzyme-based reaction with glucose oxidase to determine glucose levels [4, 5].

The field of biosensors has since expanded, with biomedical diagnostic applications, including infectious diseases and cancer, at the forefront as the need for point-of-care diagnostics persists in health settings. More specifically, DNA/RNA/aptamer-based as well as immune-based

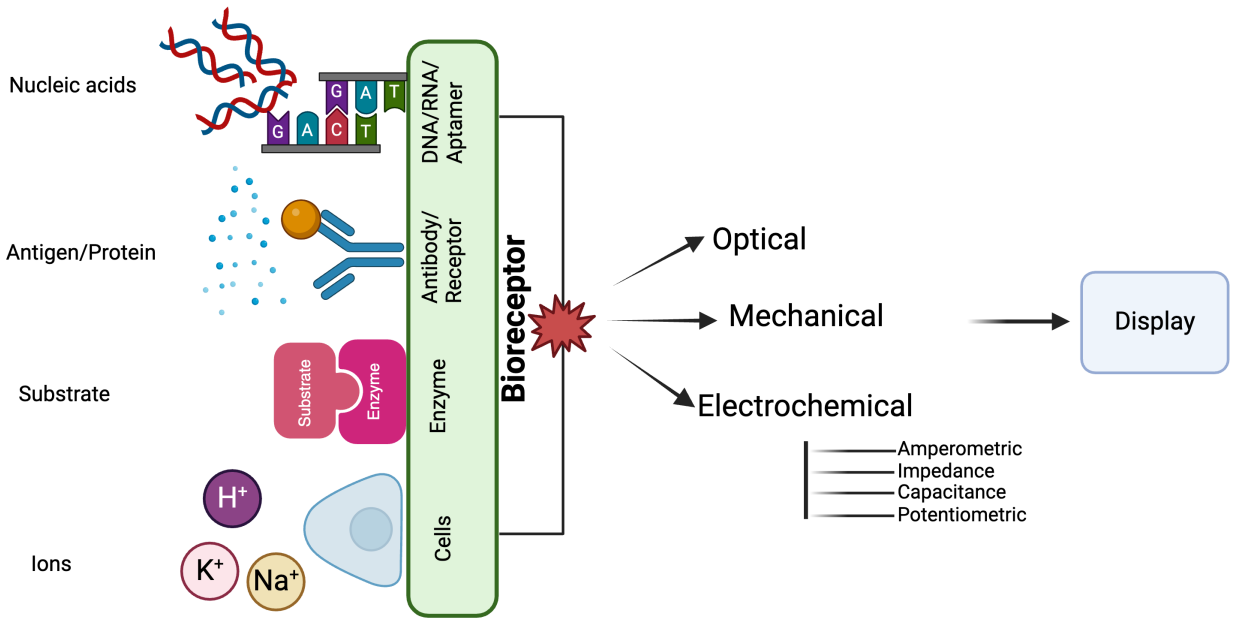


Figure 3.1: **Biosensor modular schematic summary.** From left to right: analytes, bioreceptors, transducer mechanisms and output display. (Created in BioRender. Beykou, M. (2024) BioRender.com/l46n267.)

biosensors have developed rapidly, especially in light of the COVID-19 pandemic [6]. The recognition mechanism of biosensors for nucleic acids is based on the specificity of nucleic acid base interactions. The advancements in DNA/RNA-based sensors have been facilitated by sequencing and amplification methodologies which can be adapted for electrochemical detection [7]. Likely the biggest success to date using CMOS chips for on-chip sequencing data has been the Ion Torrent technology [8].

Concurrently, immuno-sensors to detect infectious diseases or measure the immune response in biological specimens (e.g. cytokines), are facilitated by specific antigen-antibody recognition [9]. Unlike genetic and immuno-based bioreceptors, cell bioreceptors are dynamic modules which rely on biophysical and biochemical cell-sensor interactions. This has led to significant challenges in cell-based biosensor design, fabrication and commercialisation [10].

3.2 Mammalian cell-based biosensors

Living cells, both prokaryotic and eukaryotic, express a host of receptors, enzymes, ion channels and other cell surface molecules as well as extracellular components. This can make them the ideal candidate for biosensors. The biochemical and biophysical responses of cells to differ-

ent stimuli, e.g. drug sensitivity, are able to recapitulate what may be seen physiologically. Moreover, cells can combine detection of multiple analytes in one sensor [10]. They harbour specificity which would normally have to be designed and selected for in any biosensor due to native receptor-ligand interactions, for example. This can allow for label-free biosensor design in order to detect native cellular responses which better represent physiological scenarios [6]. Optimal sensitivity and responses combined with label-free detection of multiple analytes can result in cell-based biosensors for several applications.

The integration of live cells and electronics can be considered counter-intuitive, however cell-based biosensors have become a favourable platform for toxin sensing, contamination, drug sensitivity studies, infectious disease detection and cancer diagnostics. Different cell types have shown variable results in biosensor design, choice of transducer and applications [4, 10]. Microbial cells have been used in biosensors for environmental testing applications with the majority of transducers utilised being optical and electrochemical. On the other hand, eukaryotic cells, and more specifically, mammalian cells have faced more challenges in the design and fabrication as part of cell-based biosensors which is likely attributed to the complex inter-cellular and extracellular interactions found *in situ* [10].

Namely, some of the key challenges associated with mammalian cell-based biosensors are:

1. *Sensor stability and cell viability*: Maintaining sensor integrity in order to preserve cell-sensor coupling. Key concerns are surface fouling due to accumulation of large proteins on the sensor surface, for example from complex cell culture media. This can affect sensor sensitivity as well as cell viability due to accumulation of waste material or harmful levels of trapped substrates. Complexities of cell culture media can also impact sensor stability over long-term culturing.

2. *Selectivity*: surface chemistry and immobilization methods of bioreceptor on the sensor surface can affect selectivity of the cell to the analyte. Poor control of environmental conditions (temperature, CO_2, humidity concentration) can also affect these interactions in mammalian cell-based biosensors.

3. *Sensitivity*: the sensor can suffer by poor stability, signal drift and instrumentation noise which can affect sensor sensitivity. Drift and noise properties are often low frequency and thus in the same frequency band as chemical phenomena (1-10mHz). In addition, physiological and electrophysiological measurements across cell membranes can be rapid and small changes which are challenging to detect.

4. *Reproducibility*: repeatability in biosensor assays despite single cell biological variabilities, extracellular matrix production by cells and differential cell signaling. This can be especially important in diverse cell populations with different cell morphologies and different functions (e.g. senescent cells, stem cells).

5. *Microfluidics*: Incorporating larger cell size (10 to 100μm) for mammalian cells as compared to microbial cells can be a challenge with larger cells sitting further away from the sensor resulting in signal attenuation. Larger surface area to volume ratio in cells presents a challenge to the scalability and miniaturisation of sensors. Favouring physiologically relevant mechanoresponsiveness in mammalian cells can determine functional responses to stimuli.

6. *Sterility and continuous detection*: maintenance of sterile and controlled environment is particularly important in mammmalian cells to ensure physiological growth, proliferation and cell responses. Microbial contamination can increase stress response factors and compromise cell viability. A sterile environment is important to be able to maintain continuous and real-time monitoring over relatively longer response times (minutes to hours) in cell-based biosensors.

7. *Signal interpretation*: Delineation of complex mammalian cell responses and signaling pathways can be a challenge using sensors with a single readout property.

This review will focus on cell-based biosensors for cancer cell detection.The majority of mammalian cell-based biosensors are electrochemical sensors, with few optical and mechanical transducer implementations being explored.

Optical biosensors for cancer cell detection are represented by two main groups, photonic crystal sensors and surface plasmon resonance (SPR)/ low surface plasmon resonance (LSPR) sensors. Remaining faithful to the widely accepted definition of biosensors, in this review we will not consider microarrays and fluorescence-based markers, including Förster Resonance Energy Transfer (FRET)-based sensing as part of optical cell-based biosensors as they are not strictly integrated analytical devices [11].

In recent years, Photonic Crystal Fibers (PCFs) have garnered significant interest as they can differentiate between cancer cells and normal cells using the refractive index of cells due to their protein content. Cancer cells on average show a higher refractive index than their normal cell counterparts [12]. In photonic crystal sensors light is captured from a reflection in the crystal and transmitted to an electromagnetic field. Local changes allow the creation of a spatial map for cellular binding events allowing measurements of proliferation and apoptosis. Chan et al. (2007) demonstrated a photonic crystal sensor implemented on cell culture plates to monitor drug response to, the chemotherapeutic drug, doxorubucin in breast cancer cells, however use of a spectrometer for detection limits the applications in PoC settings [13]. Other groups have shown similar results for other cancer types [14, 15]. Additionally, PCFs can be implemented on different architectures and are characterised by air holes which allows manipulation of light wavelength and tailored patterning [16, 17]. The selectivity in the design of label-free PCFs,

offers advantages over standard optical fibers and has been demonstrated to detect a distinguishing refractive index in basal cell carcinoma. cervical and breast cancer cells [17]. On the other hand, SPR sensors have been very popular for technologies detecting immobilized proteins in lab settings, however not as applicable to PoC testing [18]. SPR detection is based on the transfer of energy from photons in a specific wavelength of light to the electrons at the gold metal surface of the chip to produce surface plasmon waves [10]. In a similar manner to other optical sensors, changes at the sensor surface, determine the refractive angle of light to be detected. For example, SPR for whole cell cancer detection has been shown in melanoma and lung cancer cells [19, 20]. Generally, SPR has been found to be most appropriate for detection of intracellular signal transduction events due to the changes upon stimulation of cell receptors because it can sensitively detect variations in cell membrane surface charge [10].

Mechanical/Piezoelectric detection of cancer cells is most commonly designed in the format of Quartz Crystal Microbalance (QCM) sensors. QCM sensors are sensitive to the mass changes on the surface of a quartz crystal. Cell binding on the surface imparts a pressure change as an increase in mass is detected on the quartz crystal surface as a linear shift in the oscillation frequency [10]. This type of piezoelectric detection has been particularly used for detection of drug response and resistance in cancer cell applications. Notably, QCM chips have been used to interrogate the effects of nocodazole on cytoskeletal kinetics in epithelial and breast cancer cells [21]. In addition, quantitative data from QCM chips have shown that they can be used to predict drug resistance to doxorubicin via detection of drug interactions with key breast cancer receptor protein, HER2 [22]. Similar studies have also been reported in colon and ovary adenocarcinoma cells [23, 24]. Recent advancements have combined both electrochemical and QCM-based approaches in integrated sensors making it a potential approach for physiological whole cell-based cancer detection [10]. Alternative piezoelectric sensors include shear mode acoustic sensors coupled with a quartz resonator for detection of cell adhesion in epithelial cells [25].

3.3 Electrochemical detection

Electrochemical biosensors rely on the transfer of electrons or ionic species between the analyte and an electrode during a biochemical reaction to produce a measurable electrical signal in the form of current, potential or conductivity [6]. Electrochemical transducers can be sub-classified into three groups based on their detection mechanism: amperometric, conductimetric and potentiometric. Changes in measured current, capacitance and potential result in a quantitative output. A sub-classification of conductance are impedance sensors whereby the resistance and reactance of a circuit is recorded. Solid-state chemical sensors have been investigated for biological applications including DNA sensing, enzyme reactions and cell-based applications

with a primary focus on neuronal networks and cardiomyocytes due to their electrogeneic properties [6].

3.3.1 Complementary Metal-Oxide Semiconductor (CMOS) technology

Application of electrochemical sensors in PoC diagnostic devices is accompanied by a set of prerequisites for use of these devices in both an urban clinical and rural areas. Cost-effectiveness, portability, ease-of-use and integrated signal processing are key challenges to applying many innovative sensor technologies to PoC settings [26]. The miniaturisation of silicon-based electronics has been at the forefront of the 21st century. Since 1975, Moore's law has guided advancements in the semiconductor industry with its realisation seen in modern day electronic devices. Moore's law states that the transistors incorporated in integrated circuits (ICs) will double every two years [27]. Manufacturing sensors in unmodified or modified CMOS technology has become a driver of incorporating systems on-chip. Advancements in lithography and smaller feature size led to the nanotechnology era in CMOS fabrication with 65nm CMOS technology being used in mass fabrication of silicon chips nowadays. We are now arguably reaching the limitations of this phenomenon with silicon-based ICs using CMOS technology however, silicon-based ICs still remain the major manufacturing and commercialisation technology. LoC technology where the integration of all microfluidic components and substrates is integrated onto a single microchip has gained considerable interest. CMOS fabrication lends itself to LoC technology for PoC devices as it allows scalable sensor manufacturing with integrated processing circuitry, low power functioning for portable devices, and reproducibility in terms of mass production [7, 27]. On a molecular level, CMOS-based devices benefit from the ability to perform reliable and repeatable experimentation in the form of sensors as arrays on a single chip [27]. Importantly, sensor arrays benefit over single sensor output with redundancy in case of sensor failure, increased resolution to perform averaging and application-based design allowing for flexible LoC applications. Whilst the advantages of manufacturing in CMOS have been realised in electrochemical sensors, limitations due to complexity in microfluidic design and electronics packaging and assessing biocompatibility with minimal post-processing to ultimately limit production costs remains to be optimised in a standardised manner for cell-based applications for cancer detection [7, 27].

Amperometric sensors measure current flow between electrodes due to an active species in a reduction-oxidation (redox) reaction, most commonly, under DC potential whereby voltage remains constant. In turn, the active species concentration is directly proportional to the current measured. Enzyme-based sensors lend themselves well to amperometry with redox reactions causing a current flow at the sensor interface whilst whole cell-based applications are limited [2, 28]. Notably, the first reported biosensor, was an amperometric sensor where an

enzymatic reaction with glucose oxidase was used to measure glucose concentration in blood samples [5].

Capacitance sensors and ***Impedance*** sensors can both be classified as conductimetric. Capacitance sensors have been used for determining cell adhesion, viability and proliferation by measuring the changes in capacitance at the sensor surface due to the dielectric properties of cells [29–31]. This provides a label-free and sensitive detection method for cell isolation and adhesive properties. Most importantly, the integration of capacitive sensors with integrated circuits in CMOS technology allows scalable design for LoC applications in biomedical settings (Table 3.1) [31]. Notable work by Prakash and Abshire reported a 0.5 μm CMOS capacitance sensor evaluating proliferation and adhesion of MDA-MB-231 breast cancer cells [29, 32]. They demonstrated that morphological changes correlate with capacitance due to the cells themselves acting as electric dipoles at the passivation layer-cell interface. When introduced to a low frequency electric field, a negatively charged cell forms a positively charged cloud thereby creating instances where it acts as a dipole. As a result, capacitance varies significantly between cells in suspension and cells adhered to the sensor surface [29]. Other groups have shown similar implementations, where proliferation has been evaluated in lung cancer cell line, H1299, for long-term and label-free monitoring [33]. Additional work by Nabovati et al (2019) included both a biocompatible polyelectroylyte membrane but also an evaluation of drug cytotoxicity. The effects of the drug geneticin resulted in weaker cell-electrode interactions and a decrease in output capacitance [34].

Electric-cell substrate Impedance Sensing (ECIS) is also commonly used technology for cell culture studies to measure cytotoxicity and drug sensitivity *in vitro*. Some of the advantages of impedance sensing is the ability to distinguish between cell types due to their bioelectrical properties [35]. Pioneers of impedance technology for cell culture applications, Giaever and Keese (1993), demonstrated the variability of impedance spectroscopy to assess cell morphology across gold electrodes [36, 37]. Advancements in impedance technology have resulted in studies of cell adhesion, drug response and cell migration [35]. Notably, Zhang et al., (2018) reported an ECIS biosensor where measurements of capacitance and resistance properties in skin cancer cell line A431 could be differentiated from a healthy cancer cell line [38]. Similar evidence has been reported for other cell type including squamous cell carcinoma and colon cancer-derived cell lines [35]. Correlation of impedance with cell cycle staging has also been demonstrated in HeLa cells, where adherence and morphology in a mitotically coordinated cell population were evaluated [39]. Significant work in impedance sensors manufactured in commercial CMOS technology has been reported by Chen et al., (2012) where an electrical-impedance spectroscopy (EIS) 96 x 96 array performed single cell resolution sensing (Table 3.1) [40]. This device was designed to trap each 17 μm breast cancer cell on a 17 x 17 μm sensor which is a promising technology for detection and enumeration of circulating tumour cells found in liquid biopsies [40].

Potentiometric sensors, also known as Field-Effect devices (FEDs), are commonly used as pH sensors to determine the concentration of H^+ ions in an aqueous solution which is in contact with an ion-sensitive membrane [7]. They can also be adapted for detection of other ionic species (e.g. Na^+, K^+ and Ca^{2+}) [41]. The principle of detection is based on measuring the change in potential (voltage) between an ion-sensitive electrode (ISE) and a reference electrode under negligible current flow. The ion concentration is related to the voltage change by a logarithmic relationship which quantitatively determines the ion concentration in solution [42, 43]. In recent years, potentiometric sensors have undergone considerable research and commercial efforts, with Ion-Sensitive Field-Effect Transistors (ISFETs) and Light-Addressable Potentiometric sensing (LAPS) emerging as inexpensive and sensitive sensors for real-time monitoring of biochemical phenomena. As compared to capacitance and impedance sensors, potentiometric sensors rely solely on the extracellular concentration of analytes without the need for cells to harbour significant electrogenic properties for detection [6]. More specifically, LAPS have been reported for cell-based detection in drug screening, taste testing and extracellular pH monitoring [6]. Implementations of LAPS to detect extracellular pH, have reported an increase in photocurrent upon glucose injection due to metabolic release of H^+ [44]. In another study, nanofiber LAPS coated with biocompatible hydrogel coatings were used to evaluate the metabolic response of cancer cells and healthy cells to various glucose concentrations. They demonstrated an increase in pH change over a period of 90 minutes for high glucose breast cancer cells which was not seen for healthy cells [45]. Despite the applications of LAPS for pH detection, their reliance on a photodiode makes it challenging to implement integration in compact point-of-care devices due to the need for bulky, external electronics and optics. Conversely, ISFETs have been found to be a promising sensor for PoC devices due to its monolithic integration of sensing and processing circuitry [26].

Table 3.1: CMOS-based capacitance and impedance sensors for cancer cell applications.

Application	Electrochemical transducer	Array size	Cell type	Sensing layer	CMOS	Year	Ref
Proliferation/Adhesion	Capacitance	16 sensors (4 x 4)	MDA-MB-231 (breast) Caco-2 (colonic adenocarcinoma)	Silicon nitride	0.5um	2008	[29]
Proliferation/Adhesion	Capacitance	8 x 8	H1299 (lung carcinoma)	Aluminium + PDMS	0.35um	2017	[33]
Proliferation/Viability	Capacitance	8 x 8	HEK293 (embryonic kidney) H1299 (lung carcinoma)	Polyelectrolyte membrane (PEMS)	0.35um	2019	[34]
Viability	Capacitance	4x4	Ovarian cancer cells CP70 and A2780		0.35um	2018	[31]
Manipulation/migration	Dielectrophoresis/Impedance	320 x 320	K562 (myelogenous leukaemia)	Glass?	0.35um	2003	[46]
Adhesion/counting	Impedance (EIS)	96 x 96	MCF-7 (breast)	Gold	0.18um	2012	[40]

3.4 Ion-Sensitive Field-Effect Transistors (ISFETs) in CMOS

ISFETs were first introduced by Bergveld in 1972 as an adaptation of the MOSFET (Metal–Oxide-Semiconductor Field-Effect transistor) with the addition of an aqueous solution in contact with the reference electrode and the insulating membrane on top of the floating gate [43, 47]. A schematic of the ISFET structure and macromodel are shown in Figure 3.2).

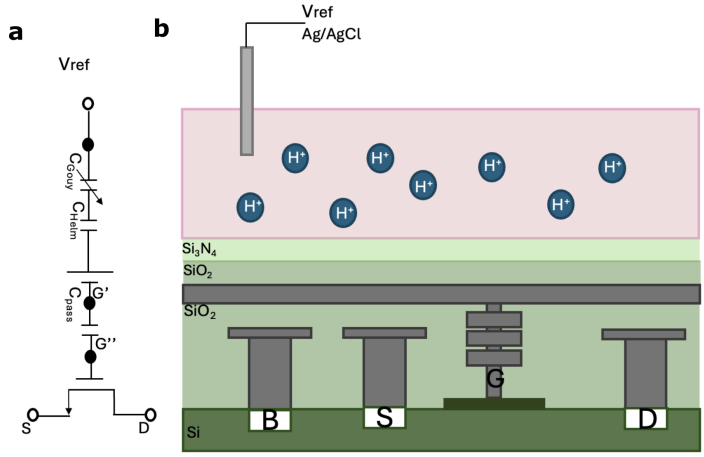


Figure 3.2: **Ion-Sensitive Field-Effect Transistor (ISFET) in Complementary Metal-Oxide Semiconductor (CMOS) technology.** **(a)** ISFET macromodel. **(b)** Schematic model.

The ISFET structure relies on applying voltage through a reference electrode (most commonly Ag/AgCl) in order to bias the system. As a result, ISFETs act as dynamic pH sensors by detecting a change from a threshold voltage. The operation of the ISFET as a pH sensor can be described in relation to the MOSFET with the addition of the relevant chemical terms, V_{chem}, as in Eq. 3.1, where γ represents the potential changes which are not related to the H^+ ion concentration (the analyte), α is the deviation from an ideal chemical sensor sensitivity, known as the Nernstian sensitivity (S_N=59.2mV/pH at ambient temperature 298K) and pH (as defined in Eq. 3.2) [48].

$$V_{th(ISFET)} = V_{th(MOSFET)} + V_{chem} = V_{th(MOSFET)} + (\gamma + \alpha\, S_N\, pH) \tag{3.1}$$

$$\mathrm{pH} = -\log[\mathrm{H}^+] \tag{3.2}$$

The electrochemical behaviour of the ISFET is determined by two components: the threshold voltage and the interaction of ions at the gate interface. The latter can be described in terms of the site-binding model whereby the passivation layer of the floating gate acts as a buffer. Thereby, a change in ion concentration in solution results in a change in the potential at the

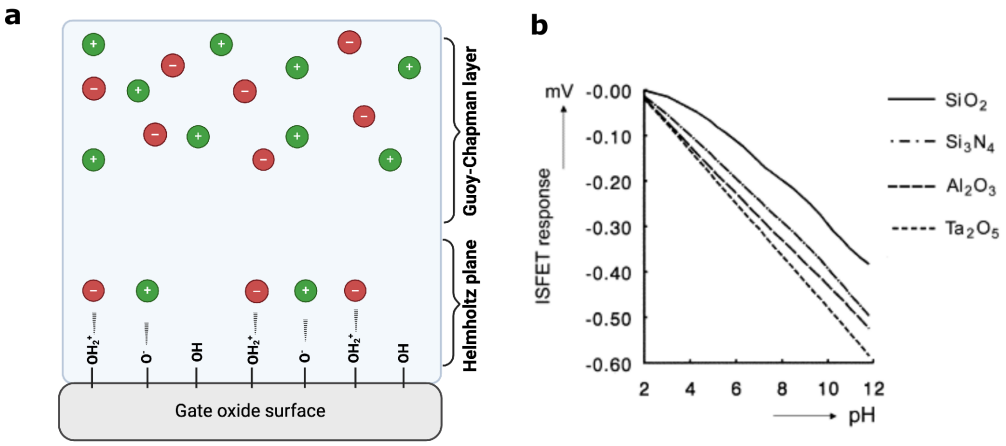


Figure 3.3: **Site-binding model and ISFET passivation layers.(a)** Site-binding model at the passivation surface of the ISFET sensor in contact with an electrolyte. (Created in BioRender. Beykou, M. (2024) BioRender.com/l26s107) **(b)** ISFET sensitivity to pH with different passivaiton layers. Re-printed with permission from Bergveld, P.,(2003) [43].

gate surface due to a change in charge distribution [43]. Taking the example of SiO_2 as the gate material, hydroxyl (-OH) groups on the surface are known as "amphoteric" because they can exist in three protonation forms (positive, negative or neutral). Depending on the availability of H^+, the amphoteric sites will act as proton donors or proton acceptors. The positive, negative and neutral charges at the gate surface will result in a variation in overall charge. In turn, the formation of an equivalent opposite charge in the solution is collectively known as the Guoy-Chapman layer [49, 50]. The electrical double-layer that is found when a surface is submerged in a liquid phase, coupled with the resultant charge at the semiconductor/electrolyte interface creates what is known as the Helmholtz plane (Figure 3.3). The diffusion of charges from the surface to the bulk solution is known as the Boltzmann distribution [49]. While the capacitive model offers a simplified view of the electrochemical interface, it fails to account for the non-idealities that occur in the real cases. The interface between the ISFET gate and the electrolyte is much more complex than a simple capacitor, with factors such as non-uniform charge distribution and frequency-dependent behaviour playing significant roles. In this context, the Constant Phase Element (CPE) provides a better representation by modeling the interface as a fractional capacitor where the impedance changes depending on the frequency. This allows for better predictions of the ISFET's behaviour, particularly in dynamic and real-world conditions.

The primary ISFET design featured a hydrated SiO_2 coating of the p-channel which exploited the material's natural capacity to sense pH through H^+ ion detection. The application of ISFETs in commercially available unmodified CMOS technology by Baussels et al (1999) altered the field in a considerable way and initiated a host of possibilities for ISFET sensors [51]. A Si_3N_4 top passivation layer as part of the extended gate in CMOS fabrication preserves the

sensitivity and specificity to pH and allows scalable manufacturing [47, 51, 52]. Although other modifications have been made to the gate material, such as Al_2O_3 and Ta_2O_5, the additional post-processing not only increases the distance of the reference electrode from the gate but also imposes additional costs in fabrication and complexity to the system through differential buffer capacities (Figure 3.3) [43, 53].

The sensitivity of ISFETs in unmodified CMOS will vary considerably when performing measurements due to a set of *non-idealities* affecting sensor performance, namely: drift, temperature, trapped charges, capacitive signal attenuation and material degradation [7, 52]. *Sensor drift* affects threshold voltage and presents as a gradual but randomly directed voltage signal without pH change in solution. This phenomenon arises due to the slow hydration of the surface [54]. A number of methodologies have been investigated to compensate for drift depending on the passivation material and sensor implementation. For example, Si_3N_4 on average suffers from greater drift phenomena than other high-κ dielectric materials which are more resistant to hydration [54]. Additionally, *trapped charge* can affect ISFET performance. Charges can be trapped on the surface of the gate during fabrication that can offset the output signal [7]. Methods such as exposure to UV have alleviated the effects of trapped charge in modern ISFET designs [55]. On the other hand, capacitive signal attenuation is an inherent limitation of SiO_2 or Si_3N_4 as in unmodified CMOS technology. *Temperature stability* is important to consider when evaluating ISFET output with electron agitation causing an increase equivalent to 1 pH with deviation from ambient temperature by +/- 7K. In cell-based ISFET applications, temperature control is an integral component to cell culture and concurrent monitoring to allow compensation of changes due to temperature variation is a key consideration. Noise which can be attributed to both electronic, chemical and thermal components of the sensor can also result in signal hysteresis [7]. In the case of biological ISFET applications, aspects of "biological noise" warrant additional consideration to delineate the event of interest. Whilst several methods have been employed to reduce the effects it is important to take them into consideration in signal interpretation.

3.5 Related works: Extracellular pH on CMOS-based ISFETs

3.5.1 Reported work in the literature

The first measurements on ISFETs, demonstrated by Bergveld, were based on ionic fluctuations and electrophysiological recordings of neurons [43, 47, 56]. The unique sensitivity of ISFETs to pH changes in a liquid phase has been exploited for a range of applications with ionic changes.

One of the most popular applications of CMOS ISFETs to date has been the Ion Torrent chip for next generation DNA sequencing on a portable and inexpensive platform [57]. The technology used the pH changes induced by nucleotide incorporation during DNA sequencing and revolutionised modern DNA detection. CMOS-based ISFETs for DNA/RNA detection by other technologies, such as Loop-Mediated Isothermal Amplification (LAMP), have since been developed to detect Single-Nucleotide Variants (SNVs) and DNA methylation sites [58–60]. The applications of DNA/RNA detection have varied greatly within the biomedical diagnostics field as ISFETs have found a place in infectious disease diagnosis, antimicrobial resistance and specific mutational signatures for cancer cell detection being only a few examples [52, 61–64].

Whilst TME acidification has only recently been recognised as a possibility for ISFETs, it is well-known that ISFETs could help delineate aspects of biochemical reactions [10]. In this section, we will explore some of the most notable contributions to the field to date with a particular focus on cancer cell detection on ISFETs and the exclusion of electrogenic cell types and chondrocytes, both of which harbour unique properties amenable to electrochemical detection (Table 3.2). Notably, not all technologies utilise unmodified CMOS as some works report modification of the ISFET passivation surface for the purposes of sensor sensitivity and cell culture attachment.

Early work by Lehmann et al., (2000) reported a 1.2μm CMOS setup of an ISFET array where the objective was to detect pH measurements at the cell membrane to differentiate between tumorigenic and healthy cells [65]. Using a fluid perfusion system with a pump to control cell culture flow, cells on the sensor were distinguishable by an acidification peak which was absent when no cells were cultured on the ISFET sensor. The addition of iodoacetate to inhibit glycolysis and induce toxicity showed a decreased acidification rate for sensors both with and without cells [65]. Despite increasing sensitivity, the modified CMOS setup made use of an Aluminium oxide (Al_2O_3) layer that increases the thickness of the sensing layer and cost of production [65]. Notably, the authors also raised concerns over ion diffusion in the system. A later adaptation to the system, and towards what is now known as the Cell Monitoring System (CMS^{TM}), made use of an ISFET sensor coupled with a palladium electrode as an oxygen sensor to integrate both acidification and respiration sensing (Figure 3.4(a)) [66].

On the other hand, a Glaswegian group has had progressive success in implementing extracellular ion sensing. Whilst their original design did not require post-processing they reported a leaking current through the SU-8 encapsulation material which affected their signal output [69]. In later adaptations, they manufactured a larger 16 x 16 ISFET array with a manifold, allowing for the integration of a vacuum pump and a heating module [67]. In that instance, they determined that threshold voltage was constant in pixels and dispensed with previous steps to eliminate trapped charges. In addition, their sensitivity was increased to 46mV/pH as they included etching steps to remove excess SiO_2 from the chip surface [67, 69]. This was a

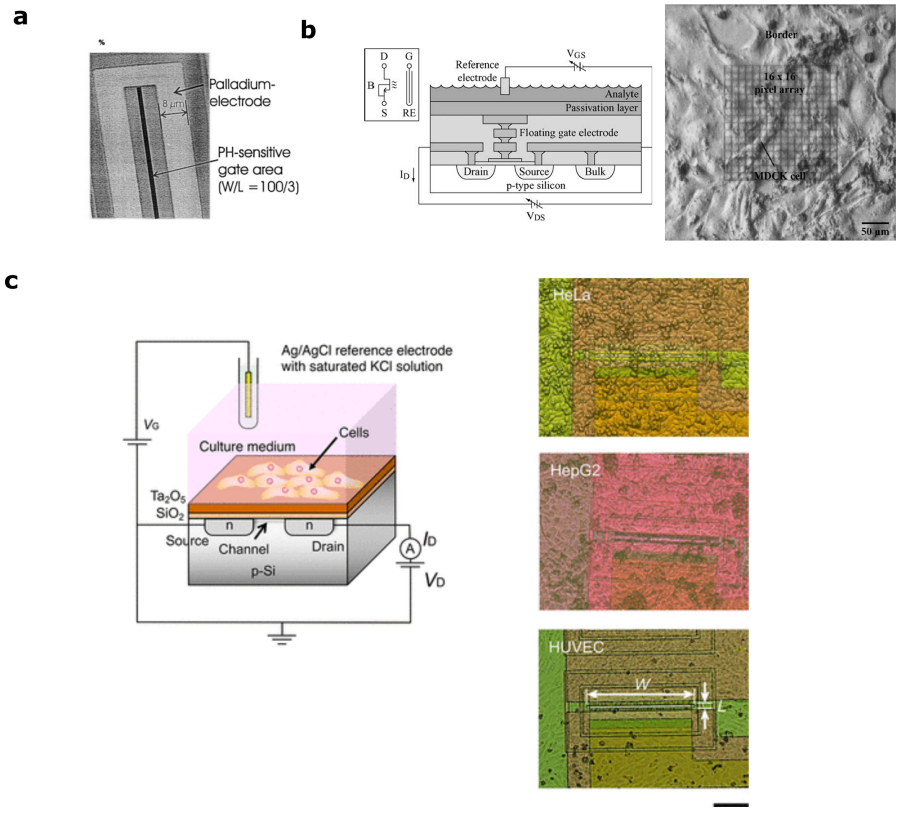


Figure 3.4: **Related works of mammalian cell-based ISFET detection in CMOS (a)** ISFET design reported by Lehmann et al., (2001) [66]. **(b)** ISFET microchip and cells on pixel array reported by Milgrew et al., (2005) [67]. **(c)**ISFET with Ta_2O_5 passivation layer and cells on ISFET reported by Sakata et al., (2018) [68]. Reprinted with permission from [66–68].

significant step forward however, aspects such as drift are likely to differ between arrays and as such compensation should always be considered an essential step. Finally, their data indicated a significant component of noise which should be addressed to eliminate measurement artefacts [67]. Most notably, the group was one of the first to report a microscopy confirmation of cells on the sensor as an evaluation of biocompatibility (Figure 3.4(b)) [55].

More recently, Sakata et al., (2018) reported an ISFET sensor manufactured in silicon technology with a thin-film high-κ dielectric, tantalum pentoxide (Ta_2O_5), passivation layer for the detection of multiple cancer cell lines [68] (Figure 3.4(c)). The study reported a pH sensitivity of 58mV/pH and showed a *Delta* potential a the cell/surface nanogap for cancer cells versus a model cell line. Whilst no particular focus was placed on the cell response in the cell culture system or integrated microfluidic platform, the study paved the way for a novel interpretation of results with a novel appreciation for the reactions taking place at the cell/sensor interface [68]. Additional work in the group has utilised chondrocytes towards extracellular matrix detection and implemented sensing of cells on glass substrates to allow for concurrent microscopy, however, their manufacturing in glass pertains them from mass manufacturing for point-of-care diagnostics [70, 71].

3.5.2 Lacewing: CMOS-based ISFET arrays integrated on a Lab-on-Chip platform

This work capatilises on an ISFET array acting as an ion imaging platform designed by Dr. Nicolas Moser, called "Lacewing". The platform has relied on incremental iterations of microchip design in 0.35um CMOS technology (Table 3.2) (unpublished designs). The Georgiou lab has developed a series of ISFET arrays as part of a LoC platform, known as Lacewing.

The designs feature in-pixel quantisation to provide analogue front-end sensing coupled with a digital memory to allow for full integration on a portable, LoC platform. The technology addresses some of the common challenges associated with ISFET sensors. Namely, high drift rates, material degradation over time, low signal-to-noise ratio both on the chemical sensors and front-end implementation, as well as trapped charges interfering with pixel output [43, 48, 52]. Firstly, temperature pixels interspersed within the ISFET array, allow drift compensation and can be important in biological applications to monitor fluctuations [52]. Additionally, integrated memory capacity and compensation through the source voltage of the ISFET allows post-processing and the implementation of a trapped charge compensation algorithm [52]. The platform results in a favourable, high signal-to-noise ratio and pH sensitivity of 0.019 pH [52]. It has been successfully tested and implemented for RNA and DNA amplification detection by LAMP for a range of infectious diseases, including SARS-CoV-2 and Zika virus, as well detection of prostate and breast cancer mutations [52, 60, 62, 63, 72].

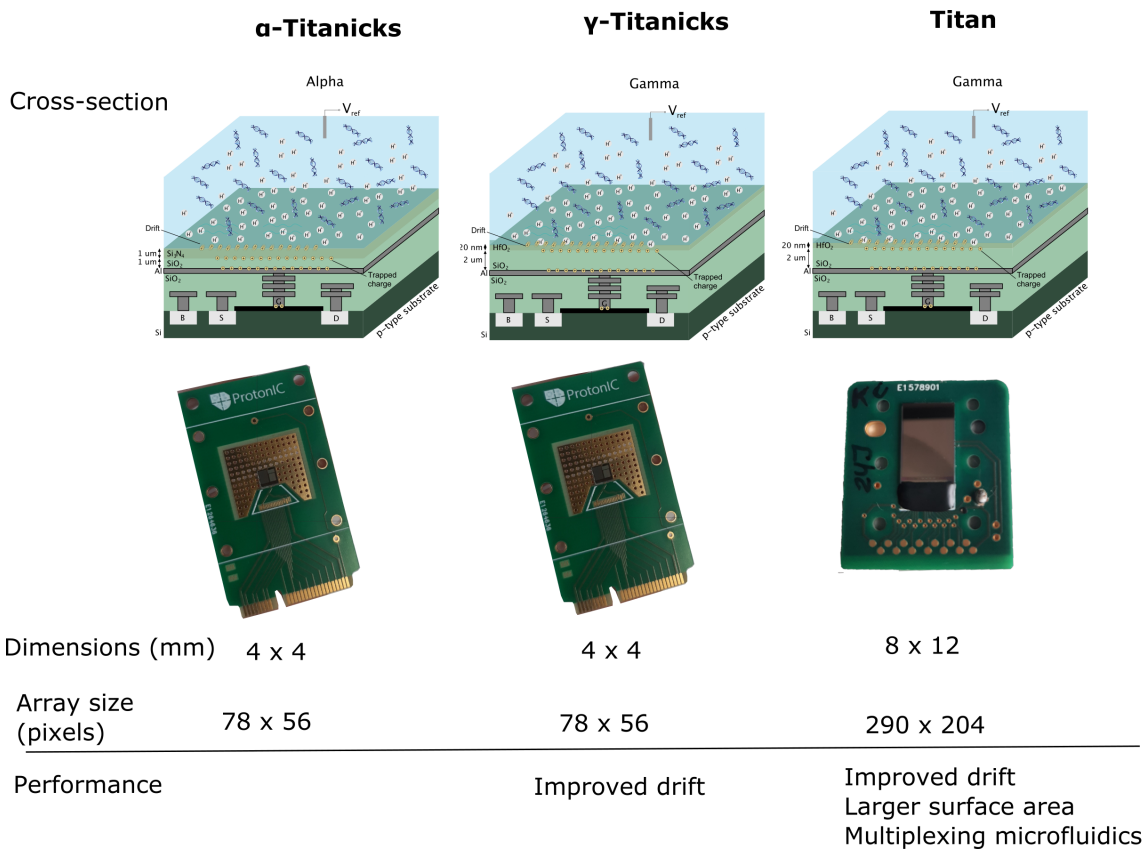


Figure 3.5: **ISFET macromodels designed by Dr. Nicolas Moser for the Lacewing platform.**

The three designs are summarised in Figure 3.5. Firstly, a 78 x 56 ISFET array, therein known as Titanicks α, manufactured in unmodified CMOS technology was reported by Moser et al.,(2018) with a $1\mu m$ silicon dioxide and $1\mu m$ silicon nitride sensing surface [51, 52]. A subsequent design of a 78 x 56 ISFET array, therein referred to as Titanicks γ, is an adaptation to earlier iterations with the addition of a thin film high-κ dielectric passivation layer which has the desired effect of increasing pH sensitivity (Figure 3.6). Finally, the extension of the aforementioned designs has cultivated in a large sensor of 290 x 204 dimensions, referred to as Titan (Figure 3.7). The readout circuit employs pH-to-time encoding, generating a Pulse Width Modulation (PWM) output of width τ that is exponentially related to pH (Eq. 3.3), where nU_t represents thermal voltage and earlier terms are defined in section 3.4. The sensor output is then the number of time pulses of a high frequency clock with resolution 12.8ns-33.1ns within the pulse width of the PWM signal [52]. Notably, a large sensing area in combination with microfluidic components to allow efficient packaging has allowed sample multiplexing creating the opportunity for multiple assaying on a single sensor.

$$\text{Time pulses} \propto \tau \propto \exp\left(\frac{\alpha\, S_N\, pH}{nU_t}\right) \tag{3.3}$$

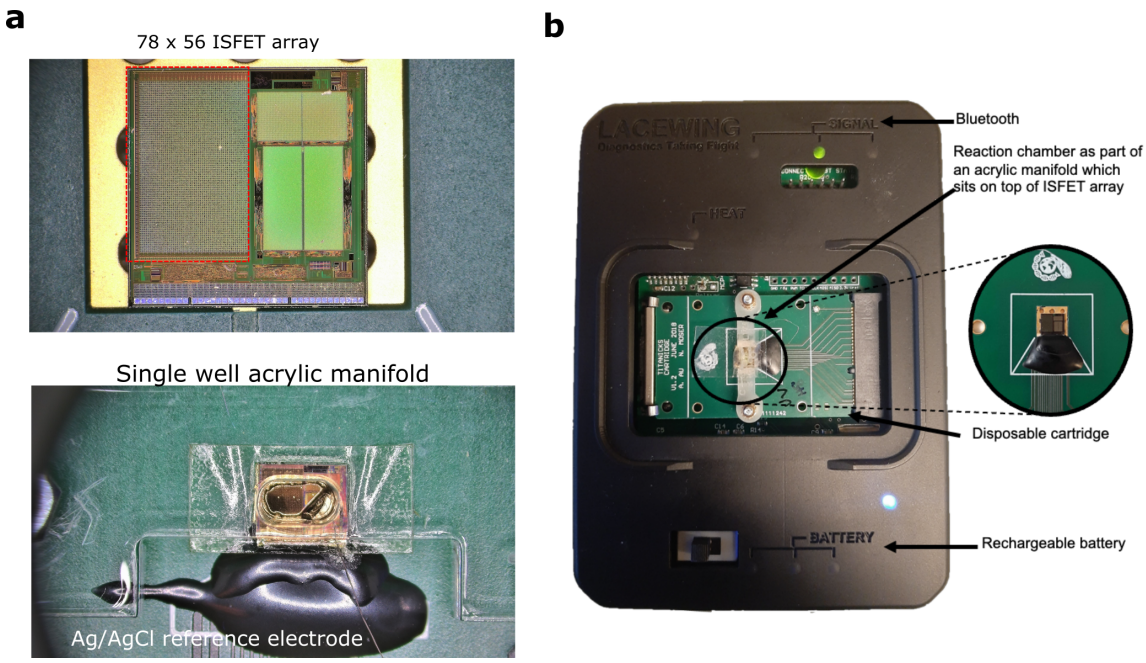


Figure 3.6: **Titanicks α and γ hardware. (a)** ***Top:*** Light microscopy image of the Titanicks ISFET array (highlighted in red) epoxy glued on a disposable cartridge. ***Bottom:*** Single well acrylic manifold fitted on the array and connected to an Ag/AgCl reference electrode. **(b)** Portable Lab-on-Chip device for Titanicks with rechargeable battery and bluetooth connection. Previously reported in Moser et al., (2018) [52].

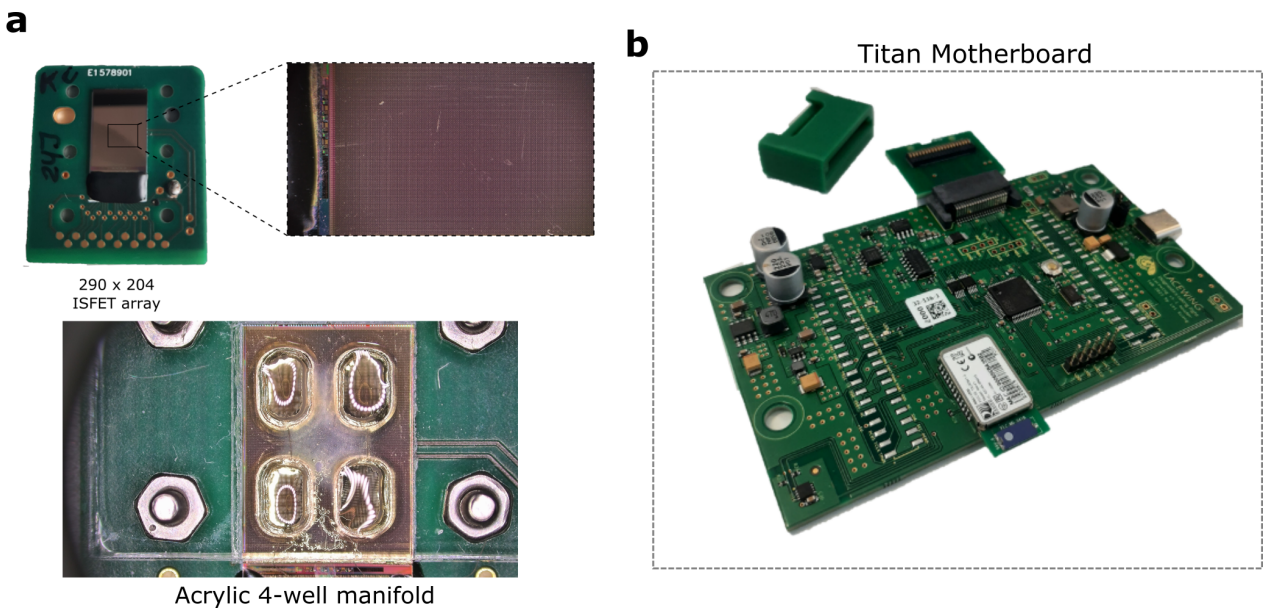


Figure 3.7: **Titan ISFET array hardware. (a)** ***Top:*** A 290 x 204 ISFET array epoxy glued and wire bonded to a disposable cartridge. Magnified light microscopy image of array pixels.***Bottom:***A 4 well acrylic manifold fitted on the Titan array for multiplex experimental setup. **(b)** Titan motherboard with 3D printed extension for portable Lab-on-Chip implementation.

Table 3.2: CMOS ISFET sensors for mammalian cell detection.

Year	Ref	CMOS	Array	Passivation	Sensitivity	Cell type	Application	Cell attachment	Other biocompatibility
2000	Lehmann [65]	x(1.2um)	2 x 2	aluminium oxide	56.11mV/pH	LS 174T (colon adenocarcinoma)	Cell respiration	_	_
2001	Lehmann [66]	x	single ISFET	_	45mV/pH	LS 174T (colon adenocarcinoma)	Cell respiration	_	_
2003	Lorenzelli [73]	x	12 ISFETs	silicon nitride	56mV/pH	CHO (hamster epithelial) and cheratinocytes	Drug screening	not shown	_
2004	Milgrew [69]	x (0.35um)	2 x 2	silicon oxynitride	40mV/pH	BHK21 C13 cells (fibroblasts kidney hamster)	Extracellular pH	x	Long-term culture
2005	Milgrew [67]	x (0.35um)	16 x 16	silicon nitride	46mV/pH	MDCK (canine kidney cell line)	Extracellular pH	x	_
2008	Milgrew [55]	x (0.35um)	16 x 16	silicon nitride	45-56mV/pH	fibroblasts	Extracellular pH/Respiration	x	_
2017	Nabovati [33]	x (0.35um)	8 x 8	silicon nitride	50mV/pH	H1299 (lung carcinoma) HeLa (cervical cancer immortalized line)	Extracellular pH Extracellular pH	not shown	_
2018	Sakata [68]	x	_	tantalum pentoxide	58mV/pH	HepG2 (Hepatocellular carcinoma) HUVEC (Human umbilical vein endothelial)	Adhesion Viability	x	_
2022	Xiao [74]	x	_	graphene FET with PLL	52.9 mV/pH (with PLL)	MCF-7 (breast cancer)	Extracellular pH	x	cell count/viability
2023	Yang [75]	x (0.35um)	640 x 640	silicon nitride	33 +-mV/pH	Caski cells (epidermoid carcinoma)	Cell media pH	NA	_
2023	Noyan [76]	x (0.5um)	_	silicon dioxide	35mV/pH	adenocarcinoma	Extracellular pH	not shown	3 days culture capacitive sensing
		x (0.35um)	78 x 56	silicon nitride	_	MDA-MB-231 (triple negative breast cancer)		x	morpohology
This work	Moser	x (0.35um)	78 x 56	hafnium oxide	_	MCF10A (mammary epithelial)	Extracellular pH	x	mechano-response
		x (0.35um)	290 x 204	hafnium oxide	_	U2OS CDK1 AS (Osteosarcoma)		x	proliferation viability

3.6 Summary

In this chapter, we have introduced the concept of biosensors and the associated challenges in implementations for live cell detection. The focus on mammalian cell cultures presents an aspect of complexity which is excluded in other applications, such as the more resilient microbial cells. Challenges include: maximising sensor sensitivity and selectivity by considering surface chemistry and biocompatibility, sterility, real-time detection, reproducibility and delineation of cell signal complexity that can be hindered by biological noise. We have reviewed the modern possibilities of cell-based biosensors in different classes of transducers: optical, mechanical and electrochemical.

CMOS technology for the monolithic integration of silicon-based sensors and processing circuity has been highlighted as the future of electrochemical cell-based sensors for PoC diagnostic devices. We have reviewed key advances in electrochemical sensing technologies for cell-based applications in cancer detection: capacitive, impedance and potentiometric sensing. Finally, a closer review of ISFETs manufactured in CMOS technology which have been implemented in mammalian cell cultures for detection of extracellular pH. The few implementations of whole, mammalian cells on ISFET arrays in CMOS show a poor understanding of cell morphology and physiological reactions at the interface. With a lack of recent contribution to the field, we present timely implementation of using potentiometric sensing for cell cultures in this work. The three types of ISFET arrays known as Titanicks α, Titanicks γ and Titan are summarised and results using these designs are presented in the following results chapters.

References

[1] N. Bhalla et al. "Introduction to biosensors". In: *Essays in Biochemistry* 60.1 (June 2016), pp. 1–8.

[2] D. R. Thévenot et al. "Electrochemical biosensors: Recommended definitions and classification". In: *Biosensors and Bioelectronics* 16.1-2 (Jan. 2001), pp. 121–131.

[3] G. D. Griffin and D. N. Stratis-Cullum. "Biosensors". In: *Encyclopedia of Microbiology, Third Edition* (Jan. 2009), pp. 88–103.

[4] V. Naresh and N. Lee. "A review on biosensors and recent development of nanostructured materials-enabled biosensors". In: *Sensors (Switzerland)* 21.4 (Feb. 2021), pp. 1–35.

[5] L. C. Clark and C. Lyons. "ELECTRODE SYSTEMS FOR CONTINUOUS MONITORING IN CARDIOVASCULAR SURGERY". In: *Annals of the New York Academy of Sciences* 102.1 (Oct. 1962), pp. 29–45.

[6] D. Özsoylu, T. Wagner, and M. J. Schöning. "Electrochemical Cell-based Biosensors for Biomedical Applications". In: *Current Topics in Medicinal Chemistry* 22.9 (Mar. 2022), pp. 713–733.

[7] N. Moser et al. "ISFETs in CMOS and Emergent Trends in Instrumentation: A Review". In: *IEEE Sensors Journal* 16.17 (Sept. 2016), pp. 6496–6514.

[8] B. Merriman, I. Torrent, and J. M. Rothberg. "Progress in Ion Torrent semiconductor chip based sequencing". In: *Electrophoresis* 33.23 (2012), pp. 3397–3417.

[9] H. Chen et al. *The Applications of Electrochemical Immunosensors in the Detection of Disease Biomarkers: A Review*. Apr. 2023.

[10] Q. Liu et al. "Cell-based biosensors and their application in biomedicine". In: *Chemical Reviews* 114.12 (June 2014), pp. 6423–6461.

[11] X. Wu et al. "A breast cancer cell microarray (CMA) as a rapid method to characterize candidate biomarkers". In: *Cancer Biology and Therapy* 15.12 (Dec. 2014), pp. 1593–1599.

[12] A. H. Aly and Z. A. Zaky. "Ultra-sensitive photonic crystal cancer cells sensor with a high-quality factor". In: *Cryogenics* 104 (Dec. 2019), p. 102991.

[13] L. L. Chan et al. “A label-free photonic crystal biosensor imaging method for detection of cancer cell cytotoxicity and proliferation”. In: *Apoptosis* 12.6 (June 2007), pp. 1061–1068.

[14] N. R. Ramanujam et al. “Enhanced sensitivity of cancer cell using one dimensional nano composite material coated photonic crystal”. In: *Microsystem Technologies* 25.1 (Jan. 2019), pp. 189–196.

[15] D. Mohammad and K. Behnam. “Design of a label-free photonic crystal refractive index sensor for biomedical applications”. In: *Photonics and Nanostructures - Fundamentals and Applications* 31 (Sept. 2018), pp. 89–98.

[16] M. De, T. K. Gangopadhyay, and V. K. Singh. “Prospects of photonic crystal fiber as physical sensor: An overview”. In: *Sensors (Switzerland)* 19.3 (Feb. 2019).

[17] N. Ayyanar et al. “Photonic Crystal Fiber-Based Refractive Index Sensor for Early Detection of Cancer”. In: *IEEE Sensors Journal* 18.17 (Sept. 2018), pp. 7093–7099.

[18] I. E. Tothill. “Biosensors for cancer markers diagnosis”. In: *Seminars in Cell and Developmental Biology* 20.1 (Feb. 2009), pp. 55–62.

[19] N. Chandra Shekar et al. “Detection of melanoma cancer cell by designing a SPR based biosensor”. In: *Journal of Physics: Conference Series* 1362.1 (Nov. 2019), p. 012011.

[20] M. Z. Mousavi et al. “Label-free detection of rare cell in human blood using gold nano slit surface plasmon resonance”. In: *Biosensors* 5.1 (Mar. 2015), pp. 98–117.

[21] K. A. Marx et al. “A comparative study of the cytoskeleton binding drugs nocodazole and taxol with a mammalian cell quartz crystal microbalance biosensor: Different dynamic responses and energy dissipation effects”. In: *Analytical Biochemistry* 361.1 (Feb. 2007), pp. 77–92.

[22] D. Peiris et al. “Cellular glycosylation affects Herceptin binding and sensitivity of breast cancer cells to doxorubicin and growth factors”. In: *Scientific Reports* 7.1 (Feb. 2017), pp. 1–11.

[23] X. Li et al. “Real-time and label-free analysis of binding thermodynamics of carbohydrate-protein interactions on unfixed cancer cell surfaces using a QCM biosensor”. In: *Scientific Reports* 5.1 (Sept. 2015), pp. 1–9.

[24] L. Elmlund et al. “Study of the interaction of trastuzumab and SKOV3 epithelial cancer cells using a quartz crystal microbalance sensor”. In: *Sensors (Switzerland)* 15.3 (Mar. 2015), pp. 5884–5894.

[25] K. Barbee et al. “The study of a cell-based TSM piezoelectric sensor”. In: *Proceedings of the Annual IEEE International Frequency Control Symposium* (2002), pp. 260–267.

[26] Y. Adiguzel and H. Kulah. “CMOS cell sensors for point-of-care diagnostics”. In: *Sensors (Switzerland)* 12.8 (Aug. 2012), pp. 10042–10066.

[27] S. E. Thompson and S. Parthasarathy. “Moore’s law: the future of Si microelectronics”. In: *Materials Today* 9.6 (June 2006), pp. 20–25.

[28] J. L. Hammond et al. “Electrochemical biosensors and nanobiosensors”. In: *Essays in Biochemistry* 60.1 (June 2016), pp. 69–80.

[29] S. B. Prakash and P. Abshire. “Tracking cancer cell proliferation on a CMOS capacitance sensor chip”. In: *Biosensors and Bioelectronics* 23.10 (May 2008), pp. 1449–1457.

[30] S. Forouhi, R. Dehghani, and E. Ghafar-Zadeh. “CMOS based capacitive sensors for life science applications: A review”. In: *Sensors and Actuators, A: Physical* 297 (Oct. 2019), p. 111531.

[31] B. Senevirathna and P. Abshire. “CMOS Capacitance Biosensors to Monitor Cell Viability”. In: *Handbook of Biochips: Integrated Circuits and Systems for Biology and Medicine* (Jan. 2022), pp. 553–570.

[32] S. B. Prakash and P. Abshire. “On-Chip Capacitance Sensing for Cell Monitoring Applications”. In: *IEEE Sensors Journal* 7.3 (Mar. 2007), pp. 440–447.

[33] G. Nabovati et al. “Towards High Throughput Cell Growth Screening: A New CMOS 8 × 8 Biosensor Array for Life Science Applications”. In: *IEEE Transactions on Biomedical Circuits and Systems* 11.2 (Apr. 2017), pp. 380–391.

[34] G. Nabovati et al. “Smart Cell Culture Monitoring and Drug Test Platform Using CMOS Capacitive Sensor Array”. In: *IEEE Transactions on Biomedical Engineering* 66.4 (Apr. 2019), pp. 1094–1104.

[35] H. Moghtaderi et al. “Electric cell-substrate impedance sensing in cancer research: An in-depth exploration of impedance sensing for profiling cancer cell behavior”. In: *Sensors and Actuators Reports* 7 (June 2024), p. 100188.

[36] I. Giaever and C. K. Keese. “A morphological biosensor for mammalian cells”. In: *Nature* 366.6455 (Dec. 1993), pp. 591–592.

[37] J. Wegener, C. R. Keese, and I. Giaever. “Electric cell-substrate impedance sensing (ECIS) as a noninvasive means to monitor the kinetics of cell spreading to artificial surfaces”. In: *Experimental Cell Research* 259.1 (Aug. 2000), pp. 158–166.

[38] F. Zhang et al. “Distinguishing skin cancer cells and normal cells using electrical impedance spectroscopy”. In: *Journal of Electroanalytical Chemistry* 823 (Aug. 2018), pp. 531–536.

[39] L. Wang et al. “Real-time, label-free monitoring of the cell cycle with a cellular impedance sensing chip”. In: *Biosensors and Bioelectronics* 25.5 (Jan. 2010), pp. 990–995.

[40] Y. Chen et al. “CMOS high density electrical impedance biosensor array for tumor cell detection”. In: *Sensors and Actuators, B: Chemical* 173 (Oct. 2012), pp. 903–907.

[41] N. Moser et al. “Complementary Metal-Oxide-Semiconductor Potentiometric Field-Effect Transistor Array Platform Using Sensor Learning for Multi-ion Imaging”. In: *Analytical Chemistry* 92.7 (Apr. 2020), pp. 5276–5285.

[42] P. Bergveld. “The operation of an ISFET as an electronic device”. In: *Sensors and Actuators* 1.C (1981), pp. 17–29.

[43] P. Bergveld. “Thirty years of ISFETOLOGY: What happened in the past 30 years and what may happen in the next 30 years”. In: *Sensors and Actuators, B: Chemical* 88.1 (Jan. 2003), pp. 1–20.

[44] T. Liang et al. “Light Addressable Potentiometric Sensor (LAPS) Integrated Microfluidic System for Real-Time Cell Acidification Detection”. In: *ISOEN 2019 - 18th International Symposium on Olfaction and Electronic Nose, Proceedings* (May 2019).

[45] P. M. Shaibani et al. “Metabolic Study of Cancer Cells Using a pH Sensitive Hydrogel Nanofiber Light Addressable Potentiometric Sensor”. In: *ACS Sensors* 2.1 (Jan. 2017), pp. 151–156.

[46] N. Manaresi et al. “A CMOS Chip for Individual Cell Manipulation and Detection”. In: *IEEE Journal of Solid-State Circuits* 38.12 (Dec. 2003), pp. 2297–2305.

[47] P. Bergveld. “Development, Operation, and Application of the Ion-Sensitive Field-Effect Transistor as a Tool for Electrophysiology”. In: *IEEE Transactions on Biomedical Engineering* BME-19.5 (Sept. 1972), pp. 342–351.

[48] N. Moser et al. “ISFET arrays for lab-on-chip technology: A review”. In: *2019 26th IEEE International Conference on Electronics, Circuits and Systems, ICECS 2019* (Nov. 2019), pp. 57–60.

[49] A. Allagui, H. Benaoum, and O. Olendski. “On the Gouy–Chapman–Stern model of the electrical double-layer structure with a generalized Boltzmann factor”. In: *Physica A: Statistical Mechanics and its Applications* 582 (Nov. 2021), p. 126252.

[50] D. E. Yates, S. Levine, and T. W. Healy. “Site-binding model of the electrical double layer at the oxide/water interface”. In: *Journal of the Chemical Society, Faraday Transactions 1: Physical Chemistry in Condensed Phases* 70.0 (Jan. 1974), pp. 1807–1818.

[51] J. Bausells et al. “Ion-sensitive field-effect transistors fabricated in a commercial CMOS technology”. In: *Sensors and Actuators, B: Chemical* 57.1-3 (Sept. 1999), pp. 56–62.

[52] N. Moser et al. “A scalable ISFET sensing and memory array with sensor auto-calibration for on-chip real-time DNA detection”. In: *IEEE Transactions on Biomedical Circuits and Systems* 12.2 (Apr. 2018), pp. 390–401.

[53] H. S. Wong and M. H. White. “Self-contained CMOS integrated pH sensor”. In: *Technical Digest - International Electron Devices Meeting* (Dec. 1988), pp. 658–661.

[54] S. Jamasb, S. Collins, and R. L. Smith. "A physical model for drift in pH ISFETs". In: *Sensors and Actuators, B: Chemical* 49.1-2 (June 1998), pp. 146–155.

[55] M. J. Milgrew, M. O. Riehle, and D. R. Cumming. "A 16×16 CMOS proton camera array for direct extracellular imaging of hydrogen-ion activity". In: *Digest of Technical Papers - IEEE International Solid-State Circuits Conference* 51 (2008), pp. 590–638.

[56] P. Bergveld. "Short Communications: Development of an Ion-Sensitive Solid-State Device for Neurophysiological Measurements". In: *IEEE Transactions on Biomedical Engineering* BME-17.1 (1970), pp. 70–71.

[57] J. M. Rothberg et al. "An integrated semiconductor device enabling non-optical genome sequencing". In: *Nature* 475.7356 (July 2011), pp. 348–352.

[58] C. Toumazou, T. S. L. K. Thay, and P. Georgiou. "A new era of semiconductor genetics using ion-sensitive field-effect transistors: The gene-sensitive integrated cell". In: *Philosophical Transactions of the Royal Society A: Mathematical, Physical and Engineering Sciences* 372.2012 (Mar. 2014).

[59] M. Kalofonou and C. Toumazou. "An ISFET based analogue ratiometric method for DNA methylation detection". In: *Proceedings - IEEE International Symposium on Circuits and Systems* (2014), pp. 1832–1835.

[60] M. Kalofonou et al. "A novel hotspot specific isothermal amplification method for detection of the common PIK3CA p.H1047R breast cancer mutation". In: *Scientific Reports* 10.1 (Mar. 2020), pp. 1–10.

[61] J. Broomfield et al. "Handheld ISFET Lab-on-Chip Detection of TMPRSS2-ERG and AR mRNA for Prostate Cancer Prognostics". In: *IEEE Sensors Letters* 7.8 (Aug. 2023), pp. 1–4.

[62] J. Rodriguez-Manzano et al. "Handheld point-of-care system for rapid detection of SARS-CoV-2 extracted RNA in under 20 min". In: *ACS Central Science* 7.2 (Feb. 2021), pp. 307–317.

[63] N. Moser et al. "Live demonstration: A CMOS-based ISFET array for rapid diagnosis of the Zika virus". In: *Proceedings - IEEE International Symposium on Circuits and Systems* (Sept. 2017).

[64] J. Rodriguez-Manzano et al. "Rapid Detection of Mobilized Colistin Resistance using a Nucleic Acid Based Lab-on-a-Chip Diagnostic System". In: *Scientific Reports* 10.1 (May 2020), pp. 1–9.

[65] M. Lehmann et al. "Non-invasive measurement of cell membrane associated proton gradients by ion-sensitive field effect transistor arrays for microphysiological and bioelectronical applications". In: *Biosensors and Bioelectronics* 15.3-4 (June 2000), pp. 117–124.

[66] M. Lehmann et al. “Simultaneous measurement of cellular respiration and acidification with a single CMOS ISFET”. In: *Biosensors and Bioelectronics* 16.3 (May 2001), pp. 195–203.

[67] M. J. Milgrew, M. O. Riehle, and D. R. Cumming. “A large transistor-based sensor array chip for direct extracellular imaging”. In: *Sensors and Actuators, B: Chemical* 111-112.SUPPL. (Nov. 2005), pp. 347–353.

[68] T. Sakata, H. Sugimoto, and A. Saito. “Live Monitoring of Microenvironmental pH Based on Extracellular Acidosis around Cancer Cells with Cell-Coupled Gate Ion-Sensitive Field-Effect Transistor”. In: *Analytical Chemistry* 90.21 (Nov. 2018), pp. 12731–12736.

[69] M. J. Milgrew, P. A. Hammond, and D. R. Cumming. “The development of scalable sensor arrays using standard CMOS technology”. In: *Sensors and Actuators, B: Chemical* 103.1-2 (Sept. 2004), pp. 37–42.

[70] T. Sakata et al. “Ion Sensitive Transparent-Gate Transistor for Visible Cell Sensing”. In: *Analytical Chemistry* 89.7 (Apr. 2017), pp. 3901–3908.

[71] H. Satake et al. “Long-term and real-time monitoring of chondrocyte behavior synthesizing extracellular matrix with biologically coupled field effect transistor”. In: *Japanese Journal of Applied Physics* 56.4 (Apr. 2017), p. 04CM03.

[72] J. Broomfield et al. “Detection of YAP1 and AR-V7 mRNA for Prostate Cancer Prognosis Using an ISFET Lab-On-Chip Platform”. In: *ACS Sensors* 7.11 (Nov. 2022), pp. 3389–3398.

[73] L. Lorenzelli et al. “Bioelectrochemical signal monitoring of in-vitro cultured cells by means of an automated microsystem based on solid state sensor-array”. In: *Biosensors and Bioelectronics* 18.5-6 (May 2003), pp. 621–626.

[74] L. Xiao et al. “A pH-sensitive field-effect transistor for monitoring of cancer cell external acid environment”. In: *Talanta* 252 (Jan. 2023), p. 123764.

[75] L. Yang et al. “A 640 × 640 ISFET array for detecting cell metabolism”. In: *Journal of Semiconductors* 44.2 (Feb. 2023), p. 024101.

[76] U. Noyan et al. “Scalable biosensors using standard CMOS process”. In: *Technical Digest - International Electron Devices Meeting, IEDM* (2023).

Chapter 4

Translation of mammalian cell culture protocols on ISFETs

This chapter chapter presents an overview of the considerations for cell culture protocols applied on ISFET arrays for real-time sensing of pH changes. Firstly, the complex formulation of cell culture media is presented and the environmental conditions which can affect media pH is discussed. The next section describes the molecular methods implemented and experimental setup for α and γ-Titanicks. Lastly, the experimental results for pH change recorded *in vitro* and sensor voltage traces with conditioned media from a range of cell lines is described. A summary and future directions section guides the next steps for future culture protocol implementations on chip.

4.1 Introduction

The complex pH regulation recorded in the TME has been attributed many roles as it can promote rapid proliferation, angiogenesis, tumour metastasis and immune evasion [1, 2]. The interplay of signaling mechanisms that lead to pHe acidification can be challenging to recapitulate *in vitro* as the complex TME dynamics are often defined by the mammalian living system [3]. To summarise, tumour microenvironment acidosis is driven, to a large extent, by a perturbed cancer cell metabolism known as ***the Warburg effect***. This results in an increase in glycolytic metabolism, irrespective of oxygen availability, whilst oxidative phosphorylation rates also remain stable leading to accumulation of excess end-products. Namely, lactate ions and CO_2 and are regulated in the intracellular space to maintain acid-base balance and prevent rate-limiting pHi levels. *In vivo*, the activity of acid-base membrane transporters and a bicarbonate (HCO_3^-) buffering system as well as complex signaling mechanisms, maintain a delicate pHi/pHe homeostasis [4, 5]. In healthy tissues, pHe is maintained at a range of 7.3-7.4 pH [5]. On the other hand, malignant tissue pHe tends to be acidic and will vary dependent on factors such as oxygen perfusion and hypoxic regions, as well as metabolic product accumulation. The pHe range of malignant tissue has been measured in the acidic range of 6.4-7 pH, whilst pHi values are in the alkaline range $\geq$ 7.2 [5, 6]. This amounts to significant changes in H^+ ions extracellularly and intracellularly in cancer cells due to the logarithimic relationship of pH and H^+ concentration. Furthermore, the sensitivity of the pHe/pHi balance has been exploited for therapeutic purposes with the application of proton efflux inhibitors to disturb homeostasis, indicating the importance of understanding and modeling TME pH in cancer cell technologies [7].

4.1.1 pH regulation in cell culture media formulations

Three key components of cell culture are the media formulation, the environmental conditions (CO_2 availability, temperature, hydration) and the "health" status of cells themselves. Concertedly, these components will both control and affect pH in mammalian cell cultures. As a result, maintaining physiologically relevant pH in cell cultures is an important factor which can have a significant impact on cell proliferation and survival [8–11]. Highly acidic or alkaline pH values may inhibit cell growth both in healthy and malignant cells [8, 11, 12]. Various basal cell culture media recipes are formulated with different concentrations of amino acids, vitamins, inorganic compounds, growth factors and buffering agents which will impact cell viability. Supplementation with foetal bovine serum (FBS) is commonly utilised in cell culture studies for the addition of necessary proteins, as well as addition of antimicrobial agents, such as penicillin and streptomycin. Some of the most universally utilised, cell culture medium formulations are Dulbecco's Modified Eagle's Medium (DMEM), DMEM/F12 (DMEM supplemented with

Ham's F12 base medium) and Roswell Park Memorial Institute 1640 (RPMI) medium. Dependant on the cell type and experimental conditions, it may be formulated with either sodium bicarbonate as a buffer or other zwitterion-based buffering agents such as HEPES buffer, that are considered more stable to pH changes [1, 4, 13–15]. The role of the buffering agent is to maintain a physiological pH range in culture media solution during cell culture incubation. In a bicarbonate (HCO_3^-) system, pH of the solution will inherently be affected by the CO_2 concentration in cell culture incubators which is typically set at 5%. Dissolved CO_2 will result in pH fluctuations in growth media, coupled with efflux of metabolites arising from cell growth and metabolism [16]. A further component which can vary in a cell culture medium formulation is the availability and range of metabolites e.g. glucose and pyruvate [2] which can become rate-limiting. This will have important consequences on cell metabolism and net TME acidification by lactate production [2].

Isolating pH changes which are normally found in the tumour microenvironment can be complex as several cellular components, e.g. stromal cells and immune cells, as well as metabolic and perfusion events, are all factors which contribute to a final pH [4–6]. Current practices for *in vitro* studies are often centered on the recommendations of international resource centres such as the ATCC and government recommendations [17, 18]. A non-uniform pH throughout the TME, however, makes it difficult to model in adherent cultures which remain the most ubiquitously comparable technique in cell culture [2, 4, 6, 18]. More recently, newer culture media formulations which more closely mimic physiological environments have been studied, such as Plasmax, however, they can be costly and not widely used by the scientific community in order to allow [19]. In existing culture media formulation, fluctuations in CO_2 gas exchange and buffering capacity, which can vary, significantly affect the outcome of *in vitro* experiments [2, 4, 20]. In this chapter, we explore the pH changes which are detectable in cell culture media with standard DMEM and DMEM/F12 formulations for a Triple Negative Breast cancer (TNBC) cell line, MDA-MB-231, and a non-malignant cell line derived from mammary epithelial tissue, MCF10A.

4.2 Molecular Methods

4.2.1 Cell lines

Maintenance Cell lines MDA-MB-231, Cal51 and hs578t were utilised as breast cancer models in this study. Mammary epithelial cell line, MCF10A, were used as a healthy, control cell line in the following experiments. The maintenance media used for breast cancer cell lines is DMEM (1X) with 4.5g/L D-Glucose, L-Glutamine and Pyruvate (Gibco), 3.7g/L sodium bicarbonate, 10% Fetal Bovine Serum (FBS) (Gibco) and 1% Penicillin-Streptavidin (Invitrogen).

The MCF10A media formulation consists of: DMEM/F12 (Ham) (1:1) + GlutaMAX (1X) with 2.438g/L sodium bicarbonate and sodium pyruvate, 5% Horse serum (Invitrogen), Epidermal Growth Factor (20 ng/ml final concentration) (Peprotech), Hydrocortisone (0.5 mg/ml final concentration) (Sigma), Cholera Toxin (100 ng/ml final concentration) (Sigma), Insulin (10 μg/ml final concentration) (Sigma) and 1% Penicillin/Streptavidin (P/S)(Invitrogen). All media were stored at 4°C.

Passaging All cultures were incubated at 37°C and 5% CO_2. Cells were passaged when they reached 70-80% confluency. The current media was aspirated and 5ml sterile PBS was used to wash the flask. Trypsin-EDTA (0.25%) (Gibco) was added to the falcon – 1ml in a T25 flask and 2ml in a T75 flask – and allowed to incubate at 37°C, 5% CO_2 for 5-7 mins until all cells appeared in suspension under the light microscope. For MCF10A cultures the incubation period for trypsinization was 15 mins. Addition of 5ml of the relevant media inhibits trypsinization. The entire volume was collected in a 15ml falcon and centrifuged at 1000 rpm at room temperature for 5 mins. Media was aspirated and the pellet was resuspended in the volume required for the given dilution i.e. 6ml for a 1:6 dilution. In a T25, cells were maintained in 5ml media or 10ml in a T75.

4.2.2 pH measurements

pH probe To obtain pH measurements a Sentron S1600 pH meter with a MicroFET probe was used. Before each use the pH probe was calibrated with three buffers: pH 4, pH 7, pH 10. There are two methods with which pH measurements were taken at 37°C. Firstly, when the cell culture plate was placed in the Muvicyte imaging system (PerkinElmer), the probe was placed in each well individually and set to log mode for 5 mins. The pH probe was flushed with distilled H_2O, shaken gently to dry and placed into the next well. In case of long-term monitoring in T25 flasks, the probe was placed in the flask, ensuring the tip was fully immersed in culture media. The pH meter was set to log mode for an average of 8 hours with a measurement obtained every 5 mins. To ensure minimum CO_2 diffusion into the media, the opening of the flask was covered with parafilm and a pinhole was made through which to place the probe.

4.3 Experimental Setup

All dies were previously been glued, wire-bonded and epoxied with glob-top epoxy. Cartridges were subsequently exposed to UV for 12 hours for the removal of trapped charges. All cartridges were gently cleaned with IPA prior to assembly.

Ag/AgCl electrode A reference electrode made of Ag wire (0.03mm) is chlorinated using 3M KCl with a voltage of 0.9V for 5mins or until a dark coat appears.

Cartridge Single well acrylic manifolds were cut from a 5mm acrylic sheet. The single well volume maximum was 20ul with an operating volume of 15ul.

pH buffers Buffers were made from a stock solution of 100ml 1M Tricine, 333.33ml 3M KCl made up to 1l with distilled H_2O. Buffers were adjusted using HCl or NaOH to the desired pH and validated with a Sentron pH probe. All buffers were stored at ambient temperature for no more than a period of 1 month.

Experimental setup The reference electrode was placed at the centre of the array and attached to the acrylic manifold using a cut TESA tape. The manifold was then attached on to the chip and secured with screws and bolts at either end. The reference electrode was subsequently soldered to the PCB. Experiments were performed at ambient temperature on a Lacewing motherboard for Titanicks.

4.4 Characterisation of pH changes in cell culture media from cancerous and non-cancerous cell lines

To better understand pH changes in cell cultures in order to translate to our experimental setup on chip, we sought to explore the pH changes that take place in cell cultures of triple negative breast cancer cell line, MDA-MB-231, and a non-malignant mammary epithelial cell line, MCF10A. We hypothesized that a malignant cell line would change the pH of cell culture media to a greater extent than a non-malignant cell line, predominantly due to cancer cell metabolism. This allowed us to determine the factors to be taken into consideration when transferring cell culture techniques onto lab-on-chip technology for assay development.

Monitoring pH changes in intervals for a period of 2 days in MDA-MB-231 cell cultures as compared to DMEM complete media with no cells seeded, reveals a final pH change of 0.56 units due to cell activity (Figure 4.1a). On the other hand, media fluctuations which arose due to other factors, such as any fluctuations in temperature and CO_2 concentration or serum protein decomposition in DMEM (10% FBS, 1% P/S) resulted in a total pH change of 0.3 units (Figure 4.1a). Figure 4.1 reveals a pattern of pH during the time intervals where monitoring took place. Linear changes in pH from the start of an interval to the end of an interval, suggest that CO_2 gas hydration is likely influencing pH readings. This results in H^+ increase throughout the measurement intervals which is re-equilibrated to an extent after a few hours (review Equation 2.2). This is confirmed to a large extent due to the fact that at the start of an interval the pH tends to be higher than where the previous interval concluded. An external pH probe was used for these experiments which is likely affecting the cell culture media exposure

to CO_2 levels to a greater extent than would be the case in an enclosed microfluidic system on chip. Moreover, the effect of lactate production from the cells likely has an additive effect to the reduction of pH in cell culture media over time (Figure 4.1a).

The buffering capacity of a cell culture media and the glucose availability will affect pH change and lactate production. Commercial DMEM media is formulated with 3.7g/L sodium bicarbonate buffer which is equivalent to 44mM sodium bicarbonate that is considered to be a requirement excess according to the Henderson-Hasselbach equation (Equation 4.1).

$$pH = pK_a + log\frac{[B]}{[HB]} \tag{4.1}$$

In the context of DMEM culture media formulated with 3.7g/L sodium bicarbonate buffer and incubated at 5% CO_2 concentration, where [B] denotes the concentration of HCO_3^- and [HB] denotes the concentration of H_2CO_3, we can calculate the theoretical pH of the solution [15, 21]:

1. The concentration of sodium bicarbonate in DMEM is 44mM with a molar mass of 84 g/mol. $[\mathrm{HCO_3^-}] = \dfrac{3.7\ \mathrm{g/L}}{84\ \mathrm{g/mol}} = 0.044\ \mathrm{M} = 44\ \mathrm{mM}$

2. Following Henry's law for dissolved gases we calculate the CO_2 dissolved in solution. Dissolved CO_2 concentration in 5% incubator which is equivalent to pCO_2 0.05 atm. Henry's law constant at 37 °C $K_{CO_2} = 3.0 \times 10^{-2}$ mol/L.
   $C_{CO_2} = K_{CO_2} \cdot P_{CO_2}$
   $C_{CO_2} = 3.0 \times 10^{-2}\ \mathrm{mol/L \cdot atm} \times 0.05\ \mathrm{atm}$
   $C_{CO_2} = 1.5\mathrm{mM}$

3. With the Henderson-Hasselbach equation (Equation 4.1, where pK_a of carbonic acid = 6.1, a theoretical pH of 7.5 is calculated.
   $\mathrm{pH} = 6.1 + \log\left(\dfrac{1.5\ \mathrm{mM}}{44\ \mathrm{mM}}\right)$
   $\mathrm{pH} = 6.1 + 1.57 = 7.5$

Previous studies show that DMEM will equilibrate to approximately pH 7.7 at 5% CO2 concentration, with some variations due to external conditions (e.g. temperature, serum) (Figure 4.1a) [21]. Theoretical fluctuations in the order of 0.1-0.2 pH may occur due to theoretical calculations not taking into consideration the additive effect of serum in complete media determining intrinsic solution buffering [21]. Of note, we can appreciate the importance of buffering capacity in cell culture medium as in subsequent experiments where media was formulated with no buffering agent, cells were unable to survive, likely due to extreme pH values reached.

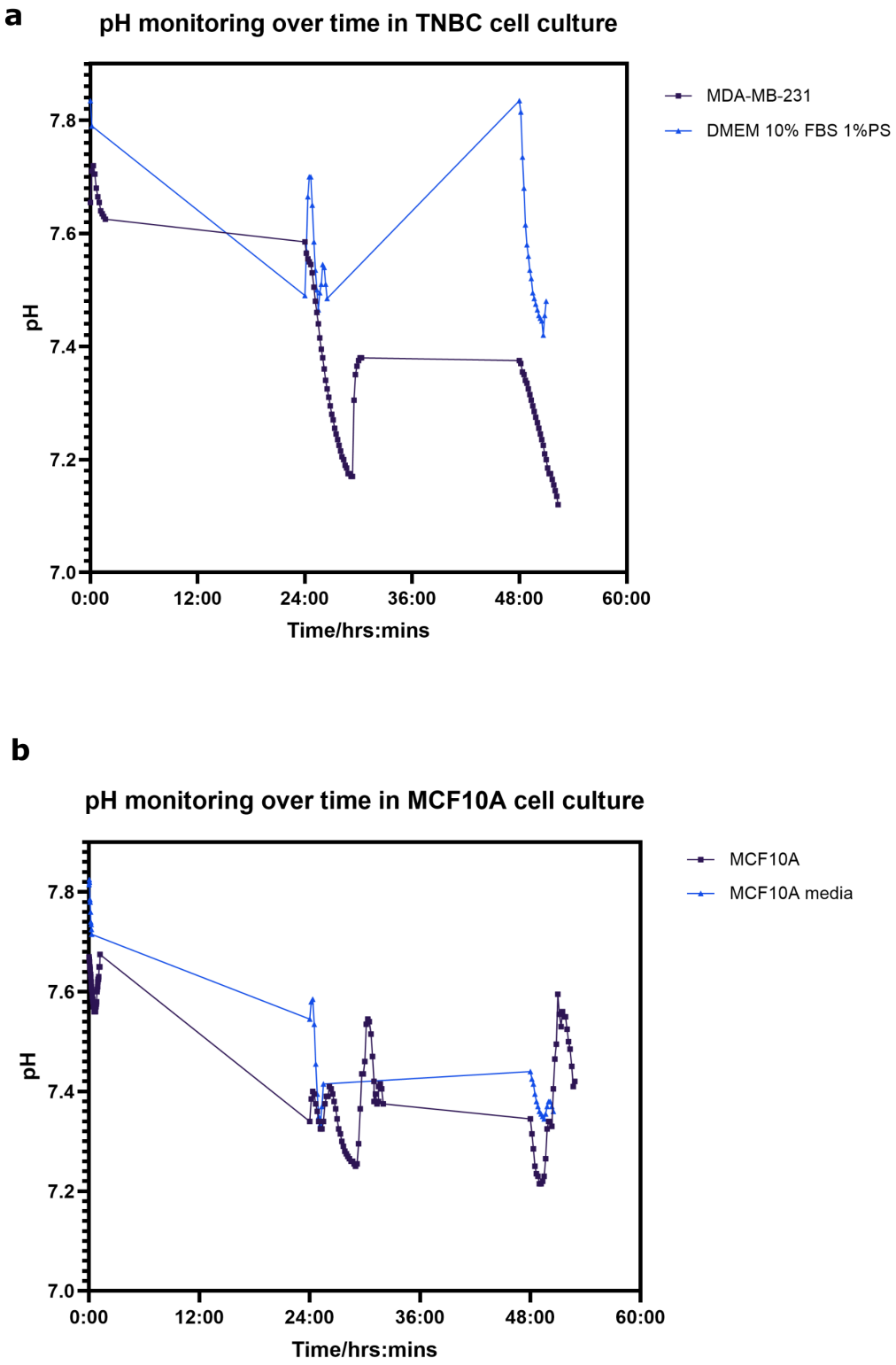


Figure 4.1: **Conditioned media pH changes monitored in a triple negative breast cancer cell line, MDA-MB-231, and an epithelial mammary cell line, MCF10A.(a)** pH measurements of MDA-MB-231 cells in DMEM culture media formulation (DMEM, 10% FBS, 1% PS) and media only under standard cell culture conditions* **(b)** Conditioned media pH measurements in non-malignant MCF10A cell cultures in DMEM/F12 MCF10A media formulation and media only under standard culture conditions*. * = 37 °C, 5% CO_2.

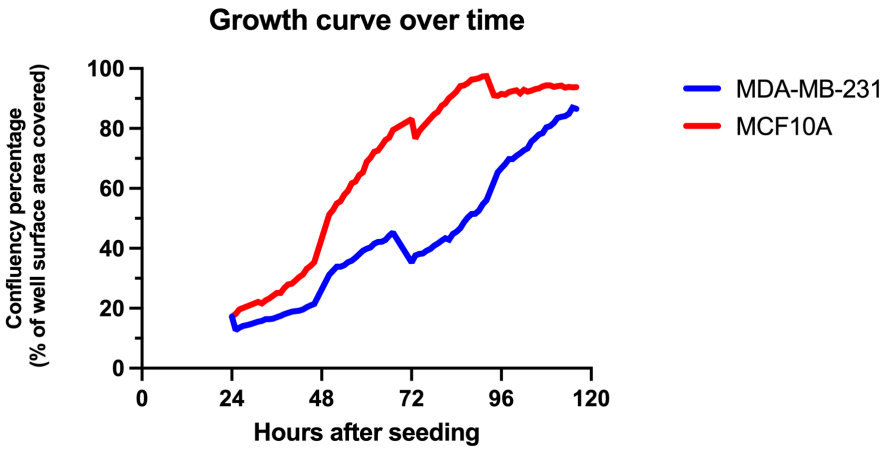


Figure 4.2: **Growth curve of breast cancer and control cell lines.** Breast cancer cell line,MDA-MB-231, and mammary epithelial, MCF10A, cell cultures monitored over 120 hours using timelapse microscopy. An automated segmentation algorithm (Muvicyte imaging system, PerkinElmer) was used to calculate the confluency per well as a percentgae of well surface area covered over time.

On the other hand, monitoring pH changes in cell culture of a non-malignant cell line, MCF10A, shows an overall 0.215 pH change in buffered MCF10A media (Figure 4.1b). Figure 4.1b shows the pH changes that can be expected from MCF10A media with no addition of cells is 0.355 pH, which indicates that the predominant pH change seen in MCF10A cultures is a result of intrinsic factors and CO_2 hydration rather than lactate production from cells. A subsequent peak of pH is evident in both malignant and non-malignant cell cultures at 30 hours (Figure 4.1). This may take place due to a number of reasons, including cell density increasing which may increase the time it takes the media to buffer the excess acidity as the diffusion of CO_2 can be rate-limiting. On the other hand, a proportion of this pH increase may be attributed to a level of circadian rhythm present in mammalian cells which can influence metabolic activity and growth rate.

We confirm cell growth over time in both MDA-MB-231 and MCF10A cell cultures (Figure 4.2). Notably, although MDA-MB-231 and MCF10A cells have similar media formulations, DMEM/F12 is used as the base medium for MCF10A cell cultures which includes DMEM and F-12 media formulations in a 1:1 ratio. A wider range of amino acids and vitamins are required for MCF10A cell culture, and a lower concentration of sodium bicarbonate (2.438 g/L, 29mM) is used. This will result in a lower buffering capacity in the medium used for MCF10A versus MDA-MB-231 cells (3.7g/L, 44mM sodium bicarbonate). Despite lower buffering capabilities of MCF10A media, the pH changes recorded in media only are in the same range, although fluctuations in MCF10A media for the duration of the experiment are greater. As a result, despite the higher buffering capacity of MDA-MB-231 media, the pH changes arising from MDA-MB-231 cell cultures are greater than in MCF10A cell cultures with a lower buffering capacity.

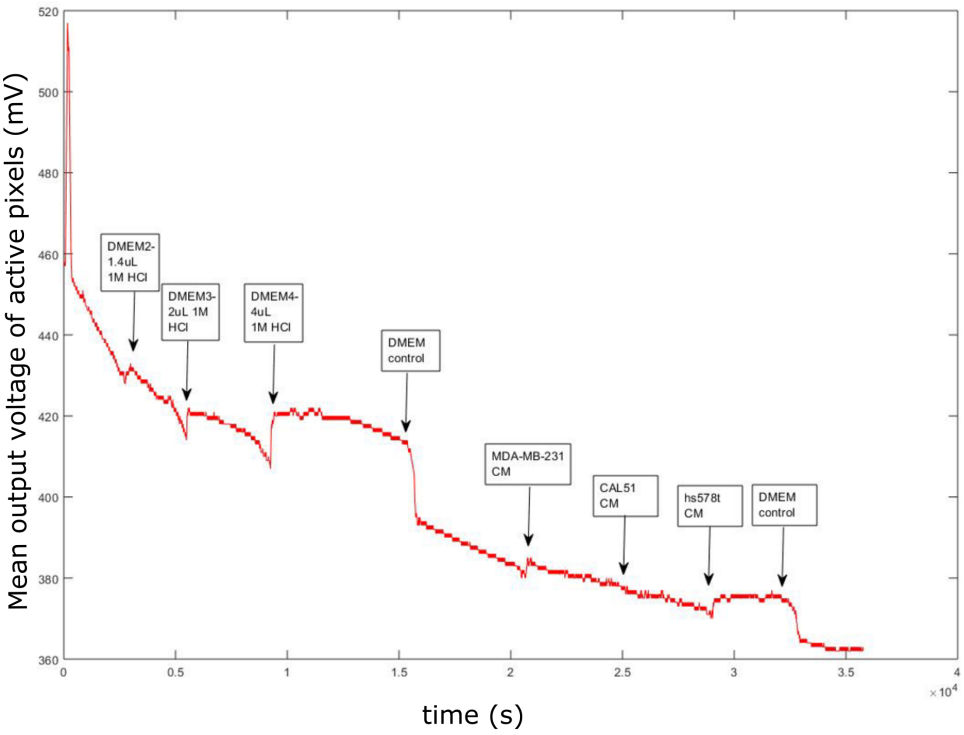


Figure 4.3: **Voltage trace of α-Titanicks ISFET array treated with acidified cell culture media and conditioned media from breast cancer cell lines.**

4.5 pH detection on the Titanicks ISFET array

This section will focus on determining the effects of complex culture media formulations on sensor sensitivity. More specifically, a study by Moser et al, (2020), investigated the use of multi-ion membranes on ISFET arrays which reported the compartmentalization of the chip surface to simultaneously detect several ion species (K^+, Ca^{2+}, Na^+, H^+) [22]. One of the reported outcomes shows that there may be some artefact resultant from Na^+ on the ISFET array with sensitivity increasing. This raises the hypothesis that the sensitivity of the sensor to complete cell culture medium (i.e. supplemented with 10% FBS and 1%P/S) alone must be considered before the addition of cells as the variations in ion content may unknowingly affect the sensor. To identify whether we can detect pH changes in cell culture media without inadvertently inhibiting pH sensitivity in the ISFET sensors, titration of complete DMEM culture medium (10% FBS, 1% PS) was performed on α-Titanicks arrays.

Figure 4.3 reports the mean output voltage of active pixels in an α-Titanicks chip previously hydrated with complete 20μl DMEM media (denoted as "DMEM control"). The first three peaks in the voltage trace indicate where 20μl DMEM has been titrated with increasingly acidified complete DMEM media where acidification of media is detected, however with considerable drift making it difficult to discern changes. The output change between the most

acidified DMEM condition (DMEM4 - titrated with 4ul 1M HCl), shows an output change of approximately 30mV. Subsequently, conditioned media was used from triple negative breast cancer cell lines with different growth patterns: MDA-MB-231, Cal51 and hs578t. All lines were maintained in complete DMEM cell culture media throughout their incubation. Distinct changes are recorded in output voltage which indicates an acidic pH change between MDA-MB-231 and DMEM control media, between Cal51 and hs578t conditioned media as well as between hs578t conditioned media and DMEM control (Figure 4.3). A different pH change is recorded for MDA-MB-231 and hs578t indicating a more acidic culture media in hs578t cell cultures. Notably, no evident difference is recorded between MDA-MB-231 and Cal51 conditioned media. Whilst all conditioned media was collected at the same time and from cell cultures incubated for 48 hours, discrepancies in pH may also arise due to cell confluency dependant on cell proliferation rates in culture for different cell lins. In addition, changes to conditioned media may occur upon exposure to different CO_2 pressures which are inevitable upon removal from cell culture incubators [15]. The presence of a significant gradual and stochastic change in output signal over time, even under constant pH conditions, known as drift, is a common issue in ISFET sensors. Drift makes it particularly challenging to distinguish the effects of changing pH on the output signal. Additionally, temperature fluctuations, charge trapping and ageing of the sensor can contribute to gradual drift. To mitigate the effects of drift a set of techniques is available including regular calibration, temperature compensation and improved passivation materials.

The Titanicks ISFET array was recently adapted to include additional passivation layers which have considerably improved ISFET non-idealities such as drift. The γ-Titanicks with a 20nm passivation layer of hafnium oxide was primarily used henceforth in these studies as preliminary experiments reported a comparatively lower drift rate. Characterisation of the γ-Titanicks with pH buffers surrounding physiological ranges was performed (Figure 4.4). The data shows minimal drift in Figure 4.4a as the voltage change from a threshold voltage is the same at a baseline pH 7 throughout the experiment. The differential of the output voltage is used to identify the points of buffer changes and calculate both the $\Delta V_{in}/\Delta pH$ (pH sensitivity) for the range pH 6 to pH 8, as well as ΔV_{out} for the same range (Figures 4.4b-d). Overall the $\Delta V_{in}/\Delta pH$ is in the scale of 45.53 mV/pH for pH 6 to 7 and 46.1 mV/pH for pH 7 to 8, showing an improved near-Nernstian sensitivity (Nernstian sensitivity $\approx$ 59-60mV/pH at ambient temperature) as compared to the earlier α-Titanicks design.

Furthermore, in order to determine the output voltage we can detect with the addition of complete DMEM media on γ-Titanicks, titration was performed to obtain DMEM media at variable pH values. Figure 4.5 reports the voltage trace of DMEM media at pH 8.02, 6.57 and 8.99. Minimal drift is observed in the chemical output signal indicating that the voltage changes reported are, to a large extent, solely due to pH change in the media. Prominent spikes in output voltage can be attributed to the exchange of volume within the well causing

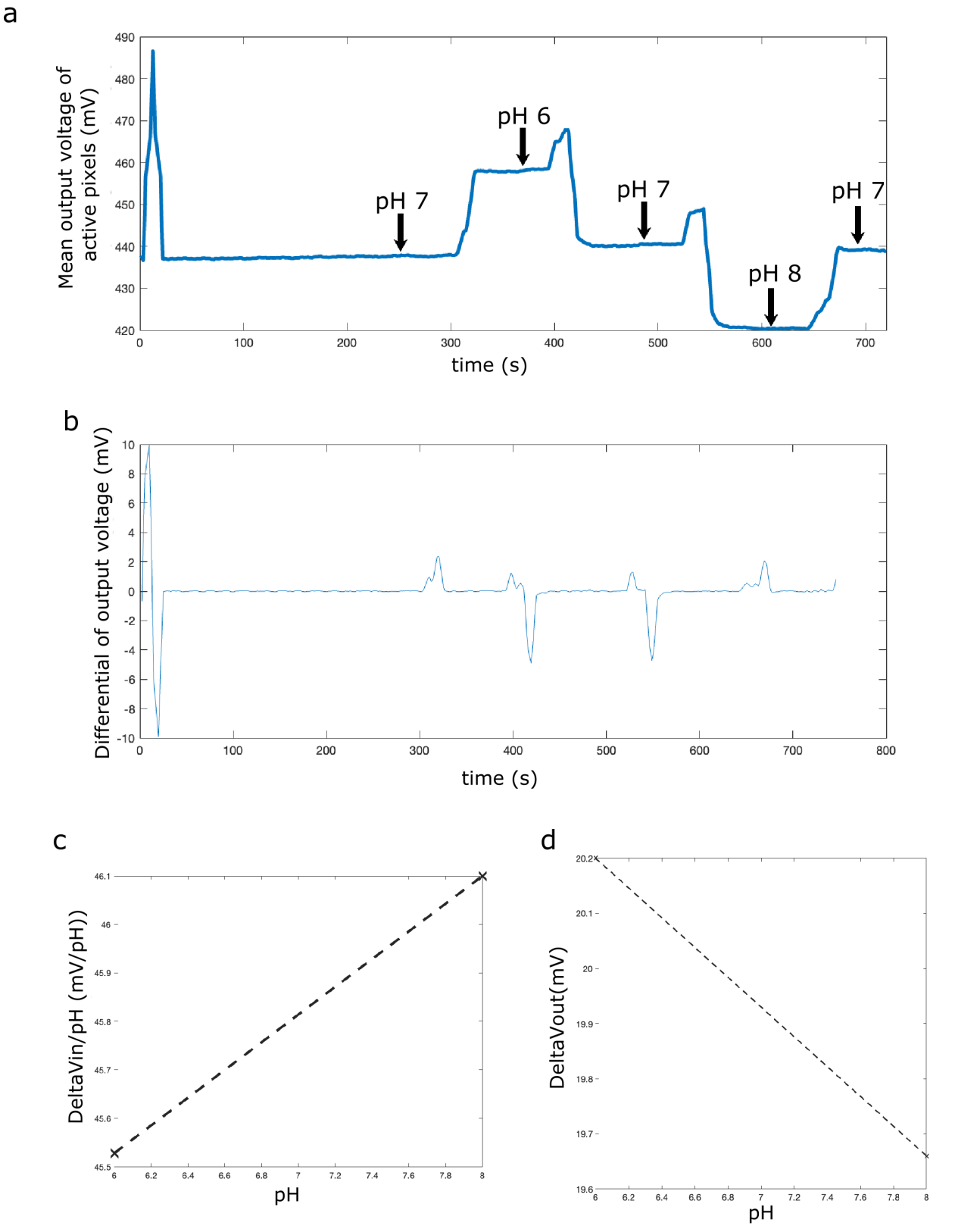


Figure 4.4: **γ-Titanicks pH sensitivity detection with pH buffers 6, 7 and 8. (a)** Mean output voltage of active pixels (mV) over the experiment timecourse where the pH of the solution is indicated. Peaks indicate where solution has been exchanged. **(b)** Differential of output voltage over the experiment timecourse identifies significant changes in output voltage where pH change has occurred. **(c)** $\Delta V_{in}/\Delta pH$ plotted against the pH range 6 to 8 indicating the pH sensitivity recorded for this experiment over the specific pH range. **(d)** ΔV_{out}, change in mV of output voltage per pH in the pH range 6 to 8.

sharp spikes as manual disturbance to the ISFET surface occurs. As a result, these peaks can be disregarded when looking at voltage change. In addition, DMEM pH 6.57 results in a higher mean output voltage in active pixels, than we might expect. This is likely to the excess of chloride ions which is added upon titration with HCl. Variations in chloride ions may limit biasing in the setup of our microfluidic components as an Ag/AgCl reference electrode is used to provide an input voltage. Thus, fluctuations in chloride ions may be important considerations in future implementations where DMEM culture medium is used as it may result in artefacts, however physiological variations of single cells are unlikely to have such extreme impacts. Studies of commercially available and commonly used cell culture media have shown that DMEM and RPMI are both formulated to extreme supplies of amino acids, glucose and other components [3, 23]. Despite the availability of these studies, these media formulations remain the most ubiquitously used throughout the international scientific community making it challenging to stray from these norms and have the ability to obtain comparable cell cultures. Finally, the development of human plasma-like media (HPLM) and Plasmax, has reported viability, proliferation and physiological relevance [3, 18, 23]. Once these growth media become cost effective and widely used, *in vitro* cell culture is likely to better recapitulate the human physiology in future studies. In this chapter, sensor sensitivity is confirmed with cell culture media and no significant inhibition is seen due to other ion species. We conclude that Cl^- ion addition may increase sensor sensitivity due to the Ag/AgCl electrode utilised and comprimise device biasing.

4.6 Summary and Future direction

This chapter, characterised pHe acidificiation in conditioned media from both tumorigenic and non-tumorigenic cell lines of the same tissue origin and evaluated the chemical output response of Titanicks chips variants *alpha* and *gamma*. The following outcomes reported:

1. We evaluate long-term pHe acidification of triple negative breast cancer cell line, MDA-MB-231, and mammary epithelial cell line, MCF10A in commercial, complete DMEM media. We corroborate evidence of tumorigenic cell lines have a greater degree of pHe acidification.

2. Commercial cell culture media on chip and the sodium bicarbonate buffering system is characterised. The lack of a buffering agent leads to extreme pH in culture which is not viable for cells.

3. pH sensitivity of ISFET α-Titanicks and γ-Titanicks treated with a pH range of complete cell culture media, featuring a silicon nitride (Si_3N_4) and hafnium oxide (HfO_2) passivation layer, respectively.

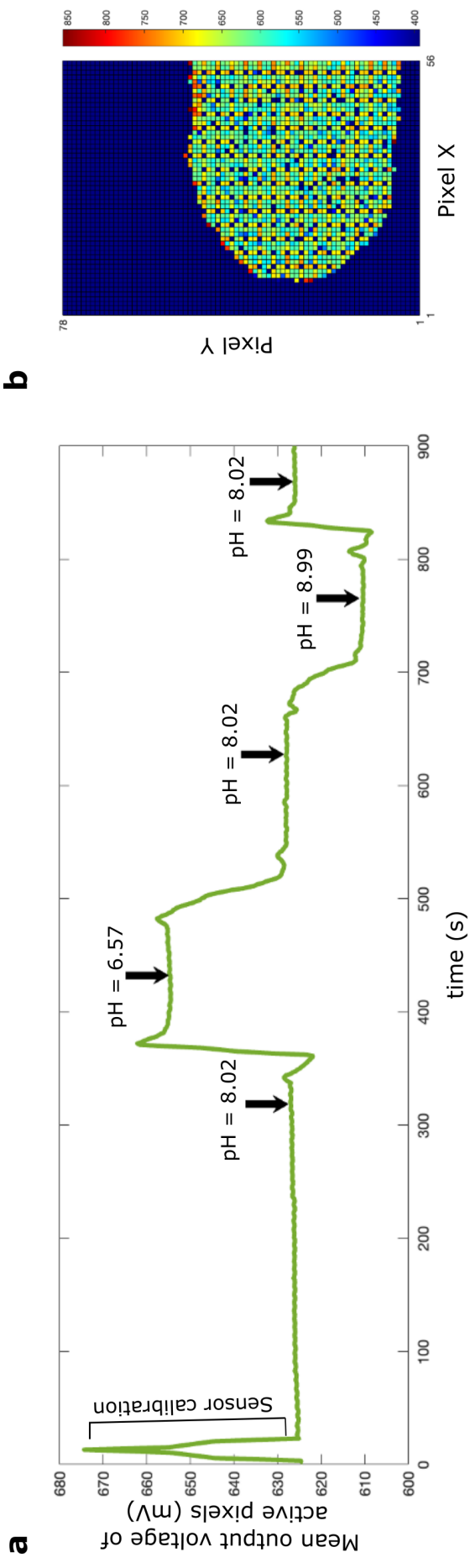


Figure 4.5: **Detection of complete DMEM media on γ-Titanicks.(a)** Mean output voltage of active pixels over the experiment timecourse where each peak corresponds to a solution change. The pH of the DMEM media is shown in arrows at the point of drift stabilisation. **(b)** Pixels considered active and within range are illustrated in 2D.

4. We report an average 45.5-46.1 mV/pH ΔV_{in}/pH for the γ-Titanicks array with pH buffer range pH 6-8.

5. Chloride ion and sodium ion variations in titrated, DMEM culture media may result in artefacts on the sensor.

Future research should address some of the limitations identified in this experimental setup. Namely, the limitations by an Ag/AgCl wire electrode which may present instability and additional sensitivity due to fluctuating Cl^- ion concentrations in solution leading to artefacts. Furthermore, the experimental setup could benefit from an integrated optical visualisation of pH to avoid any CO_2 dynamics changing in a sodium bicarbonate buffering system and have consistently pre-equilibrated cell culture media. This was evaluated in preliminary studies by transfection of the pHLuc plasmid in breast cancer cells, however the instability of the FRET reaction made it challenging to integrate on long-term pHe monitoring experiments [24]. The adaptation of cell culture protocols to include cell culture media with physiologically relevant concentrations of amino acids, glucose and buffering agent concentrations normally found in human plasma will make assays on chip more physiologically relevant with the aid of appropriate microfluidic platforms. This will re-capitulate TME pHe to a greater extent than current, universally utilised culture protocols.

References

[1] B. A. Webb et al. "Dysregulated pH: A perfect storm for cancer progression". In: *Nature Reviews Cancer* 11.9 (Sept. 2011), pp. 671–677.

[2] D. Neri and C. T. Supuran. "Interfering with pH regulation in tumours as a therapeutic strategy". In: *Nature Reviews Drug Discovery* 10.10 (Oct. 2011), pp. 767–777.

[3] T. Ackermann and S. Tardito. "Cell Culture Medium Formulation and Its Implications in Cancer Metabolism". In: *Trends in Cancer* 5.6 (June 2019), pp. 329–332.

[4] L. E. Gerweck and K. Seetharaman. "Cellular pH gradient in tumor versus normal tissue: Potential exploitation for the treatment of cancer". In: *Cancer Research* 56.6 (1996), pp. 1194–1198.

[5] N. Rohani et al. "Acidification of tumor at stromal boundaries drives transcriptome alterations associated with aggressive phenotypes". In: *Cancer Research* 79.8 (Apr. 2019), pp. 1952–1966.

[6] A. Anemone et al. "Imaging tumor acidosis: a survey of the available techniques for mapping in vivo tumor pH". In: *Cancer and Metastasis Reviews* 38.1-2 (June 2019), pp. 25–49.

[7] T. Koltai, R. A. Cardone, and S. J. Reshkin. "Synergy between low dose metronomic chemotherapy and the pH-centered approach against cancer". In: *International Journal of Molecular Sciences* 20.21 (Nov. 2019).

[8] D. Hanahan and R. A. Weinberg. "Hallmarks of cancer: The next generation". In: *Cell* 144.5 (Mar. 2011), pp. 646–674.

[9] S. Y. Lunt and M. G. Vander Heiden. "Aerobic glycolysis: Meeting the metabolic requirements of cell proliferation". In: *Annual Review of Cell and Developmental Biology* 27 (Oct. 2011), pp. 441–464.

[10] S. K. Parks, W. Mueller-Klieser, and J. Pouysségur. "Lactate and Acidity in the Cancer Microenvironment". In: *Annual Review of Cancer Biology* 4 (2020), pp. 141–158.

[11] H. Eagle. "The effect of environmental pH on the growth of normal and malignant cells". In: *Journal of Cellular Physiology* 82.1 (Aug. 1973), pp. 1–8.

[12] V. Estrella et al. “Acidity generated by the tumor microenvironment drives local invasion”. In: *Cancer Research* 73.5 (Mar. 2013), pp. 1524–1535.

[13] E. Boedtkjer and S. F. Pedersen. “The Acidic Tumor Microenvironment as a Driver of Cancer”. In: *Annual Review of Physiology* 82 (2020), pp. 103–126.

[14] J. W. Wojtkowiak et al. “Drug resistance and cellular adaptation to tumor acidic pH microenvironment”. In: *Molecular Pharmaceutics* 8.6 (Dec. 2011), pp. 2032–2038.

[15] J. Michl, K. C. Park, and P. Swietach. “Evidence-based guidelines for controlling pH in mammalian live-cell culture systems”. In: *Communications Biology* 2.1 (Apr. 2019), pp. 1–12.

[16] R Maniarasu and Mohan Kumar R. “A Mini-Review on CO2 Role in Cell Culture and Medicinal Applications”. In: *Journal of Cell Science & Therapy* 13.3 (Apr. 2022), pp. 1–4.

[17] ATCC. *ATCC: The Global Bioresource Center. Bacterial Products*. 2020.

[18] M. Fischer. “Physiological media advance cell culture experiments”. In: *Trends in Biochemical Sciences* 48.2 (Feb. 2023), pp. 103–105.

[19] M. Chen et al. “Extracellular pH is a biomarker enabling detection of breast cancer and liver cancer using CEST MRI”. In: *Oncotarget* 8.28 (July 2017), pp. 45759–45767.

[20] G. M. Nava and L. A. Madrigal Perez. “Metabolic profile of the Warburg effect as a tool for molecular prognosis and diagnosis of cancer”. In: *Expert Review of Molecular Diagnostics* 22.4 (2022), pp. 439–447.

[21] UK Health Security Agency. *CO2 concentration and pH control in the cell culture laboratory — Culture Collections*. Apr. 2020.

[22] N. Moser et al. “Complementary Metal-Oxide-Semiconductor Potentiometric Field-Effect Transistor Array Platform Using Sensor Learning for Multi-ion Imaging”. In: *Analytical Chemistry* 92.7 (Apr. 2020), pp. 5276–5285.

[23] T. J. McKee and S. V. Komarova. “Is it time to reinvent basic cell culture medium?” In: *American Journal of Physiology - Cell Physiology* 312.5 (May 2017), pp. C624–C626.

[24] T. T. Ong et al. “pHLuc, a Ratiometric Luminescent Reporter for in vivo Monitoring of Tumor Acidosis”. In: *Frontiers in Bioengineering and Biotechnology* 8 (May 2020), p. 412.

Chapter 5

Biocompatibility of ISFET arrays in unmodified CMOS technology

This chapter investigates the biocompatibility of an ISFET array surface manufactured in unmodified CMOS technology with regards to typical passivation post-processing. Cytocompatibility of the LoC device used in this study is investigated through quantitative and qualitative characterisation of both tumorigenic and non-tumorigenic cell culture on the interface of ISFET arrays and evaluated against standardised, cell culture-grade plastics. Chemical modifications of the CMOS ISFET arrays is carried out in the form of extracellular matrix treatment to increase the comparability of the passivation material of ISFET arrays and plastics is evaluated.

The first section presents an overview of protocols and regulations surrounding the assessment of biocompatibility of biomedical devices, current evaluation of cell viability on the ISFET interface and the significance of cell features evaluated in this study. The following section describes the methodology and results for the evaluation of cell response to ISFET arrays manufactured in unmodified CMOS technology. Lastly, discussion of experimental results and significance of the study for the future implementations of this LoC device are presented.

Work included in this chapter has previously been published in:

Beykou, M., Bousgouni, V., Moser, N., Georgiou, P., & Bakal, C. "Biocompatibility characterisation of CMOS-based Lab-on-Chip electrochemical sensors for in vitro cancer cell culture applications". In: *Biosensors and Bioelectronics* 262,(Nov. 2024).

5.1 Introduction

Biocompatibility, when referring to biomedical devices has been defined as the following: "Biocompatibility refers to the ability of a biomaterial to perform its desired function with respect to a medical therapy, without eliciting any undesirable local or systemic effects in the recipient or beneficiary of that therapy, but generating the most appropriate beneficial cellular or tissue response in that specific situation, and optimising the clinically relevant performance of that therapy" [1, 2]. Nevertheless, biomaterial biocompatibility has undergone several iterations of re-definition to encompass the ever-growing field of biomedical devices including implantable devices, nanotechnologies and in our case, potentiometric sensors. The importance of cytocompatibility, i.e. cellular biocompatibility, to the development of biomedical devices can be highlighted by the establishment of standardised regulations and protocols for in vitro cytotoxicity testing under the International Organization for Standardization (ISO) [3, 4]. More specifically, ISO 10933-5 protocol sets out three parameters for testing biomedical devices which may come into contact with human cellular material: extract, indirect and direct contact testing [3, 4]. For the purposes of our study we focused on direct contact testing of our LoC potentiometric sensor as its most relevant application to test surface cytotoxicity. Crucially, the choice of material in biomedical device development can drive both biochemical and mechanical cues that lead to response and cellular reprogramming [5]. Whilst our device currently pertains to working with cell culture lines, the aims of this work lie in the development of a lab-on-chip device for cell detection. As a result, considerations of material biocompatibility, cell morphology, proliferation and viability remain similar to other PoC devices.

5.2 The cell-ISFET interface

The first ISFET design featured a silicon oxide (SiO_2) passivation layer whose sensitivity to hydrogen ions rendered the ISFET a pH sensor [6–8]. The reaction of silanol groups (Si-OH) at the gate interface determines the availability of H^+ ions in solution and hence the resulting pH [9]. Subsequently, implementation of ISFETs on standard CMOS technology and Moore's law, has made it an inexpensive and scalable sensor for commercial production [6, 8, 10–12].The standard top material for CMOS passivation is silicon nitride (Si_3N_4). With unmodified CMOS integration, the Si_3N_4 passivation layer is retained making production rapid and low-cost by alleviating the need for extensive post-processing.

The first measurements on ISFETs, demonstrated by Bergveld, were based on ionic fluctuations and electrophysiological recordings of neurons [6, 7, 13]. A number of studies have developed ISFET sensors for cell-based assays, however, there is little focus on whether the interaction with a silicon-based interface has an effect on cell phenotype. Lehmann et al (2000), first reported a

modified CMOS ISFET array with an Al_2O_3 passivation layer, where extracellular acidity was recorded in adenocarcinoma cells with a near-Nernstian sensitivity of 56mV/pH [14]. Milgrew et al (2008), also reported a 16 x 16 ISFET array with a Si_3N_4 interface for detection of pH in fibroblast cultures [15]. Finally, another high κ-dielectric gate material, Ta_2O_5, has also been investigated with success in increasing sensor sensitivity [16–18]. The variable materials which can be found at the interface of ISFET sensors have all been successfully implemented and demonstrate sensor sensitivity. However, the biophysical interactions at the Si_3N_4 interface remain unappreciated. Notably, Bogner et al (2006) investigated the proliferation and differentiation of Caco-2, adenocarcinoma cells, and determined that proliferation and adhesion rates were comparable between glass and p-type Si wafers with a Si_3N_4 coating [19].

Bio-material design has been shown to play a central role in cell behaviour [20, 21]. Varying degrees of stiffness, roughness, patterning and elasticity contribute to cell adhesion and shape [22, 23]. In this investigation we utilise markers for proliferation (Ki67), morphology (α-tubulin, paxillin and f-actin) and mechanical response (YAP/TAZ) to evaluate surface biocompatibility. Key regulators of mechanotransduction in mammalian cells are the transcriptional co-activators YAP/TAZ. YAP/TAZ translate biophysical changes in the microenvironment to transcriptional changes, allowing cells to be mechanically responsive to their surroundings. The activation of YAP/TAZ is most notably affected by mechanical microenvironmental changes, such as substrate stiffness, and the resulting formation of focal adhesions and cell shape [24–26]. When activated, YAP/TAZ translocates from the cytoplasm to the nucleus where it can impact intracellular pathways to activate downstream signaling pathways, such as the Hippo pathway and Wnt signaling cascade [26–28]. In particular, the relevance of its activity can be appreciated through its wider effects on cell proliferation, growth and metabolism [26–28].

5.3 Materials & Methods

5.3.1 ISFET array configurations

The ISFET arrays used in these experiments were previously reported in Moser et al (2018) [29]. The ISFET arrays, also referred to as chips, are comprised of 4,368 pixels each. They are manufactured in standard 0.35μm technology hence retaining the native silicon nitride, Si_3N_4, top passivation layer as the interface of the sensor with the electrolyte. ISFET arrays are planarised and cut by an external party to ensure surface roughness is minimal and uniform. Untreated, control chips are attached onto the well of a 96-well plate (PhenoPlate, PerkinElmer) using a small amount of lubricant and subsequently rinsed with PBS prior to use in cell culture.

5.3.2 Extracellular matrix deposition

Collagen treatment

Collagen Type I Rat Tail (3.4mg/ml, CORNING, Lot 0295002) was prepared to 50μg/ml using 0.02M acetic acid (Fisher Scientific) for use as a surface treatment on chips. Chips were attached to the bottom of a 96-well plate, as for untreated chips, and incubated with 100μl/well 50μg/ml collagen solution, at 37 °C for 30mins within a 5% CO_2 incubator. Subsequently, chips were washed twice with PBS and allowed to dry prior to cell culturing.

Fibronectin treatment

Fibronectin derived from human plasma (Sigma-Aldrich, Ref F0895) was diluted from a 0.1% solution to 1μg/ml with PBS. Subsequently, chips in a 96 well-plate were incubated with 100μl/well 1μg/ml fibronectin solution at 37 °C for 30mins within a 5% CO_2 incubator. Subsequently, chips were washed twice with PBS and allowed to dry prior to cell culturing.

Poly-L-ornithine and Laminin (PLOL) treatment

The protocol followed for PLOL-treatment of chips was previously reported by Hirata et al (2000). Chips in a 96-well plate were incubated with 250μl Poly-l-ornithine 0.01% solution (100μg/ml) (Sigma-Aldrich, Ref P4957) for 24 hours with UV irradiation in a sterile environment for 2 hours. Chips were washed twice with sterile, deionised water. Laminin solution from Engelbreth-Holm-Swarm murine sarcoma basement membrane (Merck/Sigma-Aldrich, stock 1mg/ml, Ref L2020) was diluted to a final concentration 8 μg/ml and chips were incubated with 250μl/well for 24hrs in a 37 °C, 5% CO_2 incubator. Chips were washed twice at the end of treatment.

5.3.3 Focused Ion-Beam Scanning Electron Microscopy (FIB-SEM)

Samples prepared for SEM imaging and ion beam milling, are fixed using 2.5% glutaraldehyde solution in PBS for 2 hours at room temperature. Samples were then dehydrated through a graded series of ethanols 30%, 50%, 70%, 100% for 15 mins in each. Samples are then treated with a 50:50 mixture of 100% ethanol and Hexamethyldisilazane (HMDS) for 30 minutes, followed by 15 minutes in 100% HMDS. After 15 minutes most of the HMDS is removed and the remainder left to evaporate to dryness overnight in a fume hood. Samples are then sputter-coated with 10nm gold coating and SEM imaged on Tescan FIB-SEM Lyra3 XMU.

5.3.4 Maintenance & Passaging on plastic and ISFET arrays

Triple Negative Breast Cancer (TNBC) cell line, MDA-MB-231 was maintained in the following growth medium composition: Dulbecco's Modified Eagle Medium (DMEM 1X) (4.5g/L D-Glucose, L-Glutamine and Pyruvate (Gibco), 10% heat-inactivated Fetal Bovine Serum (FBS) (Gibco) and 1% Penicillin/Streptomycin (Invitrogen). Mammary epithelial cell line, MCF10A, was maintained in the growth medium recipe in Table 5.1. All cell lines on both standard cell culture plates (Perkin Elmer) and ISFET array chips were maintained in 37 °C, 5% CO_2 incubators. Cells were maintained in T25 flasks and passaged when at 80% confluency. Existing cell medium was aspirated, each flask was washed with 5ml PBS and aspirated once more. For each flask, 1ml Trypsin-EDTA 0.25% (Gibco) was added and returned to the incubator until cells appeared detached. Once cells were detached, the volume was added to a falcon tube and centrifuged at 1000rpm for 5mins. The supernatant was aspirated and each pellet resuspended in an appropriate volume of the relevant growth medium. Cells were counted using a Cell Countess (Invitrogen) where 10μl trypan blue and 10μl of cell suspension were mixed and added to a cell counter slide. A solution of 4x10^3 cells/ml was made for all cell lines. For conditions denoted "plastic control", 250 μl of the cell solution was added per well in a 96 well Phenoplate (Perkin Elmer). For all conditions on chip, 250 μl of the cell solution was added to each well of a 96 well Phenoplate with the relevant chip affixed to the bottom surface. All conditions were cultured for 48hrs in a 37 °C, 5% CO_2 incubator.

Table 5.1: MCF10A complete cell culture media

Reagent	**Manufacturer**	**Volume**
DMEM F/12	Invitrogen	500ml
Horse Serum	Invitrogen	25ml (5%)
Epidermal Growth Factor	Peprotech	100μl (20ng/ml final)
Hydrocotisone	Sigma	250μl (0.5mg/ml final)
Cholera Toxin	Sigma	50μl (100ng/ml final)
Insulin	Sigma	500μl (10μg/ml final)
Penicillin/Streptomycin	Invitrogen	5ml (1%)

5.3.5 Focal adhesions

Glass-bottom mattek dishes were coated with fibronectin derived from human plasma (Sigma-Aldrich) at a concentration of 10μg/ml with incubation steps as described previously. ISFET chips were coated with 1μg/ml as for all other chip experiments. Once treatment was completed, each mattek dish or ISFET chip was incubated with 20,000 cells/well overnight. Cells used in this experiment were U2OS CDK1AS-mCherry [30] (a kind gift from Dr. Helfrid Hochegger, University of Sussex), an osteosarcoma cell line which were maintained in DMEM (Gibco) supplemented with 10% FBS (Gibco) AND 1% Penicillin/Streptomycin. Cells were maintained, passaged and counted as described in sub-section 5.3.3. Subsequently, experiments were fixed

with 4% PFA, permeabilised and blocked as described in sub-section 5.3.5, with the use of anti-Paxillin (BD Biosciences, Cat 610052) as the primary antibody (Table 5.2). Focal adhesions were imaged using the TIRF (Total Internal Reflection Fluorescence) microscope. Images were processed and quantitative values extracted using the Focal Adhesion Analysis Server found at https://faas.bme.unc.edu/ [31].

5.3.6 Immunofluorescence staining and confocal microscopy

After 48 hrs, all conditions were fixed by removing the cell medium and adding a final concentration of 4% PFA for 15mins at room temperature. Wells were washed twice with PBS. Cells were permeabilised and blocked with 0.2% Triton-X for 12mins at room temperature, washed twice with PBS, followed by 2% Bovine Serum Albumin (BSA) for 1hr at room temperature. BSA solution was aspirated and primary antibodies indicated in Table 5.2 were added at the relevant dilutions in an antibody mix solution (0.5% BSA, 0.01% Triton-X and PBS), 100μl/well were added and incubated overnight at 4 °C. The solution was then aspirated and wells washed twice with PBS before adding the relevant secondary antibodies in an antibody mix solution (100μl/well) for 2hrs at room temperature (Table 5.2). Subsequently, wells were washed thrice with PBS. Sequential staining was performed where mouse and rat antibodies were utilized in the same wells. Hoescht dye and 647 Phalloidin-Atto 1:5,000 (where an α-Tubulin primary antibody was not used previously) was added in antibody mix solution for 10mins at room temperature. For focal adhesion work 488 Alexa Fluor Phalloidin 1:1,000 was used. Wells were washed once and left in PBS with NaN_3. In order to image the chips, each chip was flipped to face downwards in fresh wells before imaging on the Opera Phenix high-throughput confocal microscope (Perkin Elmer).

Table 5.2: Primary and secondary antibodies for immunofluorescence staining

Primary Antibody	Manufacturer	Dilution	Secondary antibody	Manufacturer	Dilution
Rabbit Ki67	abcam	1:250	Goat anti-rabbit IgG (H+L) Alexa Fluor 488	Invitrogen	1:1000
Mouse YAP (63.7)	Santa Cruz technology	1:1000	Goat anti-mouse IgG (H+L) Alexa Fluor 568	Invitrogen	1:1000
Rat α-Tubulin	BioRad	1:1000	Goat anti-rat IgG (H+L) Alexa Fluor 647	Invitrogen	1:1000
Mouse Paxillin	BD Biosciences	1:1000	Goat anti-mouse IgG (H+L) Alexa Fluor 647	Invitrogen	1:1000

5.3.7 Image processing and segmentation

All image segmentation and feature extraction was performed using the Columbus software version 2.9.1 (Perkin Elmer). Confocal images obtained were taken in Z stacks and were maximally projected before segmentation. Hoescht staining of the nucleus was used to obtain nuclear roundness, with to length ratio, area and dye intensity. The same measurements were made for cytoplasmic and overall cell shape using Phalloidin dye or α-Tubulin for the cytoskeleton. Subsequently, intensity for proliferation marker, Ki67, was obtained for the nucleus area and normalized to the intensity of the Hoescht dye in the nucleus (Ki67/Hoescht ratio). YAP/TAZ intensity was measured in both the nucleus and a nuclear ring region surrounding the nucleus

to create a ratio. A linear classifier was used to extract three shape populations (elongated, round and star shape) using all previously segmented features including roundness, area and SER texture as training data.

5.3.8 Statistical analysis

Cell shape measurements of MDA-MB-231 cells were obtained from two independent experiment sets of 96 well plates and hence all values were normalized to the relevant feature's plate average before further processing. The same was applied to experiments with MCF10A. Single cell values were used for all experiments. An equivalent number of single cells were sampled at random for all conditions. Data wrangling, plots and statistics of cell shape features, Ki67 and YAP/TAZ expression were performed using Python version 3.8.5 and packages scipy, matplotlib and seaborn. Number of cells attached per well or per chip, texture features and linear classifier data were plotted using GraphPad Prism version 9.5.0.

5.4 Results & Discussion

The lab-on-chip diagnostic device used in this study has been previously described in Moser et al (2018) [29]. The microchip cartridge harbouring a 4,368 ISFET pixel array is attached using a 3D printed clip mechanism onto a Printed Circuit Board (PCB) to integrate user functionality and digitization of output results (Figure 5.3a). The PCB itself enables Bluetooth connection to an Android device with an application which allows inspection and storage of real-time ISFET output. The array holds a volume of 20 μl in a clear, acrylic manifold and is connected to an Ag/AgCl reference electrode. The ISFET array used in this study, which is manufactured in unmodified CMOS technology with regards to typical CMOS post-processing and retains a Si_3N_4 passivation layer, limiting both production costs and signal decoupling from the sensor [29].

Control ISFET arrays seeded with breast cancer cell lines, MDA-MB-231, were initially evaluated using SEM coupled with focused ion-beam milling. Figure 5.1 reports an in-depth magnification of the surface attachment of a cell on the ISFET surface. The placement captured and stochastic migration of cells suggests that the resolution we can expect may be difficult to predict as cells can span 4 pixels at their intersection. This value may also vary with cell size. Furthermore, Figure 5.2(a) represents this variability in size found in a single population of MDA-MB-231 cells. Three morphologies are identified on chip (spindle, small round and large flat cells) indicating that there is likely no significant selection for any one sub-population on the surface. Mitosis is observed on chip as cells are depicted in cytokinesis (Figure 5.2(b)). To confirm that adhesion was not observed only on cell edges, a gallium ion beam was used to

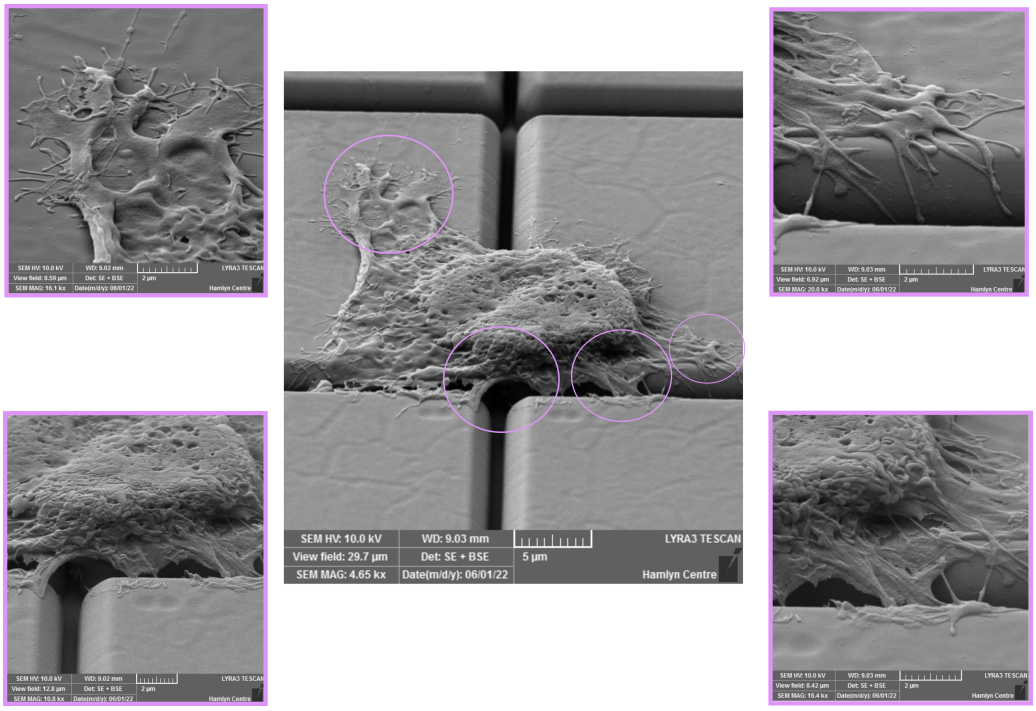


Figure 5.1: **An in depth magnification into the attachment of a single breast cancer cell at the intersection of ISFET pixels.** The central SEM image of an MDA-MB-231 cell depicts the entirety of the cell at the intersection of 4 ISFET pixels. Further magnified SEM images, show the attachment of the cells filopodia on the ISFET surface. *Acknowledgments: This experiment was performed in collaboration with Dr. Lewis Keeble.*

obtain a view of the basement membrane interaction with the ISFET surface. Figure 5.2(c) shows the close interaction observed with adhesion at the basement membrane.

5.4.1 ISFET arrays versus tissue culture plastic for cell culture

Cell adhesion and morphogenesis on ISFET arrays

The experimental workflow used in this study is outlined in Figure 5.3a. Cells are cultured on plastic or ISFET chips for 48 hours and subsequently immunofluorescently stained with markers for proliferation (Ki67), mechanotransduction (YAP/TAZ) as well as nuclear (Hoescht) and cytoskeletal stains (α-Tubulin, F-actin). Images obtained are parsed through an automated feature extraction pipeline is used to obtain quantitative values for cell shape, proliferation and mehanotransduction. Finally, we train a linear classifier to extract distinct cell shapes to assess heterogeneity in the cell population (Figure 5.3a).

Firstly, we investigated if the ISFET array with a Si_3N_4 passivation layer affected cell adhesion or cell morphogenesis. We compared cell adhesion and cell shape on ISFET arrays manufactured in standard CMOS technology to cells cultured for 48 hours on commercially-available, 96-well

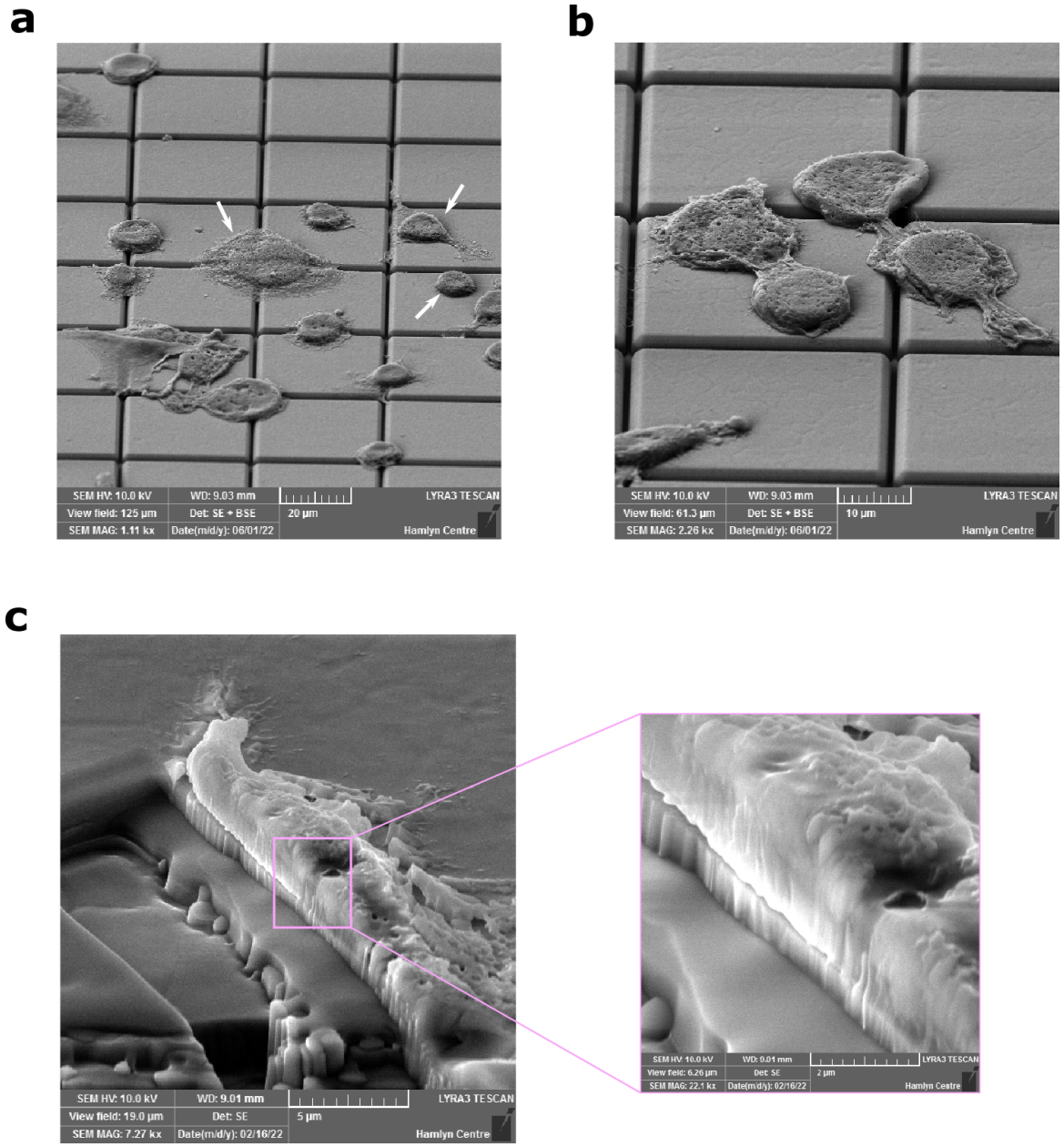


Figure 5.2: **FIB-SEM of breast cancer cells, MDA-MB-231, seeded on ISFET arrays.** **(a)** At 1.11kx magnification the attachment of MDA-MB-231 can be seen. MDA- MB-231 can be heterogenous in size and shape. Spindle, large flat and small round cell types are indicated by white arrows. **(b)** Two cells attached to eachother are shown to be moving apart in what is known as the process of cytokinesis, the final stage of cell mitosis. This provides preliminary evidence of cell division and growth. **(c)** FIB-SEM milling of a cell attached to the surface of the ISFET array shown in magnification where the basement membrane of the cell is directly adhered to the surface without any evident gap. All images were obtained after one day of cell culture incubation. *Acknowledgments: This experiment was performed in collaboration with Dr. Lewis Keeble.*

culture plates. After 48 hours, we observed approximately 1000 cells/well attached to standard plastic cell culture vessels, reflecting 100% of initially plated cell numbers, as opposed to almost 50% on untreated, control chips (Figure 5.3b). Unpaired 2-tailed t-test statistics show that cell attachment on a Si_3N_4 passivation layer is significantly lower than on plastic microplates (p-value < 0.0001, difference between means -389.571 $\pm$ 68.69) (Figure 5.3b).

To determine if cell shape or cytoskeletal organization is different in cells cultured on an ISFET array to those on standard tissue culture (TC), we quantified features describing morphology. The roundness of cells grown on plastic is significantly different to those grown on chip as the kernel density estimation (KDE) plot shows a higher peak at 0.14 a.u, which is also confirmed by 2-sample Kolmogorov-Smirnov (KS) statistical testing ($p = 3.77e^{-35}$) (Figure 5.3c). The KDE plot kurtosis also indicates a greater variation in the distribution of cell roundness on chip. On the other hand, the area of cells grown on chip versus on plastic was not found to be significantly different, suggesting that solely the shape of cells is affected by the Si_3N_4 surface (Figure 5.3d). Nucleus roundness was significantly different on chip, with a greater number of single cells with a lower nucleus roundness as indicated by the spread of the KDE plot in Figure 5.3e. It is noteworthy, that we can distinguish the singular pixels of the ISFET array as rectangles. By examination of the α-Tubulin or F-actin, the direction of growth is seen to run parallel to the pixel axes, resulting in an elongation of cell shape (Figure 5.3a & f). This is reflected in Figure 5.3f where the percentage of the total population classified as an elongated cell shape by a linear classifier is shown to be increased on ISFET chips as compared to plastic. Unpaired multiple t-test, confirms a discovery of differences in the percentage of total cells classified as elongated and star shape on chip which is likely to be attributed to the ISFET pixel architecture (Figure 5.3f). These results indicate that whilst there are subtle changes in cell roundness which may be related to the surface configuration of the ISFET interface having an impact on the cell shape, cell size remains the same on chip as on plastic.

Proliferation on ISFET arrays

To evaluate the effect of Si_3N_4 as a substrate for cell growth, we quantified the levels of proliferation marker, Ki67, in single cells [32]. Figure 5.4a is representative of the localisation and intensity of Ki67 foci found in the nuclei of MDA-MB-231 cells on chip. Mean normalised Ki67/Hoescht intensity ratio of cells grown on plastic is 0.878 a.u. The ratio is 37% higher on chip. The cumulative distribution function (CDF) of normalized Ki67 intensity in cells grown on chip shows the point where the maximum difference can be observed (ks statistic = 0.244, p-value = $1.76e^{-106}$), indicating that there is a significantly different expression of Ki67 on chip as compared to cells on plastic (Figure 5.4b). Further inspection of the KDE panel reveals that a greater proportion of the population grown on chip are actively in any stage of the cell cycle (G1,G2,M) as indicated by the presence of Ki67 foci (Figure 5.4a & b). This confirms

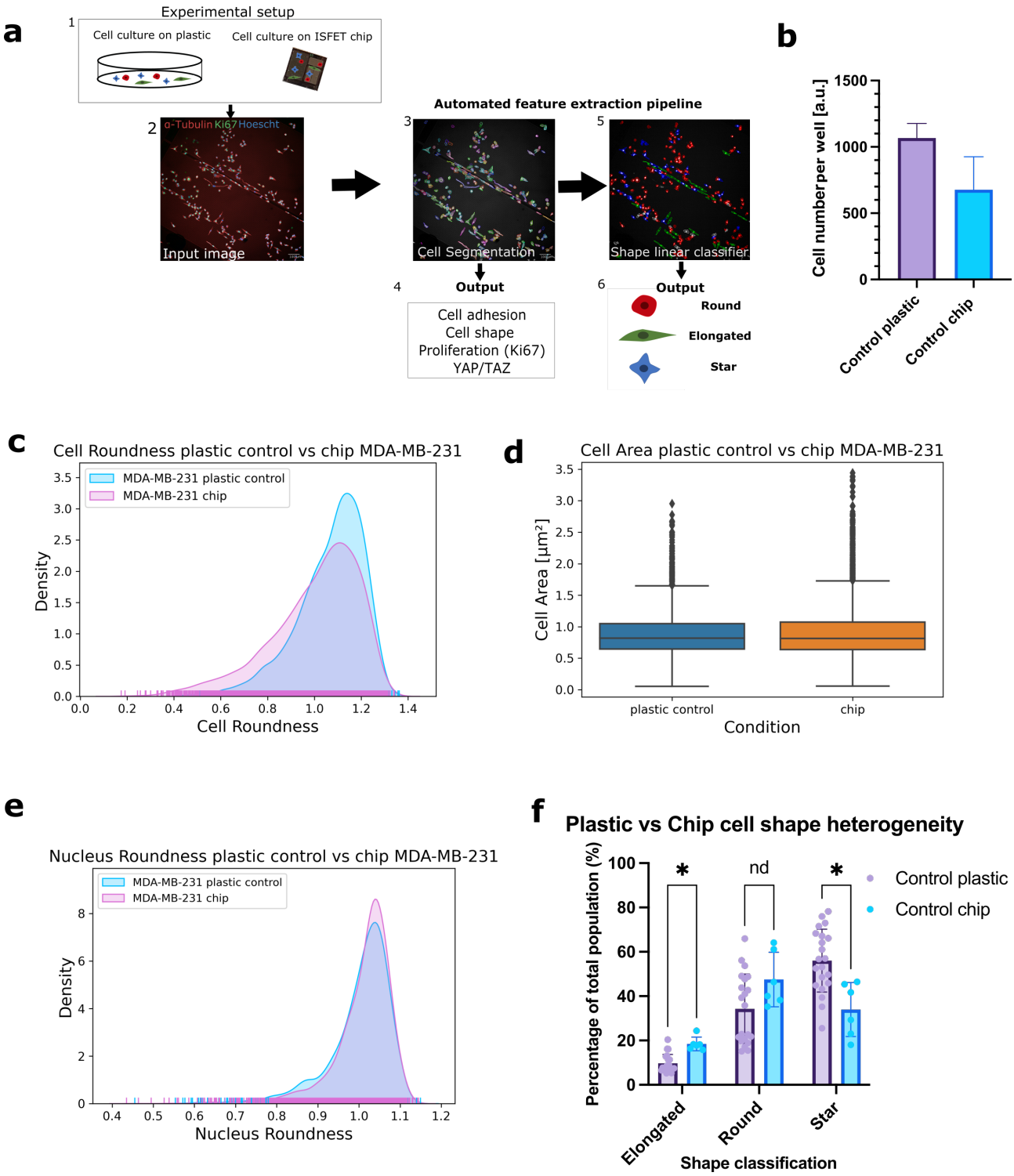


Figure 5.3: **Experimental workflow and cell morphology of triple-negative breast cancer cell line, MDA-MB-231, on tissue culture plastic versus the Si_3N_4 ISFET gate surface. (a)** CMOS-based Lab-on-Chip device previously reported in [29] (left). Experimental setup of cell culture on plastic or ISFET chips followed by automated feature extraction pipeline from high-throughput confocal microscopy, using the Perkin Elmer Columbus software. A fluorescent confocal image is used as input for segmentation of nucleus and cell shape and extraction of shape, intensity, and texture feature. Selection of training data and extracted features allow classification of three different shape classes (round, elongated, star). (Continued on next page)

(b) Number of cells attached per well, after 48 hours cell culture. N=6 chips, N=21 wells. **(c)** Kernel density estimation and corresponding rug plot of cell roundness for cells cultured on plastic 96-well cell culture plates and the ISFET array. **(d)** Cell area (μm^2) in cells cultured on plastic culture plates as a control versus the ISFET chip. **(e)** Kernel density estimation plot and corresponding rug plot of nucleus roundness for cells cultured on plastic culture plates or the ISFET chip. N = 4,062 single cells for all conditions. **(f)** Percentage of total population attached on plastic or Si_3N_4 ISFET arrays classified as elongated, round or star. Multiple t-test discovery indicated by asterisk (*) N=6 chips N=21 plastic wells. Statistics performed in python of GraphPad Prism version 9.5.0.

that there is no evident initiation of quiescence on chip, which could otherwise be distinguished through decreasing Ki67 levels [32–34].

Mechanotransduction on ISFET arrays

Most cells are responsive to mechanical forces which are a function of how cells interact with their microenvironment [27]. We have previously observed that other materials, such as Si Nanoneedles, can significantly alter the dynamics of mechanically sensitive signalling pathways such as those regulating the YAP/TAZ mechanosensors [24]. To evaluate whether culturing of breast cancer cells on chip also affected mechanically sensitive signalling pathways, we quantified nuclear localization of YAP/TAZ on cells cultured on ISFET arrays. When activated by mechanical stress, YAP/TAZ is translocated from the cytoplasm where it lies inactive, into the nucleus [35]. By segmentation of the nucleus and the cytoplasmic area surrounding the nucleus, herein referred to as nuclear ring region, we calculated a YAP/TAZ ratio. Figure 5.4c is a representative, confocal image of cells on chip showing intensity of YAP/TAZ in the nucleus and cytoplasm. The CDF plot of YAP/TAZ intensity shows a significant difference between the two populations (p-value = $1.51e^{-66}$), which is also validated by the KDE panel where the peak of the population on chip is positively skewed (Figure 5.4d). Thus, YAP/TAZ distribution is on average higher in the nuclear ring region than in the nucleus in the chip population versus plastic resulting in a greater proportion of YAP/TAZ remaining inactive in the cytoplasm of cells grown on chip. As a result, cells cultured on chip are likely less mechanically responsive to the Si_3N_4 surface than they are on plastic.

5.4.2 Extracellular matrix component (ECM) deposition on ISFET arrays

Cell adhesion and morphogenesis on ECM-treated ISFET arrays

In order to examine whether the biocompatibility of chips could be improved, chips were coated with rat tail collagen Type I, human FN or PLOL [36–38]. Figure 5.5a depicts representative

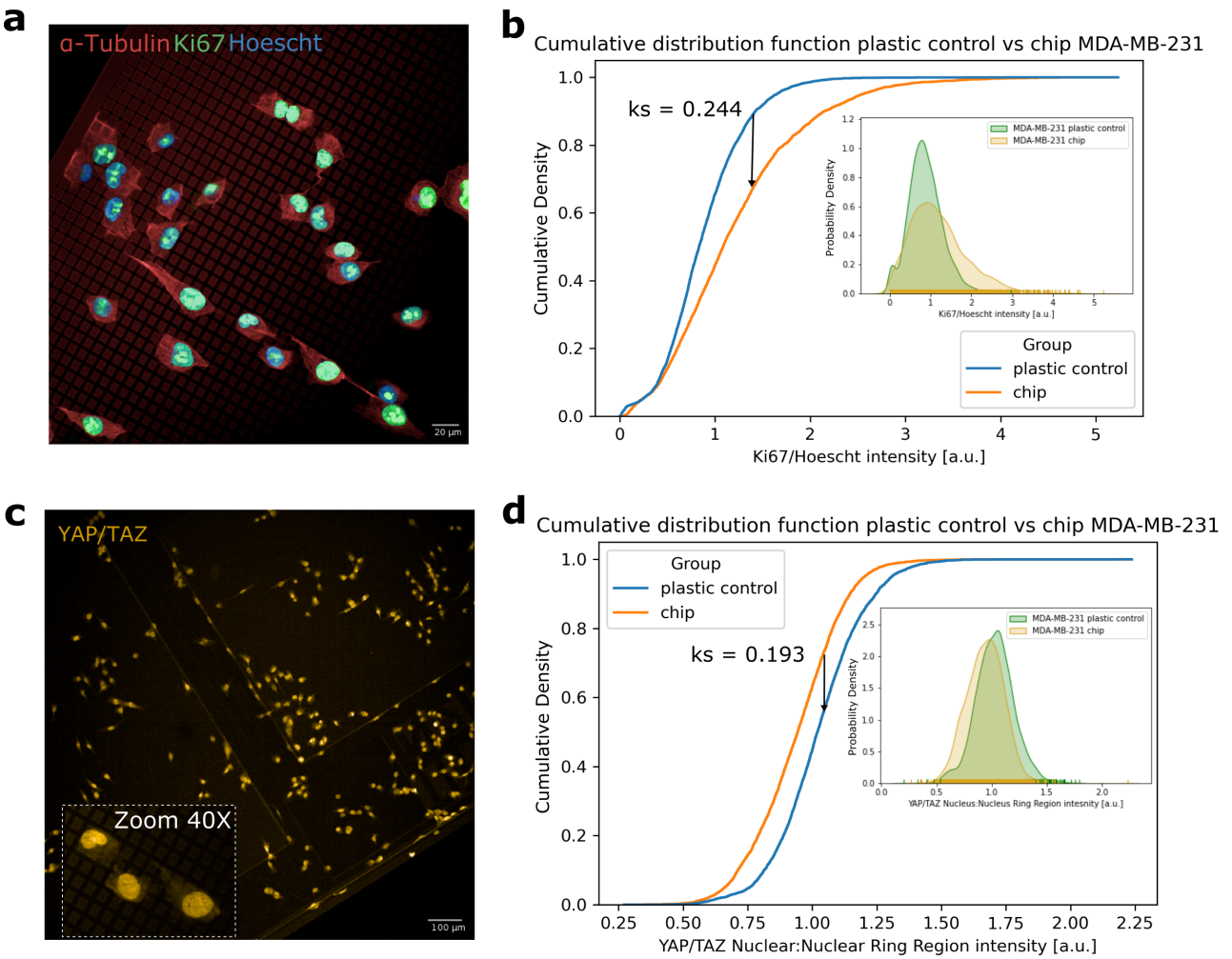


Figure 5.4: **Characterisation of changes in proliferation and YAP/TAZ expression of Triple negative breast cancer cells, MDA-MB-231, on plastic cell culture plates versus the Si_3N_4 ISFET gate surface.** **(a)** MDA-MB-231 cells cultured on the ISFET array with fluorescent antibody staining for alpha Tubulin (red), proliferation marker Ki67 (green) and Hoescht nuclear dye (blue). **(b)** Cumulative distribution function of Ki67 intensity, normalised to Hoescht dye intensity, for single cells cultured on plastic culture plates as a control versus ISFET chips. Panel of kernel density estimation and corresponding rug plot. **(c)** MDA-MB-231 cells cultured on the ISFET array and fluorescently stained for YAP/TAZ expression (yellow) with a zoom panel at 40X magnification. **(d)** Cumulative distribution function of YAP/TAZ intensity ratio in the nucleus versus the nuclear ring region in MDA-MB-231 cells cultured on plastic versus ISFET arrays. Panel of kernel density estimation and corresponding rug plot. Plastic control N = 21 wells or ISFET chip N = 6. N = 4,062 single cells for all conditions. All images obtained using the Opera Phenix (Perkin Elmer) and segmented with Columbus (Perkin Elmer). Kolmogorov-Smirnov statistics (Ks) performed using the scipy.stats module in Python.

confocal images of chips with the relevant extracellular matrix deposits where cells are stained for cytoskeletal marker, α-Tubulin, Ki67, YAP/TAZ and nuclear stain Hoescht. Firstly, a comparison of the number of cells on untreated plastic, untreated control chips and ECM-treated chips shows that cell adhesion and growth increased on all treated chips in comparison to control chips. Approximately double and triple cell numbers were observed on FN and collagen or PLOL surfaces, respectively, when compared to control chips (Figure 5.5b). In addition, collagen and FN treatment of chips resulted in rescue of cell adhesion to similar cell numbers adhered to standard cell culture plastic, whilst cell numbers on PLOL surpassed standard plastic vessels attachment efficiency (Figure 5.5b). However, it is noteworthy, that the number of cells attached to collagen and FN chips varied on a per chip level (Figure 5.5b).

Cytoplasm, nucleus shape and texture features were used to train a linear classifier to extract 3 distinct cell shapes in the MDA-MB-231 population: elongated, round and star. Strikingly, a higher percentage of the population of cells grown on PLOL are classified as round, with a corresponding decrease in the proportion of elongated cells, in comparison to control chips (Figure 5.5c). However, multiple t-test shows that there is no significant difference between the cell shape distributions of all chip configurations in comparison to untreated, control chips.

Proliferation on ECM-treated ISFET arrays

Figure 5.5d shows a KDE and corresponding rug plot of Ki67 intensity in chip configurations. A bimodal distribution can be distinguished in the PLOL-treated populations whilst all other configurations follow a positively skewed, unimodal distribution. Additionally, 2-sample KS test indicates that both collagen (p-value = $3.42e^{-10}$) and FN (p-value = $9.7e^{-08}$) groups show significantly different Ki67 expression as compared to the control (Figure 5.5d). When compared to standard cell culture plastic, PLOL-treated chips more closely resembled the proliferation profile observed under standard cell culture conditions with a normalized mean Ki67/Hoescht intensity of 1.051 a.u. (Figure 5.5e).

Mechanotransduction on ECM-treated ISFET arrays

To determine if the mechanical sensitivity of cells was impacted due to ECM treatment of ISFET chips, we quantified YAP/TAZ nuclear translocation in cells plated on chip with different substrates. Figure 5.5f shows all chip configurations following a similar trend of positive kurtosis as the control group, except the PLOL-treated population which is more normally distributed. Thus, the PLOL-treated group has a higher median YAP/TAZ intensity than all other configurations, indicating higher nuclear translocation of YAP/TAZ (Figure 5.5f). More specifically, the normalized mean YAP/TAZ N:RR intensity of PLOL-treated chips is found to be higher than recorded on plastic vessels indicating an increase in YAP/TAZ activation (Figure 5.5g).

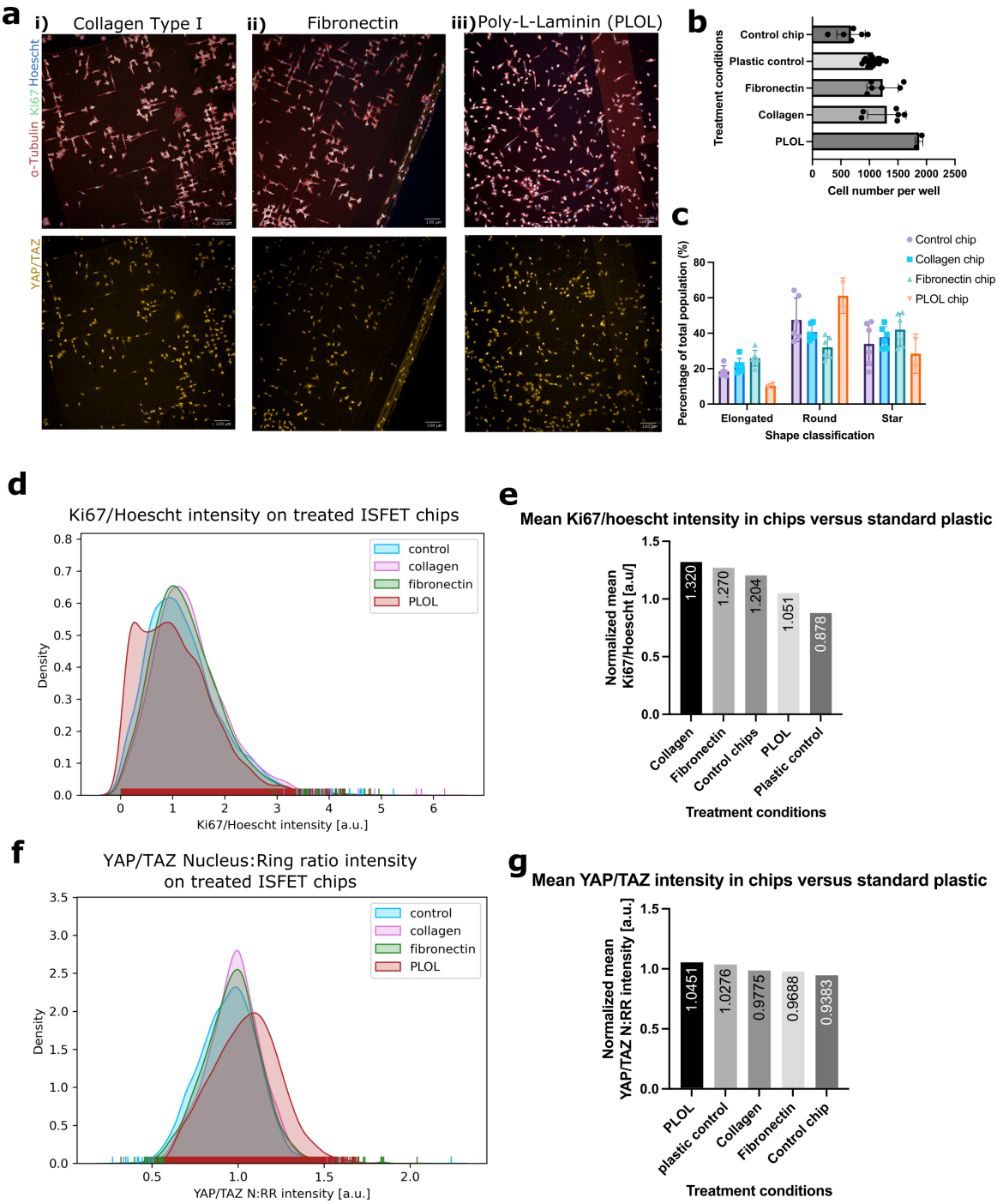


Figure 5.5: **Cell adhesion, cell shape, proliferation and YAP/TAZ expression of cancer cells on Si_3N_4 interface treated with extracellular matrix components. (a)** MDA-MB-231 attached to ISFET arrays with deposited **(i)** Collagen Type I (50 μg/ml), **(ii)** Fibronectin (1μg/ml) and **(iii)** PLOL (8 μg/ml) deposited on ISFET surface prior to cell culture (from left to right). ISFETs are fixed and stained for cytoskeletal marker, α-Tubulin (red), proliferation marker, Ki67 (green), Hoescht nuclear dye (blue) in the upper panels and YAP/TAZ (yellow) in the lower panels. All images obtained on the Opera Phenix (Perkin Elmer). **(b)** Number of cells attached per well, after 48 hours, on all treated ISFET chips or untreated control chips versus standard culture plastic vessels. **(c)** Percentage of total population of cells attached on the respective ISFET chips whose shape were classified as elongated, star or round. (Continued on next page.)

(d) Kernel density estimation and corresponding rug plot for proliferation marker, Ki67, expression normalised to Hoescht dye intensity in cells cultured on control chips and treated chips. **(e)** Normalized mean Ki67/Hoescht intensity in treated chips or untreated chips versus standard culture plastic.**(f)** Kernel density estimation and corresponding rug plot for YAP/TAZ nuclear: nuclear ring ratio intensity on control chips or treated chips. **(g)** Normalized mean YAP/TAZ N:RR in treated chips or untreated chips versus standard culture plastic. N = 3,743 single cells for all KDE plots. All images obtained using the Opera Phenix (Perkin Elmer) and segmented with Columbus (Perkin Elmer). Kolmogorov-Smirnov statistics (Ks) performed using the scipy.stats module in Python.

Collagen and FN -treated chips showed a moderately decreased YAP/TAZ activation to plastic (Figure 5.5g). However, statistical testing confirms that both the collagen and FN populations are also significantly different in YAP/TAZ intensity to the control chip group (2-sample KS, p-value = $8.04e^{-16}$, p-value = $6.10e^{e-06}$, respectively). Whilst all chip configurations improved efficiency of cell attachment without significantly skewing the cell shape heterogeneity of the MDA-MB-231 population, it can be seen that both proliferation and mechanoresponsiveness change dependant on the ECM-coating of chips when compared to an untreated Si_3N_4 interface. Most notably, PLOL-treated chips resulted in the highest number of proliferating cells, as indicated by Ki67 expression and a significant increase in the mechano-responsiveness of cells when compared to untreated Si_3N_4 chip surfaces.

5.4.3 Focal adhesion formation on a Si_3N_4 interface

The formation of focal adhesions (FAs) is an essential component at the interface between cells and their extracellular microenvironment. They have a key role in anchoring cells to surfaces but also determine proliferation, signal transduction, as well as migration and are also upstream activators of YAP/TAZ through the Hippo pathway [24, 39]. We previously observed that Si-based nanoneedles inhibited the formation of FAs at contact sites [24]. The impact of YAP/TAZ translocation in cells on chip lead us to investigate if FA morphogenesis was otherwise disrupted. FAs are found at the ends of stress fibres and can be identified through a scaffold protein, paxillin. Figure 5.6a, shows the expression of paxillin at FAs on mattek dishes (WT) and on ISFET chips (chips) treated with FN, obtained using Total Internal Fluorescence Microscopy (TIRF), to allow imaging of features closest to the coverslip. The left panels highlight the segmentation of FAs used to further characterise the pattern of FAs. The orientation of FAs under both conditions follows the same pattern, indicating that the patterning of the ISFET array, although affecting cell shape, does not affect the frequency distribution of FAs (Figure 5.6b). However, it can be distinguished that FAs formed on chip have a lower mean area, indicating stretching in their respective orientations (Figure 5.6c). This indicates that decreased activation of YAP/TAZ likely coincides with differences in FA morphogenesis on ISFET arrays.

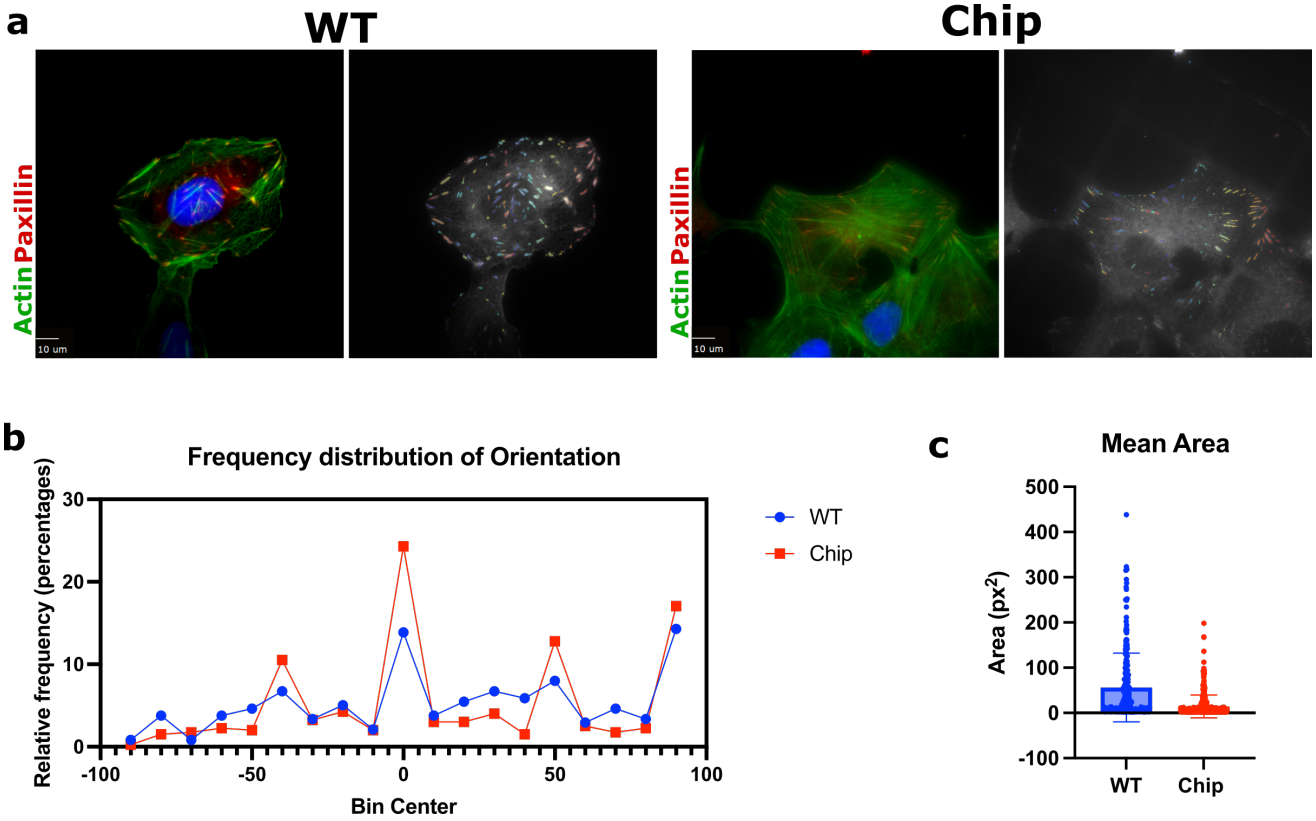


Figure 5.6: **Focal adhesions of cancerous cells on standard tissue culture conditions (WT) and ISFET chip coated with fibronectin. (a)** Cancerous cell line, U2OS CDK1 AS (osteosarcoma) was cultured on a standard tissue culture mattek dish (WT) or an ISFET array (Chip) both coated with fibronectin. In each panel: Right image shows paxillin stains of focal adhesions. Left image shows detection threshold segmentation of focal adhesions using the Focal Adhesion Analysis Server (FAAS). **(b)** Histogram of orientation of focal adhesions detection in WT versus chip conditions. **(c)** Mean area of single focal adhesions in WT versus on chip, as measured in square pixels. Images obtained on Total Internal Fluorescence (TIRF) microscope and quantitatively analysed using the Focal Adhesion Analysis Server [31]. Graphs and statistics performed with GraphPad Prism version 9.5.0.

5.4.4 Sensor sensitivity with collagen and fibronectin-coated ISFET arrays

Despite studies reporting the hydrophilicity of PLOL that presents an attribute for cell adhesion, it's instability has also been noted making it challenging to work with for long-term experiments [40]. As a result, sensor sensitivity was evaluated for Titan ISFET arrays coated with collagen or fibronectin as compared to untreated control surfaces. Surface treatment was carried out as set out in Section 5.3.2 and the experimental setup, including buffer formulations, as in Section 4.3 with the deviation of a 4-well manifold to allow for multiple conditions. Buffers were interchanged in the following order: pH 7, pH 6, pH 7, pH8, pH 7. This resulted in a 1 pH change and a calculated mean total drift between the starting chemical readout at pH 7 and the final readout also at pH 7. Figure 5.7(a) illustrates the differences in output between control, collagen and fibronectin conditions whereby collagen shows the closest sensitivity to the control surface, whilst fibronectin appears to inhibit the sensor sensitivity by almost 8 times more than collagen. The increased total drift with a 1 pH increase can be seen in the average chemical readout whereby a substantial drift may be seen at 2500 s in both collagen and fibronectin readouts (Figure 5.7(b)).

5.4.5 Cell morphogenesis, proliferation and mechanotransduction of non-tumorigenic cell culture on a Si_3N_4 surface of ISFET arrays

We also evaluated the biocompatibility of a non-tumorigenic cell line originating from mammary epithelial tissue, MCF10A. An assessment of the morphology of MCF10A cells on chip, indicates that whilst cells maintain their epithelial growth pattern, predominantly characterised by cell-cell contacts, when limited by the constraints of pixel architecture, they appear more elongated, than when cultured on standard culture vessels, whilst also maintaining cell contacts at either edge (Figure 5.8a). Quantitative evaluation of their elongation is represented in the ratio of cell width to length KDE plot where the greater number of cells concentrated at the tail of the distribution indicates the presence of more elongated cells on chip (Figure 5.8b). The significant difference between the two distributions is also confirmed with 2-sample KS statistics (p-value = $1.62e^{-06}$). Thus, the morphology of MCF10A appears to be affected by culturing on chip versus plastic as observed for cancer cells as well. The intensity of Ki67 was shown to be significantly different between plastic and chip in MCF10A cells (p-value = $1.12e^{-16}$), where a bimodal distribution in cells grown on plastic, versus an altered kurtosis in the chip population shows distinct differences in Ki67 expression of the two populations (Figure 5.8c). The distribution pattern of Ki67 on chip is comparable in both MDA-MB-231 and MCF10A cells, showing repeatability of results in different cell lines. Nonetheless, a greater maximum difference in

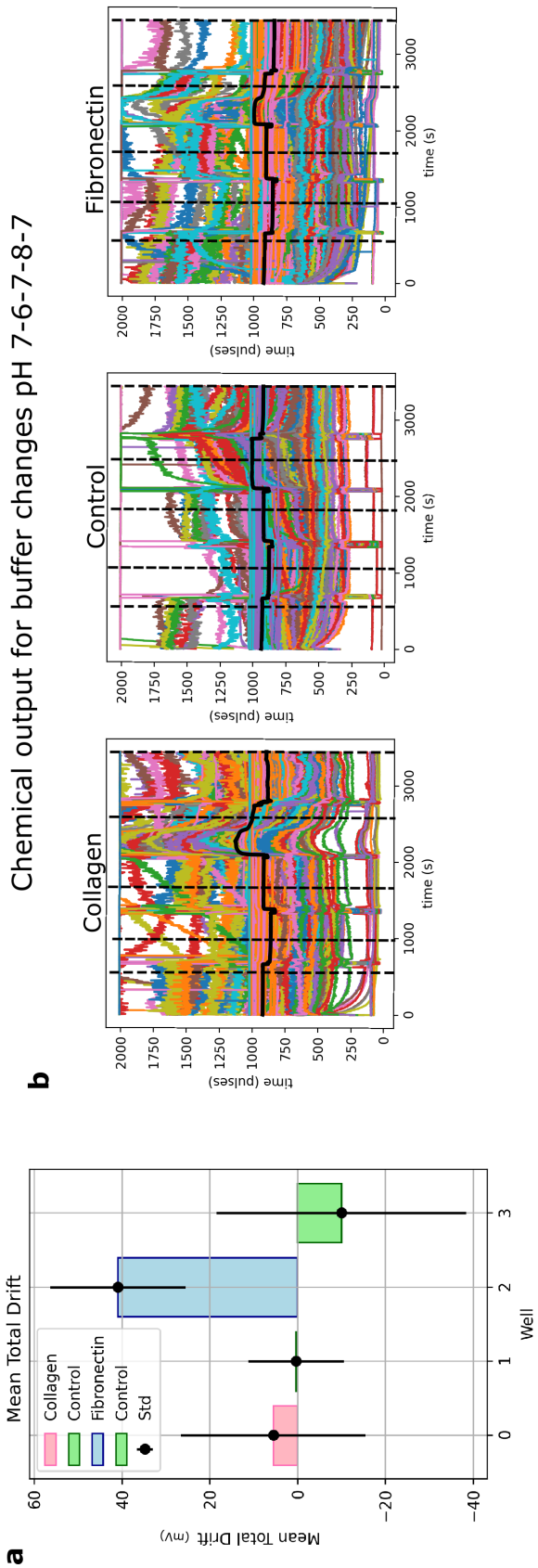


Figure 5.7: **Sensor sensitivity of Titan ISFET array coated in collagen or fibronectin as evaluated with buffers.(a)** Mean total drift of control, collagen and fibronectin conditions indicating the overall change observed between pH 7 buffers at the start and end of the chemical readout. **(b)** Raw chemical output and average chemical output (in black) of collagen, control and fibronectin-coated ISFET surfaces over time. The dotted lines indicate the different buffer points in the following order: pH 7, pH 6, pH 7, pH 8, pH 7. *Acknowledgment: Experiment performed by UROP student, Rolando Charles.*

Ki67 intensity occurs in MDA-MB-231 cells as evidenced by the ks statistic (Figures 5.4 & 5.8). Finally, YAP/TAZ intensity in the two populations shows that the peak of the chip distribution followed a negative skew and results in a significant difference in the two populations (p-value = $1.51e^{-11}$, ks statistic = 0. 077) (Figure 5.8d). In comparison to MDA-MB-231 cells, non-cancerous MCF10A cells YAP/TAZ intensity results show that the population distribution on plastic versus chip is similar in non-cancerous cells.

5.4.6 Cell morphogenesis, proliferation and mechanotransduction of non-tumorigenic cell culture on ECM-treated ISFET arrays

In order to increase the biocompatibility of the passivation layer, the same chip configurations as for cancerous cells (collagen, FN and PLOL) were deposited on chip, and attachment efficiency was evaluated. Figure 5.8e shows that whilst more cells on average attached onto the chips with a FN coating than on the untreated control chips, the difference is not significant, likely due to chip by chip variation. The KDE plot of Ki67 intensity for all chip configurations shows that the the MCF10A population of collagen-coated chips is positively skewed whilst FN and PLOL-treated are negatively skewed in comparison to the control group (Figure 5.8f). Collagen-coated chips show more actively proliferating cells, as indicated by the ratio of Ki67/Hoescht intensity, whilst FN-coated chips result in lower proliferation than the control group. All chip configurations have a significantly different proliferation profile to the control group. On the other hand, YAP/TAZ expression in all chip configurations shows that whilst there are differences in the peak location of the distributions which shows a different median, the overall shape of the distributions remains similar.

We conclude, that a similar behaviour can be observed on both native chips and ECM-treated chip configurations with both non-tumorigenic, mammary epithelial cells, MCF10A, and triple negative breast cancer cells, MDA-MB-231. Proliferation increased on chip for both cell types, whilst MDA-MB-231 cells also show an increase in YAP/TAZ intensity in the nuclear ring region which is not replicated in MCF10A cells where YAP/TAZ intensity slightly increases to indicate nuclear translocation. On the other hand, cell attachment efficiency increased in FN-treated chips for MCF10A cells, whilst attachment increased with all treatments as compared to native chips in MDA-MB-231 cells. This indicates that the choice of ECM deposition for cell-based assays is likely to be cell-type specific. PLOL treatment of chips restored both YAP/TAZ and Ki67 levels to be comparable to standard TC plastic in tumorigenic cells. Similarly, in non-tumorigenic MCF10A cells, PLOL rescued YAP/TAZ levels, however, untreated chips were most comparable to plastic in terms of proliferation levels. Both non-tumorigenic and tumorigenic cell lines showed a similar response in terms of proliferation and attachment on ISFET array chips.

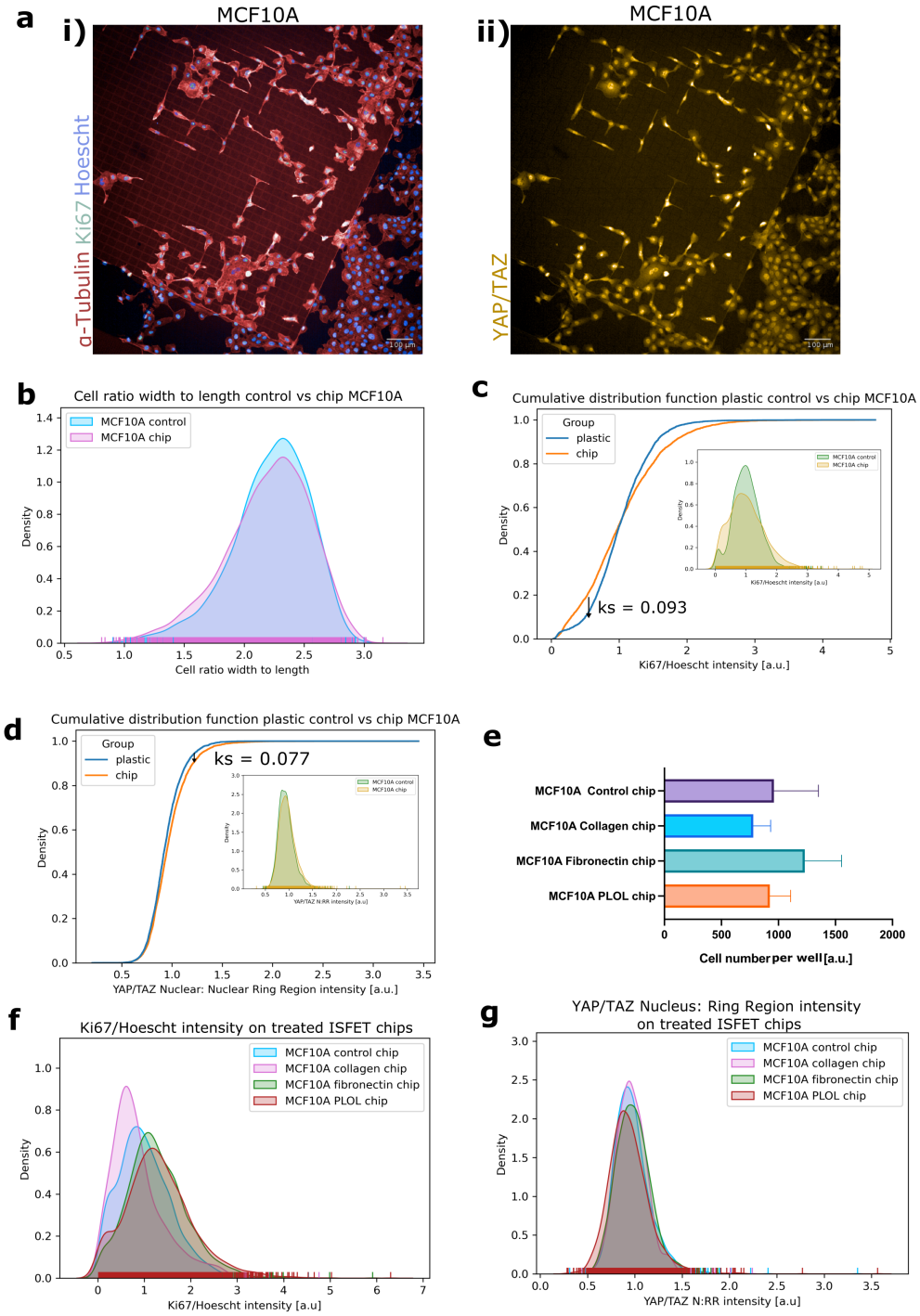


Figure 5.8: **Non-tumorigenic mammary epithelial cells, MCF10A, morphology and behavioural response to culture on ISFET chips with Si_3N_4 interface.** **(a)** MCF10A cells cultured on the Si_3N_4 interface of ISFET chips and fluorescently stained for **(i)** cytoskeletal marker α-Tubulin (red), proliferation marker Ki67 (green), Hoescht nuclear dye (blue) **(ii)** YAP/TAZ (yellow). **(b)** Kernel density estimation and corresponding rug plot of cell ratio width to length for MCF10A cells cultured on 96-well standard plastic cell culture plates as a control or ISFET chips. **(c)** Cumulative distribution function of Ki67 intensity, normalized to nuclear Hoescht dye intensity in cells cultured on plastic or ISFET chips. Panel of kernel density estimation plot showing single cell population density. **(d)** Cumulative distribution function of YAP/TAZ nuclear to nuclear ring ratio intensity in cells cultured on plastic or ISFET chips. Panel of kernel density estimation plot showing single cell population density. (Continued on next page)

(e) Number of cells attached per well for ISFET chips with extracellular matrix deposition of Collagen Type I (50 μg/ml) , Fibronectin (10ng/ml) and PLOL (8 μg/ml) or control chips with no additional deposition. **(f)** Kernel density estimation and corresponding rug plot for proliferation marker, Ki67, intensity normalised to nuclear Hoescht dye intensity in MCF10A cells cultured on control ISFET chips versus ISFET chip configurations. **(g)** Kernel density estimation and corresponding rug plot for YAP/TAZ nucleus to nuclear ring ratio intensity in MCF10A cells cultured on control, ISFET chips versus ISFET chip configurations. N = 4,282 single cells for all plastic and control ISFET chip experiments. N = 2,119 single cells for all chip configurations. All images obtained using the Opera Phenix (Perkin Elmer) and segmented with Columbus (Perkin Elmer). Kolmogorov-Smirnov statistics (Ks) performed using the scipy.stats module in Python.

The biocompatibility of Si_3N_4 has recently been scoped for biomedical applications, such as microspectroscopy and orthopaedic prosthetics, where studies have investigated cell growth and biochemical reactions at the cell-silicon interface [41–43]. A range of cell types including, peripheral blood mononuclear cells (PBMNCs), osteosarcoma, osteoblast-like, stem cells, adipocytes, cardiomyocytes and fibroblasts have shown viability and growth of cells on silicon-based materials in discs or membrane-form [23, 41, 42, 44–48]. Notably, no DNA damage or reactive oxygen species response was reported with PBMNC culture, however, release of silicic acid and NH_4^+, affected cell metabolism in osteosarcoma [42, 44]. The release of ammonium ions could result in metabolism perturbations and proliferative capacity due to ammonia recycling through biosynthetic pathways which is known to occur in a breast cancer microenvironment [49, 50]. The release of ammonia was also shown in studies to be attributed to the chemical breakdown of Si_3N_4 when in contact with an aqueous solution, to form a layer of SiO_2 [42, 51]. Hence, it can be inferred that studies on Si_3N_4 can be reasonably extrapolated to a SiO_2 interface. However, inflammatory cytokine, TNFa, was increased in culture with SiO_2 but not Si_3N_4, likely resulting in distinct cell phenotypes on the two surfaces [42]. Further evidence of prolonged growth of tumour xenografts in mice with Si_3N_4 implants showed the potential of the material as implantable sensors [52]. Key to future applications is evidence of pH buffering at the interface has been reported in both mammalian and bacterial cultures which brings to question the cell-based assays which can be performed on Si_3N_4 surfaces [44, 48].

In line with these studies, we show that the Si_3N_4 gate surface of ISFET arrays, which can be successfully used as cell culture substrates, however, we observed significant differences in mechanotransduction of cells grown on ISFET arrays. The translocation of YAP/TAZ to the nucleus indicates activation, implying that the substrate stiffness of the ISFET surface is not similar to standard plastic culture vessels [53]. Most importantly, this need not be seen as a limitation to the use of ISFET arrays, as the stiffness of standard culture vessels is well-beyond mammalian tissue norms [53]. As a result, Si_3N_4 ISFET arrays are likely to represent a more physiological surface for the growth and survival of mammalian cells. Despite these observations, it has been noted that inconsistencies arise in study results due to variations in manufacturing and post-processing, such as thermal treatments, which alter the surface

chemistry and can affect cell adhesion [51, 54, 55].

Finally, we can significantly engineer the biocompatibility of the ISFET surface through the surface treatment with ECM components. We showed that all ECM treatments with collagen, FN and PLOL, resulted in a greater attachment efficiency in cancer cell cultures. Studies to mimic standard culturing conditions have investigated the use of PLOL and PLL (Poly-L-Lysine) coating on Si_3N_4 surfaces and also reported improved cell attachment [38, 40]. Notably, a lower growth rate and higher exit into quiescence was recorded for PC12 cells with neural properties [40]. Here, we found that mean normalized Ki67/Hoescht ratio increases in breast cancer cells grown on chip as compared to plastic. This distinct difference may in fact arise due to faster proliferation in MDA-MB-231 cells on chip [33]. With a higher concentration of Ki67 in single cells, we could speculate that faster proliferation may be linked to cell adhesiveness [33]. In our study, PLOL treatment of ISFET arrays was shown to be overall most effective in increasing cell adhesion and rescuing mechanoresponsiveness of cells. Future applications of ISFET arrays for cell-based assays will require a consideration of the ISFET pixel architecture to optimise the surface for cell growth without introducing scaffolding which may affect both cell shape and mechanotransduction.

5.5 Summary and future direction

This study investigated the effects of ISFET arrays with a Si_3N_4 passivation layer on cell adhesion, morphology, proliferation and mechanoresponsiveness of cancer cells and non-tumorigenic cells in vitro. The key outcomes of the chapter are summarised as follows:

1. The Si_3N_4 surface is a substrate amenable to cell adhesion.
2. A moderate increase in actively proliferating cells and significant differences in the mechanotransduction profile of tumorigenic cells cultured on Si_3N_4 arrays is recorded.
3. PLOL treatment of ISFET surfaces recapitulates the mechanosensitivity of both tumorigenic and non-tumorigenic cells to levels comparable to those observed on plastic surfaces.
4. YAP/TAZ and proliferation marker expression on collagen and fibronectin (FN)-treated chips did not improve the resemblance of the cell phenotype to the one observed on plastic in both normal and cancer cell cultures.
5. Tumorigenic cells appear to be more sensitive to the Si_3N_4 surface than non-tumorigenic cells.
6. Sensor sensitivity of collagen-coated chips is comparable to untreated surfaces whilst fibronectin-treated surfaces have a higher total drift over time.

Based on our results we advise that the Si_3N_4 gate interface of ISFET arrays is largely biocompatible. Future studies we propose the additional evaluation of alternative passivation layers which are commonly used, such as Aluminium oxide (Al_2O_3), tanatalum pentoxide (Ta_2O_5) and hafnium oxide (HfO_2). Whilst we expect similar results to arise due to the inorganic surface chemistry of all the proposed materials there may be some variations in surface stiffness and elasticity to be considered. To an extent, this is assessed in Chapter 6 for the HfO_2 passivation surface of the Titan chip. Furthermore, piloting a Bradford assay on chip would allow further characterisation of protein retention on chip to assess the adhesive properties of cell media factors and large, globular proteins e.g. Bovine Serum Albumin (BSA). Finally, repetition with primary cell lines would better recapitulate a physiological cell response. In the current setting, immortalised cell lines may be found to be more resilient to both mechanical and chemical environmental changes.

References

[1] D. F. Williams. "On the mechanisms of biocompatibility". In: *Biomaterials* 29.20 (July 2008), pp. 2941–2953.

[2] B. D. Ratner. "The Biocompatibility Manifesto: Biocompatibility for the Twenty-first Century". In: *Journal of Cardiovascular Translational Research 2011 4:5* 4.5 (June 2011), pp. 523–527.

[3] S. Gruber and A. Nickel. "Toxic or not toxic? The specifications of the standard ISO 10993-5 are not explicit enough to yield comparable results in the cytotoxicity assessment of an identical medical device". In: *Frontiers in Medical Technology* 5 (2023), p. 1195529.

[4] *ISO 10993-5:2009 - Biological evaluation of medical devices — Part 5: Tests for in vitro cytotoxicity.*

[5] P. Vadgama. "Sensor biocompatibility: final frontier in bioanalytical measurement". In: *Analyst* 132.6 (May 2007), pp. 495–499.

[6] P. Bergveld. "Thirty years of ISFETOLOGY: What happened in the past 30 years and what may happen in the next 30 years". In: *Sensors and Actuators, B: Chemical* 88.1 (Jan. 2003), pp. 1–20.

[7] P. Bergveld. "Development, Operation, and Application of the Ion-Sensitive Field-Effect Transistor as a Tool for Electrophysiology". In: *IEEE Transactions on Biomedical Engineering* BME-19.5 (Sept. 1972), pp. 342–351.

[8] P. Georgiou and C. Toumazou. "ISFET characteristics in CMOS and their application to weak inversion operation". In: *Sensors and Actuators, B: Chemical* 143.1 (Dec. 2009), pp. 211–217.

[9] M. Yuqing, G. Jianguo, and C. Jianrong. "Ion sensitive field effect transducer-based biosensors". In: *Biotechnology Advances* 21.6 (Sept. 2003), pp. 527–534.

[10] N. Moser et al. "ISFETs in CMOS and Emergent Trends in Instrumentation: A Review". In: *IEEE Sensors Journal* 16.17 (Sept. 2016), pp. 6496–6514.

[11] J. Bausells et al. "Ion-sensitive field-effect transistors fabricated in a commercial CMOS technology". In: *Sensors and Actuators, B: Chemical* 57.1-3 (Sept. 1999), pp. 56–62.

[12] H. S. Wong and M. H. White. "Self-contained CMOS integrated pH sensor". In: *Technical Digest - International Electron Devices Meeting* (Dec. 1988), pp. 658–661.

[13] P. Bergveld. "Short Communications: Development of an Ion-Sensitive Solid-State Device for Neurophysiological Measurements". In: *IEEE Transactions on Biomedical Engineering* BME-17.1 (1970), pp. 70–71.

[14] M. Lehmann et al. "Non-invasive measurement of cell membrane associated proton gradients by ion-sensitive field effect transistor arrays for microphysiological and bioelectronical applications". In: *Biosensors and Bioelectronics* 15.3-4 (June 2000), pp. 117–124.

[15] M. J. Milgrew, M. O. Riehle, and D. R. Cumming. "A 16×16 CMOS proton camera array for direct extracellular imaging of hydrogen-ion activity". In: *Digest of Technical Papers - IEEE International Solid-State Circuits Conference* 51 (2008), pp. 590–638.

[16] S. Mohri et al. "Measurements of CO2, lactic acid and sodium bicarbonate secreted by cultured cells using a flow-through type pH/CO2 sensor system based on ISFET". In: *Sensors and Actuators, B: Chemical* 115.1 (May 2006), pp. 519–525.

[17] A. Poghossian and M. J. Schöning. "Detecting both physical and (bio-)chemical parameters by means of ISFET devices". In: *Electroanalysis* 16.22 (Nov. 2004), pp. 1863–1872.

[18] T. Sakata, H. Sugimoto, and A. Saito. "Live Monitoring of Microenvironmental pH Based on Extracellular Acidosis around Cancer Cells with Cell-Coupled Gate Ion-Sensitive Field-Effect Transistor". In: *Analytical Chemistry* 90.21 (Nov. 2018), pp. 12731–12736.

[19] E. Bogner et al. "Bridging the gap—Biocompatibility of microelectronic materials". In: *Acta Biomaterialia* 2.2 (Mar. 2006), pp. 229–237.

[20] G. Brusatin et al. "Biomaterials and engineered microenvironments to control YAP/TAZ-dependent cell behaviour". In: *Nature Materials* 17.12 (Oct. 2018), pp. 1063–1075.

[21] J. Fang et al. "Engineering Biomaterials with Micro/Nanotechnologies for Cell Reprogramming". In: *ACS Nano* 14.2 (Feb. 2020), pp. 1296–1318.

[22] A. C. Duncan et al. "Laser microfabricated model surfaces for controlled cell growth". In: *Biosensors and Bioelectronics* 17.5 (May 2002), pp. 413–426.

[23] M. Cioffi et al. "Integrating live cells with semiconductor devices: A biocompatibility assay". In: *Journal of Applied Biomaterials and Biomechanics* 3.2 (Jan. 2005), pp. 112–116.

[24] C. S. Hansel et al. "Nanoneedle-Mediated Stimulation of Cell Mechanotransduction Machinery". In: *ACS Nano* 13.3 (Mar. 2019), pp. 2913–2926.

[25] S. Dupont et al. "Role of YAP/TAZ in mechanotransduction". In: *Nature* 474.7350 (June 2011), pp. 179–184.

[26] J. M. Franklin, Z. Wu, and K. L. Guan. "Insights into recent findings and clinical application of YAP and TAZ in cancer". In: *Nature Reviews Cancer* 23.8 (June 2023), pp. 512–525.

[27] S. Dupont. "Role of YAP/TAZ in cell-matrix adhesion-mediated signalling and mechanotransduction". In: *Experimental Cell Research* 343.1 (Apr. 2016), pp. 42–53.

[28] T. Moroishi, C. G. Hansen, and K. L. Guan. "The emerging roles of YAP and TAZ in cancer". In: *Nature Reviews Cancer* 15.2 (Jan. 2015), pp. 73–79.

[29] N. Moser et al. "A scalable ISFET sensing and memory array with sensor auto-calibration for on-chip real-time DNA detection". In: *IEEE Transactions on Biomedical Circuits and Systems* 12.2 (Apr. 2018), pp. 390–401.

[30] S. Rata et al. "Two Interlinked Bistable Switches Govern Mitotic Control in Mammalian Cells". In: *Current Biology* 28.23 (Dec. 2018), pp. 3824–3832.

[31] M. E. Berginski and S. M. Gomez. "The Focal Adhesion Analysis Server: a web tool for analyzing focal adhesion dynamics". In: *F1000Research* 2 (Mar. 2013), p. 68.

[32] J. Gerdes et al. "Cell cycle analysis of a cell proliferation-associated human nuclear antigen defined by the monoclonal antibody Ki-67." In: *The Journal of Immunology* 133.4 (Oct. 1984), pp. 1710–1715.

[33] I. Miller et al. "Ki67 is a Graded Rather than a Binary Marker of Proliferation versus Quiescence". In: *Cell Reports* 24.5 (July 2018), pp. 1105–1112.

[34] B. S. Finkelman et al. "The Evolution of Ki-67 and Breast Carcinoma: Past Observations, Present Directions, and Future Considerations". In: *Cancers* 15.3 (Feb. 2023).

[35] S. Dupont. "Regulation of YAP/TAZ Activity by Mechanical Cues: An Experimental Overview". In: *Methods in Molecular Biology* 1893 (2019), pp. 183–202.

[36] D. Vasilaki et al. "Biophysical interactions between components of the tumor microenvironment promote metastasis". In: *Biophysical Reviews* 13.3 (June 2021), pp. 339–357.

[37] H. K. Kleinman et al. "Use of extracellular matrix components for cell culture". In: *Analytical Biochemistry* 166.1 (Oct. 1987), pp. 1–13.

[38] I. Hirata et al. "Surface modification of Si3N4-coated silicon plate for investigation of living cells". In: *Japanese Journal of Applied Physics, Part 1: Regular Papers and Short Notes and Review Papers* 39.11 (Nov. 2000), pp. 6441–6442.

[39] G. Nardone et al. "YAP regulates cell mechanics by controlling focal adhesion assembly". In: *Nature Communications* 8.1 (May 2017), pp. 1–13.

[40] J. J. Medina Benavente et al. "Evaluation of silicon nitride as a substrate for culture of PC12 cells: An interfacial model for functional studies in neurons". In: *PLoS ONE* 9.2 (Feb. 2014).

[41] E. A. Carter et al. “Silicon nitride as a versatile growth substrate for microspectroscopic imaging and mapping of individual cells”. In: *Molecular BioSystems* 6.7 (June 2010), pp. 1316–1322.

[42] S. Lal et al. “Biological Impact of Silicon Nitride for Orthopaedic Applications: Role of Particle Size, Surface Composition and Donor Variation”. In: *Scientific Reports* 8.1 (June 2018), pp. 1–12.

[43] B. S. Bal and M. N. Rahaman. “Orthopedic applications of silicon nitride ceramics”. In: *Acta Biomaterialia* 8.8 (Aug. 2012), pp. 2889–2898.

[44] G. Pezzotti et al. “Bioactive silicon nitride: A new therapeutic material for osteoarthropathy”. In: *Scientific Reports* 7.1 (Mar. 2017), pp. 1–11.

[45] R. Kue et al. “Enhanced proliferation and osteocalcin production by human osteoblast-like MG63 cells on silicon nitride ceramic discs”. In: *Biomaterials* 20.13 (July 1999), pp. 1195–1201.

[46] B. Cappi et al. “Cytocompatibility of high strength non-oxide ceramics”. In: *Journal of Biomedical Materials Research - Part A* 93.1 (Apr. 2010), pp. 67–76.

[47] A. Neumann et al. “Comparative investigation of the biocompatibility of various silicon nitride ceramic qualities in vitro”. In: *Journal of Materials Science: Materials in Medicine* 15.10 (Oct. 2004), pp. 1135–1140.

[48] G. Pezzotti et al. “Silicon Nitride Bioceramics Induce Chemically Driven Lysis in Porphyromonas gingivalis”. In: *Langmuir* 32.12 (Mar. 2016), pp. 3024–3035.

[49] X. Li et al. “Role of glutamine and its metabolite ammonia in crosstalk of cancer-associated fibroblasts and cancer cells”. In: *Cancer Cell International* 21.1 (Sept. 2021), pp. 1–13.

[50] J. B. Spinelli et al. “Metabolic recycling of ammonia via glutamate dehydrogenase supports breast cancer biomass”. In: *Science* 358.6365 (Nov. 2017), pp. 941–946.

[51] R. C. Dante and C. K. Kajdas. “A review and a fundamental theory of silicon nitride tribochemistry”. In: *Wear* 288 (May 2012), pp. 27–38.

[52] M. E. Gray et al. “Biocompatibility of common implantable sensor materials in a tumor xenograft model”. In: *Journal of Biomedical Materials Research - Part B Applied Biomaterials* 107.5 (July 2019), pp. 1620–1633.

[53] D. T. Butcher, T. Alliston, and V. M. Weaver. “A tense situation: Forcing tumour progression”. In: *Nature Reviews Cancer* 9.2 (Feb. 2009), pp. 108–122.

[54] R. M. Bock et al. “Surface modulation of silicon nitride ceramics for orthopaedic applications”. In: *Acta Biomaterialia* 26 (Oct. 2015), pp. 318–330.

[55] E. Laarz, B. V. Zhmud, and L. Bergström. “Dissolution and deagglomeration of silicon nitride in aqueous medium”. In: *Journal of the American Ceramic Society* 83.10 (Oct. 2000), pp. 2394–400.

Chapter 6

Mitotic Peak Detection by pH in Cancer Cells

This chapter presents a dual assay for real-time detection of long-term extracellular pH change and rapid pH fluctuations in osteosarcoma cell cultures on the Titan ISFET array. The chapter first introduces the role of intracellular and extracellular pH in coordinating phases of mitosis as well as summarising the contribution of other ionic fluctuations in pH homeostasis. The next section presents the molecular methods, experimental setup for the Titan array and data analysis. The experimental results are presented and critically discussed in context of existing data regarding pH fluctuations in cell compartments during mitosis. Lastly, a section on ISFETs for cell cultures and sustainability shows the applicability of this platform as a feasible future technology for biomedical applications. A summary and future directions section sets out the next steps for the development of Titan as a cell-based CMOS ISFET array on a portable, handheld diagnostic device.

Work included in this chapter has previously been published in:

Beykou, M., Gulli, C., Bousgouni, V., Moser, N., Bakal, C., & Georgiou, P. "Dynamic pH fluctuations in cancer cells on CMOS-based Lab-on-Chip ISFET arrays". *Accepted in IEEE BioCAS 2024* (October 2024).

Acknowledgments: Signal processing in collaboration with Costanza Gulli.

6.1 Introduction

The evolutionary advantage of a reversed pH gradient in the TME, which culminates in an acidic extracellular and pericellular pH along with a relative alkalinization of pHi, promotes a myriad of "cancer phenotype" behaviours. Summatively, an acidic pHe arises from an enhanced glycolytic metabolism in cancer cells and net H^+ efflux coupled with poor perfusion in tumours. In turn, a tightly controlled and precisely maintained homeostatic balance of pH in single cells ensures cancer progression. Cancer cells which are able to withstand the pH imbalance are evolutionary more advantageous for the tumour and are naturally selected for to replicate and promote more invasive and drug resistant clones. In addition to the direct effects of acidic pHe, such as drug resistance through "ion trapping" of weakly basic chemotherapeutics by protonation in the extracellular space [1, 2], cellular pH sensors will result in indirect effects on key functions for cell survival. More specifically, immune evasion, angiogenesis, migration and increased proliferation rate are some of the key biological processes associated with cancer cells which can benefit from tumour acidosis [3, 4]. As such, the detection of an acidic pHe has been identified as a potential biomarker for the detection of cancer cells as well as biological processes mediated by pH. Additionally, the homeostatic acid-base mechanism in cancer cells employs cellular sensors, commonly transmembrane ion channels for example, to maintain both a competitive and beneficial acidic pHe but to also ensure that pHi does not reach toxicity or rate-limiting pH ranges for cell survival functions, such as proliferation [5, 6]. It follows that pHe is a reflection of pHi through a complex network of cellular sensing mechanisms reviewed in Chapter 2. This creates two windows of opportunity for cell detection on ISFETs by using cell dynamics: (1) a net acidic pHe over time which may require real-time and long-term monitoring, and (2) rapid and short-term pHe changes in response to dynamic pHi fluctuations. This chapter will explore both long-term and rapid fluctuations in pH in response to cancer cell growth and mitosis, respectively. We first review the relevant impact of pH on mitosis entry on a single cell level.

6.1.1 Mitosis: an event coordinated by pH

The role of pH is not limited to cancer cells but has been deemed an orchestrator for signaling and timing of key cell functions in both unicellular and multicellular organisms [2, 7, 8]. In fact, a pHi range of pH 7.0-7.2 has been identified as the optimum for entry into the mitosis stage of the cell cycle in mammalian cells where a cell divides into two daughter cells [9]. Early evidence in sea urchin fertilized eggs, showed that H^+ efflux was necessary to allow cell division to proceed [10]. These early experiments indicated a complex mechanism for timing mitosis and subsequent work in mammalian cells showed that specific pHi ranges are necessary to enter and exit phases of the mitotic cycle [9].

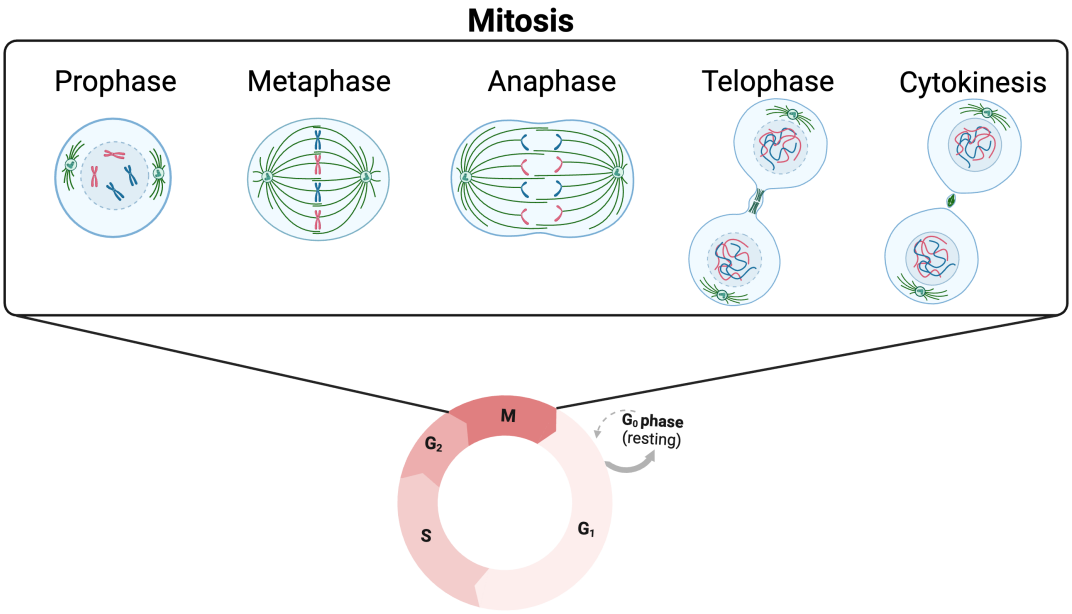


Figure 6.1: **Model summary of cell mitosis phases.** (Created in BioRender. Beykou, M. (2024) BioRender.com/a12m235).

The cell cycle of a single cell has 4 distinct phases known as: G1 (cell growth), S (DNA replication), G2 (more cell growth) and Mitosis. Mitosis takes place in stages whereby a single cell divides into two daughter cells. Stages of mitosis are summarised in Fig 6.1 [11]. Firstly, in *prophase* chromosomes condense and microtubule reorganization starts to take place for the formation of spindle fibers attaching to either poles of the cell. In *metaphase*, chromosomes align at the centre of the cell and attach to spindle fibers in preparation for *anaphase* where sister chromatids are pulled to opposite poles. In *telophase* the spindle disassembles and the nuclear envelopes re-form at either end of the cell as the cell membrane separates the two newly formed nuclei into two daughter cells in *cytokinesis*. Notably, all phases of the cell cycle are controlled by checkpoints, via Cyclin-Dependent Kinases (CDKs) interactions with activating cyclins, to ensure an even distribution of genetic and biological material in the final division [11].

Aberrant and rapid cell cycle progression is a key cancer cell behaviour [12]. Recent reports have shown dynamic fluctuations during the cell cycle and specifically G2/M pHi increase on the single cell level, using a pH-sensitive fluorescent label mCherry-pHluorin, corroborating previous evidence seen in cell populations [13]. Whilst the complex network of effectors of pH fluctuations in mitosis are incompletely understood, there is evidence for the role of pHi in driving pH-sensitive interactions of cyclins and CDKs, membrane depolarisation during mitosis and microtubule reorganisation [5, 9, 12]. An alkaline pHi, inherent in cancer cells, is likely to benefit cancer cell proliferation as it has been reported that an alkaline peak in pHi is found at

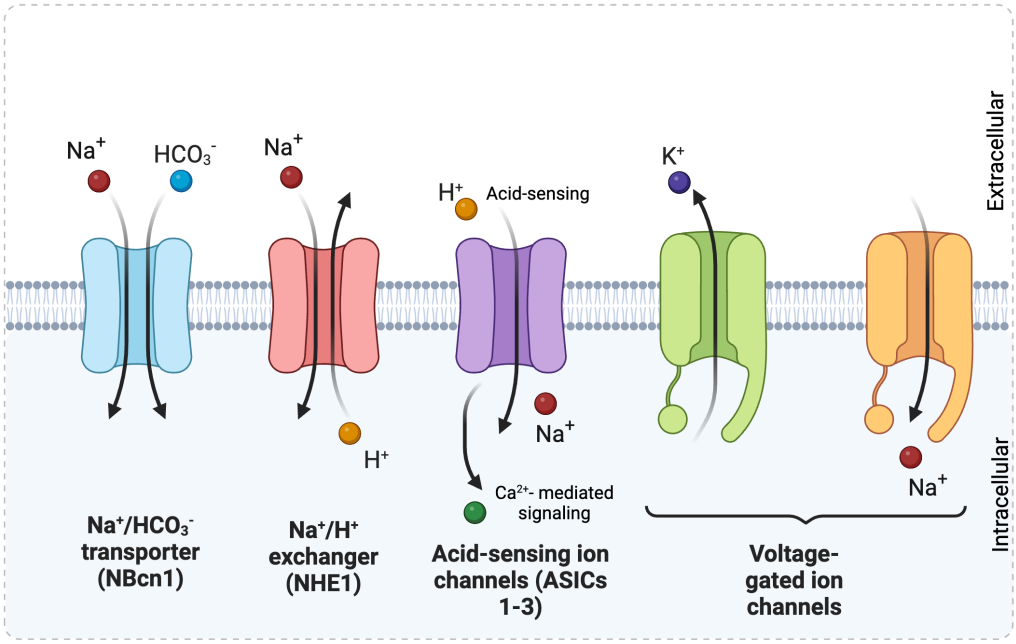


Figure 6.2: **Summary of key ion channel types in pH sensing in mitosis.**(Created in BioRender. Beykou, M. (2024) BioRender.com/g90g645).

the G2/M stage followed by a rapid acidification to stable pHi levels [2, 7, 8, 13]. Microtubule reorganisation and more specifically the formation of spindle fibres through polymerisation is favoured in alkaline pHi which is also sensitively timed to nuclear membrane breakdown [14, 15]. A pHi alkaline peak and subsequent drop by 0.3-0.5 pH has been suggested to coordinate microtubule reorganisation through net surface charge changes on the subunits making up microtubules, tubulins [16].

Furthermore, Putney and Barber (2003) reported a central role for NHE1 in pHi alkalinization at the G2/M checkpoint [17]. The study reported that fibroblasts deficient in NHE1 had lower expression levels of the cyclin-CDK pair regulating G2/M transition, cyclinB1-cdc2 (CDK1) [17]. Notably, cells were rescued with pHi alkalinization showing the regulation of pHi may act as a checkpoint for entry to mitosis. Additional loci have also been associated with a tight control on pHi such as H^+-ATPases and NBcN1, a Na^+/bicarbonate transporter. Both NHE1 and NBcn1 are commonly overexpressed in cancers types, such as breast cancer subtypes [18]. A study by Flinck et al. (2018), reporting knock-down of NHE1 or NBcn1 in breast cancer cells delayed entry into mitosis in a non-redundant fashion [19].

Concurrently, there is a significant interplay of pHi, pHe and other ion fluctuations, mediated by membrane potential changes (V_m), during mitosis [5, 9]. Membrane potential plays a role in migration, proliferation and cell volume control [5]. Specifically, depolarisation can be regarded as Na^+ influx, whilst hyperpolarization is a reflection of K^+ efflux. This is mediated by ion

channels, which can be pH-sensitive, voltage-gated or linked to H^+ efflux, such as NHE1. In mitosis, the cell membrane rapidly depolarises at G2/M [5, 9]. Studies have shown a significant feedback loop between pH-sensitive voltage-gated K^+ channels, $K_v1.5$ and $K_v11.1$ which are inhibited by an acidic pHe, as well as Na^+ channels, such as $Na_v1.5$ [5, 9, 20, 21]. Finally, intracellular Ca^{2+} concentrations are affected by an acidic pHe via Acid-Sensing Ion Channels (ASICs) [22, 23]. Despite an acidic pHe not having a direct effect on V_m in short-term exposure, and the network of different ion feedback loops being complex, the relevance of proton fluctuations during membrane depolarisation at G2/M can be appreciated [5].

6.2 Molecular Methods

Osteosarcoma cell line, U2OS CDK1 AS H2B-mCherry (identifier U2OS_as) were obtained from Helfrid Hochegger [24] . They were maintained in Dulbecco Modified Eagle Medium (DMEM) 1X 4.5g/L D-glucose, L-Glutamine, Pyruvate (Gibco) supplemented with 10% Fetal Bovine Serum (FBS) (Gibco) and 1% Penicillin/Streptomycin (P/S) (Invitrogen) at 37 °C, 5% CO_2. An experimental timeline for a single experiment is summarised in Figure 6.3. The assembled ISFET array was exposed to UV in a sterile tissue culture hood for 30mins prior to cell seeding. Cells were washed with PBS and trypsinized with 1ml 0.25% Trypsin-EDTA (Gibco) for 6 mins at 37 °C, 5% CO_2 incubator to allow detachment. The cells were resuspended in 5ml of complete DMEM media and centrifuged at 1500rpm for 5mins. DMEM media was aspirated and the pellet was resuspended in an appropriate volume. Cells were counted to $2x10^5$ cells/ml and 15ul of the cell solution were added to each cell well of an acrylic manifold fashioned onto the surface of the ISFET array. An equivalent 15ul of DMEM media was added to control wells. The array was covered with PCR tape and incubated in a 37 °C, 5% CO_2 incubator overnight. Media was replaced with DMEM with a final 2uM concentration of ATP analog inhibitor, 1NM-PP1 (AppexBio, CAT#B1299) and incubated for a further 20 hours. Wells were washed with 20ul of fresh DMEM thrice before adding 15ul fresh DMEM media and starting live ISFET measurements as in Figure 6.3.

6.3 Experimental setup and user interface

The Titan ISFET array (12mm x 8mm) was, glued, wire-bonded and epoxied with the standard operating procedure described in Chapter 4.3. A 4-well manifold was laser cut from a 3mm acrylic sheet with a working volume capacity of 15ul per well. An Ag/AgCl reference electrode was made using 3M KCl, a 0.03mm Ag wire under a voltage of 0.9V. Double-sided, transparent adhesive tape (Tesa 4980) was laser cut to the dimensions of the manifold and wells design.

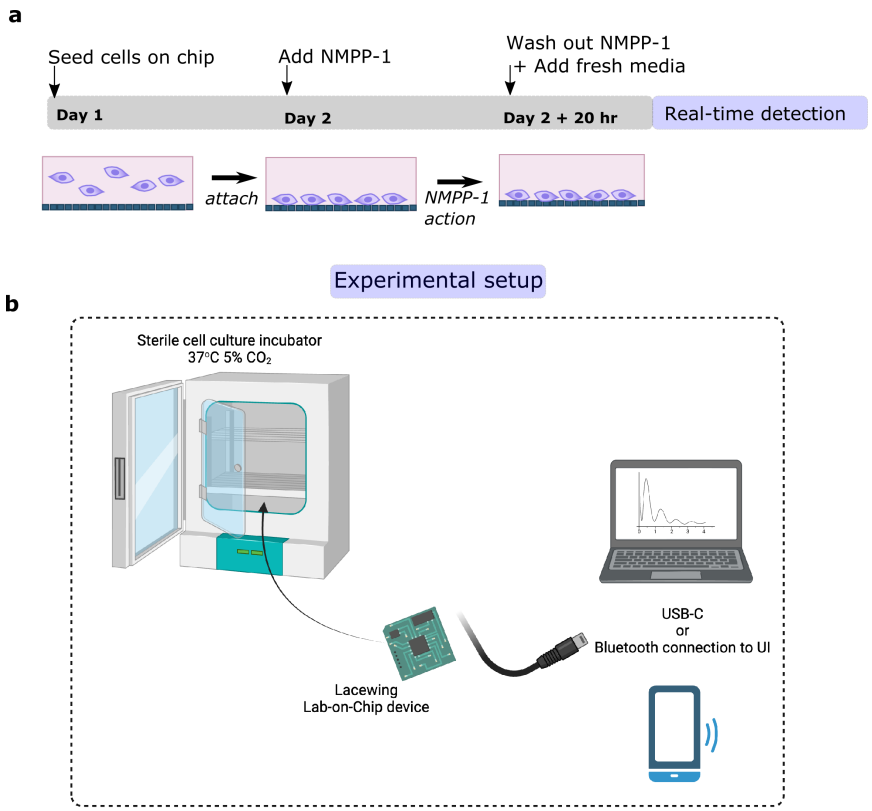


Figure 6.3: **Experimental timeline and setup.** (Figure (b) created in BioRender. Beykou, M. (2024) BioRender.com/j73h232).

A manifold was fitted with a cut Tesa tape. Assembly of the Titan PCB was carried out by looping the chloridized portion of the Ag/AgCl reference electrode through each of the wells on a manifold and soldering to the output of a wide-range on-board DAC (-12 V to 12 V). Using M1.6 x 5mm philips countersunk screws and corresponding M1.6 hexagon nuts the manifold was secured onto the Titan PCB. The cartridge is then fitted onto a connector with a 3D printed extension to connect to the Titan Lacewing motherboard. An in-house User Interface (UI) developed in the Georgiou group, Lacewing version 5, was employed as the UI for Titan to perform calibration and readout. The following calibration steps are carried out in the order depicted in Figure 6.4 which was developed by Lei Kuang and Dr. Nicolas Moser:

1. Init: checks electrical (expected I-V curve of MOSFET) and chemical (expected I-V curve of ISFET) activity of chip.

2. Acti_Pixel: evaluates each pixel's activity by variation in Vref (reference voltage) from maximum to minimum. Any pixel that responds to the Vref variation means that there is a value of Vref in which the pixel will be in range.

3. Cali_Vref: Vref calibration of each pixel by sweeping Vref values in increments of 100mV, counting pixels in range to determine the optimal Vref (V_{opt}). Subsequently sweep in increments of 10mV in the Vref optimal range $V_{opt} \pm 100$mV to determine $Vref_{optimal}$.

4. Eval_Pixel: Storing information for pixels active at any given Vref.

5. Cali_Vs: find and store optimal Vs per pixel.

6. Read_Time: store readout output in the format of rows (N) × columns (M) + additional parameters (A) multiplied by number of time frames (T).

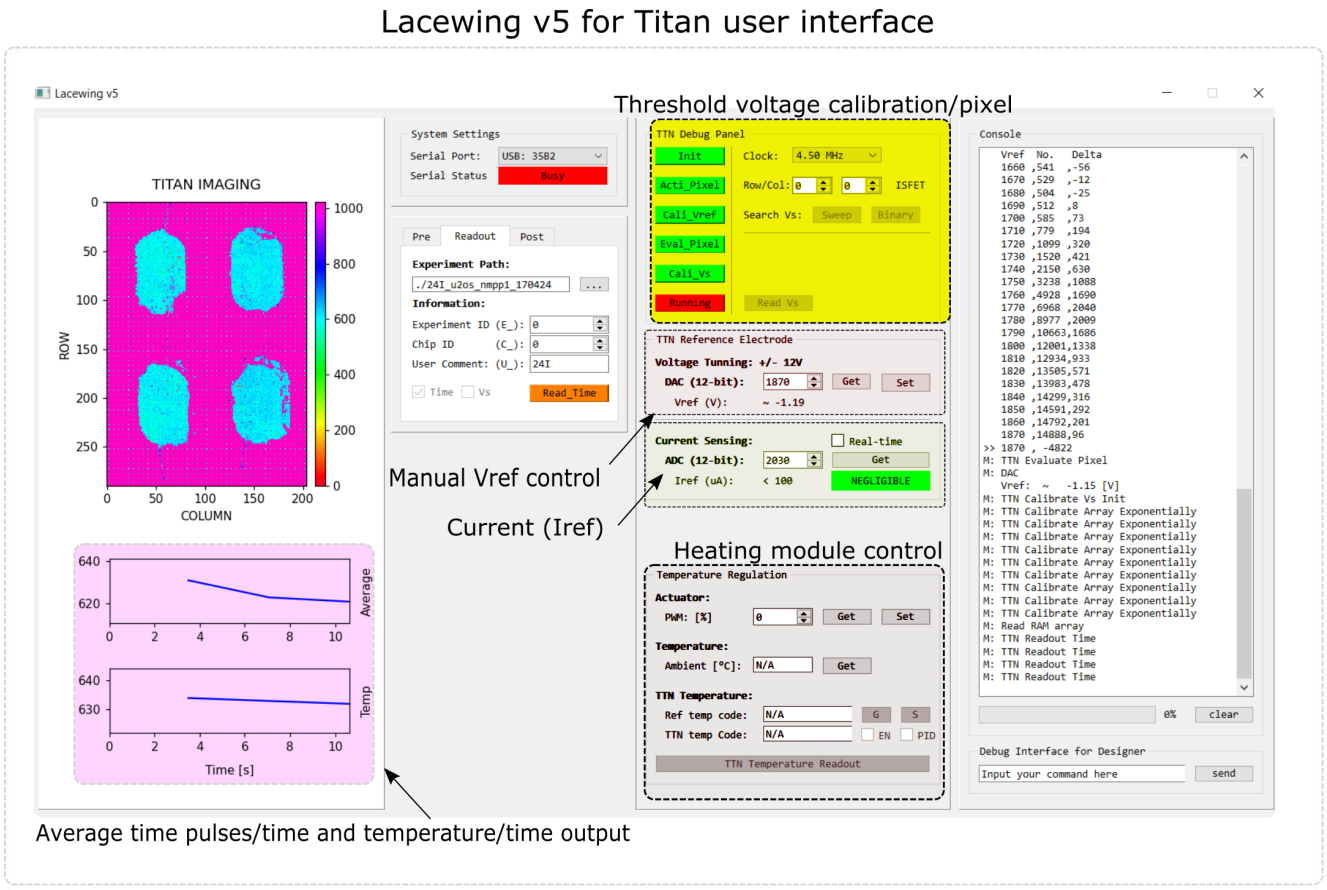


Figure 6.4: **Lacewing v5 for Titan user interface model.** Designed and implemented by Lei Kuang and Dr. Nicolas Moser.

6.4 Microscopy

High-throughput confocal microscopy of fixed samples Fully assembled ISFET arrays were fixed with 15ul 4%PFA for 10-12mins at ambient temperature. Wells were washed thrice with 15ul PBS. Screws and nuts used to maintain the manifold in place were removed. The manifold is maintained in place due to the adhesive strength of the double-sided tape. Arrays were immersed in PBS and turned upside down to remove any air bubbles from the well space. A rectangular sample holder I-3078 (Applied Scientific Instruments) with a stainless steel coverglass rectangular chamber (76 mm x 50 mm x 10.7 mm) (Applied Scientific Instruments) was

used for imaging. A 24mm x 50mm coverglass (Corning) was affixed to the coverglass chamber using lubricant and the setup was immersed in PBS where the chip was placed on the coverslip within the liquid. The setup was removed from PBS and dried externally. An appropriate volume of PBS was supplemented into the rectangular chamber to create a custom immersion stage for the chip. A basic spinning disc confocal microscope was used to perform imaging of each chip with a stitch setting to create a global image for each well.

Timelapse microscopy Unassembled ISFET arrays are used for timelapse microscopy to allow live cells visualisation with environmental control (humidified, 37 °C, 5%CO_2) on an Opera Phenix high-content confocal microscope. ISFET arrays are attached with a small amount of lubricant in a 96 well phenoplate (Revvity). Cells are seeded at the same concentration as in chip experiments per well and treated with the same experimental conditions and timeline as summarised in Figure 6.3. Subsequently, after washout, chips are overturned in clean wells and a circular agar plug is used to push them to the bottom of the well to maintain contact with media solution during the timelapse period. Signals Image artist software (Revvity) was utilised for image segmentation.

Light microscopy Light microscopy to obtain growth curves of NM-PP1 treated and untreated control cells on 96 well phenoplates utilised the Muvicyte high-throughput live cell imaging system (PerkinElmer). In-built software was used to calculate growth curve analyses during the timelapse period.

Energy-dispersive X-ray (EDX) spectroscopy EDX spectroscopy was used for the chemical analysis and mapping of the trypsin treated passivation layer of Titan ISFET arrays. Titan ISFET arrays were treated with 15ul per well 0.25% Trypsin-EDTA (Gibco) for 6 mins and subsequently washed twice with PBS and once with sterile H_2O to ensure no PBS crystallisation would occur in a vaccuum. Untreated controls were washed thrice with 15ul per well sterile H_2O and allowed to dry. All wells remained sealed with PCR tape at all times. Chips were then analysed using a Bruker QUANTAX EDX spectrometer and Tescan FIB-SEM Lyra3 XMU.

6.5 Data Analysis

A number of pre-processing steps are performed on raw time series data for each sensor to obtain representative metrics from a data output in time pulses:

- The raw time pulses output is an exponential relation to pH, compromising the possibility to compare outputs with different offsets, and introducing challenges in the interpretation of the output in the presence of drift. For this reason, the output is linearised to a signal with linear relation to pH with the transformation in (Eq. 6.1), where $x_{TP}(t)$ is the raw time pulses sensor output, $x_{LIN}(t)$ is the resulting linearised output, and a, b, c are conversion parameters that are geometry- and process-dependent.

$$x_{LIN}(t) = \frac{1}{b} \ln\left(\frac{x_{TP}(t)}{a}\right) + c \tag{6.1}$$

- Trapped charge compensation is performed by source voltage compensation [25] at chip-level and background-subtracting each sensor curve to ensure that all outputs start from the same initial value (therein referred to as output baseline) during post-processing.

- Active pixels are selected by a gain measurement through the reference electrode as those in contact with the solution, and that are in range throughout the duration of the experiment.

To explore the sensor response to the presence of cells on the insulating layer, the following metrics are employed:

Total drift The total drift during the experimental time window Δx is calculated as the cumulative end-point drift across the experiment:

$$\Delta x = x_{LIN}(end) - x_{LIN}(start) \tag{6.2}$$

This metric reflects the cumulative variation of sensor output, due to both drift (the slow monotonic variation of sensor output in time due to surface hydration) and the variation of solution pH [26]. The total drift is evaluated for each sensor in contact with the solution, and the distribution of values for each experiment is represented in a histogram.

Standard deviation The standard deviation σ of the sensor outputs across samples reflects the variation of the signal in time. As for the previous metric, the standard deviation is evaluated for each active pixel resulting in a distribution across time.

Peak analysis A peak in chemical readout was identified by calculating the mean derivative of all active pixels. Five samples before and 10 samples after the largest value in the signal were used to identify the peak spatially and in time.

6.6 Results & Discussion

6.6.1 Real-time detection of cancer cell acidification on CMOS ISFET array

To monitor extracellular acidification in real-time, cell culture of osteosarcoma cells, U2OS CDK1 AS, was carried out on ISFET arrays fitted with a 4-well acrylic manifold as part of a LoC handheld diagnostic device, therein referred to as Titan (Figure 3.5). Stable temperature and CO_2 levels were maintained by running experiments in a sealed cell culture incubator at 5% CO_2 and 37 °C. Figure 6.5 represents a sample output of a 4-well experiment where the top two wells (Well 0 & Well 1) were cultured in complete DMEM cell culture media only and the bottom two wells (Well 2 & Well 3) were seeded with U2OS cells and complete DMEM media. Temperature pixel readout indicated in blue in Fig. 6.5 (Top row) was confirmed to be stable at 0 mins onwards and thus considered not to have an effect on ISFET chemical readout change, Δx.

Dynamic chemical readout measurements were obtained for each pixel over a period of 200 mins. In a relatively short time period, a significant difference between initial amplitude at 0 mins and final amplitude at 200 mins is detected between media control wells and wells where cancer cells have been seeded (Fig. 6.5 (Middle row)). As previously mentioned, the overall change in chemical readout is represented by total drift over te experimental window as Δx. Fig. 6.6A shows that the total drift recorded for this experiment is more than double (x2.6) in cancer cell wells. Notably, cells with media establish a baseline with a mean variation of 22.57 mV and 14.76 mV, that differs considerably from the values of 47.07 mV and 50.99 mV of the experiments with cells. The variation represents an aggregate of the monotonic change introduced by drift, and the signal due to pH variation at the sensor interface.

The baseline pH change detected in control wells sets a baseline for any pH changes due to the bicarbonate buffering system of DMEM media coupled with any fluctuations of CO_2 levels in cell culture incubators which could lead to variable rates of CO_2 dissolution [27, 28]. Importantly, standard DMEM media is comprised of 3.7g/L sodium bicarbonate which is equivalent to 44mM of sodium bicarbonate, resulting in a pH buffering system considered to be in excess of the Henderson-Hasselbach equation (Equation 4.1). As a result the media is stably buffered and changes in solution pH can be attributed to cell phenotype. Notably, media composition breakdown is unlikely to affect pH levels in a short time period as in this experimental set.

Another interesting analysis emerges from the inspection of the standard deviation σ across the time series for each well. This metric brings to light the noise introduced by the presence of cells on the sensor surface. Mean standard deviation $\bar{\sigma} = 12.52$ and 12.99 for the cells experiments, in comparison to the values with media of $\bar{\sigma} = 6.45$ and 4.32, show that the presence of cells

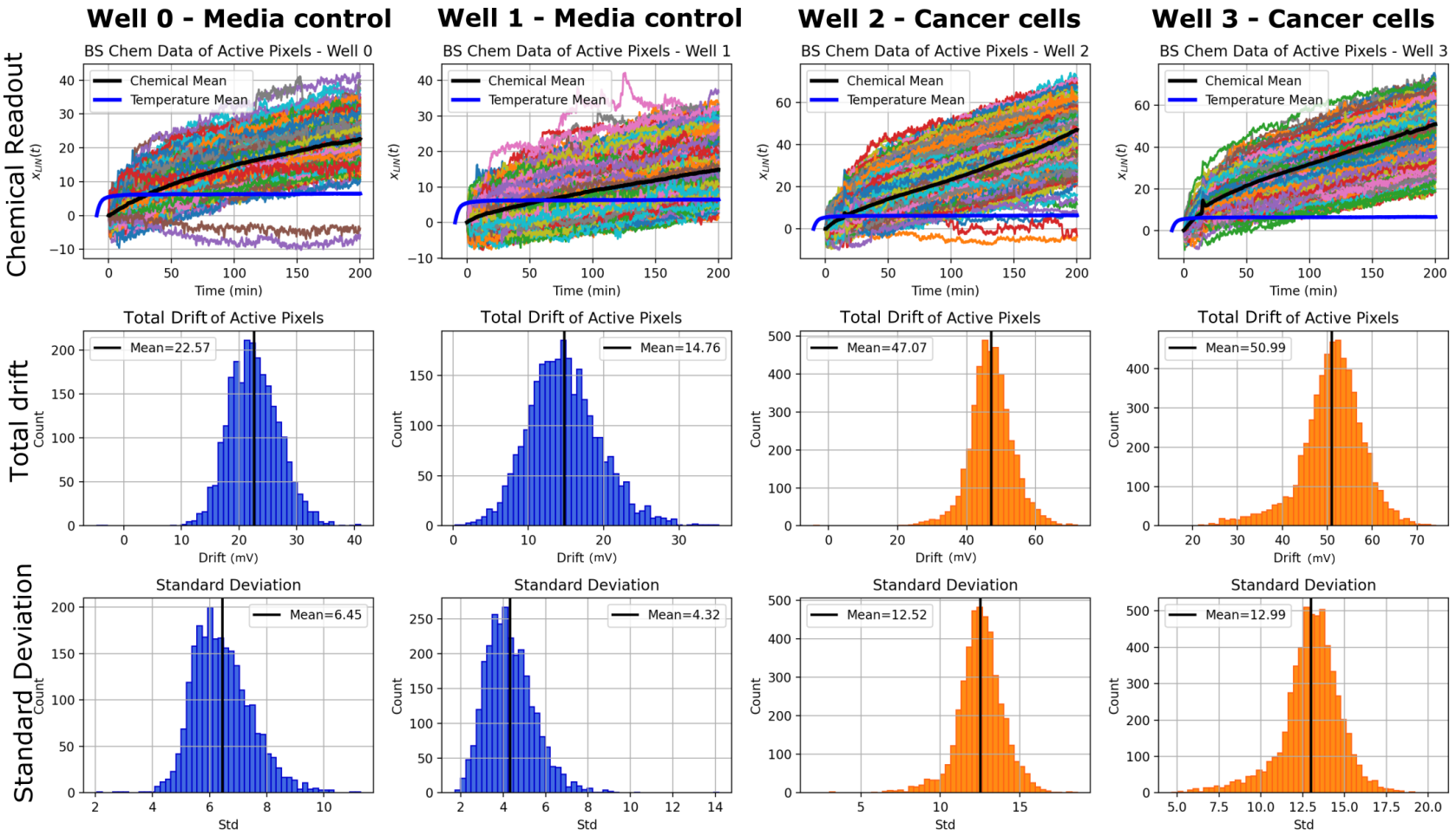


Figure 6.5: **Representative chemical readout measurements for osteosarcoma cells on Titan arrays.** Measurements obtained in DMEM (10% FBS, 1% P/S) cell culture media, as a baseline control, in Well 0 and Well 1, and U2OS CDK1 AS osteosarcoma cell line incubated with DMEM (10% FBS, 1% PS) cell culture media in Well 2 and Well 3 on an ISFET array comprised of 59,160 pixels. Each chemical pixel output over time is presented as a line graph. The mean chemical output of all active pixels at a time point is denoted in black and the mean output of temperature pixels is denoted in blue. **Middle row** – Total drift per pixel of active pixels for each well. Mean drift shown in black. **Bottom row** - Histogram of standard deviation and mean standard deviation of chemical output. N=2 for all conditions.

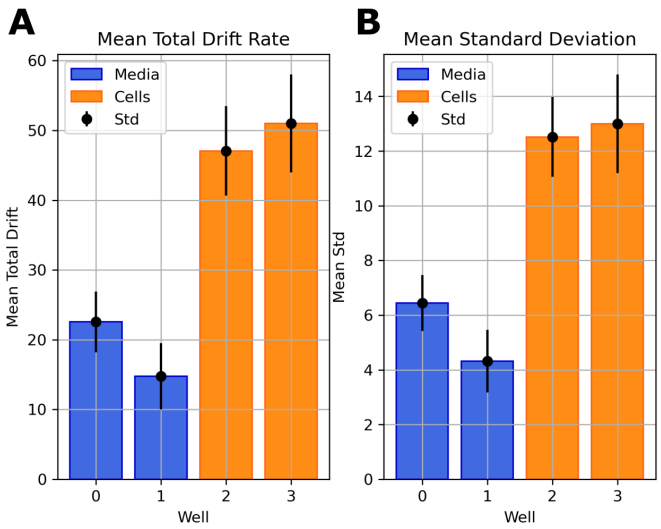


Figure 6.6: **Mean Total drift and mean standard deviation between media control and cancer cell wells on Titan. (A)** Bar plot of total drift of active pixels and error bars of each well (0-3). **(B)** Bar plot of mean standard deviation of active pixels and error bars of each well (0-3). Blue indicates wells incubated with DMEM (10% FBS, 1% P/S) cell culture media only. Orange indicates wells incubated with osteosarcoma cell line, U2OS CDK1 AS. N=2/condition

on the surface causes the time series outputs to exhibit much larger noise, most likely because of the cells living on the chip surface and moving physically on the array (Figure 6.6).

Cells were confirmed to be present solely in the wells originally seeded and absent from control wells indicating the efficiency of the acrylic manifold to contain cell movement on the ISFET array to dedicated areas. In addition, H2B, a core histone protein, labeled with mCherry (Ex/Em: 587nm/610nm) confirms an intact nuclear morphology at the experiment endpoint and confirms cell presence in relevant wells (Figure 6.7).

Repeat experiments showed the same behaviour in total drift and standard deviation as reported in Figure 6.8. A total of 7 ISFET chips with 4-well manifolds where two replicate conditions were used for these repeat experiments. A statistically significant difference in normalised total drift over the experimental time window in cell wells compared to control media wells was reported using an unpaired two-tailed Welch's t-test, assuming unequal standard deviation, which we report to be a true assumption ($p < 0.01$, $t = 6.198$) (Figure 6.8a and b). This result shows a significant difference in the overall change in chemical signal output due to pH change between media controls and wells seeded with cells. The assay timeframe is a total of 200 mins which is advantageously comparable to previous technologies in the field with sensitive and specific detectable changes between conditions [29–31]. Additionally, the current system is hands-free with no external perturbation during the experimental assay, which has previously presented both microfluidic and technical challenges to cell-ISFETs.

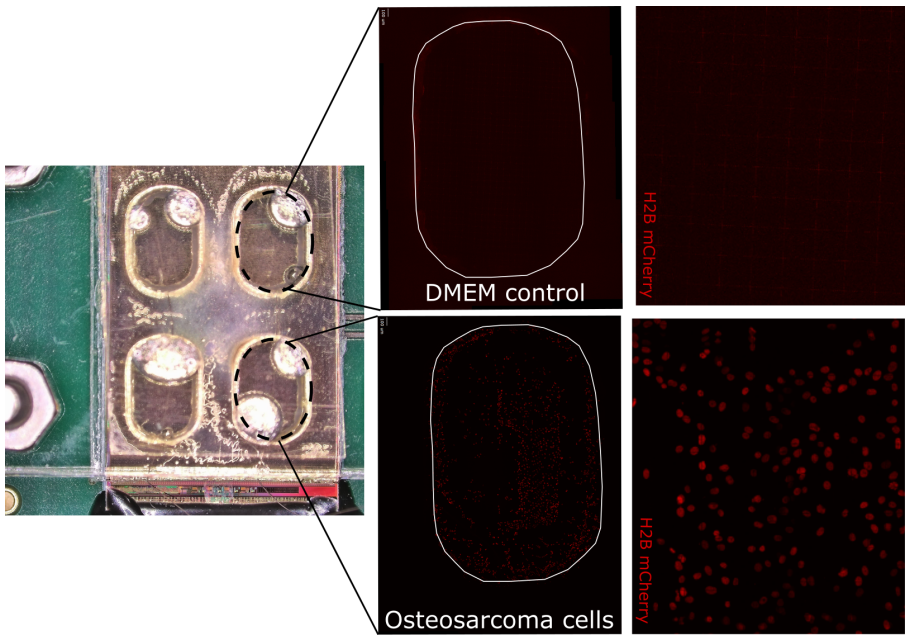


Figure 6.7: **Representative confocal microscopy images of nuclei labelled with H2B-mCherry in a 4-well manifold of a Titan ISFET array.**(Left) A 4-well manifold indicating the control and cell wells. (Right) Well outline at 5X magnification of media control (Top) and osteosarcoma cells labeled with H2B-mCherry (red) (Bottom) wells imaged on a basic spinning disc microscope. All wells were fixed with 4% PFA solution. Zoom magnifications of both wells shown nuclei shape and pixel architecture (Right).

We also report a significant difference for standard deviation between media controls and cell wells for repeat experiments using a Welch's corrected t-test ($p = 0.0072$, $t = 3.002$) (Figure 6.8c and d). The mean standard deviation per well is used as a metric to represent the added noise on the sensor, likely arising through cell adhesion, migration and stochastic movement. Previous work by Moser et al (2018) has characterized the electrical and chemical noise expected from the ISFET design. Notably, the contribution of thermal noise was found to be less significant in an ISFET than a MOSFET, which in our application where there is consistent temperature should only be significantly contributed to by any mammalian cell stochasticity.

6.6.2 Delineation of a mitotic peak detected on Titan ISFET arrays

A tightly regulated and controlled pHi, has been identified as a driving factor for mitotic entry in single cells. The assay design in this set of experiments benefited from a pH sensing duality. More specifically, the cell line U2OS CDK1 AS mCherry H2B (a kind gift from Helfrid Hochegger) harbours a mutation in CDK1 rendering it sensitive to analogs. Thus, cells are amenable to inhibition at the G2 phase of mitosis when treated with the ATP analog inhibitor NM-PP1. Under wild-type conditions, CDK1 needs to be phosphorylated by Cyclin B in order to overcome the G2/M checkpoint and enter mitosis. The inhibition of this interaction results

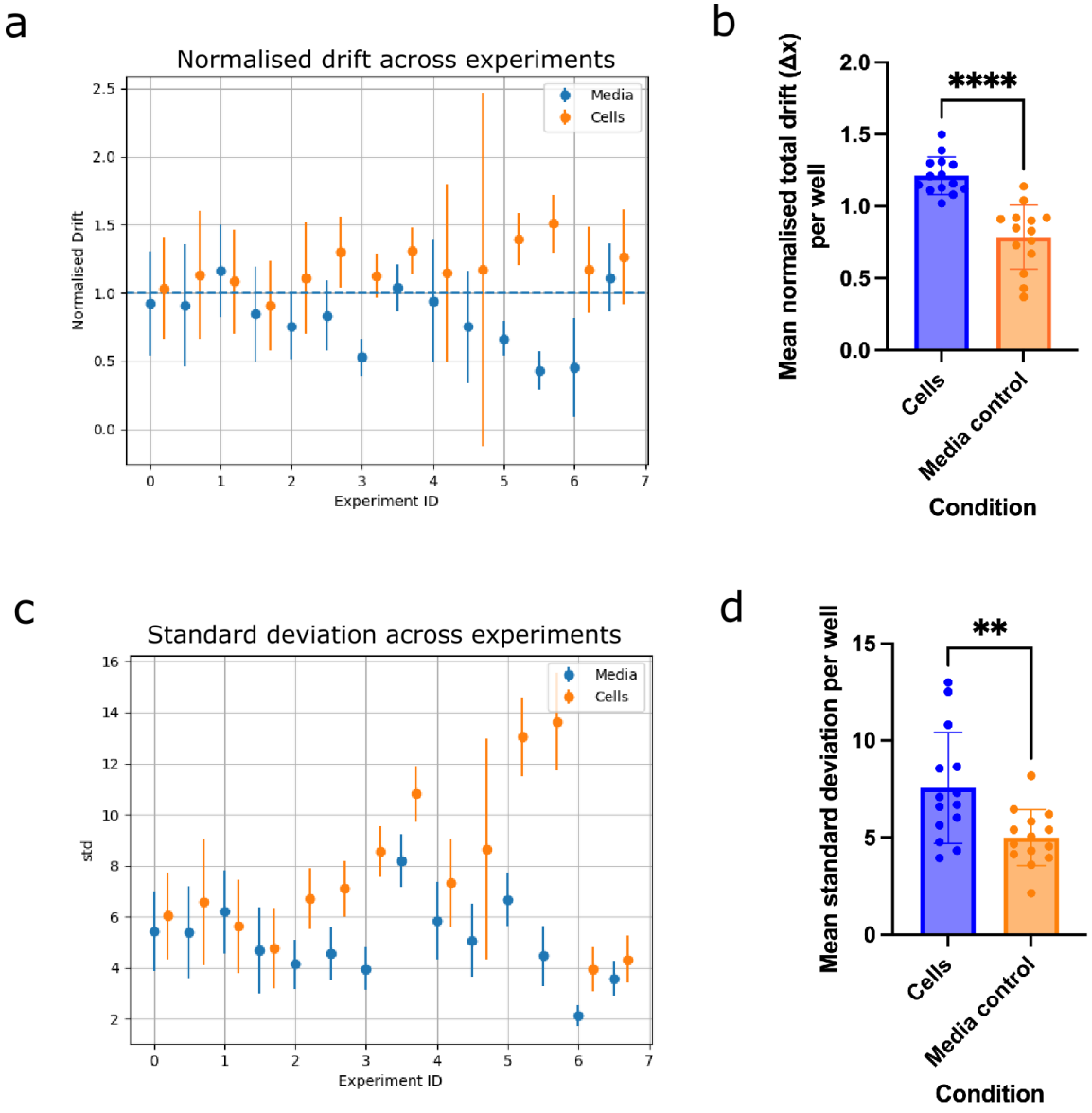


Figure 6.8: **Mean normalised drift and standard deviation between cancer cells and media cultured on Titan CMOS ISFET arrays.** **(a)** Mean normalised drift and error bars between cell and media control wells **(b)** Bar plot for mean normalised drift per well for cells and media control conditions. **(c)** Standard deviation and error bars representing noise across experiments for cells and media controls. **(d)** Bar plot for mean standard deviation per well for cells and media control conditions. Unpaired, parametric t-test with Welch's correction discovery indicated by asterisk (*). N= 7 independent ISFET array experiments and n=2 for each condition on a single experiment.

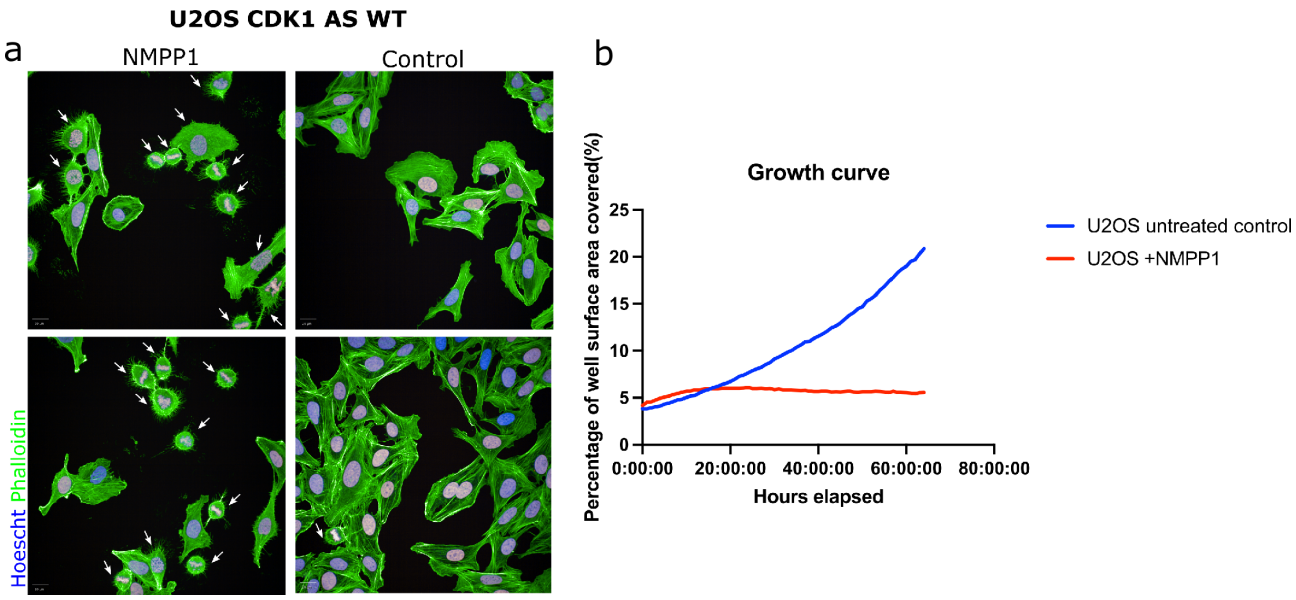


Figure 6.9: **Growth and mitotic stage of U2OS CDK1 AS cells on 2D plastic treated with ATP analog inhibitor NM-PP1 versus untreated controls.(a)** (Left panel) Confocal microscopy of a fixed timepoint of cells treated for 20 hours with NM-PP1 and released through washout. Mitotic cells indicated by white arrows. (Right panel) Confocal microscopy of a fixed timepoint of untreated control U2OS CDK1 AS cells. **(b)** Growth curve over 72 hours of NM-PP1 treated U2OS CDK1 AS cells as compared to untreated controls.

in the cell population being held at the G2/M checkpoint which coordinates the cell cycle stage of the population. Upon removal of the inhibitor, cells enter the mitosis stage in a concerted fashion. As a result, by releasing the cells into a coordinated mitosis prior to chemical voltage readout, we are able to record extracellular acidification on the CMOS ISFET array but also what is likely a "mitotic" peak as the start of significant ionic and membrane changes associated with mitosis.

We firstly report the assay design in 2D plastic cultureware to verify growth inhibition when U2OS CDK1 AS cells are treated with NM-PP1 and a coordinated entry into mitosis at a fixed timeframe when released from inhibition. Figure 6.9(a) (left) shows that with release from NM-PP1, cells are captured at the prophase or metaphase stage of mitosis at a fixed timepoint. On the other hand, mitotic cells are not typically recorded in a single timeframe in untreated controls wells (Figure 6.9(a)(right). Additionally, we confirm inhibition of mitosis by assessing growth over a period of 72 hours where NM-PP1 treated cells showed growth arrest as compared to untreated controls (Figure 6.9(b)).

To evaluate whether we could detect a change at the start of the mitotic event, the NM-PP1 release assay was performed on Titan CMOS ISFET arrays as part of the portable Lacewing device. The timeframe of this assay was allowed to reach 200 mins despite the peak expected to occur in the first 30-40 mins after washout, which along with calibration steps corresponds to 10-20 mins in chemical readout, in order to investigate dual detection of both a mitotic

event as well as extracellular acidification of cells over time. Importantly, the assay requires no perturbation during readout making it easy to perform on the PoC level. Herein we report a case study, previously shown in Section 4.6.1 to successfully differentiate between cell and control wells on the basis of net pHe change.

Figure 6.10(a) reports the first 40 mins of the experiment where a distinct peak in chemical readout is recorded in wells seeded with cells which is notably absent in media control wells. The orange line graph indicates the mean active pixel output ($x_{LIN}(t)$) over time for every 10 samples in order to better capture the trend created by this peak. Following on, the mean derivative of all active pixels in a well is evaluated to locate the peak in time and space (Figure 6.10(b)). The absence of a peak in control wells is confirmed. It is also noteworthy that with a magnification of the peak signal in time, the average peak in active pixels is shown to happen at the same time between 15.4 -15.6 mins (Figure 6.10(c)). In order to spatially visualise the active pixels in time, the pixel activity is shown by evaluating the largest value in the signal 5 samples before the time of peak and 10 samples after. Figure 6.11 illustrates the pixel activity which appears to be concentrated in Well 3 at approximately 15.6 mins whereas a later response is evident in Well 2, whilst the values in Well 0 and 1 hold no significance as no peak is seen in prior chemical readout analysis. The added active pixel area seen between wells 2 and 3 could be a sign of excess humidity. This may affect the resultant signal and result in signal propagation from one well to another although a signal delay would be expected in that case which is not recorded. Notably, the frame rate of 3s may also be masking a signal delay. In addition, we ensure that no reference electrode artefacts might occur as the two cell wells are found at opposite end of the reference electrode, leading us to question whether signal propagation should have been noted in control wells if in fact it was true.

In order to investigate whether this level of coordination in mitosis was plausible and to capture the mitotic event happening on chip we performed live timelapse microscopy using a high-content screening confocal microscope known as the Opera Phenix with controlled environmental conditions (humidified, 37 °C, 5% CO_2). Figure 6.12(a) illustrates the first four timepoints of timelapse where chromosome condensation and nuclear envelope breakdown are highlighted by white arrows. More specifically, in a single field of view corresponding to an area on the chip, cells are predominantly seen going through the same stage in mitosis. Metaphase entry and the assay endpoint (timepoint 31) is shown in Figure 6.12(b) where we show doubling of the cell population upon mitosis completion. To ensure the validity of this assay, a growth curve was used to confirm rapid growth in NM-PP1 treated cells versus untreated control cells under timelapse microscopy (Figure 6.12(c)).

Few studies have investigated pHe values in the cell cycle, however, evidence has shown that a specific range of both pHe and pHi is required to enter and exit mitosis on a population level due to their interconnected control through transporters such as NHE1. Single cell spatiotemporal

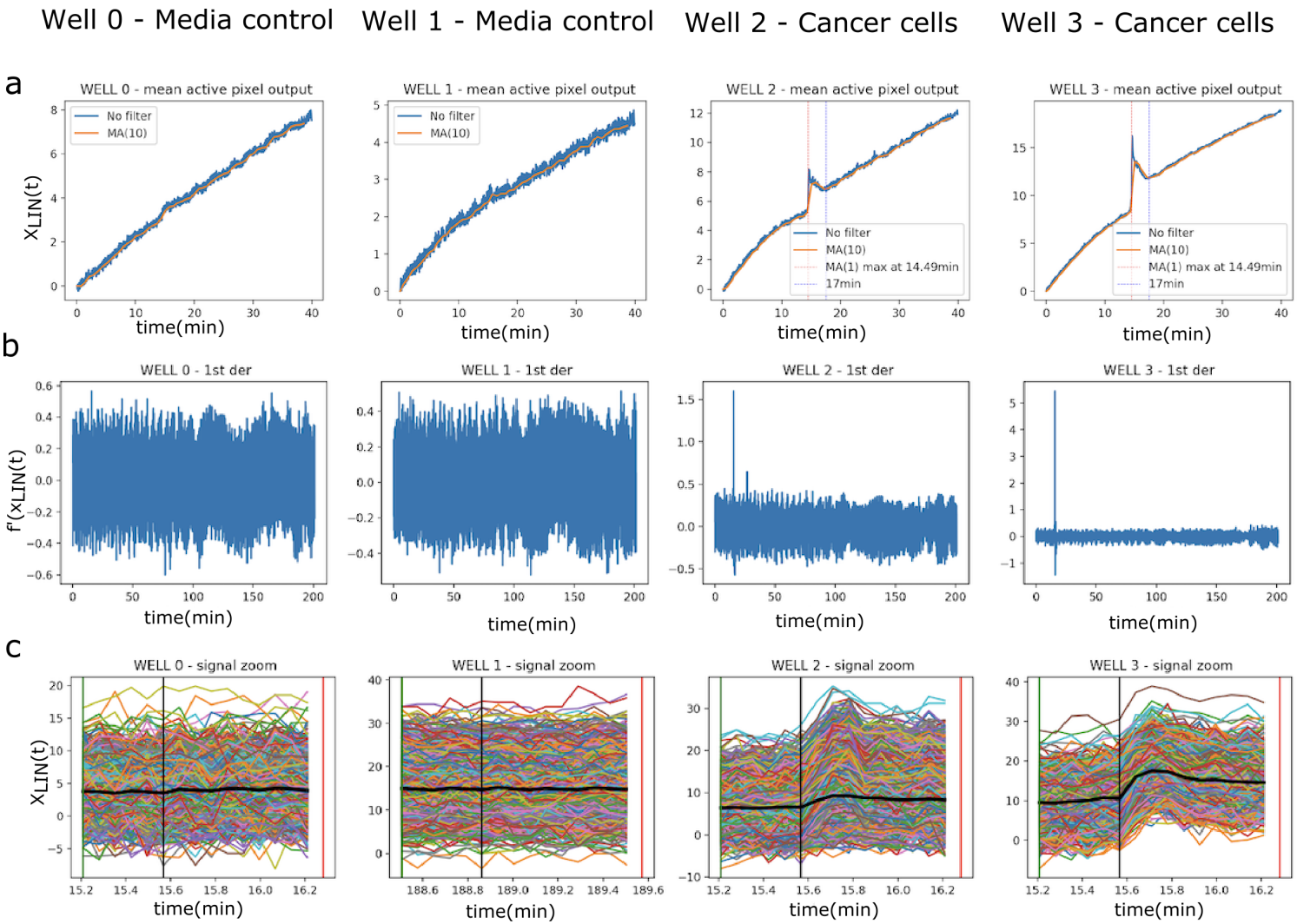


Figure 6.10: **Case study for the detection of an acidification peak at mitotic entry.** (a) Average, linearised chemical readout of active pixels per well (blue) and average of every 10 samples (orange). **(b)** Derivative of chemical readout of active pixels to identify maximum peak.**(c)** Magnification of active pixel chemical readout to show 5 samples before and 10 samples after maximum peak signal as shown in a vertical black line.

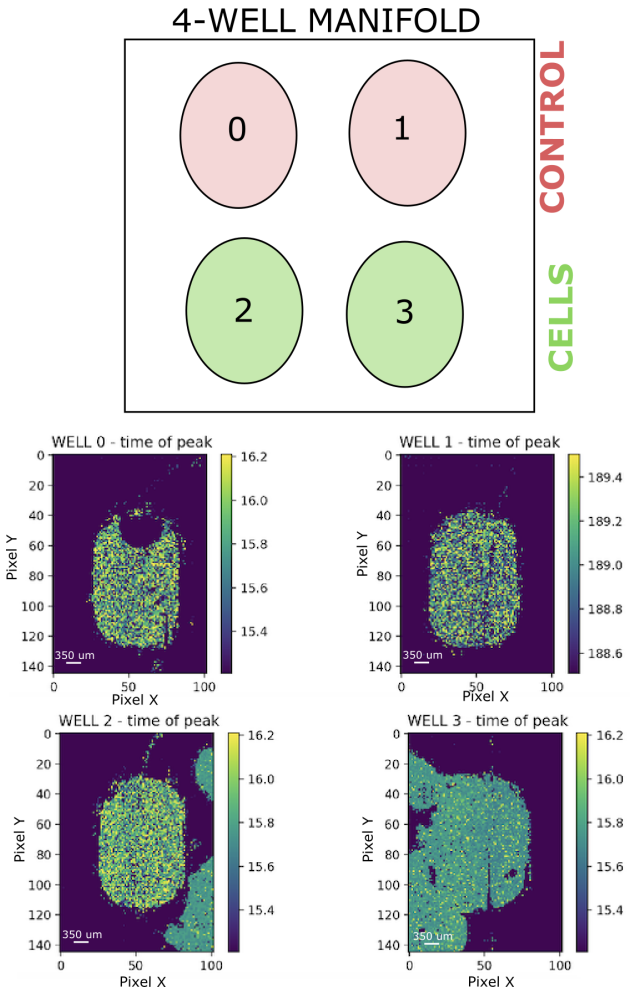


Figure 6.11: **Spatiotemporal layout of the time of peak in each Titan well.** (Top) A 4-well manifold layout where red indicates media controls and green indicates treated cells. (Bottom) Corresponding spatial mapping of active pixels at the time of peak in each well with volume capacity of 20 μl. Scale in pixels where each pixel is 35μm.

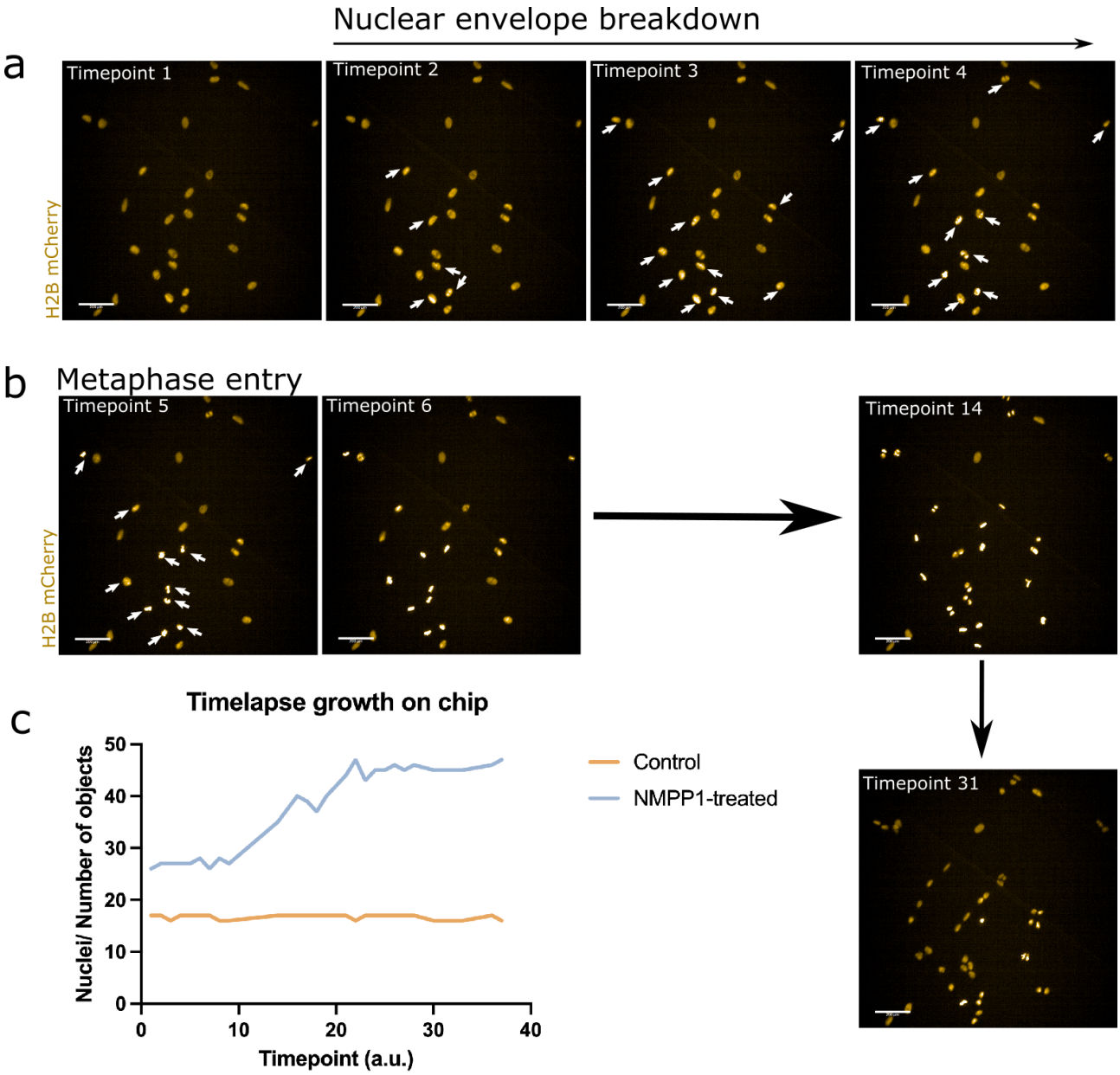


Figure 6.12: **Timelapse microscopy of NM-PP1-treated U2OS CDK1 AS H2B mCherry on a Titan ISFET array. (a)** Timepoints 1 to 4 of a field of NM-PP1-treated cells on chip where cells entering prophase are identified through chromosome condensation as identified by H2B mCherry (yellow) and shown by white arrows. Nuclear envelope breakdown is expected to occur during this time. **(b)** Timepoint 5 and 6 where metaphase entry as chromosome alignment at the centre is identified by H2B mCherry intensity. At timepoint 14 cells have undergone mitosis and are shown to have doubled in nuclei. Timepoint 31 indicates the assay endpoint where cells have doubled and re-adhered to the chip interface.**(c)** Number of nuclei per field at each timepoint in control cells which have remained untreated and NM-PP1 treated cells showing rapid doubling of number of nuclei in NM-PP1 treated and released cells. Scale bar = 200 μm.

study of pH in the cell cycle has revealed a key role for pHi in timing each phase of the cell cycle. A recent study by Spear and White (2023) using a genetic pH sensor in a lung cancer model showed that pHi became more alkaline in the 7 hours prior to prophase [13]. Rapid acidification was seen during mitosis entry and subsequent stabilisation of pH values. The same dynamic fluctuation was not found in non-dividing cells [13]. In our model the assay timeframe can succinctly explain the discrepancies from single cells as we are measuring pHe on a population level in a population which has doubled over the timecourse of the assay hence leading to net pHe acidification. Whilst this study does not explain the "acidification peak" recorded at mitotic entry, considerations of rapid microtubule re-organization and nuclear envelope breakdown corroborate potential evidence for the pHe peak seen in ISFET chemical readout via a reflection of nuclear pH (pHn) in a narrow window [32].

Microtubule dynamics play a particularly key role at the prophase stage of mitosis [15, 16]. Evidence for microtubule depolymerisation and hence an abrupt decrease in microtubule polymers transiently co-occurring with nuclear envelope breakdown has previously been reported [15]. The turnover rates of microtubules which reorganise to attach to centrosomes during spindle assembly have been shown to be strikingly rapid after nuclear envelope breakdown at rates of 0.73 ± 0.4 mins [15]. These microtubule changes are closely coupled to pHi, and as a result pHn, with studies reporting a linear relationship between pH and the charge on tubulin monomers whereby an alkaline pHi is required to start spindle assembly [16]. Furthermore, evidence of pHn in single cells showed pHn alkalinisation from entry into mitosis up until exit [32]. In this study, a nanowire waveguide with a pH-sensitive luminescence tip and connected to spectrometer was able to measure pH at specific cell compartments such as the nucleus [32]. The authors revealed a rapid change in pH between the G2 checkpoint and entry into prophase whereby an average change from pH 6.92 to 6.97 was recorded, respectively [32]. In the nucleus, pHn continued to rise gradually until telophase where pHn slightly decreased to homeostatic levels [32]. Notably, the authors attributed the likely changes in pHn dynamics to nuclear envelope breakdown at the prophase stage. In this scenario, we can hypothesize the transient connection of pHn and pHe, accompanied with nuclear envelope breakdown and abrupt tubulin charge changes leading to microtubule reorganisation and continued mitotic entry which is summarised in Figure 6.13.

Finally, we considered whether the mechanical forces of cell morphology during mitosis could be contributing to the "acidification peak" seen in our datasets. Work by Voelker and Fromherz (2006) investigated the noise in voltage arising from nerve cell adhesion on a transistor. It was suggested that thermal noise due to resistance could be used to study the electrical effects associated with cell adhesion. They found that mechanical changes on the outer adherent membrane in contact with the passivation layer did not contribute to extracellular voltage noise readings [33].

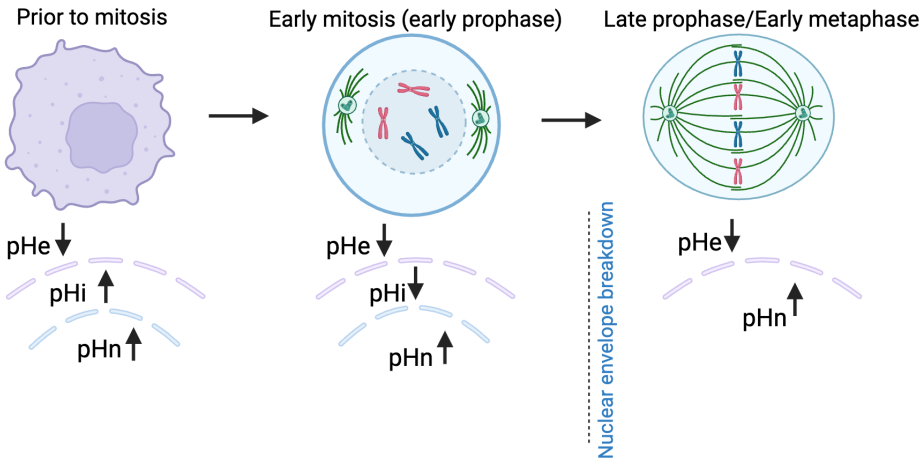


Figure 6.13: **Summary of pHe, pHi and pHn changes upon nuclear envelope breakdown from early prophase to late prophase/early metaphase stage of mitosis.**(Created in BioRender. Beykou, M. (2024) BioRender.com/j54d751).

6.6.3 Towards sustainability in LoC: characterisation of the effect of standard cell trypsinization protocols on ISFET passivation surface

The application of Moore's law to the semiconductor industry has brought environmental concerns as much as it has revolutionised microelectronic advancements by making manufacturing inexpensive. The raw materials utilised, manufacturing process and packaging microchips have led to increased chip production rates where safe disposal can be challenging [23]. Concurrently, due to the nature of point-of-care diagnostic testing and inexpensive chip production, many tests or components have become single-use. In research, similar limitations persist, with additional restraints on the availability of custom chip designs and materials. In principle, the environmental impact of a microchip remains net neutral until disposal where water and soil toxicity due to metal leakage can become a problem [23]. For this purpose, we enquired whether the passivation surface of "Titan" ISFET arrays were affected after standard trypsinization protocols where electrical and chemical activity of the aforementioned chips remained functional.

The lifecycle of both "Titanicks" and "Titan" ISFET arrays has been tested in repeat experiments for both DNA and RNA LAMP experimentation, however due to the sterile nature of cell culture, single culture chips are preferred. SEM/EDX spectroscopy was used to qualitatively characterise the chemical composition of trypsin-treated, H_2O control and untreated chip surfaces.

Figure 6.14a(i) shows the spectrogram obtained from H_2O control-treated chips where a hafnium and silicon energy peak are recorded at 1.5 and 2.5 cps/eV. The SEM image of the surface where the reference electrode remains attached and mapping of the elements on the surface shows a

relatively uniform distribution on the ISFET surface (Figure 6.14a(ii) and (iii)). The trypsin-treated passivation surface spectrogram reports both hafnium and silicon peaks, however with silicon at a relatively lower cps/eV (1.8cps/eV) as compared to control treated surfaces (Figure 6.14b(i)). Upon inspection of the elemental distribution, the reference electrode area appears to be covered in carbon, which may arise from cellular material left behind and fixed onto the reference electrode (Figure 6.14(b)(iii) and (iv)). The crystallisation seen on the SEM image in Figure 6.14(b)(ii) has previously been recorded when hydrated cells are exposed to a vacuum. To ensure the passivation layer spectrogram was indicative of an untreated chip, an area close to the chip edge that had remained unexposed to H_2O or trypsin as it was covered by a manifold, was used as a reference (Figure 6.14(c)). Both hafnium and silicon signals were recorded on a line scan with consistent readings with distance from the edge.

These results indicate the potential for long-term culturing and re-usability of "Titan" chips for cell culture conditions as the 0.25% trypsin-EDTA does not have a significant effect on the ISFET passivation layer through high adsorption or "stripping", or an impact on electrical/chemical activity. Reference electrode degradation and imprinting on the chip surface, suggests that the removal of the silver wire may yield more favourable conditions in future experiments and ensure appropriate biasing when utilising the same chip post-trypsin treatment. In principle, the lifecycle of this LoC device is not single use providing a sustainable avenue for cell culture on a semiconductor chip.

6.7 Summary

This chapter, adapted a dual readout assay to detect pHe acidification over time and mitotic entry of mammalian cells on CMOS ISFET arrays integrated on a handheld PoC device, known as Lacewing. To our knowledge, this is the first assay to evaluate coordinated mitosis of a population on an ISFET array and record a total pHe change with population doubling. In addition, we evaluated standard cell culture protocols on chip, showing how these protocols can be adapted for portable and inexpensive LoC technologies. The key outcomes of the chapter are summarised as:

1. Development of protocol for pHe acidification detection in adherent cell population with no external perturbation or interface post-processing on a CMOS ISFET array with 59,160 sensors.
2. Rapid detection of a "mitotic acidification peak" upon nuclear membrane rupture in a mitotically coordinated cell population on chip.
3. Confirmation of physiologically relevant cell attachment and morphology on CMOS ISFET arrays.

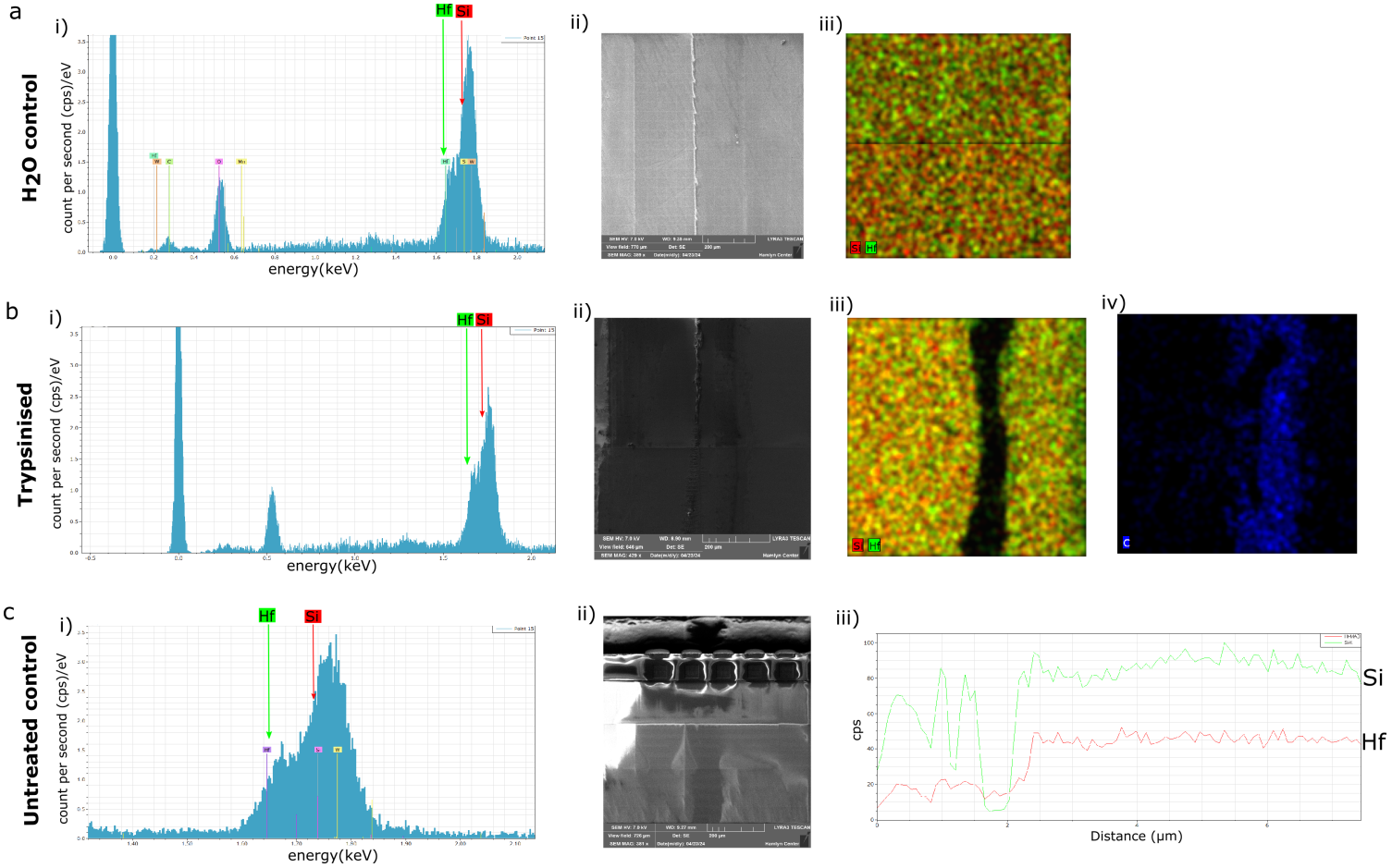


Figure 6.14: **Characterisation of hafnium and silicon elements at the Titan passivation surface after trypsinization.(a)**(i) EDX spectrogram for chip treated with water as a control. (ii) SEM image of the area used for elemental mapping. (iii) Chemical mapping of hafnium and silicon elements on the chip surface. **(b)**(i) EDX spectrogram for chip treated with 0.25% Trypsin-EDTA as a standard cell dissociation protocol. (ii) SEM image of the area sued for elemental mapping. (iii) Chemical mapping of hafnium and silicon elements. (iv) Chemical mapping of carbon over the area corresponding to the reference electrode on the chip surface. **(c)**(i) EDX spectrogram for an untreated chip edge. (ii) SEM image of chip edge. (iii) Line scan of hafnium and silicon elements with distance from the chip edge.

4. Compatibility of Titan chips with standard cell culture protocols for sustainability and re-usability of resources.

Despite our progress in reliable and repeatable detection of mammalian cells on chip, future work should focus on the adaptation of the protocols presented to other cell types, including epithelial cells with a direct comparison on tumorigenic cells in order to characterise the extent of pHe acidification in different cell types. Mammalian cell variability will play a meaningful role in the adaptability of the aforementioned protocols on chip as other cancer cell lines are known to harbour different cell cycle mutations, different morphology and proliferation rates. Secondly, one of the current limitations in our setup is the use of an incubator to maintain 5% CO_2 conditions. Whilst a humidifed environment and 37°C is available to use with sensitive control of a Peltier module placed below the bio-chip, as well as Bluetooth connection for remote data collection, a tabletop incubator may be necessary to maintain CO_2 control in a fully portable setup. To this end, a pump and flow system could allow for drug treatments during chemical readout without external disruption to the LoC system. As we extend into 6-well and 10-well manifolds, integrated microfluidics to avoid manual perturbations will be an important step to a reproducible PoC device. Finally, further work is required to fully characterise the stage of mitosis and subsequent molecular changes which occur to form a "mitotic peak", with possible drug treatments inhibiting ion channels for Na^+ and H^+. This will aid in developing a complete profile of the ion changes which we could extensively detect on CMOS ISFET arrays during cell mitosis using additional ion-sensitive membrane deposition on chip.

References

[1] B. P. Mahoney et al. "Tumor acidity, ion trapping and chemotherapeutics: I. Acid pH affects the distribution of chemotherapeutic agents in vitro". In: *Biochemical Pharmacology* 66.7 (Oct. 2003), pp. 1207–1218.

[2] B. A. Webb et al. "Dysregulated pH: A perfect storm for cancer progression". In: *Nature Reviews Cancer* 11.9 (Sept. 2011), pp. 671–677.

[3] V. Estrella et al. "Acidity generated by the tumor microenvironment drives local invasion". In: *Cancer Research* 73.5 (Mar. 2013), pp. 1524–1535.

[4] R. A. Gatenby and R. J. Gillies. "Why do cancers have high aerobic glycolysis?" In: *Nature Reviews Cancer* 4.11 (Nov. 2004), pp. 891–899.

[5] Z. Pethő et al. "pH-channeling in cancer: How pH-dependence of cation channels shapes cancer pathophysiology". In: *Cancers* 12.9 (Sept. 2020), pp. 1–37.

[6] J. Srivastava, D. L. Barber, and M. P. Jacobson. "Intracellular pH sensors: Design principles and functional significance". In: *Physiology* 22.1 (Feb. 2007), pp. 30–39.

[7] P. Swietach et al. "The chemistry, physiology and pathology of pH in cancer". In: *Philosophical Transactions of the Royal Society B: Biological Sciences* 369.1638 (Mar. 2014).

[8] K. A. White, B. K. Grillo-Hill, and D. L. Barber. "Cancer cell behaviors mediated by dysregulated pH dynamics at a glance". In: *Journal of Cell Science* 130.4 (Feb. 2017), pp. 663–669.

[9] M. Flinck, S. H. Kramer, and S. F. Pedersen. "Roles of pH in control of cell proliferation". In: *Acta Physiologica* 223.3 (July 2018), e13068.

[10] J. D. Johnson, D. Epel, and M. Paul. "Intracellular pH and activation of sea urchin eggs after fertilisation". In: *Nature* 262.5570 (1976), pp. 661–664.

[11] H. K. Matthews, C. Bertoli, and R. A. de Bruin. "Cell cycle control in cancer". In: *Nature Reviews Molecular Cell Biology* 23.1 (Sept. 2022), pp. 74–88.

[12] D. Hanahan and R. A. Weinberg. "Hallmarks of cancer: The next generation". In: *Cell* 144.5 (Mar. 2011), pp. 646–674.

[13] J. S. Spear and K. A. White. “Single-cell intracellular pH dynamics regulate the cell cycle by timing the G1 exit and G2 transition”. In: *Journal of cell science* 136.10 (May 2023).

[14] T. Koltai, R. A. Cardone, and S. J. Reshkin. “Synergy between low dose metronomic chemotherapy and the pH-centered approach against cancer”. In: *International Journal of Molecular Sciences* 20.21 (Nov. 2019).

[15] Y. Zhai et al. “Microtubule dynamics at the G2/M transition: Abrupt breakdown of cytoplasmic microtubules at nuclear envelope breakdown and implications for spindle morphogenesis”. In: *Journal of Cell Biology* 135.1 (Oct. 1996), pp. 201–214.

[16] L. J. Gagliardi and D. H. Shain. “Is intracellular pH a clock for mitosis?” In: *Theoretical Biology and Medical Modelling* 10.1 (2013), p. 8.

[17] L. K. Putney and D. L. Barber. “Na-H Exchange-dependent Increase in Intracellular pH Times G2/M Entry and Transition”. In: *Journal of Biological Chemistry* 278.45 (Nov. 2003), pp. 44645–44649.

[18] E. Boedtkjer et al. “Contribution of Na+,HCO3–cotransport to cellular pH control in human breast cancer: A role for the breast cancer susceptibility locus NBCn1 (SLC4A7)”. In: *International Journal of Cancer* 132.6 (Mar. 2013), pp. 1288–1299.

[19] M. Flinck et al. “The acid-base transport proteins NHE1 and NBCn1 regulate cell cycle progression in human breast cancer cells”. In: *Cell Cycle* 17.9 (May 2018), pp. 1056–1067.

[20] T. K. Leslie et al. “A novel Nav1.5-dependent feedback mechanism driving glycolytic acidification in breast cancer metastasis”. In: *Oncogene* 43 (June 2024), pp. 2578–2594.

[21] L. Gillet et al. “Voltage-gated sodium channel activity promotes cysteine cathepsin-dependent invasiveness and colony growth of human cancer cells”. In: *Journal of Biological Chemistry* 284.13 (Mar. 2009), pp. 8680–8691.

[22] M. Glitsch. “Protons and ca2+: Ionic allies in tumor progression?” In: *Physiology* 26.4 (Aug. 2011), pp. 252–265.

[23] A. Villard, A. Lelah, and D. Brissaud. “Drawing a chip environmental profile: Environmental indicators for the semiconductor industry”. In: *Journal of Cleaner Production* 86 (Jan. 2015), pp. 98–109.

[24] S. Rata et al. “Two Interlinked Bistable Switches Govern Mitotic Control in Mammalian Cells”. In: *Current Biology* 28.23 (Dec. 2018), pp. 3824–3832.

[25] N. Moser et al. “A scalable ISFET sensing and memory array with sensor auto-calibration for on-chip real-time DNA detection”. In: *IEEE Transactions on Biomedical Circuits and Systems* 12.2 (Apr. 2018), pp. 390–401.

[26] C. Gulli, N. Moser, and P. Georgiou. “Experimental Characterisation of Drift on ISFET Arrays and its pH Dependence”. In: *Proceedings - IEEE International Symposium on Circuits and Systems* 2023-May (2023).

[27] L. E. Gerweck and K. Seetharaman. “Cellular pH gradient in tumor versus normal tissue: Potential exploitation for the treatment of cancer”. In: *Cancer Research* 56.6 (1996), pp. 1194–1198.

[28] N. Rohani et al. “Acidification of tumor at stromal boundaries drives transcriptome alterations associated with aggressive phenotypes”. In: *Cancer Research* 79.8 (Apr. 2019), pp. 1952–1966.

[29] T. Sakata, H. Sugimoto, and A. Saito. “Live Monitoring of Microenvironmental pH Based on Extracellular Acidosis around Cancer Cells with Cell-Coupled Gate Ion-Sensitive Field-Effect Transistor”. In: *Analytical Chemistry* 90.21 (Nov. 2018), pp. 12731–12736.

[30] M. J. Milgrew, M. O. Riehle, and D. R. Cumming. “A 16×16 CMOS proton camera array for direct extracellular imaging of hydrogen-ion activity”. In: *Digest of Technical Papers - IEEE International Solid-State Circuits Conference* 51 (2008), pp. 590–638.

[31] M. Lehmann et al. “Simultaneous measurement of cellular respiration and acidification with a single CMOS ISFET”. In: *Biosensors and Bioelectronics* 16.3 (May 2001), pp. 195–203.

[32] M. J. Yong et al. “Live Streaming of a Single Cell’s Life over a Local pH-Monitoring Nanowire Waveguide”. In: *Nano Letters* 22.15 (Aug. 2022), pp. 6375–6382.

[33] M. Voelker and P. Fromherz. “Nyquist noise of cell adhesion detected in a neuron-silicon transistor”. In: *Physical Review Letters* 96.22 (June 2006), p. 228102.

Chapter 7

Proteomic characterisation and pH study of drug resistance

Mechanistically, Palbociclib inhibits CDK4/6 activity but the basis for differing sensitivity of cancer to Palbociclib is poorly understood. A common observation in a subset of Triple Negative Breast Cancers (TNBCs) is that prolonged CDK4/6 inhibition can engage a senescence-like state where cells exit the cell cycle, whilst, remaining metabolically active. In this chapter, sought to better understand the senescence-like cell state which arises after Palbociclib treatment. We used mass spectrometry to quantify the proteome, phosphoproteome, and secretome of Palbociclib-treated MDA-MB-231 TNBC cells. The next section presents the experimental results where we observed altered levels of cell cycle regulators, immune response, and key senescence markers upon Palbociclib treatment. These datasets provide a starting point for the derivation of biomarkers which could inform the future use CDK4/6 inhibitors in TNBC subtypes and guide the development of potential combination therapies. We explore the metabolic perturbations identified in treated cells and characterise the extracellular pH changes observed in different treatment groups. A summary and future direction sets out the main outcomes of the chapter and identifies the potential steps to delineate the pH changes in TNBC cultures with CDK4/6 inhibition.

Work included in this chapter has previously been published in:

Beykou, M., Arias-Garcia, M., Roumeliotis, T.I., Choudhary, J.S., Moser, N., Georgiou, P., & Bakal, C. "Proteomic characterisation of triple negative breast cancer cells following CDK4/6 inhibition". In: *Scientific Data* 395.9 (Jul. 2022).

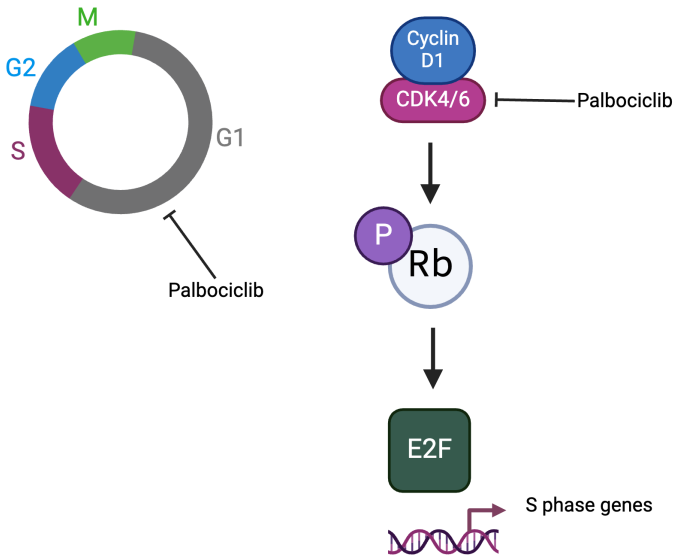


Figure 7.1: **CDK4/6 inhibitor, Palbociclib, arrests cells in the G1 phase of mitosis.**(Created in BioRender. Beykou, M. (2024) BioRender.com/v45i583).

7.1 Proteomic characterisation of triple negative breast cancer cells following CDK4/6 inhibition

A distinct characteristic of all cancer types is aberrant proliferation which can be attributed to loss of cell cycle control [1, 2]. There are four phases to the cell cycle (G1, S, G2 and M phase) where progression through the cycle is controlled by CDKs in conjunction with cyclins [3, 4]. In non-malignant cells, G1 progression is controlled by the CDK4/6 – Cyclin D1 complex which phosphorylates Retinoblastoma protein (Rb) [3–6]. The subsequent release of E2F allows the transcription of E2F target genes which are responsible for G1 progression, such as CDK2 and Cyclin E [3–6]. Therapeutic interventions targeting the cell cycle have been promising candidates, especially for Hormone-receptor positive (HR+) breast cancer subtypes where specific CDK 4/6 inhibitors, such as Palbociclib and Abemaciclib, have shown a high success rate in patient response [5, 7–9]. Whilst both CDK4/6 inhibitors harbour selectivity, Abemaciclib has exhibited off-target effects on other CDKs, including CDK9, which may result in subsequent toxicity [10, 11]. HR+ breast cancers in particular are considered the ideal target for CDK4/6 inhibitors due to a positive feedback loop between the oestrogen receptor activation and Cyclin D1 overexpression which ultimately leads to a strong dependence on the CDK4/6-Cyclin D1 mechanism for cell cycle progression [3, 5, 12].

Palbociclib's ability to block the cell cycle is largely thought to be Rb-dependent, whereby inhibition of Rb phosphorylation (pRb) results in G1 phase arrest [2, 6, 13, 14](Figure 7.1). Resistance to CDK4/6 inhibition can be due to null mutations in RB1, which alleviate de-

pendence on CDK4/6, and may be used as a predictive biomarker for response [13–16]. RB1 expression, however, may not be the only factor in determining Palbociclib sensitivity. In fact, recent studies have shown that the response of breast cancer subtypes to Palbociclib is heavily dependent on the activity of other cell cycle regulators including, CDK2, CDK6, Cyclin D and p16 [2, 13, 14, 17–19]. In addition, other signaling pathways may influence sensitivity[16, 20–22]. Thus, understanding the basis for Palbociclib sensitivity, and why some cell lines show variable resistance despite expressing functional RB1, is warranted.

A common characteristic of Palbociclib treatment is the induction of a morphologically and phenotypically distinct cell state, which resembles senescence [13, 14, 17, 18, 23]. The senescent-like state can be induced in subtypes with functional Rb such as the TNBC cell line, MDA-MB-231 [13, 15, 17, 23–26]. This cell state remains poorly understood as studies show inconclusive evidence creating uncertainty as to whether this is stable senescence [5, 13–15, 23, 25]. A set of markers, such as pRb, β-galactosidase (GLB1) and, loss of Ki67 and LaminB1, have been identified as hallmarks of senescence although they remain non-exclusive to the senescence phenotype [27, 28].

The field of senescence research has recently uncovered both beneficial and detrimental consequences of the cell phenotype for tumour growth. In particular, the pro-tumorigenic and anti-tumorigenic effects of the Senescence-Associated Secretory Phenotype (SASP) remain a point of debate [24, 28, 29]. More specifically, despite the inhibition in tumour growth that accompanies senescence induction, additional factors can result in tumour recurrence, apoptosis resistance, tumour dormancy and ultimately metastasis [30–32]. Inflammation via inflammatory cytokines secreted as part of the SASP also play an important role for tumour growth and survival [32, 33]. On the other hand, senescence can promote an adaptive immune response and some SASP components may sensitise the cell state to combination therapies [24, 32, 34, 35]. One such example is the combination therapy of an anti-PDL1 agent with Palbociclib, which is currently in clinical trials [36]. Metabolic perturbations have also been recorded in senescent cells, where the resulting “Warburg” or “anti-Warburg” phenotype has been contentious dependant on the origins of senescence - replicative, oncogenic or therapy-induced [37–40]. Proteins related to the oxidative phosphorylation pathway were reported to be upregulated in oncogene-induced senescent cells whilst therapy-induced senescent cells treated with a DNA damaging agent were shown to have an extreme Warburg phenotype [37, 38]. The effect of CDK4/6 inhibitors remains incompletely understood due to the partial sensitivity of a number of cell types, however, the importance of pHi and lysosomal pH in this scenario has been investigated [40, 41]. Acidification of pHi leading to a perturbation in homeostatic mechanisms was found in therapy-induced senescent cells by abemaciclib and doxorubicin treatment [40]. This may serve as an opportunity for senescent cell detection via pHi and pHe in future studies. Given the potential importance of the Palbociclib-induced senescent-like phenotype to the treatment of cancers,we sought to better characterize the cell state and arising pHe.

7.2 Methodology

7.2.1 Cell culture

Cell maintenance MDA-MB-231 were cultured in growth medium composed of Dulbecco's Modified Eagle Medium (DMEM 1X) (4.5g/L D-Glucose, L-Glutamine and Pyruvate (Gibco), 10% heat-inactivated Fetal Bovine Serum (FBS) (Gibco) and 1% Penicillin/Streptomycin (Invitrogen). Cell cultures were maintained in 5% CO_2, humidified incubators at 37°C.

Passaging For each passage, the existing growth medium was aspirated when cells were at 80% confluency. PBS (5ml) was added to wash the flask and was then aspirated.Subsequently, 2ml 0.25% Trypsin-EDTA (Gibco) was added and the flask was returned to the incubator for 5-10 mins to allow cell detachment. Once cells were detached, 5ml growth medium was added to the flask and cells were gently resuspended by pipetting. The entire volume of cells was added to a 15ml Falcon which was centrifuged at 1000rpm for 5 mins. Media was then aspirated whilst leaving the pellet intact. We resuspended the pellet in 2-5ml fresh growth medium. Trypan Blue (10ul) was mixed with 10ul cell solution and A 10uL aliquot of the mixture was added to a Cell Countess glass slide (EVE,NanoEnTek). Cells in solution were counted using the Cell Countess (Invitrogen) and the required parameters were input on the Cell Countess (volume and concentration of cells required). The cell solution was resuspended in the required volume to achieve the cell concentration desired which was transferred to a new vessel.

pH experiments A pH probe was calibrated and used as described in Chapter 4 Section 4.2.2.

Rescue Long-term palbociclib-treated cells were washed thrice with a relevant volume of fresh, complete DMEM cell culture media. On day 2, cells were passaged and media was replaced with fresh cell culture media once more.

Proteomics/Phosphoproteomics drug treatment regimes (Samples 1-6) For all experiments cells were seeded on T75 flasks at a concentration of 2 x10^4 cells/ml in 14ml of growth medium per flask. Cells were allowed to settle and subsequently treated. Palbociclib-treated flasks (prefixed "Palbo" in all datasets) were treated with PD0332991 (Sigma, Lot 072M4735V), commonly known as "Palbociclib", at a final concentration of 1uM (1.4ul/flask). DMSO control flasks were treated with an equivalent volume of DMSO (Sigma). Cell pellets were collected on 7 days and 1 day post-treatment for both Palbociclib-treated cells and DMSO controls (Table 7.1).

Sample	Name	Analysis	Treatment	FBS starved
1	DMSO control 7 days	Proteomics/Phospho	DMSO	N
2	DMSO control 7 days	Proteomics/Phospho	DMSO	N
3	Palbo 7 days	Proteomics/Phospho	PD0332991 1uM	N
4	Palbo 7 days	Proteomics/Phospho	PD0332991 1uM	N
5	Palbo 1 day	Proteomics/Phospho	PD0332991 1uM	N
6	Palbo 1 day	Proteomics/Phospho	PD0332991 1uM	N
7	Palbo 7 days	Secretome	PD0332991 1uM	Y
8	Palbo 7 days	Secretome	PD0332991 1uM	Y
9	Palbo 7 days	Secretome	PD0332991 1uM	Y
10	DMSO control 7 days	Secretome	DMSO	Y
11	DMSO control 7 days	Secretome	DMSO	Y
12	DMSO control 7 days	Secretome	DMSO	Y

Table 7.1: **Proteomic samples overview.** All samples collected and the analysis they were subjected to as indicated by the "Name" and "Treatment" columns. The "FBS starved" column indicates the replacement of standard growth medium containing foetal bovine serum (FBS) with FBS-free serum which is a standard procedure in secretome analysis. Y = yes. N= no.

Secretome drug treatment regimes (Samples 7-12) Cells were seeded on T75 flasks at 2x10 ^{4} cells/ml in 14ml growth medium per flask. Cell cultures were allowed to settle and were then treated with PD0332991 (Sigma, Lot 072M4735V) at a final concentration of 1uM. DMSO control flasks were once again treated with an equivalent volume of DMSO. In the 24 hours prior to sample collection, the flasks were washed with warm PBS to remove any serum. Growth medium was then replaced with an equivalent volume of FBS–free medium with 1uM Palbociclib for treatment flasks and DMSO for control flasks (Table 7.1). The overview of drug treatment is summarised in Figure 7.2.

Cell and growth media collection For the samples collected for total protein analysis (samples 1-6), cell cultures were trypsinized and centrifuged into a cell pellet as when passaging. Cells were resuspended in 1ml cold PBS. The Cell Countess was used as previously, to count 1x10^{6} cells which were aliquoted in 1.5ml Eppendorf tubes. These were centrifuged at 4 °C, 14,000 rpm for 5mins to produce a pellet. Subsequently, PBS was aspirated and the samples were snap frozen on dry ice by spraying with ethanol. The samples were frozen at – 80 °C.

For secretome analysis (samples 7-12), growth medium was filtered through 0.2um filters and collected in 50ml Falcon tubes. FBS-free growth medium (10ml) was then used to wash each T75 flask and added to the same 50ml Falcon tube. The collected media was frozen at -80 °C. Serum starvation is used for secretome studies to ensure minimal proteomic background contamination providing a more reliable reading to cell-excreted proteins.

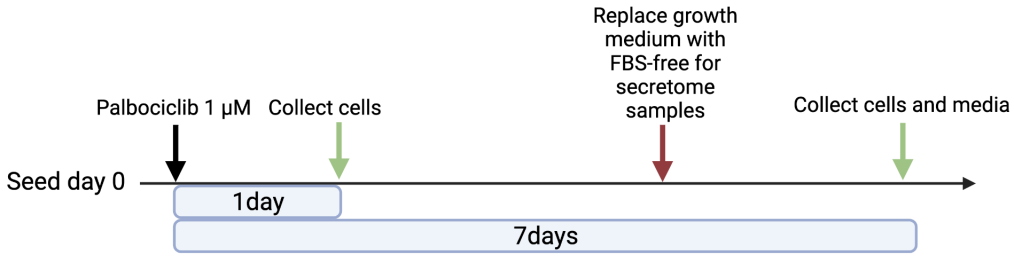


Figure 7.2: **Overview of drug treatment regime with CDK4/6 inhibitor Palbociclib.** Samples intended for secretome analysis had their growth medium replaced with fetal bovine serum (FBS) - free growth medium 24 hours prior to collection of samples.

Sample preparation for proteomics analysis of cell lines and secretome

Cell pellets were lysed in 150 ul lysis buffer of 1% Sodium Deoxycholate (SDC), 100 mM Triethylammonium Bicarbonate (TEAB), 10% Isopropanol, 50 mM NaCl and Halt protease and phosphatase inhibitor cocktail (100X) (Thermo, 78442) on ice, assisted with pulsed probe sonication for 15 sec and followed by heating at 90 °C for 5 min and re-sonicated for 5 sec. Protein concentration was measured with the Quick Start™ Bradford Protein Assay (Bio-Rad) according to manufacturer's instructions. Protein aliquots of 60 ug were reduced with 5 mM Tris-2-Carboxyethyl Phosphine (TCEP) for 1 h at 60 °C and alkylated with 10 mM Iodoacetamide (IAA) for 30 min in dark. Proteins were digested overnight with trypsin at final concentration 75 ng/ul (Pierce) and peptides were labelled with the TMTpro reagents (Thermo) according to manufacturer's instructions. The pooled sample was acidified with 1% formic acid to remove precipitated SDC by centrifugation and supernatant was SpeedVac dried. For the secretome analysis, the collected culture media were concentrated with the Amicon Ultra 15ml 3K MWCO ultrafiltration devices, the proteins were precipitated with trichloroacetic acid (TCA) and washed with cold acetone. Protein pellets were solubilized in lysis buffer and processed as above but using the TMT10plex reagents.

7.2.2 High-pH Reversed-Phase peptide fractionation and phosphopeptide enrichment

For the analysis of cell pellets and secretome, the TMT labelled peptides were fractionated with high-pH Reversed-Phase (RP) chromatography using the XBridge C18 column (2.1 x 150 mm, 3.5 um, Waters) on a Dionex UltiMate 3000 HPLC system. Mobile phase A was 0.1% v/v ammonium hydroxide and mobile phase B was acetonitrile, 0.1% v/v ammonium hydroxide. The peptides were fractionated at 0.2 ml/min with the following gradient: 5 mins at 5% B, up to 12% B in 3 min, for 32 min gradient to 35% B, gradient to 80% B in 5 min, isocratic for 5

mins and re-equilibration to 5% B. Fractions were collected every 42 sec, combined in 30 (cell pellets) and 12 (secretome) fractions and SpeedVac dried.

Phosphopeptide enrichment was performed for 24 fractions (cell pellets) with the High-Select™ Fe-NTA Phosphopeptide Enrichment Kit (Thermo) using a customized protocol in a well plate array format. A volume of 50 ul resin/buffer was transferred on top of 10 ul filter tips that were fitted on a 96-well plate using a tip rack adapter. The resin was washed three times with 40 ul wash/binding solution and centrifugation at 500 g for 1 min. Peptides were reconstituted in 30 ul wash/binding solution and were loaded onto the tip-columns with the resin. After 30 min, the flow-through from three washes with wash/binding solution were collected in a clean 96-well plate with centrifugation at 500 g for 1 min each time. Phosphopeptides were eluted twice with 40 ul elution buffer in a clean 96-well plate with centrifugation at 500 g for 1 min, transferred in glass vials (Waters, P/N 186005669CV) and SpeedVac dried. The flow-through solutions were dried and kept for total proteome analysis.

7.2.3 LC-MS analysis

LC-MS analysis was performed on a Dionex UltiMate 3000 UHPLC system coupled with the Orbitrap Lumos Mass Spectrometer (Thermo Scientific). Peptides were loaded onto the Acclaim PepMap 100, 100 um × 2 cm C18, 5 um, trapping column at flow rate 10 ul/min. Samples were analysed with the EASY-Spray C18 capillary column (75 um × 50 cm, 2 um) at 50 °C. Mobile phase A was 0.1% formic acid and mobile phase B was 80% acetonitrile, 0.1% formic acid. The separation method was: for 90 min gradient 5%-38% B, for 10 min up to 95% B, for 5 min isocratic at 95% B, re-equilibration to 5% B in 5 min, for 10 min isocratic at 5% B at flow rate 300 nl/min. MS scans were acquired in the range of 375-1,500 m/z with mass resolution of 120 k, AGC 4×105 and max IT 50 ms. Precursors were selected with the top speed mode in 3 sec cycles and isolated for HCD fragmentation with quadrupole isolation width 0.7 Th. Collision energy was 36% (TMTpro) or 38% (TMT10plex) with AGC 1×10^5 and max IT 86 ms at 50 k resolution. Targeted precursors were dynamically excluded for further fragmentation for 45 seconds with 7 ppm mass tolerance. The phosphopeptide enriched samples were analysed as above with the following differences: 60 min gradient 5%-38% B, HCD MS2 with max IT 100 ms and 30 sec dynamic exclusion.

7.2.4 Database search and quantification

The mass spectra were analysed in Proteome Discoverer 2.4 (Thermo Scientific) with the SequestHT search engine for peptide identification and quantification. The precursor and fragment ion mass tolerances were 20 ppm and 0.02 Da respectively. Spectra were searched for

fully tryptic peptides with maximum 2 miss-cleavages. TMTpro (cell pellets) or TMT6plex (secretome) at N-terminus/K and Carbamidomethyl at C were selected as static modifications. Oxidation of M, Deamidation of N/Q as well as Phosphorylation of S/T/Y for the IMAC samples only were selected as dynamic modifications. Spectra were searched against reviewed UniProt human protein entries, peptide confidence was estimated with the Percolator node and peptides were filtered at q-value < 0.01 based on decoy database search. The reporter ion quantifier node included a TMT quantification method with an integration window tolerance of 15 ppm. Only peptides with average reporter signal-to-noise > 3 were used and phosphorylation localization probabilities were estimated with the IMP-ptmRS node.

7.2.5 Immunofluorescence staining & Microscopy

Cells were plated in 384-well plate at a concentration of 400 cells/well. Cells were allowed to attach and subsequently treated with 1uM PD0332991 ("Palbociclib", Sigma, Lot 072M4735V). After 7 days of treatment, cells were fixed with 4% PFA (Thermo) and incubated for 12mins. Wells were washed twice with PBS (supplemented with NaN_3). Subsequently, 20ul 0.2% Triton-X solution was added per well and allowed to incubate for 12mins. Wells were washed twice with PBS (supplemented with NaN_3) and 20ul 2% BSA was added and incubated for 1 hour. All steps were performed at ambient temperature. Wells were aspirated. Antibody solution mix was made up with 0.5% BSA, 0.02% Triton-X and PBS (with NaN_3). In the relevant volume of antibody solution, primary antibodies were added at the required concentration (Table A.2). Plates were enclosed in Parafilm and incubated at 4°C overnight. Wells were subsequently washed thrice with PBS (with NaN_3). Secondary antibodies were added in a concentration of 1:1000 in antibody solution mix and incubated for 2hrs at ambient temperature. Wells were washed thrice with PBS (with NaN_3) and Hoescht dye was added at a concentration of 1:1000 in antibody solution mix. Plates were incubated for 10mins at ambient temperature and then washed once with PBS (with NaN_3). Wells were left in PBS (with NaN_3) and stored at 4 °C. Subsequently, imaging was performed using the Opera high-throughput microscope (PerkinElmer). Rescue and long-term treated cells were imaged using an Advanced spinning disc confocal microscope with a 63x magnification performed with an oil lens.

7.2.6 Data analysis

Statistics was performed using the Perseus Software [42]. VolcanoseR (mirror R2) was used for visualization of one sample t-test and extraction of top 50 hits in all datasets [43].The Cytoscape application version 3.9.0 was used for network analysis [44]. In addition, the Phantasus server was used for creating a similarity matrix (Pearson correlation) and hierarchical clustering (Euclidean distance with complete linkage) with the total protein scaled abundances for

technical validation [45]. Principal component analysis (PCA) was performed using the python package bioinfokit with scaled abundance values of the total proteome [46]. GraphPad Prism v. 9.2.0. was used to perform statistics. KEGG mapper was used for graphical wiring diagrams https://www.genome.jp/kegg/mapper/color.html.

7.2.7 Data Records

Raw mass spectrometry data files and post-processed, scaled abundance Excel sheets for total proteome, phosphoproteme and secretome have been deposited to the ProteomeXchange Consortium via the PRIDE partner repository [47, 48] under the dataset identifier PXD030407 [49].

7.2.8 Code availability and data processing

Statistics (one sample t-test) was performed using the Perseus software version 1.6.14.0 [42]. PCA was performed and plotted using the python bioinfokit package [46]. Pearson correlation, hierarchical clustering analysis and subsequent similarity matrix were performed and created using the Phantasus software version 1.11.0 [45]. Volcano plots were created using VolcaNoseR (mirror R2) [43]. Network analysis was performed using the String application on Cytoscape version 3.9.0 [44]. Heatmap and bar charts were created using GraphPad Prism version 9.2.0. Images were stored on Perkin Elmer Columbus server version 2.9.1.

7.3 Technical Validation

7.3.1 Reproducibility of Replicates

All samples were subjected to PCA. The first 3 principal components (PCs) were plotted to show clustering of samples under the same conditions (Figure 7.3a). A biplot was also used to illustrate the close association between the “Palbo 7 days FBS” and “Palbo 7 days starved” samples, as well as the degree of difference from their respective DMSO control samples (Figure 7.3b). Replicates for all conditions were subjected to a similarity matrix (Pearson correlation). Subsequently, hierarchical clustering using a Euclidean metric (complete linkage) was applied on the similarity matrix which showed that all replicate samples cluster together on the matrix (Figure 7.3c).

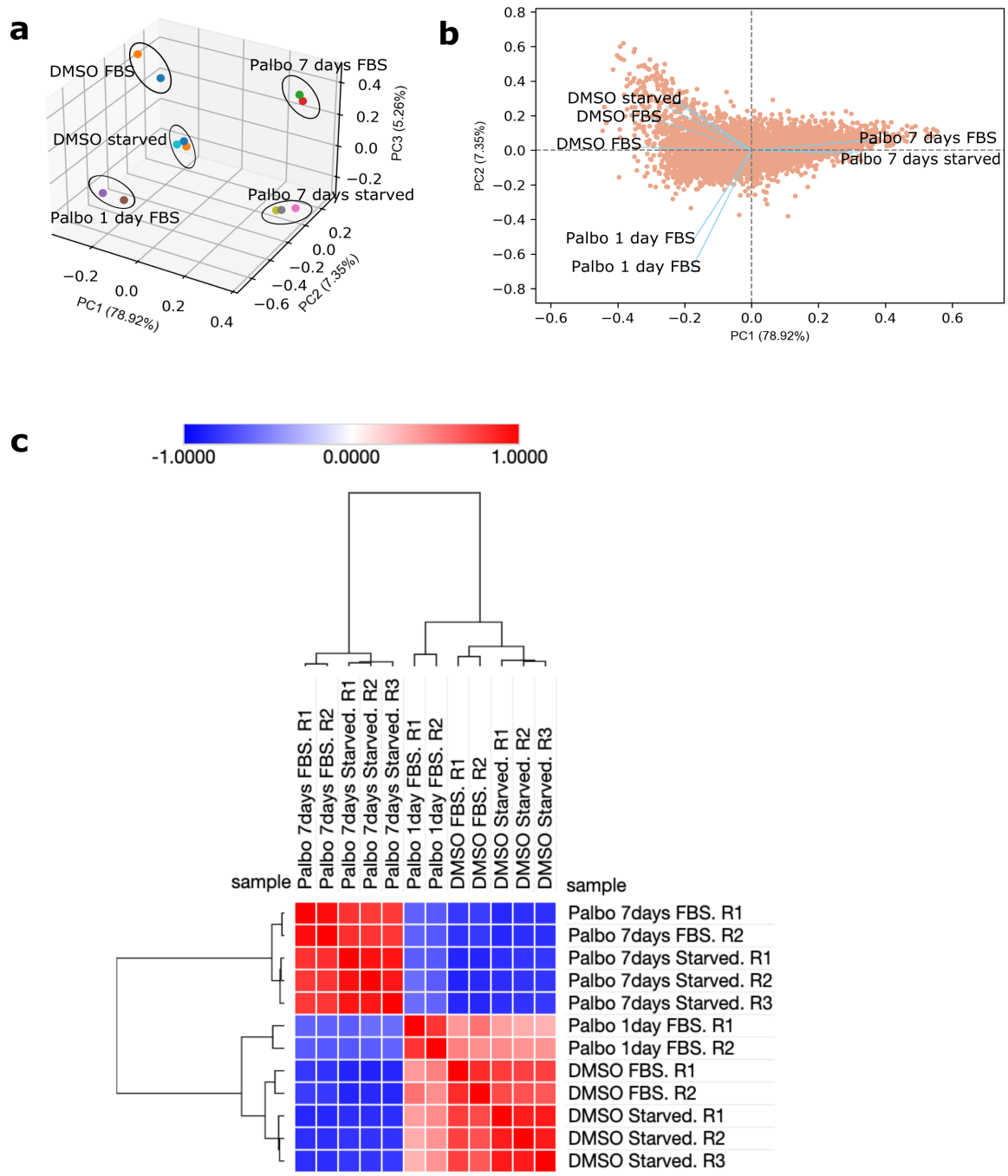


Figure 7.3: **Reproducibility of proteomic samples.** **(a)** Principal component analysis (PCA) was performed to illustrate the reproducibility of samples. The PCA plot shows clustering of samples with the same cell culture conditions.The first 3 principal components (PCs) contribute to 91.53% of the variation in the data. **(b)** A PCA biplot illustrating the PC loadings and the first two principal components, PC1 and PC2. The angle between vectors shows that Palbo 7 days FBS and Palbo 7 days starved samples are closely correlated. DMSO starved and DMSO FBS samples are correlated to eachother and have a low correlation with all Palbocicib-treated samples. The PCA analysis was carried out using the bioinfokit package in Python version 3.8.8 [46].**(c)** A similarity matrix (Pearson correlation) of total protein scaled abundances which has been subjected to hierarchical clustering (Euclidean distance with complete linkage), to reveal that samples of the same conditions cluster together on the matrix. Thus, the samples of the same condition in question are highly correlated. The Phantasus server was used for this analysis [45].

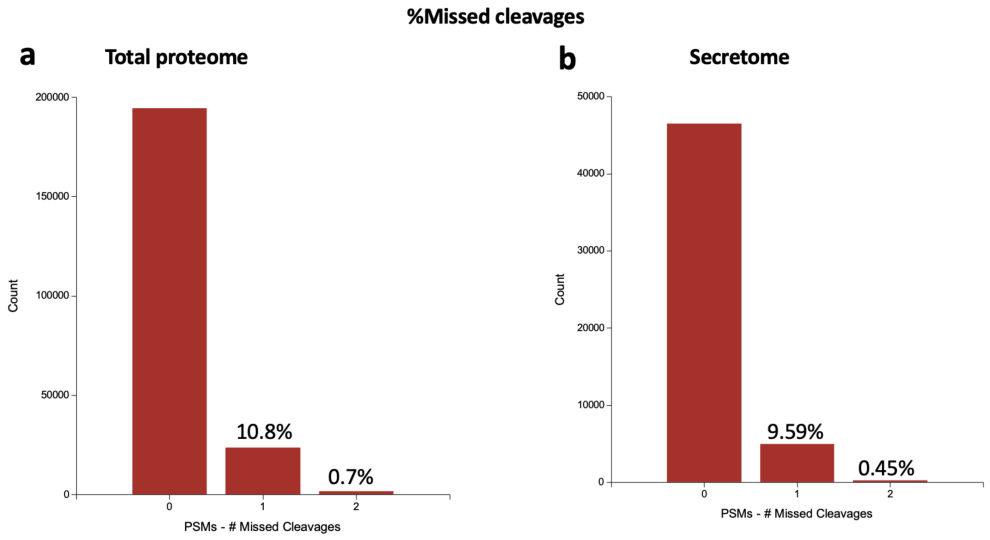


Figure 7.4: **Technical validation of mass spectrometry analysis.** Figure shows percentage of missed cleavages through trypsin digestion showing reproducibility between the total proteome **(a)** and secretome **(b)** analysis. PSMs = peptide spectrum matches

7.3.2 Mass spectrometry

TMT labeling efficiency was estimated by Mascot search of 10,000 representative MS2 scans with TMT selected as variable modification (at peptide n-term and K). The estimated labelling efficiencies were > 99% for the total proteome/phosphoproteome and 98% for the secretome data. Figure 7.4 shows the percentages of trypsin missed cleavages (10%) indicating efficient digestion in both sample types.

7.4 Results & Discussion

To better understand the senescent-like state induced by Palbociclib in MDA-MB-231 cells, we used mass spectrometry to quantify the total proteome, phosphoproteome, and secretome of Palbociclib treated cells at day 1 and day 7 (Figure 7.2). Palbociclib treatment resulted in striking morphological changes, such as the formation of flat and large cells (Figure 7.5). We confirmed a high TMT labelling efficiency and efficient trypsin cleavage for all datasets as well as sample correlation (Figure 7.3 & Figure 7.4). Palbociclib treatment resulted in changes in the proteome and phosphoproteome which demonstrate failure to progress through G1/S via significant protein expression changes to cyclins and significant Rb dephosphorylation in response to CDK4/6 inhibition[4, 5](Figure 7.6). In addition, the cell cycle pathway is found amongst the most downregulated KEGG pathways which confirms cell cycle inibition in response to Palbociclib (Table A.1). Additionally, Palbociclib-treated MDA-MB-231 have well-recognised signatures of senescence including expression of GLB1 (β-galactosidase) and, loss of

proliferation marker Ki67 and perinuclear LaminB1 [23, 27, 28] (Figure 7.7). We validate the changed levels of these markers with immunofluorescence staining in addition to total protein abundances (Figure 7.7).

Statistical analysis depicts some interesting targets which are upregulated in response to Palbociclib, including adhesion molecules and components of the immune system (Figure 7.8). Activation of the immune response is also reflected in the enrichment of KEGG pathways where proteins key to the immune response, e.g. MHC proteins, are amongst the drivers of the Top 10 upregulated pathways [34](Figure 7.9). Furthermore, we note that significantly decreased expression of both RRM1 and RRM2, for example, could also indicate changes in the metabolic state of Palbociclib-treated cells [50, 51] (Figure 7.8).

Network visualization of upregulated proteins indicates the response of a number of key markers previously associated with the senescence phenotype in response to Palbociclib, such as the upregulation of GLB1 (β-galactosidase) [27]. In-depth analysis could allow the delineation of the metabolic profile of the Palbocicib-induced cell state in TNBCs, for example, as a number or central carbon metabolic pathways are shown to be upregulated. Figure 7.10 also depicts changes to histone molecules expression indicates that there may be potential epigenetic changes with downstream effects [52]. These datasets set the stage for the development of biomarkers to better track the effects of Palbociclib use in patients or stratify patients who will best benefit from Palbociclib therapy. Moreover, these datasets open therapeutic avenues for the development of strategies to enhance Palbociclib use.

Mass Spectrometry (MS) datafiles are available to users to allow different proteome and phosphoproteome analyses in order to delineate the drug response to Palbociclib in a model TNBC cell line. Figure 7.10 shows the upregulation of a number of key senescence markers which can act as controls for the dataset. The network nodes are coloured by Log2 Fold Change (Log2FC) and sized by q-value to indicate significance. This type of analysis can reveal a number of pathways which can be used as controls for response to Palbociclib, e.g. cell cycle downregulation, but can also reveal changes which may suggest the induction of senescence. For example, FOXM1, which is thought to be an inhibitor of senescence, is shown to be downregulated [53]. Figure 7.10 also depicts changes to histone molecules expression indicates that there may be potential epigenetic changes with downstream effects [52]. In addition, a number of subnetworks could reveal further changes due to Palbociclib, such as an IFN response, metalloproteinases (e.g.MMP1) and immune system activation. These observations are also corroborated by annotation of the datasets using resources such as the KEGG pathways database [54] as well as Gene Ontology terms [55, 56] which could also provide further evidence of a wider-acting network of changes including immune activation, metabolic and transcriptional changes (Figure 7.9 and Table A.1). Lastly, statistical analysis shows upregulation and downregulation of proteins and phosphorylation states which could indicate the induction of a range of programmes which lead

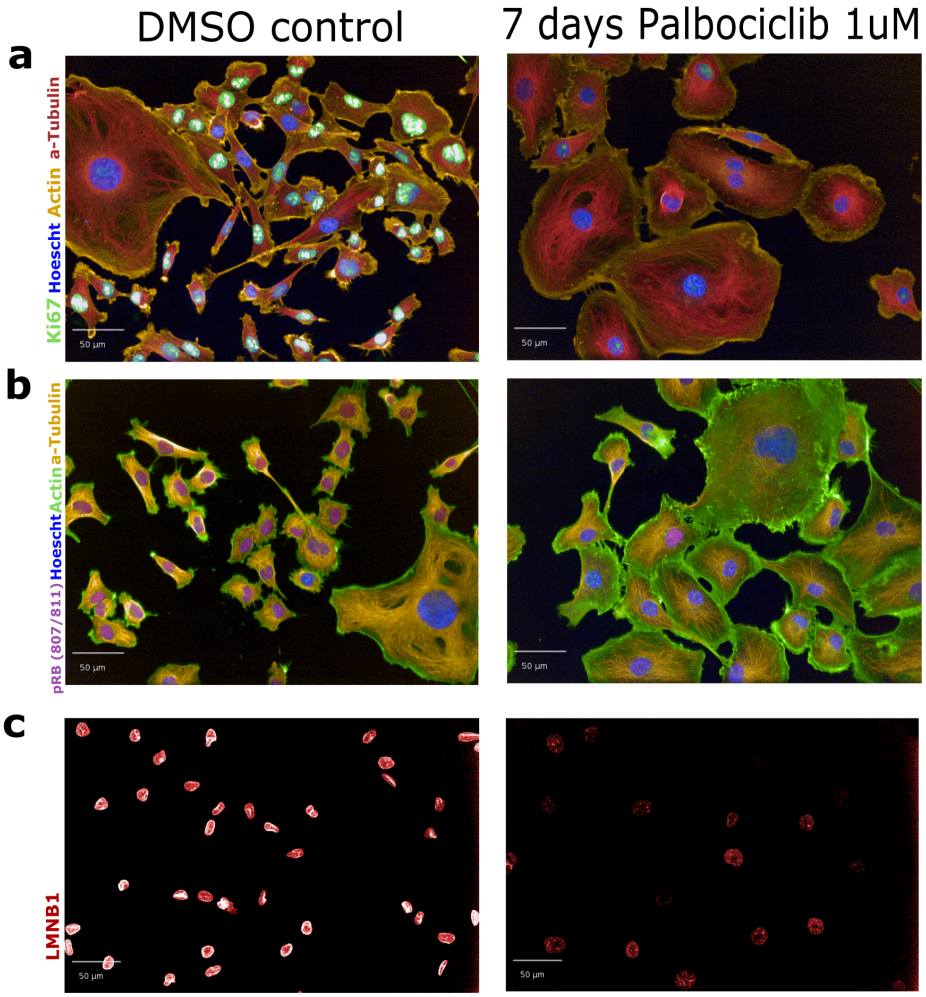


Figure 7.5: **Validation of senescence-like morphology and immunofluorescence staining of key senescence biomarkers.** Treatment of MDA-MB-231 cells with 1uM PD0332991 (known as Palbociclib) for 7 days or with an equivalent dose of DMSO as a control. **(a)** Immunofluorescence staining for Ki67. **(b)** Immunofluorescence staining for pRb (807/811). **(c)** Immunofluorescence staining for LMNB1. In all panels F-actin, α-Tubulin and Hoescht (nucleus) staining is used to image morphological features. All images were taken using the Opera high-throughput microscope (PerkinElmer).

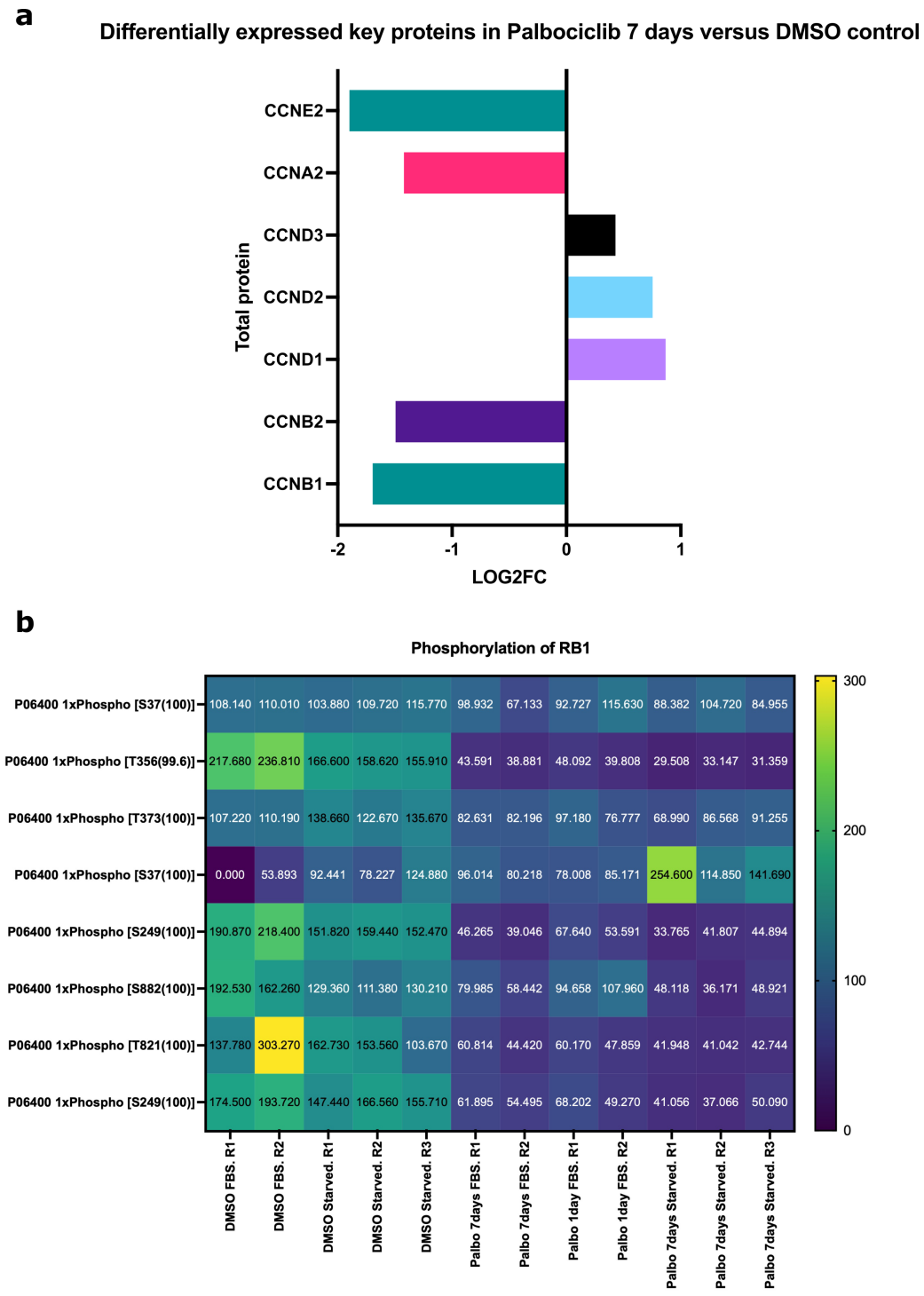


Figure 7.6: **Validation of key senescence markers in total proteome and phosphoproteome. a**Log2FC of cyclins significantly differentially expressed in Palbociclib-treated MDA-MB-231 cells, both FBS and starved samples, versus their respective DMSO controls. Log2FC was calculated using a one sample t-test and subsequent results were filtered for q-value ¡0.05 using Perseus software [42]. **(b)** Heatmap of phosphorylation sites of RB1 (pRB) showing a decrease in RB1 phosphorylation at multiple sites after Palbociclib treatment.Log2FC = Log2 Fold Change.

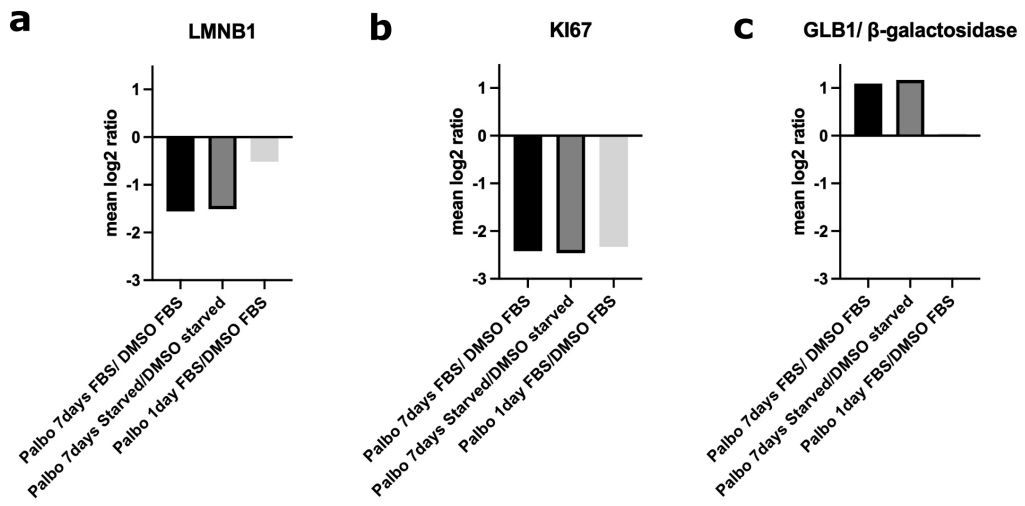


Figure 7.7: **Validation of key senescence markers in total proteome and phosphoproteome. (a)** Mean Log2 ratio of LMNB1 protein abundance of Palbociclib-treated cells versus their respective controls. **(b)** Mean Log2 ratio of KI67 protein abundance of Palbociclib-treated cells versus their respective controls.**(c)** Mean Log2 ratio of GLB1 protein abundance of Palbociclib-treated cells versus their respective controls.

to the morphological and phenotypic changes associated with Palbociclib treatment in TNBCs (Figure 7.8). Notably, TACSTD2 upregulation, which is also known as Trop-2, could point to a potential combination therapy as anti-Trop-2 antibodies and antibody-drug conjugates have shown success in TNBCs [57–60]. Feature extraction algorithms could be used to enquire further into the associations between morphological changes and senescence reprogramming.

7.4.1 The Warburg effect in a senescent-like cell population

The metabolic reprogramming associated with malignancy induction has been suggested to be either reversed or enhanced in a senescent cell sub-population with evidence towards both being found in the literature [37, 38]. KEGG pathway enrichment in 7-days Palbociclib-treated cells versus starved controls revealed the upregulation of proteins found in the TCA cycle and oxidative phosphorylation with an enrichment score > 0.5 (Figure 7.11(a)). Visualization of proteins in upregulated or downregulated on our dataset using the KEGG pathway database reveals the upregulation of both intracellular and membrane-bound subunits related to the oxidative phosphorylation pathway (Figure 7.11(b)). In 7-day Palbociclib-treated cells versus FBS control cells, enrichment score for oxidative phosphorylation was narrowly lower at 0.44 a.u.

To determine whether the metabolic changes may be detectable in the extracellular environment in cell cultures we investigated pH changes during Palbociclib treatment for 1 day, 3 days, 5 days and 7 days. Control media (DMEM, 10% FBS, 1% P/S media) supplemented with 1uM Palbociclib was found to be marginally more alkaline than control media only. Figure 7.13

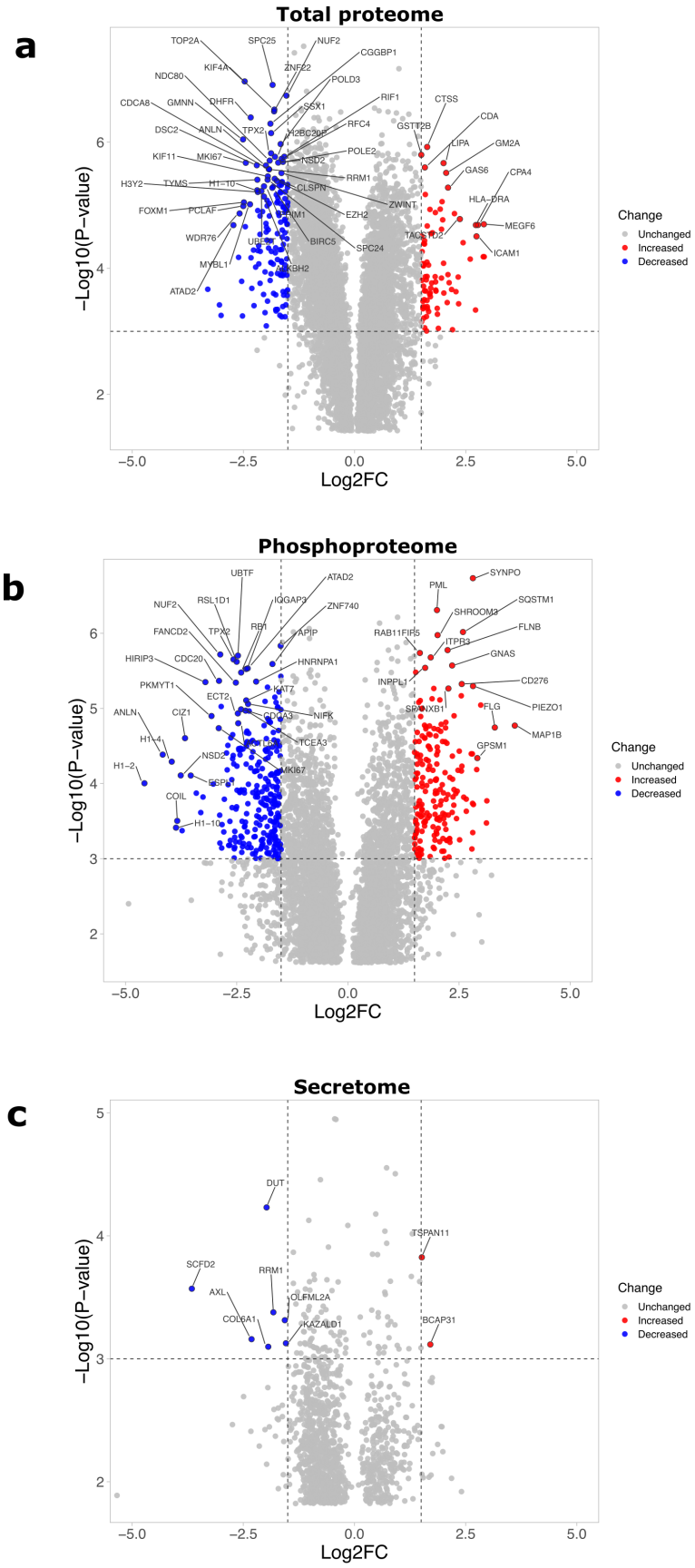


Figure 7.8: **Significantly upregulated and downregulated proteins upon 7 days Palbociclib treatment of MDA-MB-231.** (Continued on next page)

(a) Proteins with significantly different expression in total proteome of MDA-MB-231 7 days Palbociclib-treated cells (both FBS and starved samples) as compared to their respective DMSO-treated controls. **(b)** Significantly different phosphorylation profile of proteins in MDA-MB-231 7 days Palbociclib-treated cells (both FBS and starved samples) as compared to their respective DMSO-treated controls. **(c)** Significantly different expression of proteins in secretome of 7 days Palbociclib-treated versus DMSO-treated MDA-MB-231 cells. In all cases, one sample t-test was performed and subsequent results were filtered for q-value ¡0.05 using Perseus software [42]. Top 50 most significant hits were calculated with the Manhattan metric using VolcaNoseR (R2 mirror) [43]. Log2FC = Log2 Fold Change.

shows that 1 day treatment and 3 day treatment resulted in a significant difference to the initial pH. At 5 days, no significant difference was found, whilst at 7 days treatment with no media changes the greatest acidification is seen with an overall change of approximately 0.2 pH (Figure 7.13). To an extent, the evidence of pHe experiments using conditioned media from cell cultures contradicts proteomic data as acidification is found in cell media pH measurements. This is not conclusive, however, as an increased oxidative phosphorylation rate would also contribute to pHe acidification in a similar manner to glycolysis albeit at a much slower rate (Figure 7.12). Additionally, proteomics only provides a snapshot of protein states which may be affected during the experimental procedure, leading to pHe acidification not being captured to a similar extent as seen in culture. The discrepancy may be due to a range of factors including buffering capacity, biological variations and static capture of proteomic state. Similarly, the oxidative phosphorylation pathway proteins are shown to vary significantly between different cell lines of variable characteristics e.g. luminal versus basal (Appendix B.1).

Finally, as some proliferation was evident in long-term cultures of palbociclib-treated MDA-MB-231 cells, this suggested that the senescent-like cell state was a form of drug resistance and as such reversible. Long-term cell culture of cells in palbociclib-supplemented cell culture media for 54 days should a sustained large and flat cell morphology. Upon wash-out and supplementation with complete DMEM media, an average of 11-15 days were required for cells to recover into a proliferative state as prior to treatment. Figure 7.14(a) shows mitotic cells as indicated by a white arrow in 15 days post-washout. This is also corroborated by confluency measurements over 73 hours of long-term Palbociclib treated cells which show little variation in the percentage of well area covered versus washout rescue wells which reach almost 80% confluency (Figure 7.14(b)). As a result, the senescence-like phenotype induced in MDA-MB-231 with long-term exposure to a CDK4/6 inhibitor, Palbociclib, is not a permanent senescent state as rescue to a proliferative state was feasible.

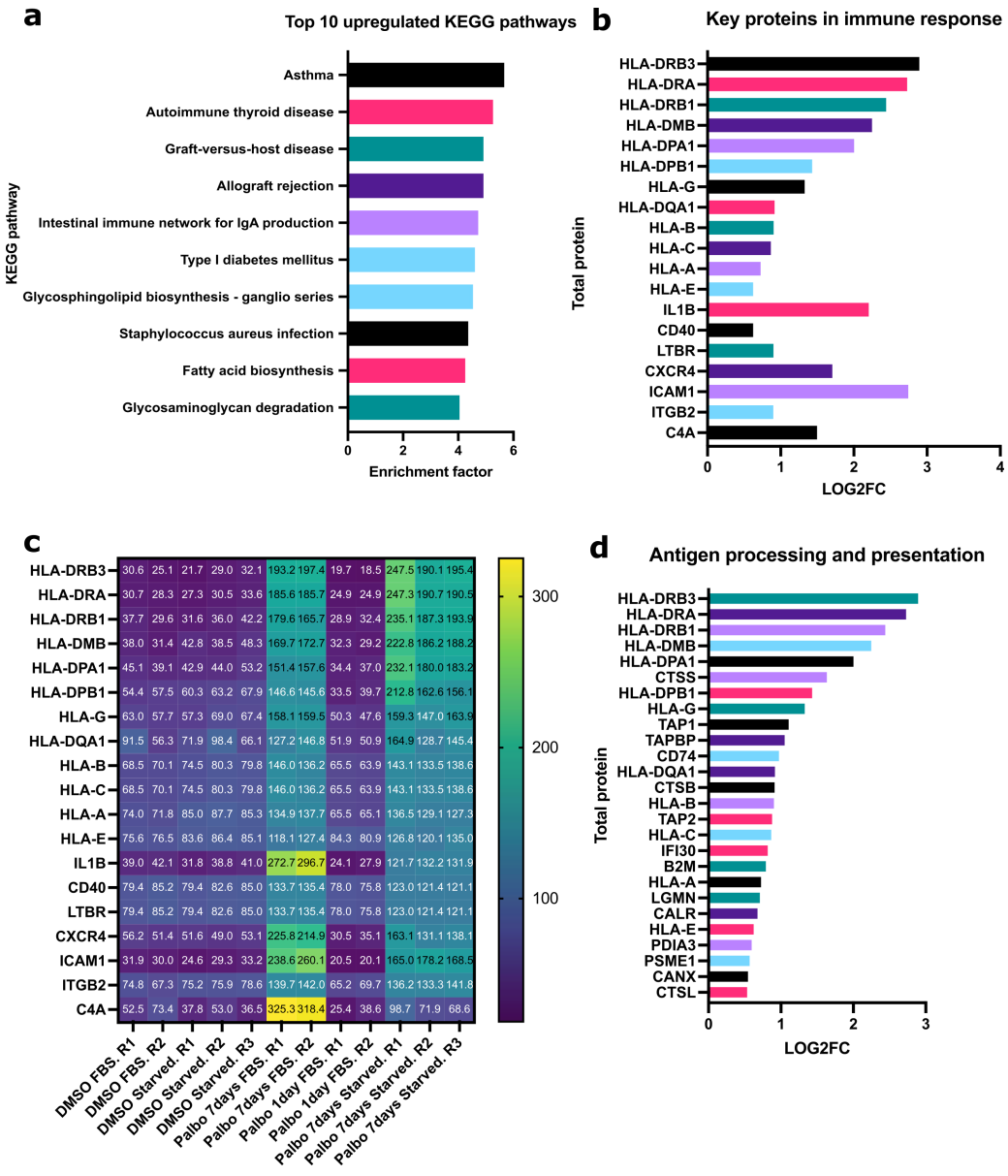


Figure 7.9: **KEGG pathway enrichment of significantly upregulated proteins in 7 days treated Palbociclib MDA-MB-231 samples (FBS and starved samples) versus their respective DMSO control samples.** **(a)** Top 10 most upregulated KEGG pathways as determined by a Fisher's exact test (Benjamini-Hochberg FDR threshold = 0.05) on 1 sample t-test results where a column indicating upregulation (Log2FC >0.5) or downregulation (Log2FC <-0.5) was added. **(b)**Log2FC of upregulated proteins in the top 10 upregulated KEGG pathways which are disease or immune-related (Asthma, Autoimmune thyroid disease, Graft-versus-host disease, Allograft rejection, Intestinal immune network for IgA production, Type I diabetes mellitus and Staphylococcus aureus infection). Log2FC of 7 days Palbociclib-treated samples (FBS and starved) compared to their respective DMSO controls (FBS and starved) was calculated using a one sample t-test and subsequent results were filtered for q-value < 0.05 using Perseus software [42]. **(c)** Total protein scaled abundances for the proteins in Top 10 upregulated KEGG pathways which are disease or immune-related. **(d)** Log2FC of proteins in the KEGG pathway named Antigen processing and presentation. Log2FC = Log2 Fold Change.

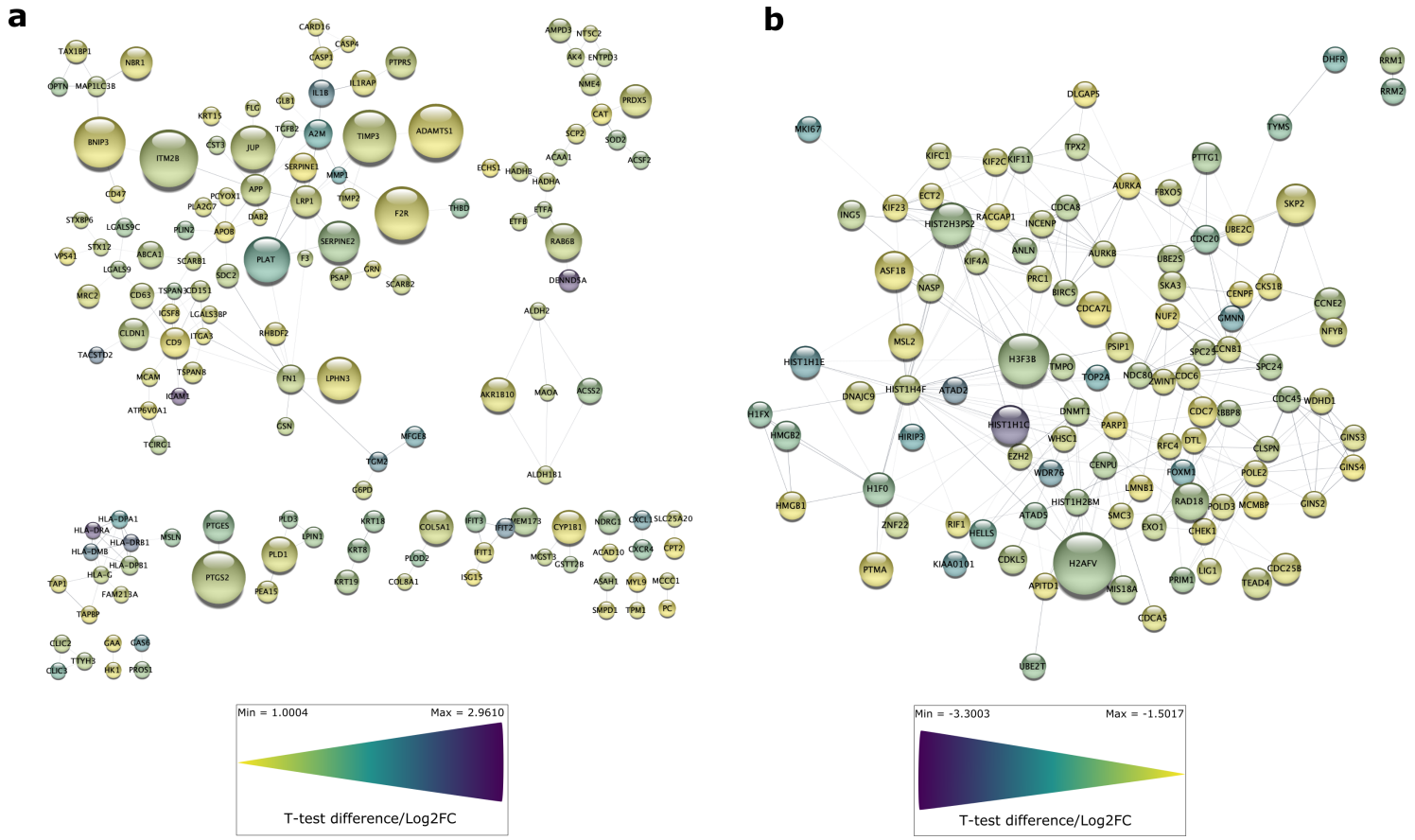


Figure 7.10: **Physical network analysis of significantly upregulated and downregulated total protein upon Palbociclib treatment of MDA-MB-231 cells. (a)** A physical network of upregulated proteins with a Log2 Fold Change (Log2FC) greater than 1 and Q-value¡0.01.**(b)** A physical network of downregulated proteins with a Log2FC less than -1.5 and Q-value¡0.01. One sample t-testing was performed using the Perseus software. Network mapping was performed using the Cytoscape application version 3.9.0 [44]. All nodes were coloured with continuous mapping to represent Log2FC and were sized to represent Q-values.

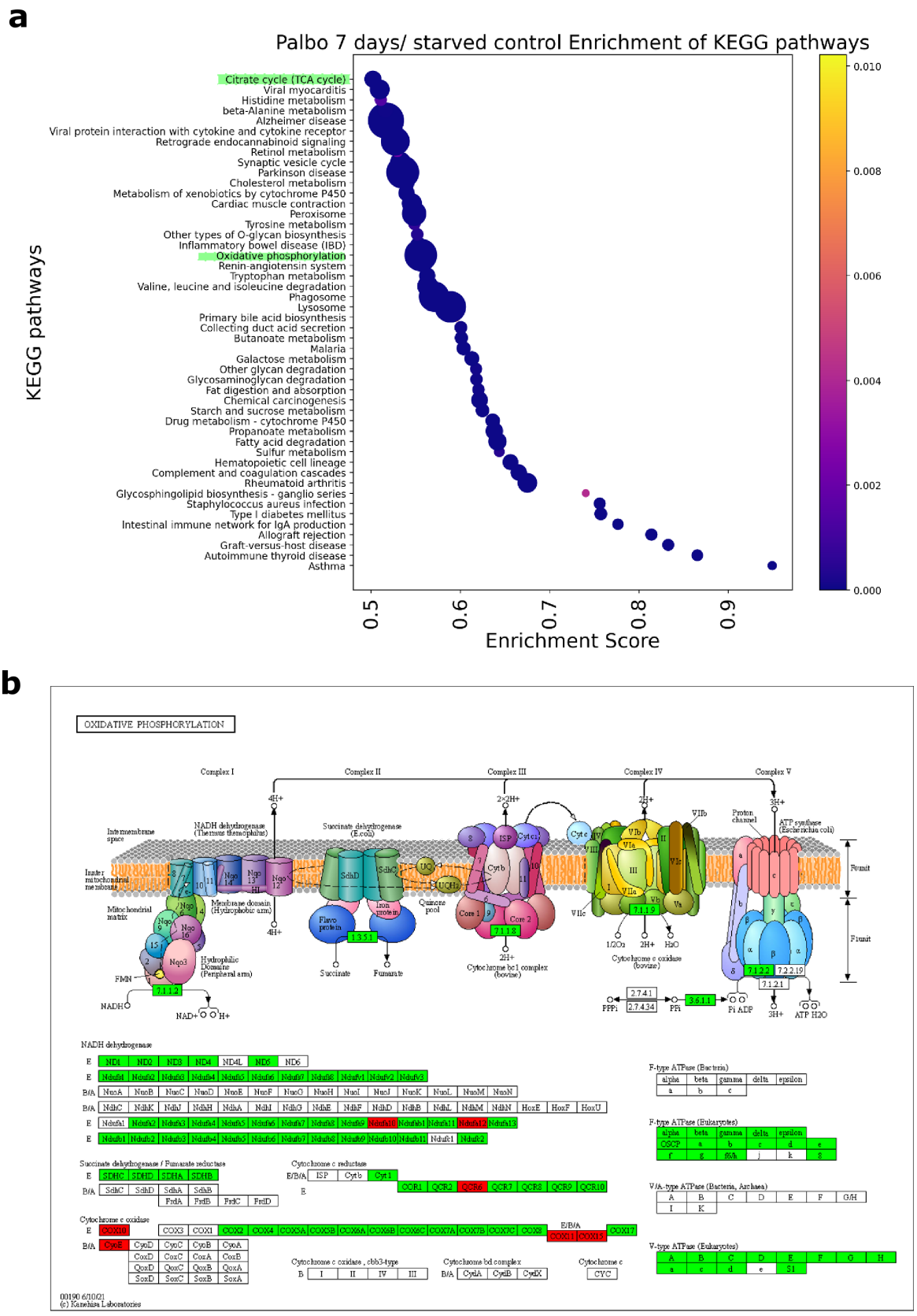


Figure 7.11: **Enrichment of proteins found in KEGG pathways for oxidative phosphorylation.** **(a)** Enrichment of KEGG pathways for Palbo 7 days versus starved control samples. Oxidative phosphorylation and TCA cycle pathways are highlighted in green. Spectrum represents p-value (Benj-Hoch) with enrichment score > 0.5. Size of markers represents count in group. **(b)** KEGG mapper wiring of oxidative phosphorylation pathway where upregulated proteins in the pathway are highlighted in green whilst downregulated proteins are highlighted in red.

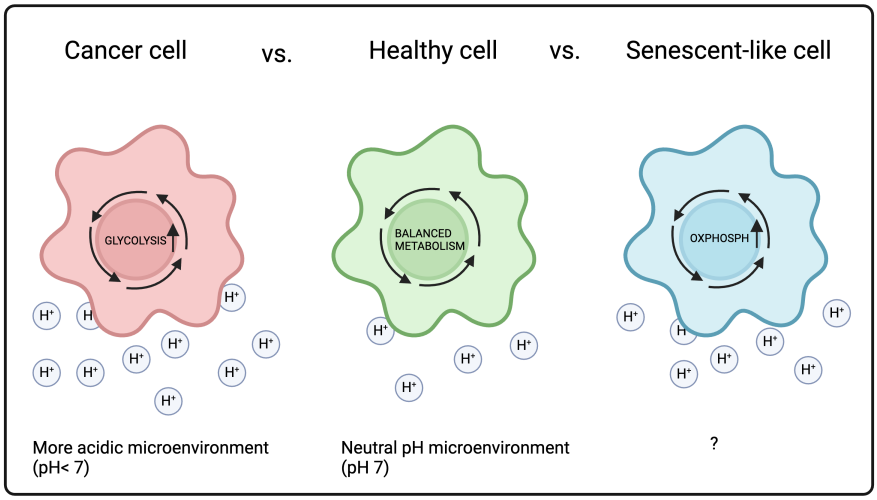


Figure 7.12: **Graphical summary of the Warburg effect in a senescent-like population arising from CDK4/6 inhibition in triple negative breast cancer cells.** (Created in BioRender. Beykou, M. (2024) BioRender.com/d64j655).

7.5 Summary and future direction

This chapter investigated the effects of CDK4/6 inhibition on a triple negative breast cancer cell model, MDA-MB-231. Proteomic, phosphoproteomic and secretome analysis, as well as a study of pHe were reported to characterise the senescent-like phenotype which was found morphologically in Palbociclib-treated breast cancer cells. The main outcomes of the study are summarised as follows:

1. Altered levels of cell cycle regulators, immune response, and key senescence markers upon Palbociclib treatment for 7 days.

2. Morphological changes and fluorescence microscopy corroborate proteomic and phosphoproteomic results

3. Proteins associated with the oxidative phosphorylation pathway are upregulated after 7 days of Palbociclib treatment

4. pH change of cell culture media in Palbociclib-treated cells shows acidification as compared to conditioned media from untreated cells.

5. The senescent-like phenotype induced after 54 days of Palbociclib-treatment can be rescued both morphologically and with return to a proliferative state after washout for an average of 15 days.

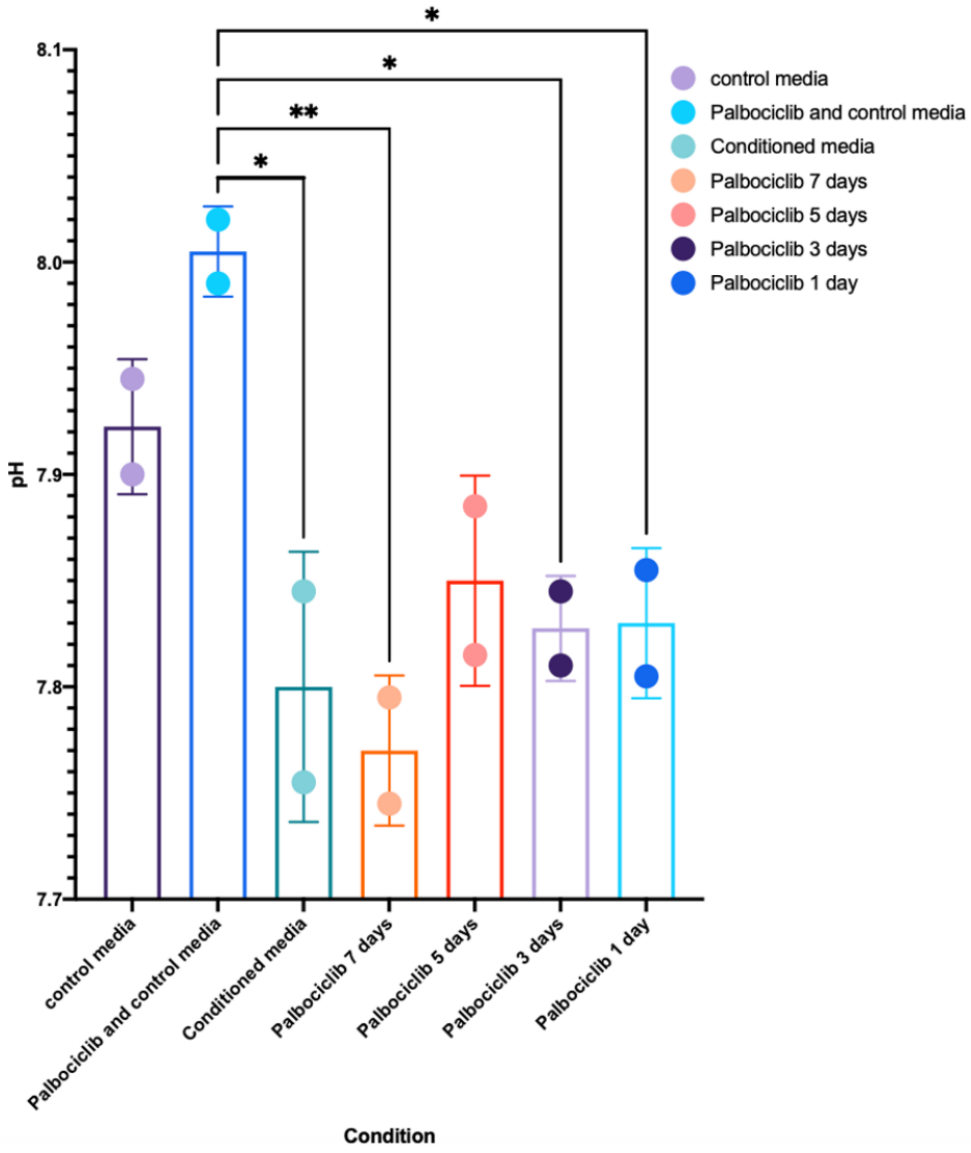


Figure 7.13: **pH changes in cell culture of Palbociclib-treated MDA-MB-231 cells.** The following conditions are evaluated for pH: Control media (DMEM 10% FBS, 1% P/S), Control media supplemented with 1uM Palbociclib, conditioned media of MDA-MB-231 cells, Palbociclib-treated MDA-MB-231 cell cultures for 1 day, 3 days, 5 days and 7 days. For all treated cultured no media changes were performed. Temperature of media at time of measurements was 31–33 °C. Ordinary One-way ANOVA and Tukey's multiple comparison test used for statistical comparison. Asterisks (*,**,***) denote p value classification.

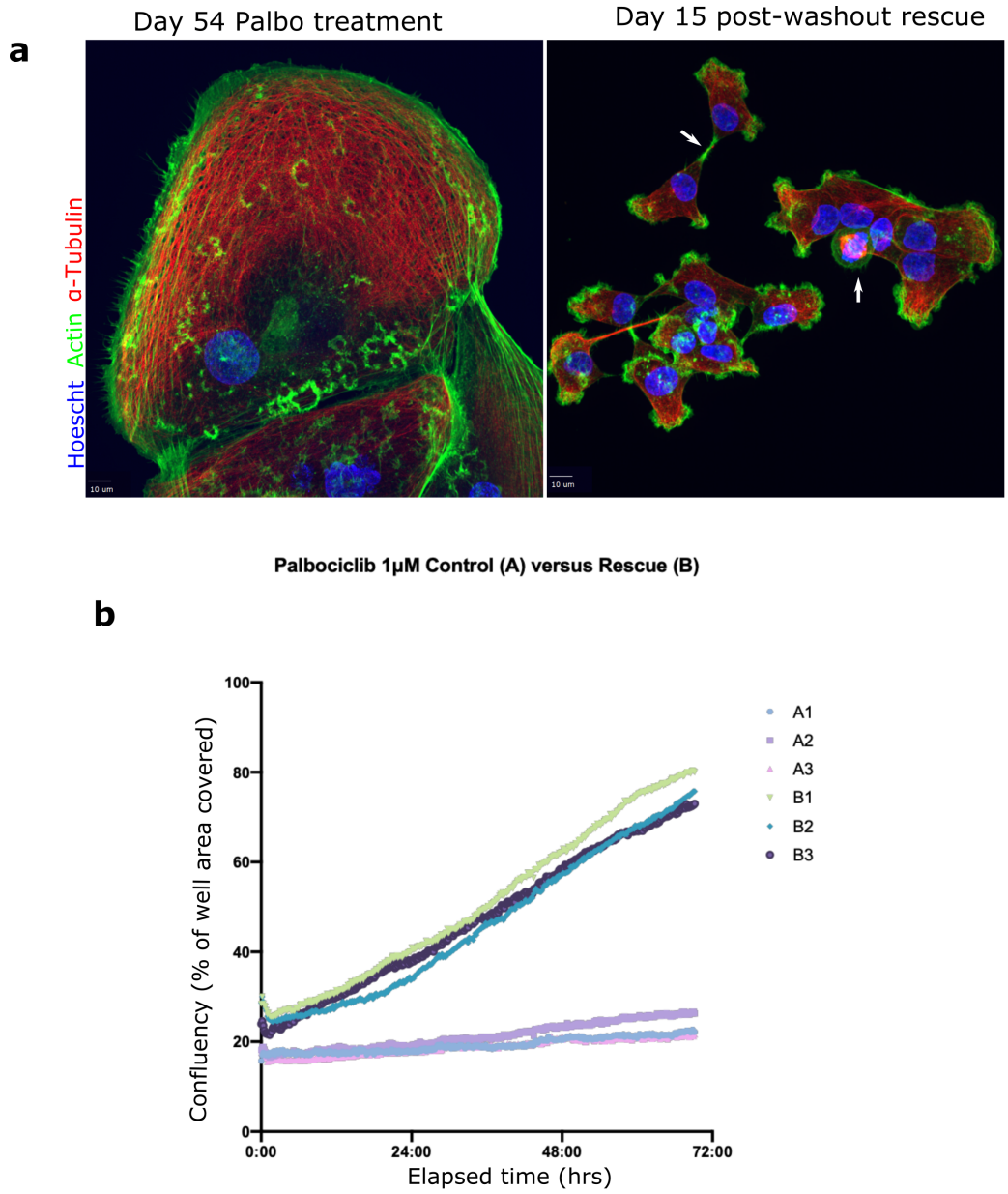


Figure 7.14: **Long-term culture of MDA-MB-231 in Palbociclib supplemented media and washout rescue.(a)** Confocal images at 63x oil magnification of cells on Day 54 of Palbociclib treatment and Day 15 post-washout. Arrows indicate mitotic cells. **(b)** Growth curve of long-term treated cells and washout rescue cells over 72 hours.

This study lays the groundwork for further investigation into the metabolic phenotype arising in senescent-like populations of breast cancer cells treated with CDK4/6 inhibitors which are not fully drug resistant or sensitive. This is likely to vary for different cell lines and the baseline of which has been investigated for a number of cell lines with a spectrum of hormone receptor positivity profiles and morphology (epithelial/mesenchymal) (Appendix). This dataset has been generated during this study and warrants further investigation with subsequent CDK4/6 inhibitor treatment as a follow up to the currently presented data. Furthermore, the use of a glycolysis inhibitor, such as 2-Deoxyglucose (a glucose analog), or an oxidative phosphorylation inhibitor, such as oligomycin, would further elucidate whether the senescent-like profile seen upon Palbociclib-treatment of MDA-MB-231 resembles oncogene-induced senescence or therapy-induced senescence phenotypes previously recorded.

References

[1] Y. A. Fouad and C. Aanei. "Revisiting the hallmarks of cancer". In: *American Journal of Cancer Research* 7.5 (2017), pp. 1016–1036.

[2] A. Rocca et al. "Progress with palbociclib in breast cancer: Latest evidence and clinical considerations". In: *Therapeutic Advances in Medical Oncology* 9.2 (Feb. 2017), pp. 83–105.

[3] B. O'Leary, R. S. Finn, and N. C. Turner. "Treating cancer with selective CDK4/6 inhibitors". In: *Nature Reviews Clinical Oncology* 13.7 (Mar. 2016), pp. 417–430.

[4] M. Malumbres and M. Barbacid. "Cell cycle, CDKs and cancer: A changing paradigm". In: *Nature Reviews Cancer* 9.3 (Mar. 2009), pp. 153–166.

[5] S. Goel et al. "CDK4/6 Inhibition in Cancer: Beyond Cell Cycle Arrest". In: *Trends in Cell Biology* 28.11 (Nov. 2018), pp. 911–925.

[6] Y. Hu et al. "Potential prospect of CDK4/6 inhibitors in triple-negative breast cancer". In: *Cancer Management and Research* 13 (2021), pp. 5223–5237.

[7] Q. Du et al. "The application and prospect of CDK4/6 inhibitors in malignant solid tumors". In: *Journal of Hematology and Oncology* 13.1 (May 2020), pp. 1–12.

[8] T. K. Eggersmann et al. "CDK4/6 Inhibitors Expand the Therapeutic Options in Breast Cancer: Palbociclib, Ribociclib and Abemaciclib". In: *BioDrugs* 33.2 (Apr. 2019), pp. 125–135.

[9] N. C. Turner et al. "Overall Survival with Palbociclib and Fulvestrant in Advanced Breast Cancer". In: *New England Journal of Medicine* 379.20 (Nov. 2018), pp. 1926–1936.

[10] M. A. George et al. "Clinical and Pharmacologic Differences of CDK4/6 Inhibitors in Breast Cancer". In: *Frontiers in Oncology* 11 (July 2021), p. 2471.

[11] C. I. Wells et al. "Quantifying CDK inhibitor selectivity in live cells". In: *Nature Communications* 11.1 (Dec. 2020).

[12] G. Bianchini et al. "Triple-negative breast cancer: Challenges and opportunities of a heterogeneous disease". In: *Nature Reviews Clinical Oncology* 13.11 (Nov. 2016), pp. 674–690.

[13] R. S. Finn et al. “PD 0332991, a selective cyclin D kinase 4/6 inhibitor, preferentially inhibits proliferation of luminal estrogen receptor-positive human breast cancer cell lines in vitro”. In: *Breast Cancer Research* 11.5 (Oct. 2009), R77.

[14] A. C. Garrido-Castro and S. Goel. “CDK4/6 Inhibition in Breast Cancer: Mechanisms of Response and Treatment Failure”. In: *Current Breast Cancer Reports* 9.1 (Mar. 2017), pp. 26–33.

[15] J. L. Dean et al. “Therapeutic CDK4/6 inhibition in breast cancer: Key mechanisms of response and failure”. In: *Oncogene* 29.28 (May 2010), pp. 4018–4032.

[16] Z. Li et al. “Loss of the FAT1 Tumor Suppressor Promotes Resistance to CDK4/6 Inhibitors via the Hippo Pathway”. In: *Cancer Cell* 34.6 (Dec. 2018), pp. 893–905.

[17] U. S. Asghar et al. “Single-cell dynamics determines response to CDK4/6 inhibition in triple-negative breast cancer”. In: *Clinical Cancer Research* 23.18 (Sept. 2017), pp. 5561–5572.

[18] K. Pandey et al. “Combined cdk2 and cdk4/6 inhibition overcomes palbociclib resistance in breast cancer by enhancing senescence”. In: *Cancers* 12.12 (Nov. 2020), pp. 1–17.

[19] X. Gong et al. “Genomic Aberrations that Activate D-type Cyclins Are Associated with Enhanced Sensitivity to the CDK4 and CDK6 Inhibitor Abemaciclib”. In: *Cancer Cell* 32.6 (Dec. 2017), pp. 761–776.

[20] A. C. Watt and S. Goel. “Cellular mechanisms underlying response and resistance to CDK4/6 inhibitors in the treatment of hormone receptor-positive breast cancer”. In: *Breast Cancer Research* 24.1 (Mar. 2022), pp. 1–11.

[21] S. F. Schoninger and S. W. Blain. “The ongoing search for biomarkers of CDK4/6 inhibitor responsiveness in breast cancer”. In: *Molecular Cancer Therapeutics* 19.1 (2020), pp. 3–12.

[22] Z. Li et al. “Mechanisms of CDK4/6 Inhibitor Resistance in Luminal Breast Cancer”. In: *Frontiers in Pharmacology* 11 (Nov. 2020), p. 1723.

[23] S. Llanos et al. “Lysosomal trapping of palbociclib and its functional implications”. In: *Oncogene* 38.20 (May 2019), pp. 3886–3902.

[24] T. Inao et al. “Different sensitivities of senescent breast cancer cells to immune cell-mediated cytotoxicity”. In: *Cancer Science* 110.9 (Sept. 2019), pp. 2690–2699.

[25] S. Vijayaraghavan et al. “CDK4/6 and autophagy inhibitors synergistically induce senescence in Rb positive cytoplasmic cyclin e negative cancers”. In: *Nature Communications* 8.15916 (June 2017).

[26] Y. Huang, H. Wu, and X. Li. “Novel sequential treatment with palbociclib enhances the effect of cisplatin in RB-proficient triple-negative breast cancer”. In: *Cancer Cell International* 20.1 (Oct. 2020), pp. 1–14.

[27] J. A. Ewald et al. “Therapy-induced senescence in cancer”. In: *Journal of the National Cancer Institute* 102.20 (Oct. 2010), pp. 1536–1546.

[28] A. Hernandez-Segura, J. Nehme, and M. Demaria. “Hallmarks of Cellular Senescence”. In: *Trends in Cell Biology* 28.6 (June 2018), pp. 436–453.

[29] H. G. Lee et al. “Senescent tumor cells building three-dimensional tumor clusters”. In: *Scientific Reports* 8.1 (July 2018), pp. 1–9.

[30] T. Saleh, L. Tyutyunyk-Massey, and D. A. Gewirtz. “Tumor cell escape from therapy-induced senescence as a model of disease recurrence after dormancy”. In: *Cancer Research* 79.6 (Mar. 2019), pp. 1044–1046.

[31] E. Fitsiou, A. Soto-Gamez, and M. Demaria. “Biological functions of therapy-induced senescence in cancer”. In: *Seminars in Cancer Biology* 81 (June 2022), pp. 5–13.

[32] B. Wang, J. Kohli, and M. Demaria. “Senescent Cells in Cancer Therapy: Friends or Foes?” In: *Trends in Cancer* 6.10 (2020), pp. 838–857.

[33] S. Lee and C. A. Schmitt. “The dynamic nature of senescence in cancer”. In: *Nature Cell Biology* 21.1 (Jan. 2019), pp. 94–101.

[34] S. Goel et al. “CDK4/6 inhibition triggers anti-tumour immunity”. In: *Nature* 548.7668 (Aug. 2017), pp. 471–475.

[35] A. Chakrabarty et al. “Senescence-Induced Chemoresistance in Triple Negative Breast Cancer and Evolution-Based Treatment Strategies”. In: *Frontiers in Oncology* 11 (June 2021), p. 2335.

[36] ClinicalTrials.gov. *PAveMenT: Palbociclib and Avelumab in Metastatic AR+ Triple Negative Breast Cancer (PAveMenT)*. 2023.

[37] M. Li et al. “Oncogene-induced cellular senescence elicits an anti-Warburg effect”. In: *Proteomics* 13.17 (Sept. 2013), pp. 2585–2596.

[38] J. R. Dörr et al. “Synthetic lethal metabolic targeting of cellular senescence in cancer therapy”. In: *Nature* 501.7467 (2013), pp. 421–425.

[39] J. Sabbatinelli et al. “Where Metabolism Meets Senescence: Focus on Endothelial Cells”. In: *Frontiers in Physiology* 10 (Dec. 2019), p. 501005.

[40] W. Li et al. “Cellular senescence triggers intracellular acidification and lysosomal pH alkalinized via ATP6AP2 attenuation in breast cancer cells”. In: *Communications Biology* 6.1 (Nov. 2023), pp. 1–17.

[41] E. S. Knudsen and A. K. Witkiewicz. “The Strange Case of CDK4/6 Inhibitors: Mechanisms, Resistance, and Combination Strategies”. In: *Trends in Cancer* 3.1 (Jan. 2017), pp. 39–55.

[42] S. Tyanova et al. “The Perseus computational platform for comprehensive analysis of (prote)omics data”. In: *Nature Methods* 13.9 (June 2016), pp. 731–740.

[43] J. Goedhart and M. S. Luijsterburg. “VolcaNoseR is a web app for creating, exploring, labeling and sharing volcano plots”. In: *Scientific Reports* 10.1 (Nov. 2020), pp. 1–5.

[44] P. Shannon et al. “Cytoscape: A software Environment for integrated models of biomolecular interaction networks”. In: *Genome Research* 13.11 (Nov. 2003), pp. 2498–2504.

[45] D. Zenkova et al. *Phantasus: visual and interactive gene expression analysis*. 2022.

[46] Renesh Bedre. *reneshbedre/bioinfokit: Bioinformatics data analysis and visualization toolkit*. 2022.

[47] Y. Perez-Riverol et al. “The PRIDE database and related tools and resources in 2019: Improving support for quantification data”. In: *Nucleic Acids Research* 47.D1 (Jan. 2019), pp. D442–D450.

[48] E. W. Deutsch et al. “The ProteomeXchange consortium in 2020: Enabling ’big data’ approaches in proteomics”. In: *Nucleic Acids Research* 48.D1 (Jan. 2020), pp. D1145–D1152.

[49] M. Beykou et al. “Proteomic characterisation of triple negative breast cancer cells following CDK4/6 inhibition”. In: *Scientific Data* 9.1 (2022).

[50] K. M. Aird and R. Zhang. “ATM in senescence”. In: *Oncotarget* 6.17 (2015), pp. 14729–14730.

[51] Z. Darzynkiewicz. “Perturbation of nucleotide metabolism - The driving force of oncogene-induced senescence”. In: *Oncotarget* 4.5 (2013), pp. 649–650.

[52] H. Paluvai, E. Di Giorgio, and C. Brancolini. “The histone code of senescence”. In: *Cells* 9.2 (Feb. 2020).

[53] T. Jost et al. “Palbociclib Induces Senescence in Melanoma and Breast Cancer Cells and Leads to Additive Growth Arrest in Combination With Irradiation”. In: *Frontiers in Oncology* 11 (Oct. 2021).

[54] M. Kanehisa et al. “KEGG as a reference resource for gene and protein annotation”. In: *Nucleic Acids Research* 44.D1 (Jan. 2016), pp. D457–D462.

[55] S. Carbon et al. “The Gene Ontology resource: Enriching a GOld mine”. In: *Nucleic Acids Research* 49.D1 (Jan. 2021), pp. D325–D334.

[56] M. Ashburner et al. “Gene ontology: Tool for the unification of biology”. In: *Nature Genetics* 25.1 (May 2000), pp. 25–29.

[57] A. Shvartsur and B. Bonavida. “Trop2 and its overexpression in cancers: Regulation and clinical/therapeutic implications”. In: *Genes and Cancer* 6.3-4 (2015), pp. 84–105.

[58] S. Son et al. “Anti-Trop2 antibody-conjugated bioreducible nanoparticles for targeted triple negative breast cancer therapy”. In: *International Journal of Biological Macromolecules* 110 (Apr. 2018), pp. 406–415.

[59] S. Zaman et al. “Targeting trop-2 in solid tumors: Future prospects”. In: *OncoTargets and Therapy* 12 (2019), pp. 1781–1790.

[60] M. Marhold. “Current state of clinical development of TROP2-directed antibody–drug conjugates for triple-negative breast cancer”. In: *Memo - Magazine of European Medical Oncology* 15.2 (Dec. 2022), pp. 129–132.

Chapter 8

Conclusion

Novel cancer diagnostic technologies have garnered significant interest in the global community as evidence grows that cancer incidence and mortality continue to be a global concern. Research to identify, characterise and deploy novel biomarkers in diagnostic technologies has become an integral part of the path to combat the diversity of cancer types identified worldwide. Concurrently, the portability, affordability, rapidness and ease of use of Lab-on-Chip has helped create Point-of-Care diagnostic devices for a host of other conditions, such as infectious disease identification. To develop the amalgamation of electrochemical sensors and cancer diagnostics, convergence science has brought the necessary tools together.

The ISFET as an electrochemical sensor has been particularly successful in the development of portable and rapid diagnostic tests for viral infectious diseases by detecting nucleic acid amplification. The inherent pH sensitivity of ISFET arrays makes them adaptable to a range of other conditions, such as cancer detection. The Warburg effect which results in cancer extracellular acidity has been a re-visited contender as a cancer biomarker for early diagnosis. Despite ISFETs for cancer detection having been investigated in previous works, the physiological relevance of measurements and scalability of use, as well as the impact of these sensing technologies on cell responses has been poorly understood. This thesis aims to present the adaptation of a 0.35um CMOS Lab-on-Chip ISFET array integrated on a handheld Point-of-Care testing device, known as Lacewing, for biophysical and biochemical cancer cell detection.

This thesis focused on the adaptation of ISFET arrays implemented in CMOS technology for cancer cell detection by extracellular pH. Firstly, the physiological relevance of the cell-ISFET interactions were confirmed by evaluating the viability, morphological, mechanical and adhesive profile of tumorigenic and non-tumorigenic cells on chip as compared to commercially available, plastic culture vessels. Additional surface treatment with collagen, fibronectin or PLOL to enhance the bio-mimetic properties of the ISFET surface moderately increased attachment efficiency, whilst sensor sensitivity of collagen-treated ISFET surface showed that it can be

used in future cell-based ISFET applications.

A novel method for real-time pH detection of cancer cells on chip is demonstrated on Titan arrays where both long-term net pH changes and rapid pH changes during mitotic entry are recorded. Timelapse microscopy of coordinated osteosarcoma cells on chip shows the moment of nuclear envelope breakdown which we hypothesize to co-occur with an abrupt "acidification peak" in sensor output. This protocol demonstrates the possibilities for whole cell-based applications of mammalian cell detection on chip deriving from pH changes. The importance of pH in coordinated metabolic, homeostatic and mitotic signaling mechanisms can be exploited for diagnostic applications in a range of conditions including cancer types.

Lastly, therapeutic intervention with CDK4/6 inhibitor, Palbociclib, in a resistant, triple negative breast cancer cell line was characterised by proteomics, phosphoproteomics and secretome data. Acidification of conditioned media despite slow growth in treated cells indicates potential metabolic changes associated with increased oxidative phosphorylation. The senescent-like population upon treatment was rescuable, it calls to question whether the detected changes in extracellular pH may be utilised to characterise drug resistance in future biomedical applications. In conclusion, the surface study, culture media and real-time pH detection from mammalian cells on ISFET arrays guide the design and detection of cell culture on chip which can be implemented as part of a handheld PoC device for diagnostic applications.

8.1 Future work recommendations

Microfluidics Current work with cell cultures on lab-on-chip can be less physiologically representative due to introduction of perturbations by the physical exchange of solutions in each well chamber. Microfluidic re-design to allow for media exchange through a flow system on multi-well manifolds (4, 6, 10-well) would allow drug additions and media replenishment in multiplexed experiments for each individual sample without perturbation to the system. Accompanied by a CO_2 perfusion on chip system, this would be a fully portable and independent system operable at the point-of-care level.

Therapeutic intervention To delineate the contributions of oxidative phosphorylation, glycolysis and inherent fluctuations in the system due to third parameters (e.g. cell growth, glucose consumption, degradation), consecutive drug additions such as of a glucose analog, 2-DG, would provide a step in the next direction for understanding the sensing parameters on chip. This could also be reflected in the use of the Seahorse analyzer as a verification tool for metabolic contributions.

Multi-ion detection The ionic fluctuations of cells are closely coupled. The addition of multi-ion sensing membranes on chip would allow a full characterisation of the changes in cells on chip. Real-time and sensitive detection of the bioelectric properties of cancer cells on an "ion imaging" platform could provide a novel diagnostic and therapeutic avenue.

Combination with aptamer-antibody sensing on chip Single biomarker detection is not a translatable option in the real-world of cancer testing. Diverse and often unknown forms of cancer types arise where biomarker testing is an integral part of diagnosis, characterisation and treatment plans. Multiple testing for common biomarkers, whose reliability and wider acceptance in the community is well-known could be an important component of advancing PoC testing. The combination of cells and antigen-antibody recognition on chip could make a portable cancer subtyping tool.

Liquid biopsy Liquid biopsies (blood, saliva, urine and cerebrospinal fluid) are minimally invasive and inexpensive sources of cellular material which makes them an attractive diagnostic tool. Circulatory Tumour Cells (CTCs) have become an attractive candidate for early diagnosis in liquid biopsies, such as whole blood samples. Commercially available techniques (such as Parsortix, ApoStream and CELLSEARCH system) face a number of caveats such as costly technology, often only intended for research use, as well as loss of marker expression during epithelial-to-mesenchymal transition, and a lack of integrated downstream functional assaying. As such, CTCs are excluded from current clinical testing procedures. Technologies in current research have shown success in utilizing CTC electrical charge for isolation, however, these tools lack downstream assaying of captured cells to provide insight into cancer state. To date, CTCs are heavily studied in non-predictive and indirect assays, such as DNA fragments, due to difficulties in retrieval post-isolation, however, an integrated extraction and detection assay on ISFETs would allow CTC isolation, monitoring and downstream identification to better understand and predict early diagnosis of a dynamic cancer state in patients.

The current ISFET LoC technology, as part of Lacewing, could be adapted for a full workflow of a PoC device for cancer subtyping using CTC extraction and detection. CTC purification and detection from liquid biopsy samples and perform real-time data collection of ion flux data from CTCs of several cancer types. They key outcomes of this endeavour would provide critical data on the efficiency of cancer cell extraction from complex mammalian cell solutions based on electrical charge properties to allow this technology to be compared sufficiently with standard CTC extraction kits available in the market. This would pave the way for PoC CTC extraction based on biophysical properties to enter the biomedical industry and create a faster, simpler, portable extraction with no pre-processing steps for the user.

Appendix A

Palbociclib proteomics supplementary tables

A.1 Regulated KEGG pathways

A.2 Antibodies and dyes for proteomics validation.

Table A.1: KEGG pathways regulated in response to Palbociclib

Selection column	Selection value	Category column	Category value	Total size	Selection size	Category size	Intersection size	Enrichment factor	P value	Benj. Hoch. FDR
regulation	up-regulated	KEGG name	Asthma	8990	1586	8	8	5.6683	9.25E-07	1.60E-05
regulation	up-regulated	KEGG name	Autoimmune thyroid disease	8990	1586	14	13	5.2635	1.78E-09	6.28E-08
regulation	up-regulated	KEGG name	Graft-versus-host disease	8990	1586	15	13	4.9126	1.10E-08	3.19E-07
regulation	up-regulated	KEGG name	Allograft rejection	8990	1586	15	13	4.9126	1.10E-08	3.19E-07
regulation	up-regulated	KEGG name	Intestinal immune network for IgA production	8990	1586	12	10	4.7236	1.28E-06	2.04E-05
regulation	up-regulated	KEGG name	Type I diabetes mellitus	8990	1586	16	13	4.6055	4.84E-08	1.12E-06
regulation	up-regulated	KEGG name	Glycosphingolipid biosynthesis - ganglio series	8990	1586	5	4	4.5347	0.0039782	0.015114
regulation	up-regulated	KEGG name	Staphylococcus aureus infection	8990	1586	13	10	4.3603	4.57E-06	6.30E-05
regulation	up-regulated	KEGG name	Fatty acid biosynthesis	8990	1586	4	3	4.2513	0.018066	0.049621
regulation	up-regulated	KEGG name	Glycosaminoglycan degradation	8990	1586	14	10	4.0488	1.32E-05	0.00016253
regulation	up-regulated	KEGG name	Aminobenzoate degradation	8990	1586	7	5	4.0488	0.0024242	0.010159
regulation	down-regulated	KEGG name	DNA replication	8990	2032	35	32	4.045	5.46E-18	1.48E-15
regulation	up-regulated	KEGG name	Complement and coagulation cascades	8990	1586	20	14	3.9678	3.29E-07	6.59E-06
regulation	down-regulated	KEGG name	Spliceosome	8990	2032	123	110	3.9566	4.52E-57	3.67E-54
regulation	up-regulated	KEGG name	Primary bile acid biosynthesis	8990	1586	6	4	3.7789	0.0098333	0.031143
regulation	up-regulated	KEGG name	Malaria	8990	1586	21	14	3.7789	8.15E-07	1.44E-05
regulation	up-regulated	KEGG name	Caprolactam degradation	8990	1586	6	4	3.7789	0.0098333	0.031143
regulation	up-regulated	KEGG name	ECM-receptor interaction	8990	1586	40	25	3.5427	2.84E-10	1.26E-08
regulation	up-regulated	KEGG name	Other glycan degradation	8990	1586	13	8	3.4882	0.00045286	0.0029167
regulation	up-regulated	KEGG name	Rheumatoid arthritis	8990	1586	36	22	3.464	6.09E-09	1.91E-07
regulation	up-regulated	KEGG name	Antigen processing and presentation	8990	1586	43	26	3.4274	3.53E-10	1.44E-08
regulation	down-regulated	KEGG name	Mismatch repair	8990	2032	22	17	3.4187	7.35E-08	1.62E-06
regulation	up-regulated	KEGG name	Benzoate degradation	8990	1586	10	6	3.401	0.0028975	0.011662
regulation	up-regulated	KEGG name	Hematopoietic cell lineage	8990	1586	17	10	3.3343	0.00014363	0.0011916
regulation	up-regulated	KEGG name	Viral myocarditis	8990	1586	41	24	3.3181	4.17E-09	1.36E-07
regulation	up-regulated	KEGG name	Drug metabolism - cytochrome P450	8990	1586	19	11	3.2817	8.08E-05	0.00078233
regulation	down-regulated	KEGG name	Base excision repair	8990	2032	29	21	3.2037	1.42E-08	3.83E-07
regulation	up-regulated	KEGG name	Fatty acid metabolism	8990	1586	32	18	3.1884	8.09E-07	1.44E-05
regulation	up-regulated	KEGG name	Cell adhesion molecules (CAMs)	8990	1586	52	29	3.1612	4.97E-10	1.92E-08
regulation	up-regulated	KEGG name	Retinol metabolism	8990	1586	9	5	3.1491	0.0098756	0.031143
regulation	up-regulated	KEGG name	Metabolism of xenobiotics by cytochrome P450	8990	1586	22	12	3.0918	8.25E-05	0.00078947
regulation	up-regulated	KEGG name	Fat digestion and absorption	8990	1586	13	7	3.0522	0.0028294	0.011444
regulation	up-regulated	KEGG name	Arachidonic acid metabolism	8990	1586	13	7	3.0522	0.0028294	0.011444
regulation	up-regulated	KEGG name	Lysosome	8990	1586	93	50	3.0475	2.07E-15	4.22E-13
regulation	up-regulated	KEGG name	Valine, leucine and isoleucine degradation	8990	1586	41	22	3.0416	1.50E-07	3.13E-06
regulation	up-regulated	KEGG name	Ether lipid metabolism	8990	1586	17	9	3.0009	0.00084214	0.0047218
regulation	up-regulated	KEGG name	Phagosome	8990	1586	92	48	2.9574	3.44E-14	4.66E-12
regulation	down-regulated	KEGG name	Cell cycle - yeast	8990	2032	59	38	2.8495	5.69E-12	4.21E-10
regulation	up-regulated	KEGG name	Tryptophan metabolism	8990	1586	26	13	2.8342	0.00013063	0.0010948
regulation	up-regulated	KEGG name	Steroid hormone biosynthesis	8990	1586	14	7	2.8342	0.0046634	0.017147
regulation	up-regulated	KEGG name	Starch and sucrose metabolism	8990	1586	20	10	2.8342	0.00076436	0.0043762
regulation	up-regulated	KEGG name	Other types of O-glycan biosynthesis	8990	1586	16	8	2.8342	0.0025355	0.010426
regulation	up-regulated	KEGG name	Galactose metabolism	8990	1586	18	9	2.8342	0.0013883	0.0064866
regulation	up-regulated	KEGG name	Butanoate metabolism	8990	1586	20	10	2.8342	0.00076436	0.0043762
regulation	down-regulated	KEGG name	Ribosome	8990	2032	83	52	2.7718	3.90E-15	6.35E-13
regulation	up-regulated	KEGG name	Propanoate metabolism	8990	1586	27	13	2.7292	0.00020772	0.0016041
regulation	down-regulated	KEGG name	Ribosome biogenesis in eukaryotes	8990	2032	70	43	2.7177	2.43E-12	1.98E-10
regulation	up-regulated	KEGG name	Steroid biosynthesis	8990	1586	15	7	2.6452	0.0072058	0.024512
regulation	up-regulated	KEGG name	Neuroactive ligand-receptor interaction	8990	1586	24	11	2.598	0.0010165	0.0052216
regulation	up-regulated	KEGG name	Peroxisome	8990	1586	58	26	2.541	1.05E-06	1.74E-05
regulation	down-regulated	KEGG name	Cell cycle	8990	2032	99	56	2.5026	1.71E-13	1.73E-11
regulation	up-regulated	KEGG name	Alzheimer's disease	8990	1586	124	54	2.4685	9.56E-12	6.48E-10
regulation	up-regulated	KEGG name	Oxidative phosphorylation	8990	1586	104	45	2.4527	6.30E-10	2.33E-08
regulation	up-regulated	KEGG name	Cardiac muscle contraction	8990	1586	35	15	2.4293	0.0003256	0.0022433
regulation	up-regulated	KEGG name	Parkinson's disease	8990	1586	101	43	2.4133	2.71E-09	9.17E-08
regulation	up-regulated	KEGG name	Glutathione metabolism	8990	1586	33	14	2.4048	0.00056719	0.0034412
regulation	up-regulated	KEGG name	ABC transporters	8990	1586	19	8	2.3867	0.0083349	0.027772
regulation	down-regulated	KEGG name	Meiosis - yeast	8990	2032	52	28	2.3823	6.94E-07	1.28E-05
regulation	up-regulated	KEGG name	Sphingolipid metabolism	8990	1586	24	10	2.3618	0.0037456	0.014364
regulation	up-regulated	KEGG name	PPAR signaling pathway	8990	1586	36	15	2.3618	0.00046025	0.0029233
regulation	down-regulated	KEGG name	mRNA surveillance pathway	8990	2032	68	36	2.3422	3.44E-08	8.48E-07
regulation	up-regulated	KEGG name	Cytokine-cytokine receptor interaction	8990	1586	46	19	2.3413	0.00010218	0.00092302
regulation	up-regulated	KEGG name	Biosynthesis of unsaturated fatty acids	8990	1586	17	7	2.334	0.014788	0.042334
regulation	up-regulated	KEGG name	Leishmaniasis	8990	1586	39	16	2.3255	0.00037192	0.0024989
regulation	down-regulated	KEGG name	Nucleotide excision repair	8990	2032	42	22	2.3174	1.81E-05	0.00021658
regulation	down-regulated	KEGG name	Homologous recombination	8990	2032	23	12	2.3083	0.0014178	0.0065866
regulation	up-regulated	KEGG name	Pyruvate metabolism	8990	1586	32	13	2.3028	0.0013703	0.0064772
regulation	down-regulated	KEGG name	RNA polymerase	8990	2032	27	14	2.294	0.00064065	0.0038581
regulation	up-regulated	KEGG name	Amino sugar and nucleotide sugar metabolism	8990	1586	40	16	2.2673	0.00051114	0.003149
regulation	down-regulated	KEGG name	RNA degradation	8990	2032	59	30	2.2496	1.36E-06	2.13E-05
regulation	up-regulated	KEGG name	Protein digestion and absorption	8990	1586	23	9	2.218	0.0088741	0.028744
regulation	down-regulated	KEGG name	Basal transcription factors	8990	2032	36	18	2.2121	0.00020796	0.0016041
regulation	up-regulated	KEGG name	Glycerolipid metabolism	8990	1586	31	12	2.1942	0.0031686	0.012554
regulation	up-regulated	KEGG name	Arrhythmogenic right ventricular cardiomyopathy (ARVC)	8990	1586	31	12	2.1942	0.0031686	0.012554
regulation	up-regulated	KEGG name	Glycerophospholipid metabolism	8990	1586	50	19	2.154	0.00034607	0.0023643
regulation	up-regulated	KEGG name	Endocrine and other factor-regulated calcium reabsorption	8990	1586	32	12	2.1256	0.0041791	0.01573
regulation	up-regulated	KEGG name	Amoebiasis	8990	1586	58	21	2.0523	0.00036795	0.0024929
regulation	up-regulated	KEGG name	Salivary secretion	8990	1586	36	13	2.0469	0.00421	0.015773
regulation	up-regulated	KEGG name	Citrate cycle (TCA cycle)	8990	1586	28	10	2.0244	0.011565	0.035202
regulation	up-regulated	KEGG name	Gastric acid secretion	8990	1586	34	12	2.0006	0.0068958	0.023655
regulation	up-regulated	KEGG name	Huntington's disease	8990	1586	144	50	1.9682	3.40E-07	6.59E-06
regulation	up-regulated	KEGG name	Dilated cardiomyopathy	8990	1586	35	12	1.9434	0.0086494	0.02849
regulation	down-regulated	KEGG name	Pyrimidine metabolism	8990	2032	85	37	1.9258	8.69E-06	0.0001122
regulation	down-regulated	KEGG name	RNA transport	8990	2032	132	57	1.9105	6.16E-08	1.39E-06
regulation	up-regulated	KEGG name	Hypertrophic cardiomyopathy (HCM)	8990	1586	33	11	1.8894	0.013841	0.040771
regulation	up-regulated	KEGG name	ko05152	8990	1586	106	35	1.8716	5.24E-05	0.00055302
regulation	up-regulated	KEGG name	Lysine degradation	8990	1586	37	12	1.8384	0.013045	0.038564
regulation	down-regulated	KEGG name	Systemic lupus erythematosus	8990	2032	32	13	1.7973	0.010649	0.032918
regulation	up-regulated	KEGG name	N-Glycan biosynthesis	8990	1586	38	12	1.79	0.015713	0.044512
regulation	up-regulated	KEGG name	Calcium signaling pathway	8990	1586	59	17	1.6333	0.012276	0.036965
regulation	up-regulated	KEGG name	Natural killer cell mediated cytotoxicity	8990	1586	60	17	1.606	0.01412	0.041146
regulation	up-regulated	KEGG name	Focal adhesion	8990	1586	121	34	1.5928	0.0013818	0.0064866
regulation	up-regulated	KEGG name	Regulation of actin cytoskeleton	8990	1586	129	36	1.5819	0.0011863	0.0058102
regulation	up-regulated	KEGG name	Endocytosis	8990	1586	152	41	1.529	0.0011747	0.0057881
regulation	up-regulated	KEGG name	Toxoplasmosis	8990	1586	82	22	1.5208	0.011634	0.035202
regulation	down-regulated	KEGG name	Purine metabolism	8990	2032	113	37	1.4486	0.0036878	0.014277
regulation	up-regulated	KEGG name	Protein processing in endoplasmic reticulum	8990	1586	137	33	1.3654	0.012858	0.03815

Table A.2: Immunofluorescence antibodies and dyes

Antibodies/Dyes	**Dilution**	**Manufacturer**
pRb(807/811) (Rabbit)	1:1000	Cell signaling (Cat 8516S)
KI67 (Rabbit)	1:50	Abcam (#16667)
LMNB1 (Rabbit)	1:1000	Abcam (#16048)
Tubulin Alpha (Rat)	1:1000	BioRad (Ref MCA78G)
Alexa Fluor 488 Phalloidin	1:1000	Invitrogen (Cat A-12379)
Alexa Fluor 568 Phalloidin	1:1000	Invitrogen (Cat A-12380)
Goat anti-Rat IgG (H+L) Cross-Adsorbed Secondary Antibody, Alexa Fluor 568	1:1000	Invitrogen (Cat A-11077)
F(ab')2-Goat anti-Rabbit IgG (H+L) Cross-Adsorbed Alexa Fluor 647	1:1000	Invitrogen (Cat A-21246, Lot 2147629)
Goat anti-Rabbit IgG (H+L) Secondary antibody Highly Cross-Adsorbed, Alexa Fluor 488	1:1000	Invitrogen (Cat A-11034)
Goat anti-rat IgG (H+L) Secondary antibody Cross-Adsorbed, Alexa Fluor 647	1:1000	Invitrogen (Cat A-21247)
Hoescht 33258	1:1000	Invitrogen (Cat H3569)

Appendix B

Breast cancer cell line subtypes total proteome panel

Acknowledgments: Cell culture and data collection in collaboration with George Skiadas (Molecular Cell Biology group, Prof. Clare Isacke lab, ICR). Proteomic dataset processing and bridging in collaboration with Dr. Theodoros Roumeliotis (Functional Proteomics group, Prof. Jyoti Choudhary lab, ICR).

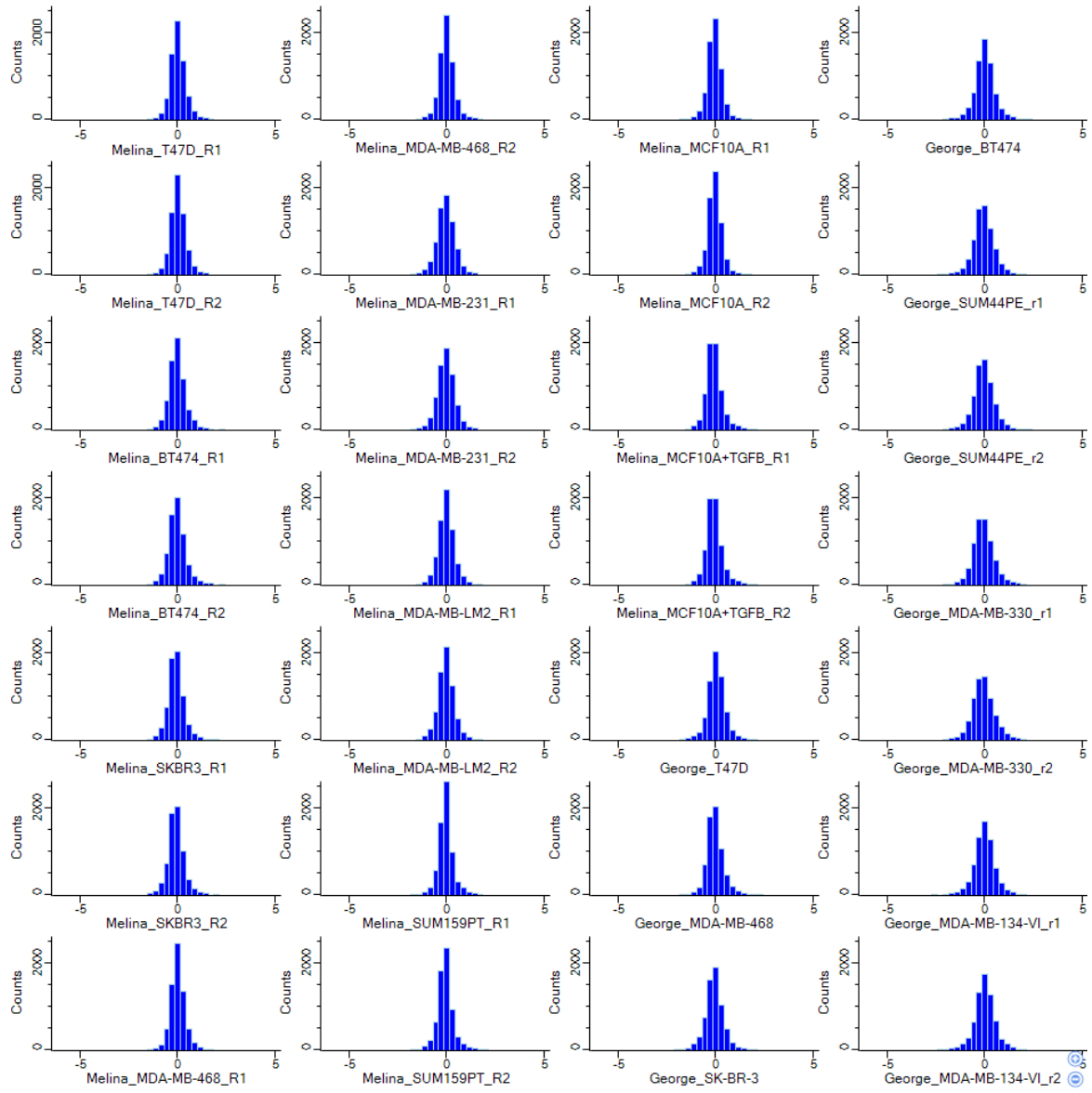


Figure B.1: Normalised counts for total proteome of each cell lines sample replicate in the dataset.

B.1 Normalisation

B.2 KEGG pathway enrichment of breast cancer cell subtypes

Table B.1: KEGG pathway 1D enrichment in breast cancer subtypes

Column	Type	Name	Size	Score	P value	Benj. Hoch. FDR	Mean	Median
BT474	KEGG pathway name	Synthesis and degradation of ketone bodies	8	0.71473753	0.00046666	0.01279438	1.32102616	1.17720747
MDA-MB-330	KEGG pathway name	Glycosaminoglycan degradation	8	0.71401047	0.00047293	0.01111393	0.72780924	0.73975411
MCF10A	KEGG pathway name	Ribosome	120	0.68789111	2.80E-38	9.20E-36	0.34173617	0.34993884
SKBR3	KEGG pathway name	Citrate cycle (TCA cycle)	28	0.66739932	1.03E-09	6.81E-08	0.49457134	0.56062236
MDA-MB-330	KEGG pathway name	Retinol metabolism	11	0.64657339	0.00020641	0.00565898	0.68974755	0.72403973
MDA-MB-330	KEGG pathway name	Other glycan degradation	12	0.62364809	0.00018523	0.00609402	0.70896663	0.5068908
MCF10A+TGFB	KEGG pathway name	ECM-receptor interaction	26	0.61690984	5.40E-08	2.54E-06	1.0168996	1.00206208
MCF10A+TGFB	KEGG pathway name	African trypanosomiasis	9	0.61198371	0.00148474	0.0093938	0.64719874	0.37366533
MCF10A	KEGG pathway name	Hematopoietic cell lineage	11	0.59980956	0.00057607	0.01263504	0.58981952	0.47159076
MCF10A+TGFB	KEGG pathway name	Cytokine-cytokine receptor interaction	9	0.58700149	0.00230421	0.01263474	0.58558596	0.2438535
SUM159PT	KEGG pathway name	Hematopoietic cell lineage	11	0.58034227	0.00086564	0.01017124	0.58246192	0.91464013
MCF10A+TGFB	KEGG pathway name	Steroid biosynthesis	14	0.56974448	0.00022572	0.00239554	0.4174782	0.50311695
SUM159PT	KEGG pathway name	Malaria	11	0.56693205	0.00113817	0.01170184	0.59635008	0.57484579
SUM159PT	KEGG pathway name	ECM-receptor interaction	26	0.55199794	1.14E-06	9.39E-05	0.62923654	0.47264732
SKBR3	KEGG pathway name	2-Oxocarboxylic acid metabolism	13	0.55158055	0.00057932	0.00866347	0.2958314	0.50056726
MDA-MB-231	KEGG pathway name	Ribosome biogenesis in eukaryotes	66	0.52882543	1.31E-13	1.44E-11	0.34069287	0.39561905
BT474	KEGG pathway name	Valine, leucine and isoleucine degradation	42	0.50805481	1.31E-08	2.15E-06	0.66375637	0.66084784
MCF10A	KEGG pathway name	Ribosome biogenesis in eukaryotes	66	0.49328747	4.94E-12	4.06E-10	0.25306046	0.26450567
MDA-MB-231	KEGG pathway name	DNA replication	33	0.49056237	1.12E-06	2.17E-05	0.33993802	0.33554322
SKBR3	KEGG pathway name	Retrograde endocannabinoid signaling	64	0.48035479	3.48E-11	1.15E-08	0.27109686	0.3941257
MDA-MB-231	KEGG pathway name	Mismatch repair	20	0.46987618	0.00027896	0.00254941	0.32654344	0.31924067
MCF10A+TGFB	KEGG pathway name	Protein digestion and absorption	15	0.46639495	0.00177784	0.01063469	0.66717574	0.27339229
SUM159PT	KEGG pathway name	Protein export	20	0.45718864	0.00040629	0.00607589	0.21155358	0.19851349
MCF10A+TGFB	KEGG pathway name	Focal adhesion	92	0.454576	6.34E-14	2.09E-11	0.52260414	0.32131724
MCF10A	KEGG pathway name	Oxidative phosphorylation	97	0.45112053	2.16E-14	3.56E-12	0.20658455	0.25271449
MCF10A+TGFB	KEGG pathway name	Protein export	20	0.44588492	0.00056363	0.00441508	0.22596523	0.16085989
MCF10A	KEGG pathway name	Parkinson disease	99	0.43594805	8.77E-14	9.62E-12	0.19221213	0.24354063
MCF10A	KEGG pathway name	Cardiac muscle contraction	30	0.43178215	4.37E-05	0.001198	0.19991649	0.34529044
MCF10A+TGFB	KEGG pathway name	Amoebiasis	32	0.42982088	2.65E-05	0.00043663	0.54406468	0.18358776
SKBR3	KEGG pathway name	Glyoxylate and dicarboxylate metabolism	23	0.41540684	0.00057188	0.00895952	0.31585884	0.40478113
MDA-MB-LM2	KEGG pathway name	Fanconi anemia pathway	35	0.411195	2.64E-05	0.00036193	0.28989773	0.25024855
MCF10A+TGFB	KEGG pathway name	Shigellosis	50	0.40558303	7.46E-07	2.46E-05	0.22579195	0.22675604
MDA-MB-231	KEGG pathway name	Homologous recombination	28	0.39897706	0.00026329	0.00247489	0.28199842	0.17898925
BT474	KEGG pathway name	Propanoate metabolism	30	0.39701435	0.00017133	0.00704598	0.48091102	0.55475569
MCF10A+TGFB	KEGG pathway name	Bacterial invasion of epithelial cells	57	0.39675639	2.39E-07	9.82E-06	0.33605645	0.28460899
MDA-MB-231	KEGG pathway name	Spliceosome	118	0.39283863	2.35E-13	1.93E-11	0.21768012	0.20815919
MCF10A+TGFB	KEGG pathway name	Hypertrophic cardiomyopathy (HCM)	27	0.39034164	0.00045502	0.00393955	0.36368826	0.29148579
SKBR3	KEGG pathway name	Oxidative phosphorylation	97	0.38977213	4.07E-11	6.69E-09	0.24513974	0.29940638
SKBR3	KEGG pathway name	Fructose and mannose metabolism	26	0.38588267	0.00067058	0.00959214	0.26481573	0.24703687
MCF10A	KEGG pathway name	Non-alcoholic fatty liver disease (NAFLD)	99	0.38344244	5.38E-11	2.95E-09	0.19164246	0.21687217
MDA-MB-468	KEGG pathway name	DNA replication	33	0.37869058	0.00017086	0.01873763	0.21155508	0.25921637
SKBR3	KEGG pathway name	Parkinson disease	99	0.37703591	1.12E-10	9.18E-09	0.21536469	0.29940638
MCF10A	KEGG pathway name	Aminoacyl-tRNA biosynthesis	42	0.37432065	2.81E-05	0.00083949	0.16861444	0.14213002
MDA-MB-LM2	KEGG pathway name	Th1 and Th2 cell differentiation	28	0.37254943	0.00065615	0.00568089	0.24975885	0.21613643
MDA-MB-330	KEGG pathway name	Lysosome	81	0.37207598	8.14E-09	6.70E-07	0.36511622	0.2604188
SUM159PT	KEGG pathway name	Leukocyte transendothelial migration	46	0.37143747	1.37E-05	0.00064428	0.33127971	0.21646594
MDA-MB-LM2	KEGG pathway name	DNA replication	33	0.36986326	0.00024161	0.00264962	0.23955198	0.25629062
SUM159PT	KEGG pathway name	Dilated cardiomyopathy (DCM)	27	0.36940907	0.00090692	0.01028885	0.43927283	0.3485682
SUM159PT	KEGG pathway name	Th17 cell differentiation	36	0.36620918	0.00014734	0.00255122	0.21103037	0.18129639
MDA-MB-134-VI	KEGG pathway name	Retrograde endocannabinoid signaling	64	0.3655943	4.61E-07	7.58E-05	0.26683625	0.37823087
MCF10A+TGFB	KEGG pathway name	Serotonergic synapse	27	0.36507782	0.00104171	0.00685443	0.1991012	0.15673244
MCF10A+TGFB	KEGG pathway name	Amino sugar and nucleotide sugar metabolism	36	0.36023102	0.00018879	0.00207043	0.2743806	0.23687719
MCF10A+TGFB	KEGG pathway name	Phagosome	69	0.36005222	2.55E-07	9.33E-06	0.2516218	0.11227918
SKBR3	KEGG pathway name	Ribosome biogenesis in eukaryotes	66	0.35989459	4.67E-07	1.92E-05	0.17096258	0.15685149
SUM159PT	KEGG pathway name	Focal adhesion	92	0.35588745	4.30E-09	4.71E-07	0.34303813	0.20425183
MCF10A+TGFB	KEGG pathway name	Regulation of actin cytoskeleton	109	0.35408566	2.13E-10	2.34E-08	0.31807398	0.22587444
MDA-MB-231	KEGG pathway name	Basal transcription factors	32	0.35367722	0.00054622	0.0043831	0.26279153	0.35258007
T47D	KEGG pathway name	Lysosome	81	0.35307118	4.48E-08	1.47E-05	0.31776683	0.28438965
SKBR3	KEGG pathway name	Carbon metabolism	90	0.35307007	8.26E-09	4.53E-07	0.25422173	0.30924977
MCF10A+TGFB	KEGG pathway name	Leukocyte transendothelial migration	46	0.35197111	3.78E-05	0.00056514	0.34147074	0.210766
MCF10A	KEGG pathway name	Alzheimer disease	114	0.35107929	1.21E-10	4.97E-09	0.16045308	0.20520576
MCF10A+TGFB	KEGG pathway name	Salmonella infection	49	0.34935098	2.44E-05	0.00042256	0.1966507	0.14300148
MCF10A+TGFB	KEGG pathway name	Cardiac muscle contraction	30	0.34814491	0.00098299	0.00673759	0.14707941	0.13206803
SKBR3	KEGG pathway name	Ribosome	120	0.34320522	1.09E-10	1.19E-08	0.12376619	0.07389155
MDA-MB-LM2	KEGG pathway name	Nucleotide excision repair	39	0.34237474	0.00022199	0.00260842	0.21145883	0.23243536
MCF10A+TGFB	KEGG pathway name	Dilated cardiomyopathy (DCM)	27	0.33983561	0.00227098	0.01266361	0.33215735	0.37521431
MDA-MB-231	KEGG pathway name	Nucleotide excision repair	39	0.3392286	0.00025355	0.00245349	0.23611334	0.21172641
MCF10A+TGFB	KEGG pathway name	Pathogenic Escherichia coli infection	37	0.33798781	0.00038365	0.00341136	0.20794444	0.19316709
MCF10A	KEGG pathway name	Huntington disease	129	0.33204364	9.79E-11	4.60E-09	0.13603253	0.18558785

Column	Type	Name	Size	Score	P value	Benj. Hoch. FDR	Mean	Median
MDA-MB-231	KEGG pathway name	Cell cycle	83	0.33033516	2.21E-07	5.59E-06	0.23805019	0.18689963
MDA-MB-330	KEGG pathway name	Glycerophospholipid metabolism	43	0.32858609	0.00019916	0.00595673	0.30310583	0.26342201
SKBR3	KEGG pathway name	Glycolysis / Gluconeogenesis	41	0.32430757	0.0003361	0.00581982	0.29724608	0.38429457
MDA-MB-LM2	KEGG pathway name	NF-kappa B signaling pathway	36	0.32254506	0.00082887	0.00681747	0.24738367	0.18922679
MCF10A	KEGG pathway name	Thermogenesis	150	0.32068498	1.72E-11	1.13E-09	0.13061466	0.1875025
SUM159PT	KEGG pathway name	Ribosome	120	0.32064055	1.64E-09	2.70E-07	0.10806045	0.14524656
MDA-MB-231	KEGG pathway name	RNA transport	126	0.31864393	8.37E-10	2.50E-08	0.18429732	0.19118626
SUM159PT	KEGG pathway name	Cholinergic synapse	32	0.31450642	0.00211119	0.01827843	0.21164562	0.15278596
SUM159PT	KEGG pathway name	Bacterial invasion of epithelial cells	57	0.31287064	4.62E-05	0.00152008	0.19372607	0.18900955
MCF10A+TGFB	KEGG pathway name	Gap junction	37	0.31263419	0.00102089	0.00685457	0.19649587	0.11029983
MCF10A+TGFB	KEGG pathway name	Protein processing in endoplasmic reticulum	126	0.31175129	1.91E-09	1.57E-07	0.17775062	0.11533875
MCF10A+TGFB	KEGG pathway name	Yersinia infection	74	0.31008663	4.33E-06	0.00010954	0.24515025	0.12264472
MCF10A+TGFB	KEGG pathway name	NOD-like receptor signaling pathway	81	0.30942583	1.63E-06	4.87E-05	0.16845923	0.1293572
MCF10A+TGFB	KEGG pathway name	Osteoclast differentiation	47	0.30794123	0.00026861	0.00276163	0.17432002	0.14110208
MDA-MB-LM2	KEGG pathway name	Cell cycle	83	0.30689415	1.49E-06	3.06E-05	0.22485787	0.17547865
MCF10A+TGFB	KEGG pathway name	Fc gamma R-mediated phagocytosis	54	0.30644068	0.00010244	0.00124822	0.18729008	0.14940464
MCF10A+TGFB	KEGG pathway name	Chagas disease (American trypanosomiasis)	40	0.30607012	0.00082928	0.00606293	0.13371213	0.11850466
MCF10A+TGFB	KEGG pathway name	Ribosome	120	0.3022099	1.32E-08	7.24E-07	0.08146882	0.13704717
MDA-MB-231	KEGG pathway name	Proteasome	41	0.30053741	0.00089074	0.00637072	0.18346054	0.13850889
MCF10A+TGFB	KEGG pathway name	VEGF signaling pathway	34	0.29583487	0.00288076	0.01458109	0.20762713	0.13390578
MCF10A+TGFB	KEGG pathway name	NF-kappa B signaling pathway	36	0.29576094	0.00217402	0.01277234	0.20119694	0.14926641
MCF10A+TGFB	KEGG pathway name	C-type lectin receptor signaling pathway	51	0.29485215	0.0002798	0.00278947	0.13504075	0.12670949
MDA-MB-231	KEGG pathway name	mRNA surveillance pathway	69	0.29269154	2.79E-05	0.00039966	0.16944419	0.15776017
MDA-MB-231	KEGG pathway name	Fanconi anemia pathway	35	0.28991867	0.0030465	0.01728102	0.21388327	0.13068552
MCF10A+TGFB	KEGG pathway name	B cell receptor signaling pathway	38	0.28782486	0.00218097	0.01258841	0.16341066	0.10698313
MDA-MB-231	KEGG pathway name	NF-kappa B signaling pathway	36	0.28550802	0.00308535	0.01720473	0.22019885	0.16267131
SKBR3	KEGG pathway name	Non-alcoholic fatty liver disease (NAFLD)	99	0.28426916	1.15E-06	3.80E-05	0.15966449	0.22586834
SKBR3	KEGG pathway name	Alzheimer disease	114	0.28359853	1.99E-07	9.33E-06	0.16349225	0.2227172
SUM159PT	KEGG pathway name	C-type lectin receptor signaling pathway	51	0.28253772	0.00049847	0.00683318	0.13937353	0.10244784
SUM159PT	KEGG pathway name	Small cell lung cancer	49	0.2806212	0.00069899	0.00851728	0.2389185	0.10540383
MDA-MB-330	KEGG pathway name	Peroxisome	56	0.27640002	0.00036014	0.00911419	0.33454714	0.2439001
SKBR3	KEGG pathway name	Biosynthesis of amino acids	54	0.27408275	0.00051172	0.00841783	0.1994707	0.2320632
SUM159PT	KEGG pathway name	Platelet activation	49	0.27399959	0.00093301	0.01023198	0.12740585	0.11382803
MDA-MB-LM2	KEGG pathway name	Small cell lung cancer	49	0.27287709	0.00097924	0.00767068	0.24814146	0.23270854
MDA-MB-LM2	KEGG pathway name	RNA transport	126	0.27253257	1.52E-07	3.86E-06	0.14600882	0.16754885
SUM159PT	KEGG pathway name	Epstein-Barr virus infection	106	0.27229763	1.45E-06	7.96E-05	0.17983893	0.08048196
MDA-MB-LM2	KEGG pathway name	Salmonella infection	49	0.27053056	0.0010828	0.00828469	0.20272373	0.17989901
SUM159PT	KEGG pathway name	Osteoclast differentiation	47	0.26253166	0.00189312	0.01683343	0.13741273	0.10244784
MCF10A+TGFB	KEGG pathway name	Axon guidance	77	0.26131213	7.85E-05	0.00103259	0.16764244	0.06988103
MCF10A+TGFB	KEGG pathway name	Small cell lung cancer	49	0.26098924	0.00161703	0.01003779	0.33983107	0.12670949
SUM159PT	KEGG pathway name	Axon guidance	77	0.2599005	8.58E-05	0.00201533	0.24015373	0.08311725
MCF10A+TGFB	KEGG pathway name	Toxoplasmosis	46	0.25987145	0.00234729	0.01265999	0.19510287	0.07492487
MCF10A+TGFB	KEGG pathway name	T cell receptor signaling pathway	50	0.2570534	0.00170938	0.01041454	0.08924671	0.08692617
SUM159PT	KEGG pathway name	HIF-1 signaling pathway	60	0.2564884	0.00061282	0.0077545	0.19369081	0.09473131
MCF10A+TGFB	KEGG pathway name	PI3K-Akt signaling pathway	115	0.25614026	2.39E-06	6.55E-05	0.22992691	0.09216882
MCF10A+TGFB	KEGG pathway name	Kaposi sarcoma-associated herpesvirus infection	86	0.25559162	4.52E-05	0.00064589	0.11697477	0.08153176
SUM159PT	KEGG pathway name	Hepatocellular carcinoma	82	0.25222015	8.42E-05	0.00230959	0.17249248	0.10443788
MDA-MB-LM2	KEGG pathway name	Focal adhesion	92	0.2514769	3.33E-05	0.00043842	0.27312814	0.17784517
MDA-MB-LM2	KEGG pathway name	Spliceosome	118	0.25088853	2.88E-06	5.57E-05	0.13039338	0.13048896
MDA-MB-330	KEGG pathway name	Phosphatidylinositol signaling system	58	0.25023866	0.00101368	0.01961763	0.25213207	0.20924527
MCF10A	KEGG pathway name	Retrograde endocannabinoid signaling	64	0.24633027	0.00068103	0.01244771	0.07765044	0.16378186
MCF10A+TGFB	KEGG pathway name	Relaxin signaling pathway	48	0.24484423	0.00341525	0.01702451	0.13283588	0.08724757
SUM159PT	KEGG pathway name	Phagosome	69	0.24444189	0.00046703	0.0066806	0.21345383	0.06511242
MCF10A+TGFB	KEGG pathway name	Non-alcoholic fatty liver disease (NAFLD)	99	0.24317743	3.18E-05	0.00049793	0.07037141	0.07054128
SKBR3	KEGG pathway name	Huntington disease	129	0.24235248	2.33E-06	6.39E-05	0.13093622	0.04917455
MDA-MB-LM2	KEGG pathway name	Oocyte meiosis	75	0.24023886	0.00033884	0.00348367	0.16075836	0.13399564
MDA-MB-468	KEGG pathway name	Spliceosome	118	0.23994309	7.63E-06	0.00251013	0.13121823	0.10898832
MCF10A+TGFB	KEGG pathway name	AGE-RAGE signaling pathway in diabetic complications	48	0.23972503	0.00415108	0.01979282	0.21751564	0.06245782
MDA-MB-LM2	KEGG pathway name	Human T-cell leukemia virus 1 infection	108	0.23807923	2.12E-05	0.00031773	0.16955381	0.14323246
MCF10A+TGFB	KEGG pathway name	Retrograde endocannabinoid signaling	64	0.23619612	0.00112459	0.00725473	0.05104915	0.07520739
SKBR3	KEGG pathway name	Thermogenesis	150	0.234439	8.73E-07	3.19E-05	0.08904996	0.10254027
MCF10A+TGFB	KEGG pathway name	Alzheimer disease	114	0.23264334	1.99E-05	0.00036333	0.07241145	0.05348378
MCF10A+TGFB	KEGG pathway name	Parkinson disease	99	0.23205232	7.19E-05	0.00098537	0.05109026	0.04951694
SUM159PT	KEGG pathway name	Herpes simplex virus 1 infection	95	0.23085652	0.00010882	0.00223752	0.16573092	0.08641892
MDA-MB-134-VI	KEGG pathway name	Oxidative phosphorylation	97	0.22980821	9.93E-05	0.00408468	0.15773414	0.25713968
SUM159PT	KEGG pathway name	Proteoglycans in cancer	99	0.22912294	8.86E-05	0.00194333	0.19969168	0.10984061
MDA-MB-LM2	KEGG pathway name	Ribosome biogenesis in eukaryotes	66	0.22836371	0.00138533	0.00949525	0.12319984	0.12977775
SUM159PT	KEGG pathway name	Influenza A	78	0.22777458	0.00053174	0.00699768	0.16956293	0.09450989
MCF10A+TGFB	KEGG pathway name	Ras signaling pathway	75	0.22670974	0.00072005	0.00538403	0.10677236	0.05463751
SUM159PT	KEGG pathway name	Regulation of actin cytoskeleton	109	0.22481397	5.51E-05	0.00164889	0.18838699	0.08961246
MCF10A+TGFB	KEGG pathway name	Autophagy - animal	82	0.22480756	0.0004572	0.0038569	0.0774167	0.04932462

Column	Type	Name	Size	Score	P value	Benj. Hoch. FDR	Mean	Median
MDA-MB-231	KEGG pathway name	Human T-cell leukemia virus 1 infection	108	0.2207849	8.06E-05	0.00098237	0.14632433	0.14258345
SUM159PT	KEGG pathway name	Chemokine signaling pathway	68	0.21927016	0.00183276	0.01674942	0.14039904	0.09221948
MCF10A+TGFB	KEGG pathway name	mTOR signaling pathway	78	0.21874164	0.00087832	0.00614826	0.06410363	0.04523966
SUM159PT	KEGG pathway name	Human cytomegalovirus infection	110	0.21799933	8.56E-05	0.00216678	0.15668161	0.09221948
MDA-MB-LM2	KEGG pathway name	MicroRNAs in cancer	88	0.21620501	0.00048277	0.00467149	0.18850721	0.13517606
MDA-MB-231	KEGG pathway name	Ribosome	120	0.21210643	6.64E-05	0.00083989	0.10706658	0.21037537
SUM159PT	KEGG pathway name	Protein processing in endoplasmic reticulum	126	0.2119502	4.45E-05	0.00162795	0.10258736	0.05575246
MCF10A+TGFB	KEGG pathway name	Human cytomegalovirus infection	110	0.20944649	0.00016066	0.0018226	0.12866369	0.06258939
SUM159PT	KEGG pathway name	Viral carcinogenesis	114	0.20895874	0.00012715	0.00246066	0.11478366	0.05531958
MDA-MB-231	KEGG pathway name	Epstein-Barr virus infection	106	0.20499768	0.0002866	0.00254843	0.16562381	0.1571339
MDA-MB-231	KEGG pathway name	Viral carcinogenesis	114	0.2043493	0.00017868	0.00195956	0.14840344	0.13193777
BT474	KEGG pathway name	Oxidative phosphorylation	97	0.20165058	0.00063704	0.01612188	0.13334072	0.13667119
SUM159PT	KEGG pathway name	Pathways in cancer	200	0.20027524	1.34E-06	8.82E-05	0.16759027	0.05727089
SUM159PT	KEGG pathway name	Kaposi sarcoma-associated herpesvirus infection	86	0.20002942	0.00141005	0.01325442	0.13952351	0.07818229
MCF10A+TGFB	KEGG pathway name	Influenza A	78	0.19787323	0.00261708	0.01366697	0.11807026	0.04598117
MDA-MB-134-VI	KEGG pathway name	Thermogenesis	150	0.1978639	3.31E-05	0.00272208	0.15878784	0.23184408
MCF10A+TGFB	KEGG pathway name	Endocytosis	164	0.19686567	1.60E-05	0.0003102	0.08246173	0.04545393
MCF10A+TGFB	KEGG pathway name	Proteoglycans in cancer	99	0.19493491	0.0008531	0.00610153	0.22623626	0.04850344
MCF10A+TGFB	KEGG pathway name	Apoptosis	77	0.19190944	0.00372919	0.01804272	0.12020126	0.05463751
MCF10A+TGFB	KEGG pathway name	MAPK signaling pathway	111	0.19096599	0.00054755	0.00439377	0.08846092	0.03866695
MCF10A+TGFB	KEGG pathway name	Hepatitis C	84	0.19045869	0.00265826	0.01366511	0.06877521	0.0307583
SUM159PT	KEGG pathway name	Human T-cell leukemia virus 1 infection	108	0.1809142	0.0012354	0.01231653	0.1132528	0.05486109
MCF10A+TGFB	KEGG pathway name	Oxidative phosphorylation	97	0.18081332	0.00219557	0.0124542	0.02608115	0.03918325
MCF10A+TGFB	KEGG pathway name	Human immunodeficiency virus 1 infection	120	0.180271	0.00069837	0.00534336	0.09320196	0.03073816
MDA-MB-330	KEGG pathway name	Endocytosis	164	0.17696989	0.00010529	0.00384892	0.10131218	0.0691563
MDA-MB-LM2	KEGG pathway name	Viral carcinogenesis	114	0.17694658	0.00117502	0.00878593	0.13285215	0.12600506
BT474	KEGG pathway name	Thermogenesis	150	0.17502598	0.00024073	0.00791996	0.13442126	0.12438326
MCF10A+TGFB	KEGG pathway name	Human papillomavirus infection	150	0.17265429	0.00029214	0.00282689	0.16192951	0.03825404
MCF10A+TGFB	KEGG pathway name	Epstein-Barr virus infection	106	0.16515488	0.00347611	0.01706925	0.04430859	0.05973398
SUM159PT	KEGG pathway name	Spliceosome	118	0.16265626	0.00241494	0.0198629	0.0246788	0.05077231
MCF10A+TGFB	KEGG pathway name	Huntington disease	129	0.15610356	0.00235174	0.01247939	0.01241808	0.02857471
MCF10A+TGFB	KEGG pathway name	Pathways in cancer	200	0.14904862	0.0003216	0.00302302	0.11036876	0.04180882
SKBR3	KEGG pathway name	Metabolic pathways	786	0.10470452	1.71E-06	5.11E-05	0.03807177	0.01490465
BT474	KEGG pathway name	Metabolic pathways	786	0.10383632	2.08E-06	0.00017121	0.12676098	0.07285821
MDA-MB-468	KEGG pathway name	Metabolic pathways	786	-0.0942919	1.64E-05	0.0026958	-0.0007456	-0.0526392
SUM159PT	KEGG pathway name	Metabolic pathways	786	-0.1532233	2.52E-12	8.28E-10	-0.0963183	-0.1205412
MCF10A	KEGG pathway name	Endocytosis	164	-0.1569144	0.00058478	0.01202449	-0.0837309	-0.143426
SKBR3	KEGG pathway name	Human immunodeficiency virus 1 infection	120	-0.1790244	0.00076053	0.01000861	-0.1869642	-0.1804231
MCF10A+TGFB	KEGG pathway name	RNA transport	126	-0.1819185	0.0004581	0.00376785	-0.17825	-0.1532883
MDA-MB-134-VI	KEGG pathway name	Regulation of actin cytoskeleton	109	-0.1939278	0.00050385	0.01381385	-0.1948296	-0.1806059
SKBR3	KEGG pathway name	Human papillomavirus infection	150	-0.1988735	3.02E-05	0.00066157	-0.1897533	-0.1940193
SKBR3	KEGG pathway name	Kaposi sarcoma-associated herpesvirus infection	86	-0.2058408	0.00101859	0.01196847	-0.1895986	-0.1940193
SKBR3	KEGG pathway name	Hepatitis C	84	-0.213582	0.000753	0.01032232	-0.1850998	-0.1965066
MDA-MB-134-VI	KEGG pathway name	Focal adhesion	92	-0.2202651	0.00027849	0.00916246	-0.2258175	-0.2200891
BT474	KEGG pathway name	Epstein-Barr virus infection	106	-0.2241801	7.29E-05	0.00342765	-0.1632213	-0.1505879
BT474	KEGG pathway name	Ribosome	120	-0.2299015	1.54E-05	0.00101015	-0.1252284	-0.2690634
SUM159PT	KEGG pathway name	Retrograde endocannabinoid signaling	64	-0.233122	0.00130467	0.01262458	-0.1548863	-0.1758757
SKBR3	KEGG pathway name	Epstein-Barr virus infection	106	-0.2387924	2.39E-05	0.00056135	-0.2059486	-0.192404
MDA-MB-231	KEGG pathway name	Biosynthesis of amino acids	54	-0.244002	0.00198003	0.01229115	-0.2192773	-0.2403762
MCF10A+TGFB	KEGG pathway name	Cell cycle	83	-0.2451193	0.00012092	0.00142082	-0.2060097	-0.2521256
MDA-MB-LM2	KEGG pathway name	Estrogen signaling pathway	58	-0.2454958	0.00126233	0.00902839	-0.2045452	-0.1436742
SUM159PT	KEGG pathway name	Oxidative phosphorylation	97	-0.2458189	3.14E-05	0.00128939	-0.17064	-0.1216407
MDA-MB-134-VI	KEGG pathway name	Yersinia infection	74	-0.2462273	0.0002636	0.00963609	-0.2272364	-0.2141817
MDA-MB-134-VI	KEGG pathway name	Ribosome biogenesis in eukaryotes	66	-0.2464771	0.00055784	0.01411762	-0.1479197	-0.1498585
SKBR3	KEGG pathway name	PI3K-Akt signaling pathway	115	-0.2493148	4.40E-06	0.00011129	-0.2099704	-0.2637976
SUM44PE	KEGG pathway name	Non-alcoholic fatty liver disease (NAFLD)	99	-0.2509891	1.76E-05	0.0028874	-0.2232117	-0.243144
MDA-MB-231	KEGG pathway name	Huntington disease	129	-0.2512472	9.79E-07	2.01E-05	-0.1645514	-0.2359589
MDA-MB-231	KEGG pathway name	Non-alcoholic fatty liver disease (NAFLD)	99	-0.2566246	1.13E-05	0.00018616	-0.1642403	-0.2175714
SKBR3	KEGG pathway name	Dopaminergic synapse	50	-0.259564	0.00153913	0.01746117	-0.2356104	-0.2462988
MDA-MB-134-VI	KEGG pathway name	Epstein-Barr virus infection	106	-0.2687044	1.99E-06	0.00021837	-0.2092296	-0.2313372
SKBR3	KEGG pathway name	Oocyte meiosis	75	-0.2688086	6.08E-05	0.001176	-0.2237879	-0.2637976
MDA-MB-330	KEGG pathway name	Spliceosome	118	-0.2689923	5.24E-07	3.45E-05	-0.2436312	-0.2765941
MDA-MB-231	KEGG pathway name	Glycerophospholipid metabolism	43	-0.2698993	0.00224568	0.01343323	-0.205811	-0.2015936
MDA-MB-LM2	KEGG pathway name	Lysosome	81	-0.2828946	1.17E-05	0.00019207	-0.2204086	-0.1775215
MDA-MB-330	KEGG pathway name	Cell cycle	83	-0.2838074	8.55E-06	0.0004017	-0.3127027	-0.2822048
MDA-MB-134-VI	KEGG pathway name	Leukocyte transendothelial migration	46	-0.2846462	0.00086099	0.01888434	-0.2739068	-0.3476738
BT474	KEGG pathway name	Focal adhesion	92	-0.2895084	1.78E-06	0.00019505	-0.2137643	-0.2174748
MDA-MB-231	KEGG pathway name	N-Glycan biosynthesis	35	-0.2955495	0.00252312	0.01456328	-0.2099749	-0.2395143
MDA-MB-231	KEGG pathway name	Estrogen signaling pathway	58	-0.2999702	8.15E-05	0.00095785	-0.2922875	-0.2094418
MDA-MB-LM2	KEGG pathway name	Huntington disease	129	-0.3040444	3.13E-09	1.14E-07	-0.1705655	-0.1920881
SUM44PE	KEGG pathway name	Ribosome biogenesis in eukaryotes	66	-0.3046968	1.99E-05	0.00217705	-0.2550407	-0.3138315

Column	Type	Name	Size	Score	P value	Benj. Hoch. FDR	Mean	Median
SUM44PE	KEGG pathway name	Ribosome biogenesis in eukaryotes	66	-0.3046968	1.99E-05	0.00217705	-0.2550407	-0.3138315
T47D	KEGG pathway name	Focal adhesion	92	-0.3047479	4.94E-07	8.13E-05	-0.1374649	-0.1999311
MDA-MB-231	KEGG pathway name	Thermogenesis	150	-0.3061064	1.35E-10	4.92E-09	-0.2078701	-0.2216089
MDA-MB-330	KEGG pathway name	Nucleotide excision repair	39	-0.3123366	0.00075548	0.0155346	-0.3276297	-0.3499253
MDA-MB-LM2	KEGG pathway name	Non-alcoholic fatty liver disease (NAFLD)	99	-0.3144829	7.44E-08	2.04E-06	-0.1622213	-0.2090498
MCF10A+TGFB	KEGG pathway name	Spliceosome	118	-0.319136	2.64E-09	1.74E-07	-0.2314137	-0.231693
MDA-MB-LM2	KEGG pathway name	Retrograde endocannabinoid signaling	64	-0.3209436	9.60E-06	0.00016616	-0.1594154	-0.2333694
MDA-MB-LM2	KEGG pathway name	Metabolic pathways	786	-0.3233884	2.00E-49	6.59E-47	-0.1875579	-0.2216881
MDA-MB-231	KEGG pathway name	PPAR signaling pathway	28	-0.3303715	0.00251508	0.01477606	-0.1817404	-0.3757532
MDA-MB-231	KEGG pathway name	Retrograde endocannabinoid signaling	64	-0.3314901	4.84E-06	8.38E-05	-0.2186036	-0.2882079
MDA-MB-LM2	KEGG pathway name	Thermogenesis	150	-0.3316862	3.44E-12	1.89E-10	-0.1843687	-0.2279678
MDA-MB-330	KEGG pathway name	Fanconi anemia pathway	35	-0.3336392	0.00065002	0.01425709	-0.3253564	-0.3504164
MDA-MB-231	KEGG pathway name	Metabolic pathways	786	-0.3389447	4.06E-54	1.34E-51	-0.2389054	-0.2755735
SKBR3	KEGG pathway name	Small cell lung cancer	49	-0.3405679	3.89E-05	0.00079908	-0.2817998	-0.3141695
MDA-MB-LM2	KEGG pathway name	Glycerolipid metabolism	28	-0.3409759	0.00181769	0.0117259	-0.2063115	-0.1608392
MCF10A	KEGG pathway name	N-Glycan biosynthesis	35	-0.3518832	0.00032279	0.00816895	-0.219218	-0.1730743
MDA-MB-134-VI	KEGG pathway name	Ribosome	120	-0.3581818	1.63E-11	5.35E-09	-0.2107012	-0.2356127
MDA-MB-LM2	KEGG pathway name	Pyruvate metabolism	29	-0.3587796	0.00084027	0.00674268	-0.182174	-0.3143103
MCF10A	KEGG pathway name	Lysosome	81	-0.3592222	2.60E-08	9.51E-07	-0.2695993	-0.2813579
SKBR3	KEGG pathway name	RIG-I-like receptor signaling pathway	34	-0.3606172	0.00028038	0.00512465	-0.302302	-0.2682542
MCF10A+TGFB	KEGG pathway name	Nucleotide excision repair	39	-0.3631767	8.97E-05	0.00113484	-0.2578842	-0.2806876
SUM44PE	KEGG pathway name	Ribosome	120	-0.364777	6.88E-12	2.26E-09	-0.2758705	-0.2845187
MDA-MB-231	KEGG pathway name	Glutathione metabolism	35	-0.3656976	0.00018588	0.00197268	-0.4108594	-0.3961011
MDA-MB-LM2	KEGG pathway name	Cardiac muscle contraction	30	-0.3667688	0.0005173	0.00472757	-0.2139542	-0.2123026
T47D	KEGG pathway name	Salmonella infection	49	-0.3702428	7.73E-06	0.00084733	-0.154295	-0.2113512
MDA-MB-231	KEGG pathway name	Lysosome	81	-0.3707369	9.21E-09	2.52E-07	-0.2979028	-0.2923802
MDA-MB-134-VI	KEGG pathway name	Cytosolic DNA-sensing pathway	28	-0.3719452	0.00066956	0.0157347	-0.3390581	-0.2701229
MDA-MB-LM2	KEGG pathway name	Carbon metabolism	90	-0.3723817	1.21E-09	5.00E-08	-0.2430221	-0.2317219
MDA-MB-231	KEGG pathway name	Alzheimer disease	114	-0.3732974	7.62E-12	3.13E-10	-0.2499018	-0.2625127
SKBR3	KEGG pathway name	ECM-receptor interaction	26	-0.3733332	0.00099932	0.01217686	-0.3329766	-0.4072155
MDA-MB-231	KEGG pathway name	Fatty acid metabolism	42	-0.3824137	1.88E-05	0.00028055	-0.2763456	-0.4108745
MDA-MB-LM2	KEGG pathway name	Alzheimer disease	114	-0.3859571	1.47E-12	9.64E-11	-0.2214417	-0.2465878
MCF10A	KEGG pathway name	Vasopressin-regulated water reabsorption	27	-0.3892399	0.00047224	0.01109755	-0.2875222	-0.1774733
MCF10A+TGFB	KEGG pathway name	Homologous recombination	28	-0.391904	0.000338	0.00308894	-0.3155794	-0.4213924
MDA-MB-231	KEGG pathway name	Glycerolipid metabolism	28	-0.392904	0.00032635	0.00282549	-0.3172392	-0.2908681
MDA-MB-330	KEGG pathway name	p53 signaling pathway	38	-0.3949713	2.61E-05	0.00107285	-0.489645	-0.4457705
MDA-MB-134-VI	KEGG pathway name	NF-kappa B signaling pathway	36	-0.3998232	3.41E-05	0.00224667	-0.3863009	-0.3673303
MDA-MB-231	KEGG pathway name	beta-Alanine metabolism	20	-0.4014567	0.00190328	0.01204188	-0.3540044	-0.3244379
BT474	KEGG pathway name	Hypertrophic cardiomyopathy (HCM)	27	-0.4024065	0.00030118	0.00900786	-0.2163411	-0.2840666
MDA-MB-134-VI	KEGG pathway name	Arrhythmogenic right ventricular cardiomyopathy (ARVC)	25	-0.4026122	0.00050116	0.01498924	-0.3749205	-0.4946518
MCF10A	KEGG pathway name	SNARE interactions in vesicular transport	23	-0.4098184	0.00067814	0.01312391	-0.2955372	-0.2647889
MDA-MB-231	KEGG pathway name	Parkinson disease	99	-0.4117806	1.86E-12	1.02E-10	-0.2632324	-0.2834184
BT474	KEGG pathway name	Dilated cardiomyopathy (DCM)	27	-0.4145037	0.00019692	0.00719835	-0.2216395	-0.3348855
MDA-MB-330	KEGG pathway name	Ribosome biogenesis in eukaryotes	66	-0.4175321	5.02E-09	5.50E-07	-0.4080281	-0.5058602
MDA-MB-231	KEGG pathway name	Fructose and mannose metabolism	26	-0.4176994	0.00023161	0.00230908	-0.3488145	-0.4337969
T47D	KEGG pathway name	ECM-receptor interaction	26	-0.4201554	0.0002127	0.01749487	-0.149486	-0.2620558
MDA-MB-231	KEGG pathway name	Carbon metabolism	90	-0.4262317	3.47E-12	1.63E-10	-0.3295439	-0.3504514
MCF10A+TGFB	KEGG pathway name	Fanconi anemia pathway	35	-0.4264526	1.31E-05	0.0002694	-0.3373378	-0.3381401
MDA-MB-231	KEGG pathway name	Tryptophan metabolism	24	-0.437084	0.00021387	0.00219886	-0.4062866	-0.3725336
MDA-MB-LM2	KEGG pathway name	Terpenoid backbone biosynthesis	18	-0.4382635	0.00129937	0.00909556	-0.3258414	-0.2910113
MDA-MB-LM2	KEGG pathway name	Fatty acid elongation	17	-0.4409024	0.0016634	0.01094515	-0.3215796	-0.3003455
MDA-MB-330	KEGG pathway name	Ribosome	120	-0.4421656	9.14E-17	3.01E-14	-0.3622902	-0.4359628
MDA-MB-231	KEGG pathway name	Metabolism of xenobiotics by cytochrome P450	20	-0.4480554	0.00052959	0.00435588	-0.4949523	-0.3722371
SUM159PT	KEGG pathway name	Tryptophan metabolism	24	-0.4501895	0.00013727	0.00250891	-0.3214626	-0.3843907
MDA-MB-231	KEGG pathway name	Terpenoid backbone biosynthesis	18	-0.4522596	0.00090396	0.00619591	-0.3349801	-0.3592875
MDA-MB-LM2	KEGG pathway name	Parkinson disease	99	-0.4533308	8.79E-15	9.64E-13	-0.2465907	-0.2704515
MDA-MB-LM2	KEGG pathway name	Collecting duct acid secretion	16	-0.4565621	0.00158177	0.01062045	-0.2629469	-0.3297329
SUM159PT	KEGG pathway name	Alanine, aspartate and glutamate metabolism	22	-0.4580292	0.00020334	0.00334498	-0.3333942	-0.3781226
MDA-MB-231	KEGG pathway name	ABC transporters	18	-0.4582949	0.00077068	0.00576257	-0.3760969	-0.3210684
MDA-MB-LM2	KEGG pathway name	ABC transporters	18	-0.4618546	0.00070087	0.00591246	-0.3378823	-0.358356
MDA-MB-231	KEGG pathway name	Fatty acid degradation	29	-0.4677906	1.34E-05	0.00020967	-0.3503622	-0.4214944
MDA-MB-LM2	KEGG pathway name	Fatty acid metabolism	42	-0.4681879	1.61E-07	3.79E-06	-0.3455523	-0.4110945
MDA-MB-LM2	KEGG pathway name	beta-Alanine metabolism	20	-0.4765914	0.00022778	0.00258414	-0.2742437	-0.3808594
MDA-MB-231	KEGG pathway name	Collecting duct acid secretion	16	-0.4805649	0.00088311	0.00645653	-0.3758765	-0.4043479
MDA-MB-231	KEGG pathway name	Chemical carcinogenesis	23	-0.4816317	6.50E-05	0.00085586	-0.5591656	-0.3961011
MDA-MB-231	KEGG pathway name	Peroxisome	56	-0.4846349	3.96E-10	1.30E-08	-0.4081328	-0.3955572
SUM159PT	KEGG pathway name	Terpenoid backbone biosynthesis	18	-0.4847661	0.00037459	0.0058685	-0.3215256	-0.3494147
MDA-MB-LM2	KEGG pathway name	Peroxisome	56	-0.48919	2.71E-10	1.28E-08	-0.35601	-0.3685406
MDA-MB-231	KEGG pathway name	2-Oxocarboxylic acid metabolism	13	-0.4938659	0.00206269	0.01256713	-0.4821184	-0.5278245
MCF10A+TGFB	KEGG pathway name	Base excision repair	26	-0.5006	1.02E-05	0.00024013	-0.3586283	-0.3885993
MDA-MB-231	KEGG pathway name	Oxidative phosphorylation	97	-0.5017314	1.93E-17	3.18E-15	-0.3246918	-0.3538475
MDA-MB-231	KEGG pathway name	Glyoxylate and dicarboxylate metabolism	23	-0.503846	2.94E-05	0.00040321	-0.4204359	-0.4668196

Column	Type	Name	Size	Score	P value	Benj. Hoch. FDR	Mean	Median
MDA-MB-LM2	KEGG pathway name	Glyoxylate and dicarboxylate metabolism	23	-0.5241215	1.39E-05	0.00021712	-0.3996562	-0.4200343
MDA-MB-LM2	KEGG pathway name	Tyrosine metabolism	11	-0.5310392	0.00230425	0.01457878	-0.3658341	-0.2321909
MDA-MB-LM2	KEGG pathway name	Tryptophan metabolism	24	-0.5317009	6.69E-06	0.00012221	-0.3395857	-0.2422696
MDA-MB-231	KEGG pathway name	Propanoate metabolism	30	-0.5343934	4.23E-07	9.94E-06	-0.4037675	-0.4128117
MDA-MB-LM2	KEGG pathway name	Oxidative phosphorylation	97	-0.5350285	1.28E-19	2.11E-17	-0.2982855	-0.3166071
MDA-MB-231	KEGG pathway name	Citrate cycle (TCA cycle)	28	-0.5515011	4.56E-07	1.00E-05	-0.4306408	-0.4050199
MDA-MB-LM2	KEGG pathway name	Fatty acid degradation	29	-0.5548525	2.42E-07	5.30E-06	-0.3813794	-0.4043801
MDA-MB-231	KEGG pathway name	Fatty acid biosynthesis	11	-0.5568281	0.00139373	0.00935793	-0.4251878	-0.5109617
MCF10A+TGFB	KEGG pathway name	Mismatch repair	20	-0.565783	1.21E-05	0.00026531	-0.4151846	-0.5152042
MDA-MB-231	KEGG pathway name	Other glycan degradation	12	-0.5692565	0.00064414	0.00504576	-0.3986252	-0.3826368
SUM159PT	KEGG pathway name	Retinol metabolism	11	-0.5696035	0.00107825	0.01144337	-0.4300367	-0.4840484
MDA-MB-LM2	KEGG pathway name	Propanoate metabolism	30	-0.5746365	5.35E-08	1.60E-06	-0.3985149	-0.5006669
MDA-MB-330	KEGG pathway name	Mismatch repair	20	-0.579563	7.38E-06	0.00040467	-0.5594313	-0.4609116
MDA-MB-231	KEGG pathway name	Steroid biosynthesis	14	-0.5816787	0.00016615	0.00188493	-0.5082721	-0.6361456
MDA-MB-231	KEGG pathway name	Tyrosine metabolism	11	-0.5892031	0.00072022	0.00551053	-0.5127018	-0.6085643
MDA-MB-LM2	KEGG pathway name	Butanoate metabolism	17	-0.5915413	2.45E-05	0.00035113	-0.443928	-0.4479209
MDA-MB-LM2	KEGG pathway name	Steroid hormone biosynthesis	11	-0.5961859	0.00062199	0.00553062	-0.5082774	-0.5454379
MDA-MB-LM2	KEGG pathway name	Citrate cycle (TCA cycle)	28	-0.5997312	4.13E-08	1.36E-06	-0.4055945	-0.4124376
MDA-MB-LM2	KEGG pathway name	Steroid biosynthesis	14	-0.602865	9.51E-05	0.00120343	-0.4678706	-0.5509967
MDA-MB-231	KEGG pathway name	Retinol metabolism	11	-0.6039622	0.00052733	0.00444852	-0.4867938	-0.5843709
MDA-MB-LM2	KEGG pathway name	Glycosylphosphatidylinositol (GPI)-anchor biosynthesis	11	-0.607004	0.0004941	0.00464457	-0.3706218	-0.3017373
MDA-MB-LM2	KEGG pathway name	Fatty acid biosynthesis	11	-0.6108922	0.00045447	0.00453092	-0.4221835	-0.4913712
MDA-MB-134-VI	KEGG pathway name	Protein digestion and absorption	15	-0.6150607	3.77E-05	0.00206709	-0.5844234	-0.4571809
MDA-MB-LM2	KEGG pathway name	Retinol metabolism	11	-0.6295924	0.000302	0.00320507	-0.4293467	-0.5333211
MDA-MB-231	KEGG pathway name	Valine, leucine and isoleucine degradation	42	-0.6337794	1.32E-12	8.70E-11	-0.5080881	-0.5146616
MDA-MB-231	KEGG pathway name	Glycosaminoglycan degradation	8	-0.6384688	0.00177322	0.01166776	-0.4184448	-0.3806743
MDA-MB-134-VI	KEGG pathway name	African trypanosomiasis	9	-0.6400362	0.00088956	0.01829158	-1.1362452	-1.2133539
MDA-MB-231	KEGG pathway name	Butanoate metabolism	17	-0.6443352	4.32E-06	7.89E-05	-0.5181802	-0.5445788
MCF10A+TGFB	KEGG pathway name	DNA replication	33	-0.6497638	1.13E-10	1.85E-08	-0.4551949	-0.5343197
MDA-MB-LM2	KEGG pathway name	Pentose and glucuronate interconversions	11	-0.65554	0.00016822	0.00204977	-0.5058892	-0.3834166
MDA-MB-LM2	KEGG pathway name	Valine, leucine and isoleucine degradation	42	-0.6676548	7.96E-14	6.55E-12	-0.4920701	-0.4930271
MDA-MB-231	KEGG pathway name	Nitrogen metabolism	7	-0.6808042	0.00182068	0.01174517	-0.8253522	-0.7531278
SKBR3	KEGG pathway name	Synthesis and degradation of ketone bodies	8	-0.6832558	0.00082262	0.01040936	-0.734722	-0.8274795
MDA-MB-134-VI	KEGG pathway name	Hematopoietic cell lineage	11	-0.6911419	7.28E-05	0.003423	-0.6448907	-0.6673414
MDA-MB-330	KEGG pathway name	DNA replication	33	-0.6959967	4.92E-12	8.09E-10	-0.7162819	-0.6582424
BT474	KEGG pathway name	ECM-receptor interaction	26	-0.699003	7.21E-10	2.37E-07	-0.5345742	-0.5308132
MDA-MB-LM2	KEGG pathway name	Ubiquinone and other terpenoid-quinone biosynthesis	7	-0.7080131	0.00118428	0.00865843	-0.5870271	-0.4601668
BT474	KEGG pathway name	Malaria	11	-0.7162166	3.94E-05	0.00216236	-0.6462177	-0.5804666
MDA-MB-231	KEGG pathway name	Ubiquinone and other terpenoid-quinone biosynthesis	7	-0.7254185	0.00089262	0.0062483	-0.6460192	-0.452377
MCF10A	KEGG pathway name	Other glycan degradation	12	-0.7711819	3.79E-06	0.00012461	-0.6077353	-0.6123677